Microengineered Electrochemical Tools for in-situ Monitoring of Marine Environment

THÈSE Nᴼ 8151 (2017)

PRÉSENTÉE LE 8 DÉCEMBRE 2017
À LA FACULTÉ DES SCIENCES ET TECHNIQUES DE L'INGÉNIEUR
LABORATOIRE DES MICROSYSTÈMES POUR LES TECHNOLOGIES SPATIALES
PROGRAMME DOCTORAL EN MICROSYSTÈMES ET MICROÉLECTRONIQUE

ÉCOLE POLYTECHNIQUE FÉDÉRALE DE LAUSANNE

POUR L'OBTENTION DU GRADE DE DOCTEUR ÈS SCIENCES

PAR

Marianna FIGHERA

acceptée sur proposition du jury:

Prof. M. Gijs, président du jury
Prof. H. Shea, Dr P. van der Wal, directeurs de thèse
Prof. A. Kaempfer-Homsy, rapporteuse
Dr E. L'Hostis, rapporteuse
Prof. N. de Rooij, rapporteur

EPFL

ÉCOLE POLYTECHNIQUE
FÉDÉRALE DE LAUSANNE

Suisse
2017

Acknowledgements

During these years I had the chance to meet extraordinary people and friends from all over the world: Alexandra and Jürg, Francisco, Camila, Carol, Liz, Andrea y Rémi, Laura y Felipe, Patrick, Juan y Cecilia, Laura and Felix, Letizia e Jasha, Dina, Giovanna, Line, Eric, Andrea, Julian, Valerie, Lina, Arlette, Sofy y Juampi, Nataly, Nneka, Mario, Olga, Sarah, Douglas, Malena, Angelica, Francesco, Victor, Mila. It was a great pleasure to meet you and to share with you incredible moments which made my life here in Neuchâtel such beautiful.

Thanks to my Italian friends who also moved to Switzerland during these years: Roberto, Alessandro, Andrea and Elena. It was great to have still the opportunity to meet and share moments together. A special thanks to my friend Annalisa with whom I shared all my academic life since the very first days of the Bachelor till now during the PhD. Annalisa, you have been always a point of reference for me and a great friend. Thank you for all your support and suggestions which helped me to be here now.

Finally I want to thank the most important people of my life, my family. Mom, you have been my model since I was a child, I have always looked at you with plenty of admiration and desiring being as you someday. I love your strength, your valor, your determination, and your kind heart. Dad, I thank you for being always such a warm-hearted person with me and my brother. You are an example to follow for us for your integrity and moral. Thank you, mom and dad, for having taught me to do always my best, to be a correct and honest person and fight to reach my objectives despite difficulties or problems, I could not be here without all your help and love. Giorgio, dear brother, I want to thank you for all your wise advice and the long conversations we had during the last years, I am proud of the man you are. I loved to live together some months during my stay here in Switzerland.

In the end, I express all my gratitude to my lovely husband, Luis Carlos. You have been all for me: my friend, my adviser, my dancer, my colleague and my guide in all these years. You have been giving me your support since I met you, pushing me to be always a better person. Thanks for helping me with my work Dr. Mendoza, for sharing with me the passion for dancing, for your love, dearness and presence, and for being as you are, full of joy and always ready to make me laugh. I can reach this achievement especially thanks to you.

Abstract

Measuring the concentration of different compounds in aquatic ecosystem and understanding their impact on the environment are some of the main objectives in the environmental monitoring field. Trace metals, nutrients, volatile organic compounds, biotoxins and algaes are among the most important targets of such assessment. Their quantification at an appropriate time scale and with high spatial resolution is in fact crucial in order to understand their dynamics and their role in the marine biogeochemical processes in which they are involved. *In situ* continuous monitoring is the key to achieve these objectives, thus pushing research to develop rugged, simple, accurate and reliable instrumentation with minimal perturbation of the marine environment. This thesis is focused on the development of new micro-engineered tools with the aim to improve the performance of well-established electroanalytical techniques by exploiting scaling and microfabrication techniques. The developed devices were designed and fabricated by using different techniques, such as thin-film technology, printing, soft lithography and additive manufacturing techniques.

Nutrients such as nitrates, nitrites and phosphates, exert a strong control on the ocean primary productivity and growth of living organisms. Their quantification is often hampered by the high sodium chloride content present in the seawater matrix for a wide range of detection techniques. Literature is rich in research for developing cost-effective and efficient desalination tools, but is weak concerning systems which provide a selective removal of chloride with respect to other ions present in seawater. Some publications report on the development of such systems. One of the developed tools of this thesis is a fast, environmentally-friendly and low-cost microfluidic platform for selective sodium chloride removal to serve as a pre-treatment unit prior to nutrients detection. In this device chloride removal occurs upon bulk electrolysis in a thin-layer configuration. The device allowed a ten times-fold reduction of chloride concentration.

Trace metals are ubiquitous in marine environment and their speciation may vary continuously in space and time reflecting changing in physicochemical conditions of the aquatic system. Their quantification is commonly achieved by voltammetric techniques in a three-electrode electrochemical cell. Voltammetric probes have been reported in literature for detection of trace metals such as lead, cadmium, copper and zinc. The core of these systems is a miniaturized sensor composed by an array of microelectrodes serving as working electrode (WE) and a counter electrode (CE); an external reference electrode (RE) placed next to the sensor is used. The reference electrode is a crucial component for the functioning of such sensors however its integration is still challenging. The second tool developed in the framework of this thesis is a three-electrode on-chip sensor for the detection of trace metals, where reference electrode integration is achieved by using a poly(vinyl chloride) membrane plasticized with ionic liquids as diffusion barrier on top of a silver/silver chloride electrode. These sensors were capable to detect trace metals, but further improvement is required for their quantification.

Marine biotoxins are compounds with toxic activity that accumulate in fish and shellfish and can cause human illnesses when they enter the trophic chain. Among the various species of biotoxins, another target of this work is saxitoxin, a low molecular weight neurotoxin mainly produced by marine dinoflagellates. Its detection is hindered by its low concentration, therefore a pre-concentration unit is required. Another herein developed tool is a simple microfluidic platform predisposed for pre-concentration of saxitoxin; its working principle is based on the binding of the saxitoxin to a specific aptamer and its release upon a temperature increase.

Volatile organic compounds (VOCs), such as hydrocarbons and chlorinated hydrocarbons, are pollutants contaminating coastal waters and are considered as significant indicators of urban and industrial pollution. To monitor the changes in VOCs concentration and their impact on the environment, accurate and precise measurements of a large number of organic compounds in seawater, even at very low concentration levels, are required. Among different detection techniques, mid-infrared fiber-optic evanescent wave sensors constitute one of the most promising approaches for continuous multicomponent VOCs pollution monitoring in seawater. In this thesis a simple and low-cost microfluidic platform designed to optimize the enrichment of the polymer layer coating the fiber with the target analytes is developed. The optimization of the design has allowed the simultaneous detection of ten VOCs species with this platform.

All the tools developed within this thesis are intended to be integrated in submersible probes for *in situ* deployment. The herein developed two-electrode (WE-CE) on-chip trace metal sensors have been successfully deployed in several field campaigns, while the other devices have to be further optimized to allow their integration in the probes.

Keywords

Electroanalytical tools, environmental monitoring, trace metals sensing, square wave voltammetry, thin-film technology, SU-8, solid state reference electrode, sample pre-treatment, desalination, thin-layer coulometry, Ag ink, screen printed electrodes, biotoxins pre-concentration, microfluidic device, VOCs detection, 3D printing

Résumé

Mesurer la concentration de différents composés dans l'écosystème aquatique et la compréhension de leur impact sur l'environnement sont quelques-uns des principaux objectifs dans le domaine de la surveillance environnementale. Les métaux traces, les nutriments, les composés organiques volatils, les biotoxines et les algues sont parmi les cibles les plus importantes d'une telle évaluation. Leur quantification à une échelle de temps appropriée et avec une résolution spatiale élevée est en effet cruciale pour comprendre leur dynamique et leur rôle dans les processus biogéochimiques marins dans lesquels ils sont impliqués. La surveillance continue *in situ* est la clé pour atteindre ces objectifs, poussant ainsi la recherche à développer des instruments robustes, simples, pratiques et fiables avec une perturbation minimale de l'environnement marin. Cette thèse se concentre sur le développement de nouveaux outils de micro-ingénierie dans le but d'améliorer les performances des techniques électro-analytiques bien établies en exploitant les techniques de miniaturisation et de micro-fabrication. Les dispositifs développés ont été dessinés et fabriqués en utilisant différentes techniques, telles que la technologie de couche mince, les techniques d'impression, la lithographie douce et les techniques de fabrication additive.

Les éléments nutritifs tels que les nitrates, les nitrites et les phosphates exercent un fort contrôle sur la productivité primaire de l'océan et la croissance des organismes vivants. Leur quantification est souvent entravée par la teneur élevée en chlorure de sodium présente dans la matrice d'eau de mer pour une large gamme de techniques de détection. La littérature est riche en recherche pour le développement des outils de dessalement rentables et efficaces, mais est faible en ce qui concerne les systèmes qui fournissent une élimination sélective du chlorure de sodium par rapport aux autres ions présents dans l'eau de mer. Peu d'études ont été conduites sur le développement de tels systèmes. L'un des outils développés de cette thèse est une plateforme microfluidique rapide, écologique et peu coûteuse pour l'élimination du chlorure de sodium, qui sert comme unité de prétraitement avant la détection des nutriments. L'élimination du chlorure se produit lors d'une électrolyse complète dans une configuration en couche mince. Le dispositif a permis une réduction de la concentration de chlorure à dix fois.

Les métaux traces sont omniprésents dans l'environnement marin et leur spéciation peut varier continuellement dans l'espace et le temps, ce qui reflète l'évolution des conditions physico-chimiques du système aquatique. Leur quantification est généralement obtenue par des techniques voltamétriques dans une cellule électrochimique à trois électrodes. Des sondes voltamétriques ont été décrites dans la littérature pour la détection de métaux traces tels que le plomb, le cadmium, le cuivre et le zinc. Le noyau de ces systèmes est le capteur miniaturisé composé d'un array de microélectrodes servant d'électrode de travail et d'une contre-électrode; une électrode de référence externe est placée à côté du capteur. L'électrode de référence est une composante cruciale pour le fonctionnement de ces capteurs, mais son intégration est encore un défi. Le deuxième outil développé dans le cadre de cette thèse est un capteur à trois électrodes sur puce pour la détection de

métaux traces, où l'intégration de l'électrode de référence est réalisée en utilisant une membrane de polychlorure de vinyle plastifiée avec des liquides ioniques pour fournir la barrière de diffusion au-dessus d'une électrode d'argent/chlorure d'argent. Ces capteurs sont capables de détecter les métaux traces, mais des améliorations supplémentaires sont nécessaires pour permettre leur quantification.

Les biotoxines marines sont des composés à activité toxique qui s'accumulent dans les poissons et les crustacés et peuvent causer des maladies humaines lorsqu'ils entrent dans la chaîne alimentaire. Parmi les différentes espèces de biotoxines, une autre cible de ce travail est la saxitoxine, une neurotoxine de faible poids moléculaire produite principalement par des dinoflagellés marins. Sa détection est entravée par sa faible concentration, donc une unité de pré-concentration est nécessaire. Un troisième outil développé dans cette thèse est une plate-forme microfluidique prédisposée à la pré-concentration de la saxitoxine ; son principe de fonctionnement est basé sur la liaison de la saxitoxine à un aptamère spécifique et sa libération par une augmentation de température.

Les composés organiques volatils (COV), tels que les hydrocarbures et les hydrocarbures chlorés, sont des contaminants des eaux côtières et sont considérés comme des indicateurs importants de la pollution urbaine et industrielle. Pour surveiller les changements dans les concentrations de COV et leur impact sur l'environnement, des mesures précises d'un grand nombre de composés organiques dans l'eau de mer, même à des niveaux de concentration très faibles, sont nécessaires. Parmi les différentes techniques de détection, les capteurs à fibre optique à ondes évanescentes dans le moyen infrarouge constituent une des approches la plus prometteuse pour la surveillance continue de la pollution des COV à composants multiples dans l'eau de mer. Dans cette thèse, une plateforme microfluidique peu coûteuse conçue pour optimiser l'enrichissement des analytes cibles dans la couche de polymère qui recouvre la fibre est développée. L'optimisation du dessin a permis la détection simultanée de dix espèces de COV avec cette plateforme.

Tous les outils développés dans le cadre de cette thèse sont destinés à être intégrés dans des sondes submersibles pour un déploiement *in situ*. Les capteurs de métaux traces ont étés déployés avec succès dans plusieurs campagnes de mesures, tandis que les autres appareils doivent encore être optimisés pour permettre leur intégration dans les sondes.

Mots-clés

Outils électroanalytiques, surveillance de l'environnement, détection des métaux traces, voltamétrie des ondes carrées, technologie de couche mince, SU-8, électrode de référence à l'état solide, prétraitement des échantillons, dessalement, coulométrie à couche mince, encre d'argent, électrodes imprimées, préconcentration de biotoxines, dispositif microfluidique, détection des COV, impression 3D

Riassunto

Misurare la concentrazione di differenti composti nell'ecosistema acquatico e comprendere il loro impatto sull'ambiente, sono alcuni dei principali obettivi nel campo del monitoraggio ambientale. Tracce metalliche, nutrienti, composti organici volatili, biotossine e alghe rientrano tra i piú importanti target di tale analisi. La loro quantificazione in una scala temporale appropriata e con alta risoluzione spaziale è infatti cruciale per comprendere le loro dinamiche e il loro ruolo nei processi biogeochimici marini in cui sono coinvolti. Il monitoraggio continuo *in situ* è la chiave per raggiungere questi obiettivi, spingendo cosí la ricerca verso lo sviluppo di strumenti robusti, semplici, precisi e affidabili, con minima perturbazione dell'ambiente marino. Questa tesi è incentrata sullo sviluppo di nuovi strumenti micro-ingegnerizzati con l'obiettivo di migliorare le prestazioni di tecniche elettroanalitiche consolidate sfruttando tecniche di scala e di microfabbricazione. I dispositivi sviluppati sono stati progettatti e fabbricati utilizzando differenti tecniche, come la tecnologia a film sottile, tecniche di stampa, litografia morbida e tecniche di manufattura additiva.

Nutrienti quali nitrati, nitriti e fosfati, esercitano un forte controllo sulla produttività oceanica primaria e sulla crescita di organismi viventi. La loro quantificazione è spesso ostacolata dall'alto contenuto di cloruro presente nella matrice d'acqua marina per una vasta gamma di tecniche di rilevazione. La letteratura è ricca di ricerche focalizzate sullo sviluppo di dispositivi di desalinizzazione efficienti ed economici, ma è carente in quanto a dispositivi che forniscono una rimozione selettiva del cloruro rispetto ad altri ioni presenti nell'acqua di mare. Pochi studi sono stati infatti condotti in merito allo sviluppo di tali sistemi. Uno degli strumenti sviluppati in questa tesi è una piattaforma microfluidica rapida, ecologica ed economica per la rimozione di cloruro di sodio, da utilizzare come unità di pretrattamento a monte dello strumento di misura dei nutrienti. La rimozione del cloruro avviene tramite elettrolisi esaustiva in una configurazione a strato sottile. Tale dispositivo ha permesso una riduzione della concentrazione di cloruro pari a dieci volte.

Le tracce metalliche sono onnipresenti nell'ambiente marino e la loro speciazione puó cambaire continuamente nello spazio e nel tempo rifettendo cambiamenti nelle condizioni fisico-chimiche del sistema acquatico. La loro quantificazione è comunemente ottenuta tramite tecniche voltammetriche in una cella elettrochimica a tre elettrodi. In letteratura sono state descritte delle sonde voltammetriche per la detezione di tracce metalliche come piombo, cadmio, rame e zinco. Il nucleo di questi sistemi è un sensore miniaturizzato composto da un array di microelettrodi che funge da elettrodo di lavoro e da un contro-elettrodo; l'elettrodo di riferimento è esterno ed è posizionato vicino al sensore. L'elettrodo di riferimento è una componente fondamentale per il funzionamento di tali sensori, tuttavia la sua integrazione rappresenta ancor oggi una sfida. Il secondo dispositivo sviluppato nel quadro di questa tesi è un sensore con tre elettrodi a bordo per la rilevazione di tracce metalliche, in cui l'integrazione dell'elettrodo di riferimento è ottenuta utilizzando una membrana di polivinilcloruro pastificata con liquidi ionici come barriera di diffusione sull'elettrodo

d'argento/cloruro d'argento. Questi sensori sono in grado di rilevare la presenza ditracce metalliche, ma ulteriori miglioramenti sono necessari per permetterne anche la quantificazione.

Le biotossine marine sono composti con attività tossica che si accumulano nei pesci e nei molluschi e possono causare malattie negli esseri umani quando essi entrano nella catena alimentare. Tra le varie specie di biotossine, un altro target di questo lavoro è la saxitossina, una neurotossina a basso peso molecolare prodotta principalmente da dinoflagellati marini. La sua rilevazione è ostacolata dalla bassa concentrazione, quindi è necessaria un'unità di preconcentrazione. Il terzo strumento sviluppato in questa tesi è una piattaforma microfluidica predisposta per la preconcentrazione della saxitossina; il suo principio di funzionamento si basa sulla cattura della saxitossina ad un aptamero specifico e sul suo rilascio tamite un incremento di temperatura.

I composti organici volatili (COV), come gli idrocarburi e gli idrocarburi clorurati, sono elementi inquinanti che contaminano le acque costiere e sono considerati come importanti indicatori dell'inquinamento urbano e industriale. Per monitorare le variazioni della concentrazione dei COV e il loro impatto sull'ambiente, sono necessarie misure accurate e precise di un gran numero di composti organici in acqua di mare, anche a concentrazioni estremamente basse. Tra le varie tecniche di rilevamento, i sensori a fibra ottica di onde evanescenti nel medio infrarosso costituiscono uno degli approcci più promettenti per il monitoraggio continuo dell'inquinamento dovuto a componenti multiple di COV nell'acqua marina. In questa tesi è stata sviluppata una piattaforma microfluidica a basso costo disegnata per ottimizzare l'arricchimento del polimero che riveste la fibra ottica con gli analiti bersaglio dell'analisi. L'ottimizzazione del disegno ha permesso la rilevazione simultanea di dieci specie di COV con questa piattaforma.

Tutti gli strumenti sviluppati in questa tesi sono destinati ad essere integrati in sonde sommergibili per l'utilizzo *in situ*. I sensori per le tracce metalliche sono stati utilizzati con successo in diverse campagne di misura, mentre gli altri dispositivi devono essere ulteriormente ottimizzati per permettere la loro integrazione nelle sonde.

Parole-chiave

Strumenti elettroanalitici, monitoraggio ambientale, detezione di tracce metalliche, voltammetria ad onda quadra, tecnologia a film sottile, SU-8, elettrodo di riferimento a stato solido, pretrattamento del campione, desalinizzazione, culometria a strato sottile, inchiostro d'argento, elettrodi stampati, pre-concentrazione di biotossine, dispositivo microfluidico, detezione di COV, stampa 3D

Resumen

Medir la concentración de diferentes compuestos en los ecosistemas acuáticos, así como la comprensión de su impacto en el medio ambiente, es uno de los principales objetivos en el campo de la monitorización ambiental. Trazas metálicas, nutrientes, compuestos orgánicos volátiles, biotoxinas y algas son unos de los objetivos más importantes de dicha monitorización. Cuantificar y monitorizar *in situ* la concentración de estos compuestos, en una escala de tiempo apropiada y además con una alta resolución espacial es crucial para entender su dinámica y rol en los procesos biogeoquímicos marinos en los que están implicados. Esto impulsa la investigación y el desarrollo de instrumentación más robusta, sencilla, precisa y fiable con una perturbación mínima hacia el ambiente marino. Esta tesis se centra en el desarrollo de nuevos dispositivos de micro-ingeniería con la finalidad de mejorar las técnicas electroanalíticas actuales mediante la explotación de técnicas de escalado y microfabricación. Los dispositivos desarrollados han sido diseñados y fabricados usando diferentes técnicas, tales como: película delgada, impresión, litografía blanda y fabricación aditiva.

Nutrientes como nitratos, nitritos y fosfatos ejercen un fuerte control sobre la productividad primaria y el crecimiento de los organismos vivientes. Su cuantificación en agua de mar es a menudo obstaculizada por el alto contenido de cloruro de sodio dificultando así el utilizar una amplia gama de técnicas de detección. La literatura ofrece gran cantidad de investigaciones para el desarrollo de herramientas de desalinización eficientes y de bajo coste, sin embargo la mayoría de estas son para desalinización no selectiva. Poca información se encuentra sobre el desarrollo de técnicas de desalinización selectiva para el cloruro de sodio respecto a otros iones presentes en el agua de mar. Uno de los dispositivos desarrollados en esta tesis es una plataforma microfluídica ecológica, de rápida medida y de bajo coste para la remoción selectiva del cloruro de sodio en agua de mar, la cual servirá como unidad de pretratamiento antes de la detección de los nutrientes. En este dispositivo se produce la eliminación de cloruro mediante electrolisis en masa en una configuración de capa fina. El dispositivo permite reducir la concentración de cloruro de sodio en una proporción de 10:1.

Las trazas metálicas son omnipresentes en el ambiente marino y su especiación puede variar continuamente en el espacio y en el tiempo, reflejando cambios en las condiciones fisicoquímicas del ecosistema acuático. Su cuantificación es comúnmente lograda mediante técnicas voltamétricas en una célula electroquímica de tres electrodos. En la literatura se han reportado sondas voltamétricas que detectan trazas metálicas tales como: plomo, cadmio, cobre y zinc. El núcleo de estos sistemas es un sensor miniaturizado compuesto por un array de microelectrodos que actúa como electrodo de trabajo y un contra-electrodo; un electrodo de referencia externo es colocado en proximidad del sensor. El electrodo de referencia es un componente crucial para el funcionamiento de estos sensores, sin embargo su integración sigue siendo un reto. El segundo dispositivo desarrollado en el marco de esta tesis es un sensor de tres electrodos para la detección de trazas

metálicas, donde la integración del electrodo de referencia se logra utilizando una membrana de policloruro de vinilo plastificada con líquidos iónicos como barrera de difusión sobre un electrodo de plata/cloruro de plata. Estos sensores son capaces de detectar trazas metálicas, pero se requiere una mejora adicional para permitir su cuantificación.

Las biotoxinas marinas son compuestos que tienen una actividad tóxica y acumulativa en los seres vivos marinos. Estos pueden causar enfermedades a los humanos cuando los seres vivos marinos que contienen esta toxina entran en nuestra cadena alimentaria. Entre las diversas especies de biotoxinas se encuentra la saxitoxina, la cual es una neurotoxina de bajo peso molecular producida principalmente por dinoflagelados marinos. Su detección se ve obstaculizada por su baja concentración, por lo cual se requiere una unidad de pre-concentración con la finalidad de llegar a tener valores de concentración medibles. El tercer dispositivo desarrollado en la presente tesis es una plataforma microfluídica predispuesta para la pre-concentración de saxitoxinas; su principio de funcionamiento se basa sobre la captura de dicha toxina mediante un aptámero específico y su liberación a través un aumento de temperatura.

Los compuestos orgánicos volátiles (COV), como los hidrocarburos y los hidrocarburos clorados, son contaminantes de las aguas costeras y se consideran indicadores directos de la contaminación urbana e industrial. Para monitorizar los cambios en las concentraciones de COV y su impacto en el medio ambiente, se requieren medidas precisas y fiables de un gran número de compuestos orgánicos en el agua de mar, incluso a bajas concentraciones. Entre las diferentes técnicas de detección, los sensores de fibra óptica de ondas evanescentes que operan en infrarrojo medio constituyen uno de los enfoques más prometedores para la monitorización continua de la contaminación por múltiples componentes de COV en agua de mar. En esta tesis se desarrolla y optimiza una plataforma microfluídica de bajo coste que permite optimizar el enriquecimiento de la capa de polímero que recubre la fibra con los compuestos objetivos del análisis. Mediante la optimización del diseño de esta plataforma se ha permitido detectar simultáneamente diez especies de COV.

Todos los dispositivos desarrollados en esta tesis se pretenden integrar en sondas sumergibles los cuales serán desplegados *in situ*. El sensor de trazas metálicas ha sido desplegado con éxito durante varias campañas de medidas, mientras que los otros dispositivos serán ulteriormente optimizados con la finalidad de ser integrados en las sondas.

Palabras-clave

Instrumentos electroanalítico, detección de trazas metalicas, voltametría de onda cuadrada, tecnología de película delgada, SU-8, electrodo de referencia de estado sólido, pretratamiento de muestras, desalinización, coulometría de capa fina, tinta de plata, electrodos impresos, pre-concentración de biotoxinas, dispositivo microfluídico, detección de COV, impresión 3D

Contents

List of Figures

List of Tables

List of Equations

Chapter 1   Introduction

Seawater quality monitoring is one of the most challenging branches of environmental monitoring. It concerns the activities and techniques needed to characterize the status of marine environment and to establish the trend of different chemical and biological parameters. By using specialized equipment and analytical methods, the concentration of different compounds which can potentially affect marine ecosystems can be monitored, leading to the understanding of their interactions and impact on the environment. In this context a collaborative project funded by the European Union Seventh Framework Program (FP7/2007-2013) has been initiated in 2013 and allowed EPFL to collaborate with researchers from eight other European Institutions on the development of chemical sensor submergible systems for *in situ* ocean water monitoring. The project title is "SCHeMA" (in Situ CHemical MApping probe) and funded the herein presented thesis, whose structure will be introduced in this chapter together with the description of the SCHeMA project and the interactions with the other eight institutions.

1.1 Electrochemical sensing and electroanalytical methods

Analytical chemistry is the area of chemistry which concerns the separation, identification and quantification of chemical compounds in natural and artificial materials. One of the first instrumental analysis method, the flame emissive spectrometry, was developed by R. Bunsen and G. Kirchhoff in 1860 [1]. The major developments in the field of analytical chemistry were achieved during the twentieth century when several analytical methods such as electrogravimetry [2], chromatography [3], infrared (IR) spectroscopy [4], and electrochemical analyses including polarography [5], were developed. The application of analytical chemistry to solve issues and questions coming from the biomedical, industrial and environmental fields occurred during the late 20th century [6] which saw an expansion in sensors and biosensors technology development.

Among the wide variety of sensors based on optical, electrical and thermal transduction, electrochemical sensors are amongst the simplest, low-cost, reliable and practical sensors [7]. The analyte concentration can be studied by electroanalytical methods in which the quantity of the chemical analyte is transduced into an electrical signal, a voltage change or a current flowing at the electrode interface. The main electroanalytical methods are potentiometry (the difference between the electrode potentials is measured), voltammetry (the cell current is measured while actively altering the cell potential), coulometry and amperometry (the cell current is measured over time at constant potential).

In the biomedical and physiological field the main target analytes are commonly blood parameters such as blood gases (pH, pO_2, pCO_2) [8], electrolytes present in biological fluids such as calcium, potassium, sodium [9], metabolites such as glucose [10], urea and lactate [11], neurotransmitters present in brain extracellular fluid [12], biomarkers and hormones. Some examples of the achievements of the electrochemical methods in this field are reported below.

Jovic et al. [13] demonstrated the quantification of thyroid-stimulating hormone (TSH) in aqueous samples by using multiplexed three-electrode sensors in a point-of-care device platform which couples a magnetic bead-based immunoassay strategy with amperometric detection. Ochiai et al. [14] developed an electroanalytical device constructed using a cotton thread as solution channel and carbon nanotubes (CNTs) modified screen-printed electrodes (SPE) for the amperometric determination of estriol hormone in pharmaceutical samples. Macêdo et al. [15] investigated the antioxidant capacity of commercial dried extracts from red fruits by evaluating their redox behavior through electroanalytical approaches (cyclic, differential and square wave voltammetry profiles). Chaocharoen et al. [16] demonstrated that the detection limit of a potential molecular marker for several cancers, measured by electrochemical methods, could be significantly lowered with respect to the standard enzyme-linked immunosorbent assay (ELISA), thus allowing an earlier stage detection than currently possible with ELISA. Teixeira et al. [17] deployed a copper(II) hexacyanoferrate(III) modified carbon paste electrode for the electroanalytical determination of pyridoxine (vitamin B6) in pharmaceutical preparations using cyclic voltammetry. Furthermore, electroanalytical methods can be useful for the detection of DNA damage, such as abasic lesions, base mismatches, non-covalent interactions with drugs and other substances thanks to the electrochemical activity of the nucleic acids. In particular adenine, cytosine and guanine

nucleobases can be reduced at mercury-based electrodes such as the hanging mercury drop electrode (HMDE) and voltammetric DNA signals measured at HMDE are strongly sensitive to changes in DNA structure [18].

In the environmental monitoring field analytes commonly targeted are toxins, trace metal species, and gases; their detection has to be achieved in different media such as natural waters, soil, and air. In the last few years the research and technology development of sensors and biosensors for environmental analytical purposes has clearly increased due to the need to solve problems related to conventional analytical techniques which provide precision and accuracy, but often require expensive and complex instrumentation, high reagent and sample consumption and are characterized by lack of portability [19,20]. These techniques require in fact sampling operations before analysis in laboratory, while ensuring that the sample does not change in time. Therefore there has been great interest in researching more sensitive devices and more selective chemical sensors towards a particular analyte, when sensors are applied to complex samples, in order to allow determination of lower concentrations, and develop low cost and easily handled instrumentation to perform *in situ* measurements [21]. The development of these analytical devices simplifies and miniaturizes the whole analytical process [22] and this is supported by the increasing trend towards the miniaturization of sensors for higher speed, performance and portability. Some examples of electrochemical devices developed for environmental monitoring applications are given below.

Pang et al. [23] developed and tested a miniaturized electrochemical ozone (O_3) sensor for *in situ* monitoring of air-quality over an 18-day period producing data in good agreement with those obtained by conventional cumbersome and expensive monitoring devices based on UV absorption. Marrazza et al. [24] developed a disposable DNA-based electrochemical biosensor for detection of low-molecular weight compounds (toxins, pollutants, drugs) with affinity for nucleic acids by chronopotentiometric analysis, whose applicability to river water samples was also demonstrated. Electrochemical gas sensors based on mixed-potential gas-sensing principle have been explored extensively in recent years due to their high sensitivity and selectivity to redox gases, in particular H_2, CO and NOx, in oxygen containing atmospheres even at high temperature [25]. Li et al. [26] developed a graphene oxide (GO) film coated glassy carbon electrode (GCE) for sensitive determination of 4-nitrophenol (4-NP), a compound used to manufacture drugs and pesticides, by electrochemical impedance spectroscopy thanks to the electro-catalytic activity of the GO film towards the reduction of 4-NP. This sensor was deployed in real water samples showing promising results for simple and sensitive detection of 4-NP. Direct measurement of trace metals in anoxic sulfidic marine sediments has been achieved by deploying stripping voltammetry at mercury (Hg) electrodes [27].

Over the years seawater analysis has attracted a growing interest within the analytical chemistry community for being one of the most challenging analyses in the field of environmental monitoring. The main anthropogenic and natural chemical compounds that may have interactions and effect on the marine ecosystem equilibrium are species relevant to the carbon cycle such as carbon dioxide (CO_2) [28]; nitrate, nitrite, and phosphate nutrients [29]; essential and toxic trace metal species [30]; volatile organic compounds (VOCs) [31]; potentially toxic algae species [32] and biotoxins [33].

For the understanding of the marine carbon cycle, high quality pCO_2 measurements with good temporal and spatial coverage are required in order to monitor the oceanic uptake and identify

regions with pronounced carbonate system changes [34]. The deployment of amino groups and ferrocenes co-modified electrode sensors has been recently investigated and characterized for the electrochemical detection by cyclic voltammetry of carbon dioxide (CO_2) in saline solution containing sodium bicarbonate as CO_2 source [35].

The nitrogen (N) cycle controls the availability of nitrogenous nutrients and biological productivity in marine systems, thus is linked to the fixation of atmospheric carbon dioxide and export of carbon from the ocean's surface [36], and to algae-related eutrophication in case of excess [32]. Nutrients detection at nanomolar levels is important in order to identify oligotrophic areas weak in nutrients due to the biological uptake. Wang et al. [37] recently developed a novel method for the detection of nitrate by using simplified nitrate reductase (SNaR) based on the combination of the enzyme-catalyzed reduction of nitrate to nitrite by thin layer coulometry and the spectroscopic measurement of the colored product generated from the reaction of nitrite with Griess reagents [38]. This SNaR-based method provides a more environmentally safe method for the nitrate reduction than the highly toxic cadmium column commonly used [39–41]. In recent years ion selective electrodes (ISEs) have proved to be an attractive method for the analysis of nitrate due to their robustness, simplicity, specificity and capacity for use in field deployable instrumentation. In 2012 Aravamudhan and Bhansali [42] have developed a nitrate-selective electrochemical sensor using doped polypyrrole (PPy) nanowires as ISE material in a microfluidic platform. The system was characterized in simulated marine conditions: the polypyrrole-doped nanowires showed high selectivity and rapid reactivity towards the nitrate ions which were electrochemically reduced by applying a negative potential. Sohail et al. [43] have developed an ISE system consisting in a porous polypropylene tube doped with a plasticizer along with dissolved nitrate ionophore and an inner Ag/AgCl wire electrode for coulometric determination of nitrate in environmental waters.

Trace metals are ubiquitous and inherently persistent in marine environment. Essential metals such as iron (Fe), cobalt (Co) and zinc (Zn), are present in the plankton biomass at micromolar concentrations and have biochemical functions which are not yet fully understood [44], while metal species such as lead (Pb), arsenic (As), mercury (Hg), aluminium (Al) are extremely toxic even at low concentrations. Detection, quantification and speciation of these compounds through real-time continuous measurements in natural waters are therefore strongly needed in order to understand the biogeochemical processes in which they are involved and study the possible detrimental effects of some trace metals (TMs) on the human and ecosystem health [30]. Electrochemical stripping analysis has been recognized as a powerful tool for trace metals measurement [45]. Up to six metal species (Cd(II), Pb(II), Cu(II), Zn(II), Mn(II), Fe(II)) can be simultaneously quantified at concentrations down to picomolar levels and its remarkable sensitivity is attributed to the combination of an effective pre-concentration step with advanced measurement procedures that generates an extremely favorable signal-to-background ratio [46]. The main electrode systems used for voltammetric analysis of trace metals are the hanging mercury drop electrode (HMDE) and the mercury-film electrode (MFE) [47]. Due to mercury toxicity, alternative materials have been investigated such as carbon [48,49], gold [50], iridium [51], bismuth [52]. Bismuth is an environmentally friendly element and seems to offer the closest behavior to mercury [46]. Its anodic voltammetry performance has been investigated by several research groups who obtained well-defined, sharp and reproducible stripping peaks for low concentrations of lead, cadmium and zinc

[46,53,54]. However the overall performances in terms of sensitivity, limit of detection, and continuous monitoring are not as well as for Hg plated electrodes in the field application.

The development of new micro-engineered tools for enhancing the performance (mainly sensitivity and limit of detection) of in *situ* electrochemical measurements of chemical compounds such as nutrients and trace metals, as well as biotoxins and VOCs, is the subject of this thesis.

1.2   SCHeMA project

This thesis was supported by a four-year project funded by European Union Seventh Framework Program from October 2013 until September 2017. The title of the project is "SCHeMA", acronym for "in Situ CHemical MApping probe".

1.2.1   SCHeMA project objectives

The goal of the SCHeMA project was to provide a miniaturized chemical sensors probe network for *in situ* high resolution measurement of different compounds which may affect the equilibrium of marine ecosystem, thus having adverse effect on living organisms and, ultimately, on human health. These probes can help to identify relevant hazardous chemicals at an appropriate temporal and spatial scale, detect their sources and origin, understand the processes governing their distribution, and finally to evaluate marine environment quality and manage the possible risks and consequences. When installed in coastal areas, estuaries, etc., these tools should allow minimizing the impact and the perturbation to the environment and operations such as sampling, pre-treatment (if necessary) and transport to the core of the system, i.e. the sensing devices. Figure 1.1 shows a schematic diagram of the SCHeMA interfaced chemical multi-sensor mapping probes and the web-based network and data information system [55]. Each sensor performs measurements which are temporarily stored in the dedicated memory of the probe and then transferred to the network controller where they are formatted and sent to the web for storage and dissemination to the end users which can be government institutions, small enterprises or research groups in the biogeochemistry field.

The main target compounds in the framework of this project were inorganic nutrients, essential/toxic trace metals, species relevant to the carbon cycle, VOCs, algaes and biotoxins. Three submersible modular systems were successfully developed and tested in field: one unit for the detection of the species relevant to the carbon cycle (pH, CO_3^{2-}, Ca^{2+}), a three-module unit for detection of trace metals (one module for Pb(II), Cd(II), Cu(II) and Zn(II), one module for Hg(II), one module for As(III) and As(V)), and one unit integrating the detection system for nutrients and algaes. A submersible probe for the optical VOCs detection system is still under development, while the approach for pre-concentrating and detecting biotoxin is still under investigation.

All the developed units were hosted in a submersible housing together with the battery and the mechanical components such as pumps and filters. A dedicated wired/wireless communication network with OGC-SWE (Open Geospatial Consortium-Sensor Web Enablement) standards and web-based front-end system were integrated for gathering the information on water quality and

status. Filters were needed in order to remove particulate, bacteria, and microorganisms thus avoiding biofouling of the sensors and damage to the internal mechanical and electronic components.

The development of sensors for monitoring the concentrations of the different compounds listed above required the investigation of different technologies and experimental approaches. In the following section the contribution and the interactions between the different partners of the project will be commented.
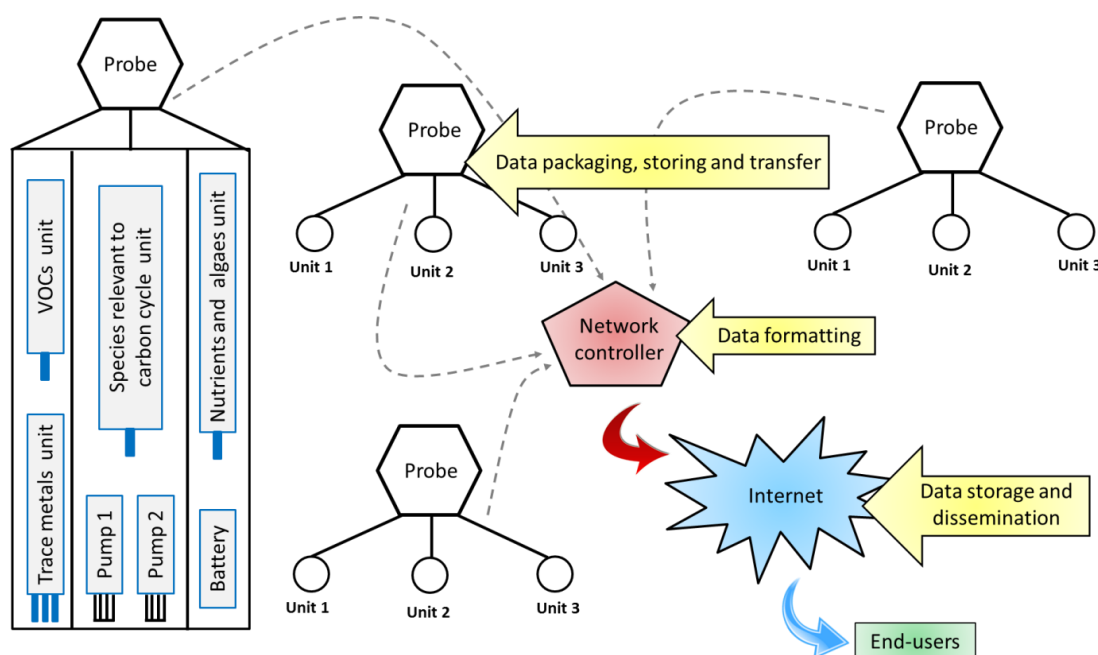
Figure 1.1. Schematic diagram of the SCHeMA chemical multi-sensor mapping probes and the web-based network and data information system [55]. On the left-hand side it is possible to distinguish the different modules of each probe.

1.2.2 Partners and their role in SCHeMA project

Different groups of investigators from six universities and three companies were involved in the SCHeMA project: University of Geneva - UNIGE (Switzerland), University of Ulm - UULM (Germany), Technische Universitaet Graz - TUGRAZ (Austria), École Polytechnique Fédérale de Lausanne – EPFL (Switzerland), University of Bordeaux I (France), University of Genova (Italy), and the companies Idronaut Srl (Milano, Italy), NanoMyP S.L. (Granada, Spain), and ETT Srl (Genova, Italy).

The contribution of EPFL-LMTS to the project was providing the technology for the development of sensors and microfluidic platforms needed throughout the project.

Three research groups from the University of Geneva were involved in the project. One group developed miniaturized handmade glassy carbon electrodes coated with ion selective films for

potentiometric detection of pH, carbonate and calcium, and coulometric detection of nutrients. Detection of nutrients required the additional development of two pre-treatment units in order to achieve limit of detection in the nanomolar range: a desalination and an acidification step were necessary in order to lower the concentration of chloride in the sample and to lower the pH from 8 to 4. These two pre-treatment units were homemade. EPFL has been working in parallel on the development of a microfabricated platform to overcome the current limitations of the homemade desalination device, subject that will be presented in detail in Chapter 2.

A second group at the University of Geneva has been working on the optimization of the experimental protocol for quantification of different trace metal species by using microelectrode arrays produced by EPFL. We worked on the design, fabrication and electrochemical characterization of the microelectrode arrays which were plated either with Hg hemispheres for cadmium, lead, copper and zinc detection, or with gold nanoparticles (AuNPs) for arsenic speciation and Hg(II) detection, and on the integration of an on-chip reference electrode. Testing of the sensors for Cd, Pb, Cu, Zn and As was performed in synthetic and real samples in collaboration with the University of Geneva group. This group also explored the possibility to detect Hg(II) by peptide functionalized polymer brushes immobilized on the electrode surface or by multiwall carbon nanotubes (MWCNTs) embedded in a polymeric membrane.

The third group from University of Geneva was in charge of developing the chemical procedure to immobilize aptamers for biotoxins binding in a microfluidic platform developed by EPFL for achieving pre-concentration of biotoxins and release and transport towards the detection unit under development at TUGRAZ.

The University of Ulm developed polymer-coated infrared evanescent field chemical sensors for the detection of VOCs by infrared (IR) spectroscopy. The polymer-coated optical fiber was hosted in a microfluidic platform designed and fabricated at EPFL for optimizing the enrichment of the polymer with VOCs and analyzing the absorption spectra. The University of Graz developed the optical system for algae detection based on the analysis of the excitation spectra of the algae species and on the discrimination of the pigmentation of photosynthesis reaction which differs from species to species. NanoMyP worked on the design and synthetization of new polymers and copolymers for the functionalization of the sensors developed by the other partners (e.g. the polymer brushes for Hg(II) detection).

Idronaut Srl worked on the assembling of the different sensing probes, on their integration in a titanium deployment cage together with the pumps and a system for sensing pH, conductivity, temperature, and dissolved oxygen. Moreover they developed the probe management firmware, the operator interface, the measurement methods setup, special OGC-SWE protocols and services dedicated to alarms, errors and probe remote configuration. Idronaut also supported all the project partners while carrying out preliminary tests in the laboratory and during the field campaigns.

ETT Srl developed the web interface for the data management of the SCHeMA project, created and kept updated the SCHeMA official website, and organized and took part to activities for dissemination of the SCHeMA achievements, such as workshops and international meetings.

University of Bordeaux and University of Genova were responsible for the organization of the field campaigns, choosing the most representative sites in the European coastal areas where to perform

the field tests, and for the demonstration activities to the end-users. Throughout the project, six short-term field tests (two in Arcachon Bay, two in Genova Harbor, one in Plentzia, and one at Gironde estuary) and one long-term field test in Genova were organized.

1.3   Thesis structure

The work of this thesis has been carried out following the work plan of the SCHeMA project in order to support all the partners in the development of sensors and pre-treatment units for *in situ* detection of different chemical compounds. The most intense collaboration was with the group of the University of Geneva working on the development of the trace metal sensors and with the University of Ulm. Several challenges were encountered and in many cases were successfully overcome. Three main goals were achieved in this work and will be presented in the following chapters.

The first goal was the development of a pre-treatment unit for sample desalination prior to coulometric detection of nutrients. This device was designed for allowing removal of sodium chloride ions from the seawater sample before introducing it in the sensing unit for nutrients detection. Chapter 2 describes the design, fabrication and characterization of this device, as well as the optimization of the first designed unit for improving its desalination performance. A proof-of-concept of the desalination capabilities of the device was achieved and some guidelines for its further optimization are given in the last part of the chapter, towards the development of an *in situ* deployable device.

Chapter 3 focuses on the second goal of this thesis which was developing a three-electrode (WE-CE-RE) on-chip sensor for trace metals detection. Design and fabrication of the device is presented together with the electrochemical characterization of the microelectrode arrays and of the two kinds of on-chip solid state reference electrodes (REs) developed: an Ag/AgCl pseudo-RE and an Ag/AgCl electrode coated with a poly(vinyl chloride) (PVC) membrane plasticized with ionic liquids (ILs). These sensors proved to be successful for detection of trace metals (Pb(II), Cd(II) and Cu(II)) in synthetic and real samples showing a constant shift in time with respect to an external Metrohm RE. Further optimization is required in order to allow quantification of the trace metals and to achieve sensitivity values close to the two-electrode (WE-CE) on-chip sensors. Investigations carried out for the detection of other metal species such as arsenic are also presented.

Chapter 4 focuses on the work carried out for the development of two microfluidic platforms for biotoxin pre-concentration and VOCs detection. The design and fabrication of the two devices are presented together with the optimization of the first designs towards the improvement of their performance. The third generation of the VOCs microfluidic platform excellently worked in the optical setup developed by partners at UULM allowing simultaneous detection of up to ten analytes and lowering the limit of detection (LOD) achieved with their homemade flow cell. The microfluidic platform for biotoxin pre-concentration and release was not tested by the partners in Geneva therefore no conclusions are available concerning the performance of this device.

Finally, Chapter 5 presents a summary of the whole thesis, its conclusions and the guidelines for future work.

Chapter 2 Microfluidic platform for seawater desalination

Measurements of nutrients concentration are among the most commonly performed analyses in oceanographic research since they strongly control the oceanic primary productivity [56] and their excess as well as their lack can be dangerous for the marine ecosystem. Nitrate and phosphate distributions typically span up to five orders of magnitude in the stratified open ocean, from low nanomolar levels at the surface to micromolar levels at depth. Accurate and high-resolution profiles of nitrate and phosphate distributions in the open ocean are difficult to obtain using conventional techniques. One of the objectives of the SCHeMA project is to develop an *in situ* monitoring unit for coulometric detection of nutrients. However their detection is hampered by the high salt content in seawater matrix (0.6 M), therefore the salt concentration in the sample should be lowered to millimolar levels prior to the coulometric measurement due to the high background signal coming from chloride ions. In this chapter a microfabricated device for sodium chloride removal is presented. The design of the unit is based on exploiting bulk electrolysis by controlled potential thin layer coulometry. The device was tested in synthetic samples and a proof-of-concept of its desalination capabilities was achieved: a final sodium chloride concentration of 51.6 mM, ten times-fold lower with respect to the initial value of 0.6 M, was reached in a time frame of 360 s. It presented a lifetime in the order of some tens of redox cycles. Guidelines for its optimization and performance improvement are given. Parts of this chapter have been published in [57] and [58].

2.1   Introduction and state-of-the-art

The direct *in situ* detection of nutrients at low concentration is important in order to gather information concerning marine ecosystem health but is often hampered by the high salt content in seawater matrix. A variety of analytical techniques such as atomic spectroscopy [59], mass spectrometry [60], chromatography [61], ion-selective potentiometry and coulometry [62] require a desalination system to pretreat the sample prior to analysis. Of these techniques, ion-selective coulometry is a promising technique to develop robust and calibration-free sensors for *in situ* analysis since it is simple, portable, reagent-free and does not produce any toxic waste. A small-scale, simple, efficient, and inexpensive sample pretreatment system is required to effectively reduce the level of dissolved salts in seawater, mainly sodium and chloride ions (0.6 M NaCl), thus allowing *in situ* quantitative nutrient analysis through this technique.

The most widespread seawater desalination technologies are reverse osmosis (RO) [63], electrodialysis (ED) [64], multi-effect distillation (MED) [65] and multi-stage flash (MSF) distillation [66], which are high cost and large scale technologies intended to deliver drinkable water. The RO process exploits the generation of high pressure to overcome the osmotic pressure of seawater across semi-permeable membranes. The ED process uses electric currents to move ions through perm-selective membranes, thus producing pure water.

Less energy intensive technologies are capacitive deionization (CDI) and membrane CDI (MCDI). In CDI desalination technology water with various anions and cations is pumped through the electrochemical cell. After polarization, ions are electrostatically removed from the water and held in the electric double layers formed at the surface of the electrodes, therefore the principal ion removal mechanism is through electrostatic adsorption by direct contact of the electrodes with the solution [67]. MCDI was introduced to overcome limitations of CDI during the purification step due to incomplete regeneration of the electrodes [68–70]. Ion exchange membranes are added to the concept of CDI with the aim to prevent adsorption of oppositely charged ions during the regeneration process. These techniques are mainly used for desalination of brackish water at large scale [71].

In the last years research has focused on developing new small-scale and portable seawater desalination systems with low power consumption.

Recently, ion concentration polarization (ICP) has attracted great attention from the microfluidics research community due to its potential applications for desalination, pre-concentration and separation [72]. ICP is a fundamental electrochemical transport phenomenon that occurs when an ion current is passed through ion-selective membranes [73,74]. Han and coworkers were the first to recognize that ICP could be exploited for desalination in 2010. They developed a microfluidic device in which a continuous stream of seawater was divided into desalted and concentrated streams by ICP [75]: salts and larger particles (cells, viruses and microorganisms) were pushed away from the membrane (a Nafion nanojunction) and the conductivity of the desalted stream dropped to 0.5 mS/cm (3 mM) from the original conductivity value of seawater 45 mS/cm (500 mM). More recently, in 2013, Knust et al. [76] demonstrated desalination by ICP at a carbon bipolar electrode (BPE) in a PDMS/glass device. A seawater feed is separated into brine and desalted water streams

at the junction of a microchannel where a bipolar electrode (BPE) is placed. The anodic pole of the BPE generates an ion depletion zone, and hence a local electric field gradient that redirects ions present in seawater to the brine channel. This device allowed 25% salt rejection. Other authors have been working on the improvement of the performance of the ICP devices in order to increase their throughput. MacDonald et al. [77] developed a desalination device using ICP in the out-of-plane direction: the interfacial area between the microchannel and a Nafion membrane was increased and a salt rejection as high as 95% was achieved.

The ICP approach allows the development of simple, low-cost and portable microfluidic devices for seawater desalination, however it implies the removal of all charged ions from seawater. The pre-treatment needed for allowing detection of nutrients requires selectivity towards chloride ions, since ions such as nitrate (NO_3^-) and nitrite (NO_2^-) are the target of the analysis and should not be removed from the sample. Therefore a device and technique selective to chloride are needed.

In 2016 a new device concept, based on Na-ion Desalination (NID) has been introduced by Smith and Dmello [78] to desalinate NaCl from seawater by using symmetric Na-ion battery (NIB) intercalation-electrodes separated by an anion-selective membrane that blocks Na ions. They proposed a porous-electrode model to investigate Na-ion intercalation, ion transport in NaCl solution and electron transport inside electrodes, and showed promising predictions of the performance of NID cells. Smith [79] simulated the performance of ED stacks using nickel-hexacyanoferrate electrodes and predicted that Na-ion intercalation can be used as efficient electrodes for electrodialysis: the nickel-hexacyanoferrate Prussian Blue Analogue was capable of continuously removing 0.4-0.5 M NaCl from 0.7 M influent. "Desalination batteries" based on redox-active hexacyanoferrate nanoparticles and on Prussian Blue electrodes for electrochemical water desalination have been recently reported respectively by Porada et al. [80] and by Lee et al. [81]. The latter allowed desalination during both the charge and discharge steps showing a good cycling stability of Prussian blue materials and a Na ion removal efficiency of 40% (298 mM average deionized NaCl concentration for one desalination cycle): Na ions are captured in the battery material, while Cl ions are removed by diffusion through the anion-selective membrane.

This configuration is the inverse of another type of electrochemical desalination cell developed by Bakker et al. [82]. In this small-scale pretreatment system, a rapid removal of NaCl upon thin-layer electrolysis using the coaxial arrangement of an Ag wire electrode and a tubular Nafion membrane has been achieved. This system allows coupling to an ion-selective coulometric nutrient sensor and reducing sodium chloride concentration down to 3 mM by electrolysis of seawater at 400 mV: chloride is removed by oxidation of Ag to AgCl and sodium by passing through the Nafion membrane into a 0.1 M NaCl solution (NO_3^- and NO_2^- concentrations remain unchanged after electrolysis). The reduction of chloride concentration to millimolar levels is in fact crucial for the measurements of nutrients through ion-selective coulometry due to the limitations imposed by the ionophore selectivity [83].

Table 2.1 reports the main constituents of seawater (pH=8.1), showing that the concentration of compounds such as nitrate is hundred thousand times lower than chloride concentration, thus the need to remove chloride before its analysis.

Table 2.1 Main constituents of seawater (Castro and Huber's, Marine Biology textbook).

Chemical Ion	Concentration in g/kg of seawater	Concentration in moles/kg of seawater	Relative concentration
Chloride (Cl^-)	19.345	0.546	1.0000
Sodium (Na^+)	10.752	0.468	0.8571
Sulfate (SO_4^{2-})	2.701	0.028	0.0513
Magnesium (Mg^{2+})	1.295	0.053	0.0971
Calcium (Ca^{2+})	0.416	0.0104	0.0190
Potassium (K^+)	0.390	0.0099	0.0181
Bicarbonate (HCO_3^-)	0.145	0.002	0.0037
Bromide (Br^-)	0.066	0.0008	0.0015
Borate (BO_3^{3-}))	0.027	0.0005	0.0009
Strontium (Sr^{2+})	0.013	0.0002	0.0004
Fluoride (F^-)	0.001	0.00005	0.0001
Others	<0.001	-	-
Nitrate (NO_3^-)	<0.0007	<0.00001	0.00002

The system proposed by Bakker et al. has a major drawback: the seawater volume (less than 20 µl) is too small to allow downstream nutrients detection and due to its geometry the system would require meters of length to increase this volume. The key to increase the sample volume without exceeding with the device dimensions consists in moving from a coaxial arrangement to a planar one in which a better control of the channel thickness is also obtained. A planar device for chloride removal based on the coulometric approach has been recently reported [84]: silver foils were used as electrodes and the fluidic compartment for seawater was a 230 µm high rubber channel (80 µl volume). This system allowed NaCl concentration reduction down to 5.5 mM by applying 900 mV in a time frame of 600 s against the 240 s needed with the tubular cell [82]. A reduction step of 1200 s was required to regenerate the Ag electrode, therefore the analysis time was 2 samples per hour. This time frame is primarily limited by the speed of the desalination process and can decrease if a shallower channel for the seawater sample is used, as it will be explained in the following section.

In this chapter a device for NaCl removal fully fabricated using microfabrication techniques is presented. The technique allowing NaCl removal is the controlled potential thin-layer coulometry. The developed microfluidic platform is made up of two parallel glass plates with patterned Ag and Ag/AgCl electrodes and two microfluidic compartments separated by a flat Nafion membrane, a shallow one for the seawater sample (80 µm thick) and a deep one for the 0.1 M NaCl solution. After chloride removal upon oxidation of the Ag electrode to AgCl, the Ag electrode is regenerated by reversing the potential.

2.2 Theoretical background

Coulometry is an electroanalytical technique that determines the amount of matter transformed during an electrolysis reaction by measuring the amount of electricity passed though the electrolyte. In controlled potential coulometry, the potential of the WE is maintained constant with respect to

the RE and the quantity of material involved in the reaction is determined by Faraday's electrolysis law:

$$m = \frac{Q}{F} \cdot \frac{M}{z}$$

Equation 2.1

where m is the mass of the substance altered at the electrode, Q is the total electric charge passed through the electrode, F is Faraday constant (96485 Cmol^{-1}), M is the molar mass of the substance, and z the valence number of the substance.

There are circumstances where one desires to appreciably alter the composition of the bulk solution by electrolysis, as for example in the case of desalination where the concentration of chloride has to be ideally lowered to zero. In these cases bulk (or exhaustive) electrolytic methods are required, which are characterized by large A/V (electrode area/solution volume) ratios and effective mass transfer conditions. These techniques are classified as thin-layer electrochemical methods. In controlled potential thin-layer coulometry, where a constant potential E is applied for a reaction O + ne^- →R, the current is given at any time by:

$$i(t) = nFAm_0 C_0^*(t)$$

Equation 2.2

where n is the number of electrons involved in the reaction, m_0 is the mass transfer coefficient of the species O expressed in mm/s and $C_0^*(t)$ is the concentration of the species O. The current also indicates the total rate of consumption of the species, dN/dt (mol/s), due to electrolysis (assuming 100% current efficiency):

$$i(t) = -nF \left[\frac{dN_0(t)}{dt} \right]$$

Equation 2.3

where N_0 is the total number of moles of the species O in the system. If the solution is assumed to be completely homogeneous, then

$$C_0^*(t) = \frac{N_0(t)}{V}$$

Equation 2.4

where V is the total solution volume. Combining Equation 2.3 and Equation 2.4 yields to the current profile described by the equation:

$$i(t) = -nFV \left[\frac{dC_0^*(t)}{dt} \right]$$

Equation 2.5

Equating the two relations for *i(t)*, we obtain:

$$\frac{dC_0^*(t)}{dt} = -\left(\frac{m_0 A}{V} \right) C_0^*(t) = -pC_0^*(t)$$

Equation 2.6

with the initial condition: $C_0^*(t) = C_0^*(0)$ at t=0. Equation 2.6 is characteristic of the kinetics of a first-order, homogeneous chemical reaction, where the parameter $p = m_0 A/V$ is analogous to the first-order rate constant. The solution to this differential equation is:

$$C_0^*(t) = C_0^*(0)e^{-pt}$$

<div align="right">Equation 2.7</div>

and using Equation 2.2, we obtain the *i-t* behavior:

$$i(t) = i(0)e^{-pt}$$

<div align="right">Equation 2.8</div>

where *i(0)* is the initial current [85] and *p* is the first-order rate constant which determines the velocity of the reaction depending on the geometrical parameters of the device (*A* and *V*). Therefore a controlled-potential bulk electrolysis is alike a first-order reaction, with the concentration and the current exponentially decaying with time during the electrolysis and eventually attaining a background (residual) current level. Equation 2.7 can be used to determine the duration of the electrolysis for a given conversion:

$$\frac{-p}{2.3}t = log\left[\frac{C_0^*(t)}{C_0^*(0)}\right]$$

<div align="right">Equation 2.9</div>

For 99% completion of electrolysis, $C_0^*(t)/C_0^*(0) = 10^{-2}$, and $t = 4.6/p$; for 99.9% completion, $t = 6.9/p$. This means that for higher values of *p*, less time is required to complete electrolysis, therefore for effective rates of electrolysis, *A* should be as large as possible, thus achieving large A/V ratios. In thin-layer electrochemical methods large A/V ratios are attained by trapping a very small volume (tens of microliters) of solution in a thin (20-100 μm) layer against the working electrode, and in many practical devices porous working electrodes [86] of large surface area are employed.

In controlled potential coulometry the total number of coulombs consumed in an electrolysis reaction is used to determine the amount of substance electrolyzed through Equation 2.1. To enable a coulometric method, the electrode reaction has to satisfy the following requirements: (i) it must be of known stoichiometry; (ii) it must be a single reaction or at least have no side reactions of different stoichiometry; (iii) it must occur with close to 100% current efficiency. The current is monitored during the electrolysis so that the background current can be determined and the completion of electrolysis observed. The total quantity of electricity Q(t) (in coulombs) consumed in the electrolysis is given by the area under the *i-t* curve:

$$Q(t) = \int_0^t i(t)dt$$

<div align="right">Equation 2.10</div>

The ideal *i-t* and *Q-t* profiles are shown in Figure 2.1 in a dimensionless form, however a background (residual) current, due to competitive processes occurring at the electrode/solution interface, is often observed. In this case, the residual current value multiplied by the electrolysis time is subtracted to the value of the integral. The shape of the *i-t* curves can be diagnostic of the mechanism of the electrode reaction and instrumental problems. For example, if at the beginning of the electrolysis the current remains constant for some time before showing the usual exponential decay, the output current or voltage of the potentiostat is probably insufficient for the electrolysis conditions (electrode area, C_0^*, cell resistance) to maintain the electrode at the potential chosen.
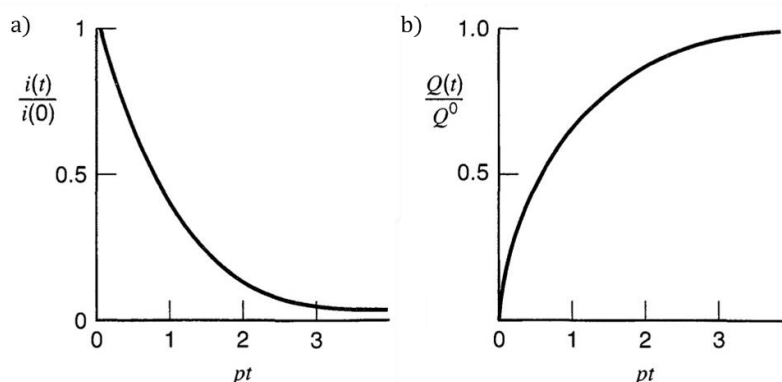
Figure 2.1. Current-time (a) and charge-time (b) curves in dimensionless form during controlled potential electrolysis.

Electrolysis at controlled potential is the most efficient method of carrying out a bulk electrolysis, because the current is always maintained at the maximum value (for given cell conditions) consistent with 100% current efficiency [87].

2.3   First generation of the desalination platform

Based upon the theoretical background presented in section 2.2, a microfluidic platform for removal of NaCl by thin-layer coulometry was developed.

2.3.1   Design and working principle

The 3D drawing of the designed microfluidic platform is shown in Figure 2.2 together with a schematic cross section of the device. It consists of the following components, from the top down: a glass substrate (top glass) with a patterned Ag electrode serving as the working electrode (WE), a shallow channel (40 μm thickness) defined by a double-side pressure sensitive adhesive (PSA) filled with the 0.6 M NaCl sample, a 25 µm thick Nafion cation-exchange membrane, a 5 mm deep polydimethylsiloxane (PDMS) chamber filled with the 0.1 M NaCl solution, a second glass substrate (bottom glass) with patterned Ag/AgCl electrode serving as the counter/reference electrode (CE/RE).

Removal of sodium chloride occurs upon electrolysis. The shallow microfluidic compartment is filled with the sample and a positive potential is applied to the WE with respect to the CE/RE: chloride anions are removed by oxidation of Ag to AgCl, while sodium cations are transported through the Nafion membrane towards the second microfluidic compartment, being attracted by the negatively charged CE/RE (see Figure 2.2). The electrolysis (oxidation) reaction is expressed by the following equation, where Ag is the species being oxidized:

$$Ag(s) + Cl^-(aq) \rightarrow AgCl(s) + e^-$$

Equation 2.11

After the oxidation step, the shallow channel is filled with a regeneration solution (10^{-3} M NaCl) to allow the regeneration of the Ag electrode by reversing the potential. In the regeneration step, a negative potential is applied to the WE with respect to the CE/RE: chloride ions are released from the Ag electrode and the sodium ions are transported back to the channel.
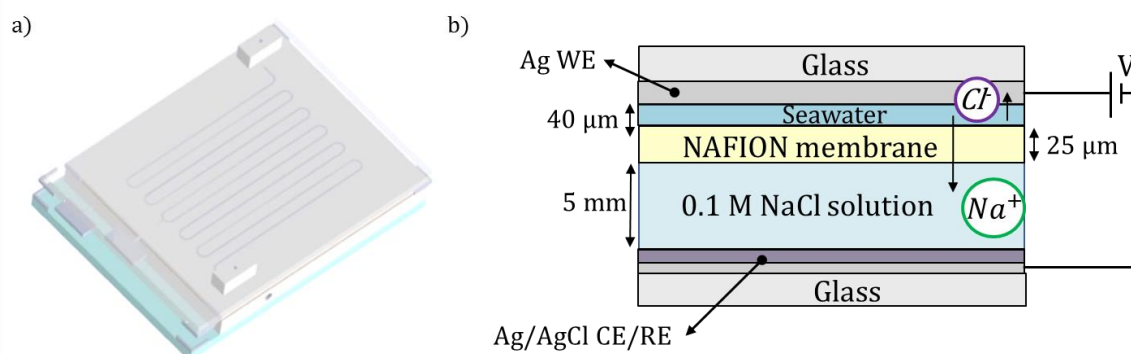
Figure 2.2. (a) 3D drawing of the microfluidic platform for desalination. The printed Ag working electrode has a serpentine shape corresponding to the fluidic channel. (b) Schematic cross section of the device in desalination mode (drawing not to scale for clarity).

The microfluidic platform was designed based upon the following guidelines: i) the silver electrode serving as WE should have a thickness in the range of tens of microns to allow sufficient chloride removal- and regeneration capacity; ii) the condition of large area/volume ratio has to be met by trapping a small volume of solution in a thin layer (20-100 µm) over the WE in order to achieve effective mass transfer conditions and exhaustive electrolysis [87]; iii) the total dimension of the device should fit the submersible probe under development for *in situ* deployment which has an inner diameter of 70 mm [88].

The first generation microfluidic platform had dimensions of 65 x 50 x 11 mm. The WE is a serpentine with a total length of 466 mm and a width of 0.8 mm, while the CE/RE is a rectangle of 43 x 37 mm. The fluidic compartments for the seawater and the 0.1 M NaCl solution have a total volume of 17 µl and 8.7 ml, respectively.

The fabrication process flow whose main steps are shown in Figure 2.3 consists of thirteen steps: WE and CE/RE patterning on top and bottom glass, respectively (i), PSA laser cutting for shallow channel patterning (ii), PSA channel bonding to the top glass (iii), mechanical drilling of two holes in the top glass (iv), partial chloridation (by applying 0.9 V for 300 s in a 0.6 M NaCl solution) of the Ag electrode of the bottom glass to AgCl (v), poly(methylmethacrylate) (PMMA) mold laser cut (vi), PDMS molding in the PMMA mold for 0.1 M NaCl solution chamber patterning (vii), oxygen plasma bonding of the PDMS to the bottom glass (viii), laser cutting of a PSA frame to be used as adhesive between the PDMS chamber and the Nafion membrane (ix), Nafion membrane laser cut (x), bonding of the Nafion membrane to the top glass (xi), bonding of the top glass to the PDMS through the PSA frame (xii), bonding between the top glass and two PDMS blocks in correspondence to the two holes to provide fluidic connections and avoid leakage (xiii).
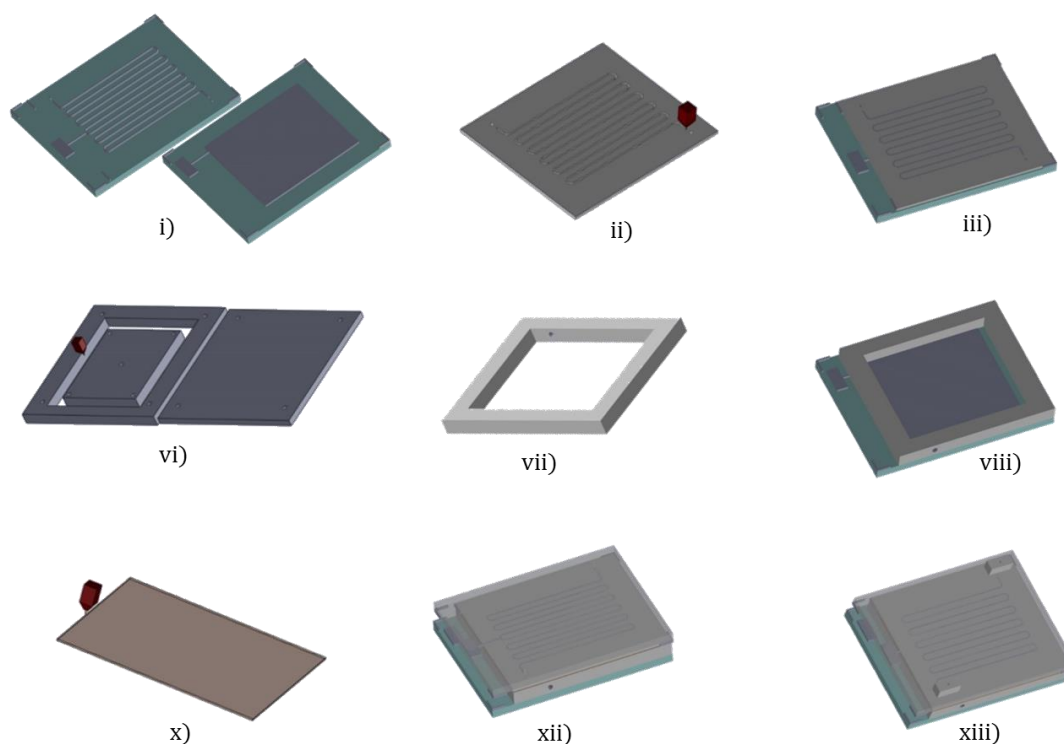
Figure 2.3. Main steps of the fabrication process flow of the microfluidic platform: electrodes patterning (i), microfluidic compartments fabrication (ii, vi, vii), Nafion cutting (x) and assembly (iii, viii, xii, xiii).

The following two sections will describe the detailed steps needed for the fabrication of the electrodes and the microfluidic compartments.

2.3.2 Electrodes fabrication

The planar Ag electrodes must fulfil several requirements: chloride ions removal through Ag oxidation to AgCl upon electrolysis, complete regeneration of Ag electrode and ability to withstand repetitive redox cycle, good adhesion to the glass substrate, and thickness in the range of tens of microns. Standard techniques for Ag deposition such as DC sputtering, evaporation and e-beam evaporation have adhesion issues due to the thermal stress for layer thicknesses above $2 \ \mu m$. Electrodeposition techniques are commonly used to overcome this limit and to obtain thicknesses of a few microns. Electroplated noble metal films generally have lower stresses than sputtered films due to the larger grain sizes [89]. In a first series of experiments, electrodeposition was performed on a titanium/platinum (Ti/Pt) seed layer: after a Ti/Pt lift off process, the wafer was immersed into a silver cyanide (AgCN) solution and different techniques (cyclic voltammetry, potentiostatic and galvanostatic deposition) were applied for the electroplating step. However, the adhesion of Ag to the Pt surface was not strong, and delamination of the d eposited Ag was observed as shown in Figure 2.4. The explanation of such deposition failure is that electroplating presents a significant

drawback when carried out on a large area resistive substrate [90]: when increasing the working electrode area, a significant voltage drop occurs due to the surface resistance, resulting in a very inhomogeneous current distribution [91] and hence in patchy films with poor adhesion. This was experimentally confirmed.
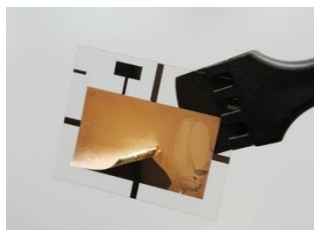
Figure 2.4. Picture of the electroplated Ag layer peeling off from the Ti/Pt seed layer.

In recent years printing techniques have been successfully used to pattern numerous materials, such as metal nanoparticles [92,93], semiconductors [94], dielectric materials [95], conducting polymers [96], cells [97] etc. at high speed and suitable resolution on large areas [98]. Among them, inkjet printing and screen printing are characterized by simplicity, low cost and compatibility with a wide range of substrates. Screen printing technology is a widely used technique for the fabrication of electrochemical sensors [99] and inkjet-printed Ag electrodes have been recently used for the development of a solid-state Ag/AgCl pseudo-reference electrode [100].

The feasibility to deploy these two techniques for the fabrication of Ag electrodes for NaCl removal was therefore investigated. Among the large variety of inks available on the market, six Ag inks with the best glass adhesion properties were selected. The chosen inks have different formulations in terms of solvent, particles size and solid content, parameters which can have an influence on the oxidation ability of the electrodes, as well as different curing conditions and resistivity (bulk silver resistivity: 1.59 $\mu\Omega\cdot$cm). Table 2.2 and Table 2.3 summarize the main properties of the inks chosen for screen printing and inkjet printing, respectively, as reported in their data sheets. All the inks were printed and thermally cured at the temperatures recommended by the manufacturers.

Table 2.2. Comparison of the properties of the different Ag inks chosen for screen printing.

Ink	Particle type	Viscosity (cP)	Curing T (° C)	Resistivity ($\mu\Omega\cdot$cm)	Solvent
5064H	Ag powder and resin (63-66%)	10000-20000	130	$\leq$12.8	C11-Ketones, Dimethyl succinate
HPS-021LV	Ag flake (75 wt%)	>1000	190	2.13 – 16.9	Water
PE825	Ag powder (73-77%)	15000-35000	230	$\leq$64.4	2-(2-Ethoxyethoxy)ethyl acetate

After printing and curing, the electrodes were observed using scanning electron microscopy (SEM) and energy dispersive X-ray spectroscopy (EDX) to analyze their morphology and elemental composition, respectively. Figure 2.5 shows the morphology of the different printed inks.

Table 2.3. Comparison of the properties of the different Ag inks chosen for inkjet printing.

Ink	Particle type	Viscosity (cP)	Curing T (° C)	Resistivity (μΩ·cm)	Solvent
SicrysTM I50TM-119	50% w/w Ag NPs	34	170	≤10	Triethylene glycol monomethyl ether
U5603	20 wt% Ag NPs	10-13	180	5-30	Ethanediol, ethanol, glycerol, 2-isopropoxyethanol
JS-B40G	40wt% Ag NPs	Not specified	250	2.7	Diethylene glycol monobutyl ether (0-20% w/w)
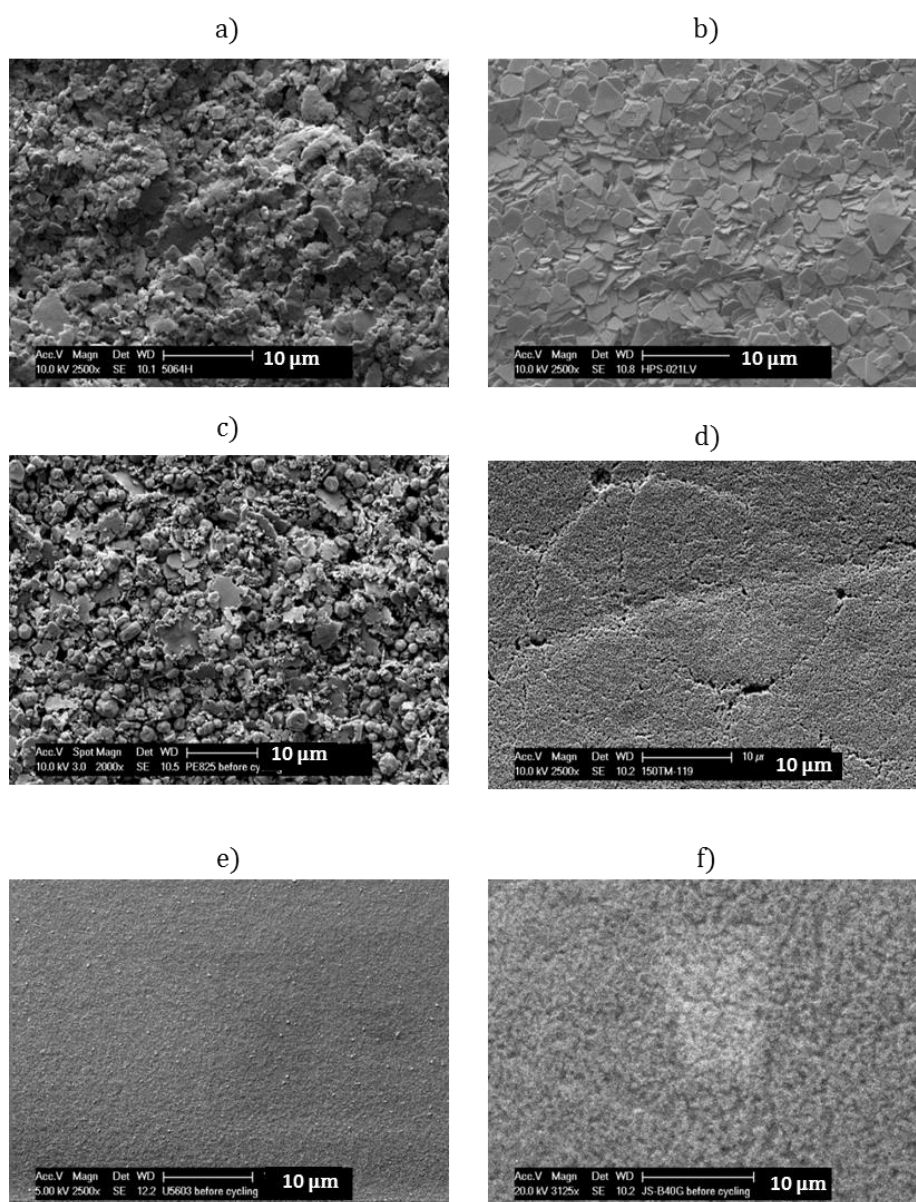
Figure 2.5 SEM pictures showing the morphology of the different printed inks after printing and curing: a) 5064H, b) HPS-021LV, c) PE825, d) Sicrys I50TM-119, e) U5603, f) JS-B40G.

The inks clearly have different morphologies. The three screen printed inks present an average particle size of around 5 μm, while the inkjet-printed inks have an average particle size of 150 nm, 50 nm and 100 nm respectively for Sicrys I50TM-119, U5603 and JS-B40G. The EDX analysis showed the same spectra for all the inks (only Ag and C) except for the ink PE825 which revealed the presence of copper and/or copper oxide. Figure 2.6 shows the EDX spectra of the Sicrys I50TM-119 ink and the PE825 ink for comparison. The spectra of the other four inks are almost identical to the former.

The thickness profile of the printed electrodes was measured with a Wyko white light optical profiler. Figure 2.7 shows the thickness profile of the different printed inks. The PE825 and Sicrys I50TM-119 inks were highly reflective hampering accurate thickness measurements. The average thickness measured was 5.1 µm for the 5064H ink (a), 6.2 µm for the HPS-021LV ink (b), 8.7 µm for the PE825 ink (c), 3.8 µm for the Sicrys I50TM-119 ink (d), 4.8 µm for the U5603 ink (e), and 6.1 µm for the JS-B40G ink (f).
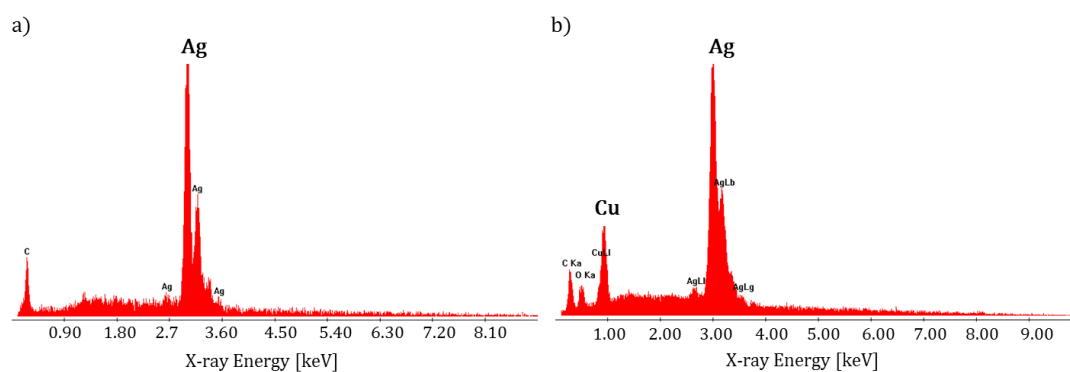
Figure 2.6. EDX spectra for the ink Sicrys I50TM-119 (a) and PE825 (b).
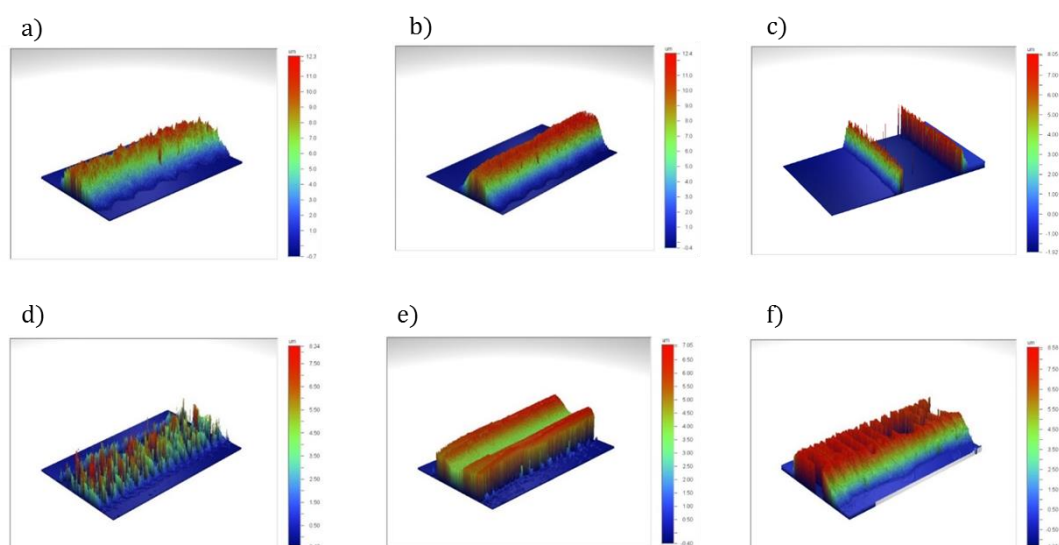
Figure 2.7. Wyko 3-D thickness profile of the different printed inks: a) 5064H, b) HPS-021LV, c) PE825, d) Sicrys I50TM-119, e) U5603, f) JS-B40G.

2.3.3 Microfluidic compartments fabrication and device assembly

The shallow channel was patterned by CO_2 laser cutting a pressure sensitive adhesive (PSA) sheet, AR clear 8932EE. For fabricating the deep PDMS chamber a PMMA mold was laser cut by CO_2 laser and assembled using screws. The PDMS (Sylgard 184) was mixed (base/curing agent ratio 10:1), injected into the mold through a hole until completely filling the cavity, cured in an oven for 2 hours at 65 °C, and finally demolded. A hole was punched in one side of the PDMS frame in order to allow filling the chamber with the 0.1 M NaCl solution after assembly.

The device was afterwards assembled. The shallow adhesive channel was attached by applying pressure to the top glass with the patterned WE after releasing the first protective sheet (liner). The Nafion membrane was later fixed to the other side of the adhesive channel after removing the second liner. The PDMS chamber was irreversibly bonded to the bottom glass by oxygen plasma treatment (power: 50 W, time: 65 s) and an additional heating step of 10 minutes at 70 °C. A PSA frame was laser cut and attached to the PDMS chamber for completing the assembly of the device serving as adhesive between the Nafion membrane and the PDMS chamber. Finally two PDMS blocks (5 mm thick) were bonded to the top glass in correspondence to the holes through an UV ozone treatment of 30 minutes. Figure 2.8 shows a picture of the final assembled device where it is possible to distinguish the working and counter/reference electrodes, the microfluidic compartments, and the holes for filling the channel (inlet and outlet) and the chamber with the solutions.
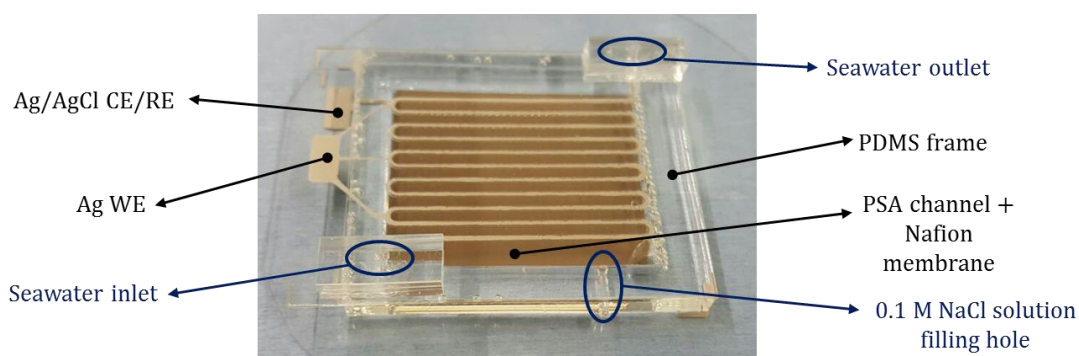
Figure 2.8. Picture of the assembled microfluidic platform.

PDMS-Nafion bonding alternative procedure

Bonding between silicone components and membranes is an important issue for integration of membranes into microfluidic devices where functions such as separation, purification or sample pre-treatment are needed. In such cases, strong bonding is required to avoid leakage of liquids flowing inside the microfluidic system. An alternative procedure to the use of PSA for bonding Nafion and PDMS was explored. This procedure was not applied for the development of the microfluidic platform, but it is worthwhile mentioning since it successfully worked.

Kim et al. [101] reported an irreversible bonding of PDMS to a Nafion film directly patterned on a glass substrate by O_2 plasma treatment of the surfaces. In this thesis plasma bonding was

investigated by using different values for the power and time parameters, as well as its combination with heating and/or vapor-phase silanization steps. Among the different tested procedures, only one allowed achieving a tight and irreversible bonding between Nafion and PDMS.

The successful method consists of the following steps: (i) activation of the Nafion surface with oxygen plasma (50 W for 45 s), (ii) overnight vapor-phase silanization of the Nafion surface with (3-aminopropyl)triethoxysilane (APTES), (iii) cleaning of the PDMS surface with acetone, isopropanol, DI water and drying with nitrogen blow, (iv) preheating of the Nafion membrane on a hot plate at 70 °C for 5 minutes, (v) activation of the PDMS surface with oxygen plasma (50 W for 45 s), (vi) manual pressure of the PDMS sample on the Nafion one and heating on the hot plate for 10 minutes at 70 °C, (vii) cooling down to room temperature. After a few hours an attempt to separate the two layers resulted in the rupture of PDMS showing that an irreversible bonding was achieved.

2.3.4   Materials and instrumentation

The glass plates serving as substrates for printing the Ag electrodes were purchased from Schott, Switzerland. Ag ink HPS-021LV was purchased from Novacentrix, Austin, USA and Ag ink 5064H and PE825 were purchased from Dupont, Hertfordshire, UK. Ag ink SicrysTM I50TM-119, U5603, and JS-B40G were purchased respectively from PV Nanocell, Israel, SuntronicTM SunChemical, USA, and Novacentrix-Metalons, USA. Polydimethylsiloxane (PDMS) Sylgard® 184 (Dow Corning) was used for patterning the microfluidic compartment for the 0.1 M NaCl solution, while AR clear 8932EE Pressure Sensitive Adhesive (Adhesive Research, USA) was used to pattern the microfluidic shallow channel for seawater. A 25 μm thick Nafion membrane (NAFION® Membrane NR-211) was purchased from Dupont. Nafion is a fluoropolymer-copolymer which incorporates perfluorovinyl ether groups terminated with sulfonate groups onto a tetrafluoroethylene (Teflon) backbone. DuPont Nafion® XL membrane is a reinforced membrane based on chemically stabilized perfluorosulfonic acid/PTFE copolymer in the acid (H^+) form.

A Metrohm Autolab PGSTAT12 was used for the cyclic voltammetry (CV) and chronoamperometric tests of the inks and microfluidic platform. Sodium chloride (NaCl) solutions were prepared from p.a. quality NaCl (Sigma Aldrich) in de-ionized water. A NEMESYS syringe pump, Cetoni GmbH Germany, was used for pumping the sample (0.6 M NaCl) and the regeneration solution (1 mM NaCl) through the microfluidic channel.

2.3.5   Electrochemical characterization of the electrodes

The electrochemical performance in terms of oxidation ability (mC/mm^2) and adhesion of the Ag electrodes patterned by printing the six different inks was investigated and compared in order to choose the most appropriate ink for building the microfluidic platform. The oxidation ability (charge registered per mm^2) and the adhesion (number of oxidation/regeneration cycles before adherence loss from the glass substrate) gives information about the efficiency in chloride removal and lifetime of the electrode, respectively.

A 400 mm^2 square design was used for all the inks. The printed Ag electrodes were electrochemically tested in 0.6 M NaCl solution in a three electrode setup against a standard Ag/AgCl/3 M KCl RE and a Pt plate CE in order to (i) identify the oxidation and reduction current peak potentials in the cyclic voltammograms (CVs) of the six inks, (ii) measure the charge passing through the printed electrodes during the chronoamperometry measurements carried out at different potentials, (iii) identify the ink with the highest oxidation ability, (iv) identify the ink with the highest robustness in water environment and adhesion to glass in terms of number of repetitive oxidation/reduction cycles.

Firstly, the electrodes underwent voltammetric cycles between -1.5 V and +1.5 V: a staircase sweep with step amplitude of 2.5 mV and scan rate of 25 mV/s was applied. Figure 2.9 shows the CVs registered for the six printed electrodes after cycle stabilization. Each ink shows a different voltammogram with oxidation and reduction peaks at different potentials: oxidation peaks range from +0.3 V to +1.3 V and reduction peaks from -0.6 V to -1.4 V.
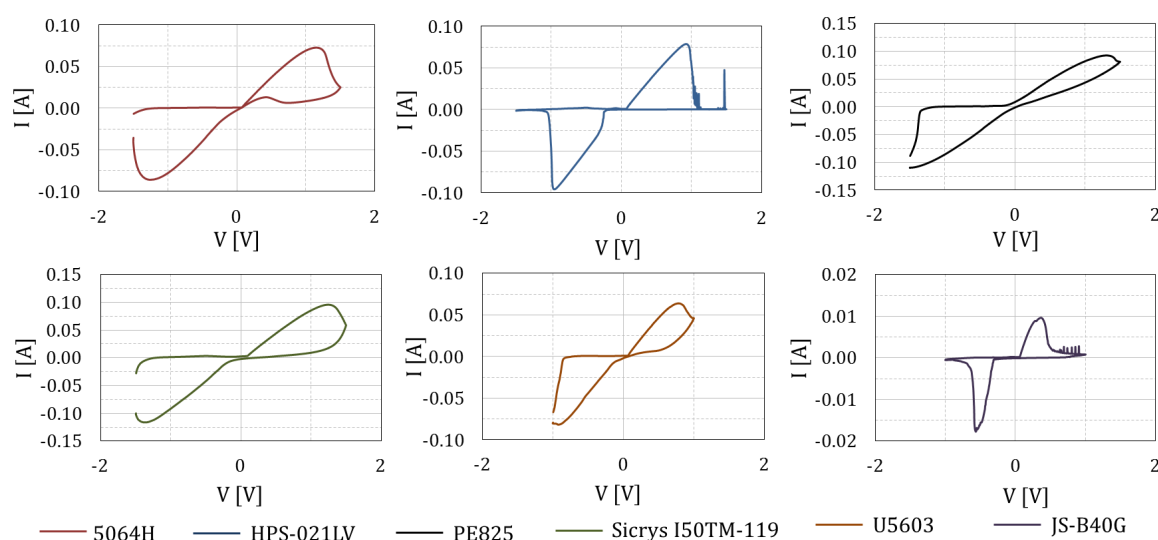
Figure 2.9. Comparison of the cyclic voltammograms of the electrodes (400 mm^2 area) printed with the six different Ag inks vs. Ag/AgCl/3 M KCl RE, scan rate of 25 mV/s.

In order to compare the different inks under the same conditions in terms of potential and time, chronoamperometric tests were carried out for each ink at different oxidation and reduction potentials.

Figure 2.10 shows the comparison of the charge registered during 60 s oxidation and 120 s regeneration chronoampeometric tests of the printed electrodes. The charge increases with increasing potential for the 5064H and PE825 inks, while it is almost constant for the other inks. The 5064H and PE825 inks showed also the highest oxidation ability and very similar electrochemical behavior up to an applied potential of +1.1V, above which the 5064H ink performed better and showed the same oxidation ability of a silver wire electrode (15.5 mC/mm^2).

Based upon this consideration related to the oxidation ability, the most suitable ink for chloride removal is the 5064H ink. However another parameter to take into account is the adhesion to glass. Therefore the inks underwent repetitive redox cycles at +0.9 V and -1.0 V and their adhesion to glass was qualitatively evaluated in terms of repetitive oxidation/regeneration cycles.
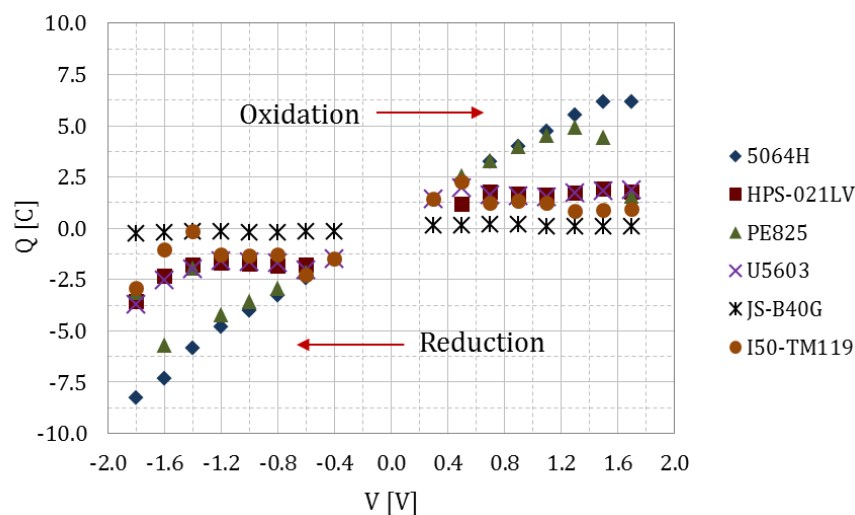
Figure 2.10. Comparison of the charge registered for each ink at different oxidation and reduction potentials.

The PE825 ink offered the best adhesion to glass withstanding more than 60 oxidation/regeneration cycles compared to 25 cycles for the 5064H ink. Table 2.4 reports the average thicknesses of the printed inks along with their oxidation ability and adhesion properties (adhesion after several cycles of oxidation at +0.9 V for 60 s and of regeneration at -1.0 V for 120 s).

Table 2.4. Thickness and performance (oxidation ability and adhesion) of the different printed Ag inks.

Ink	Thickness (µm)	Loss of adhesion after cycles #	Max. Oxidation ability (mC/mm^2)
5064H	5.1	~25	15.5 (at +1.5 V)
HPS-021LV	6.2	50	4.75 (at +1.5 V)
PE825	8.7	>60	12.3 (at +1.3 V)
SicrysTM I50TM-119	3.8	~30	5.6 (at +0.5 V)
U5603	4.8	~10	4.9 (at +0.5 V)
JS-B40G	6.1	20	0.4 (at +0.5 V)

The printed inks were observed by SEM a second time after several oxidation/regeneration cycles. As shown in Figure 2.11 their morphology significantly changed after the redox cycles showing a much more porous surface.

Since adhesion is a key issue for the lifetime of the device and since the oxidation ability of the ink PE825 is only slightly lower than that of the 5064H ink (12.3 mC/mm^2), the PE825 ink was initially chosen for fabricating the electrodes of the microfluidic platform.
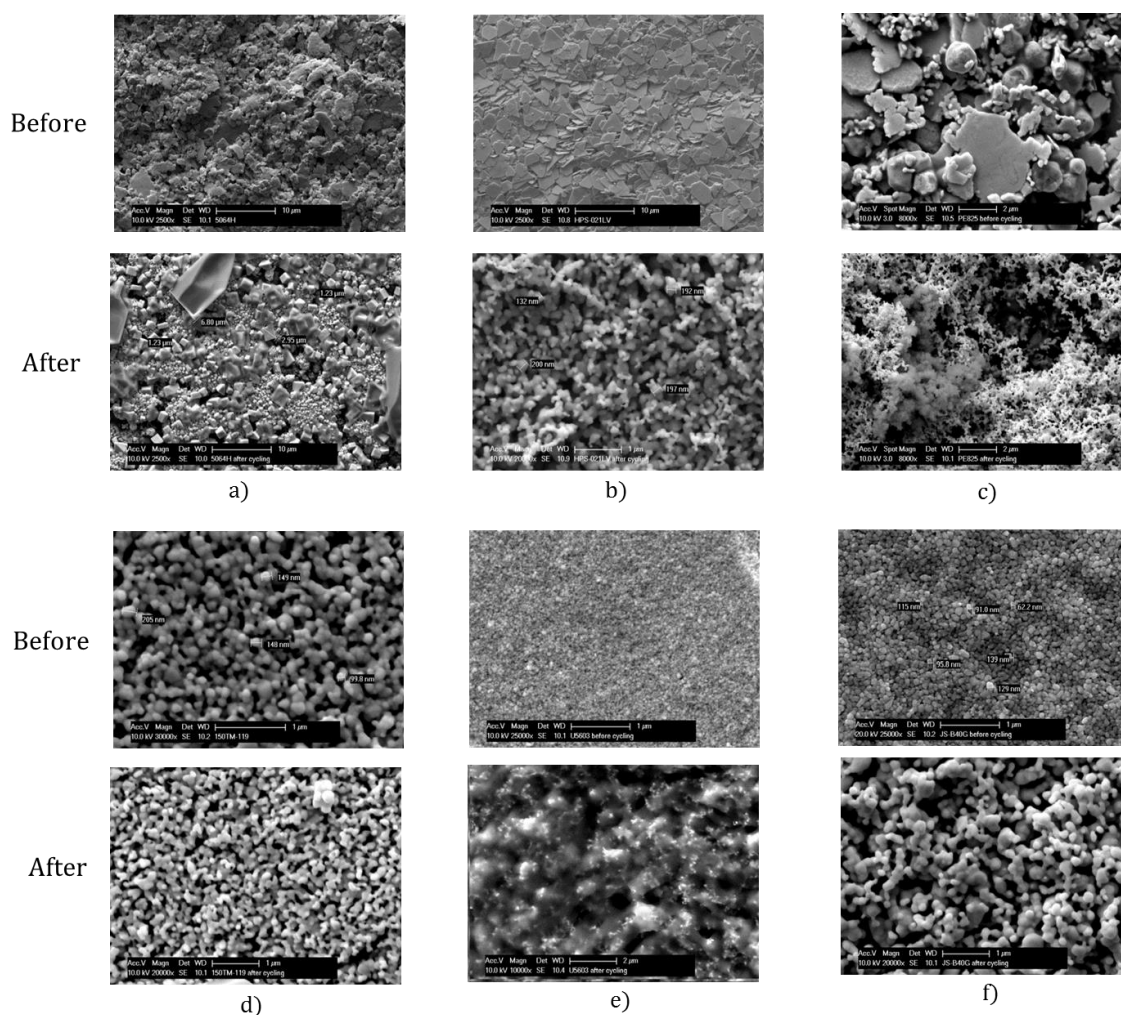
Figure 2.11. SEM pictures showing the morphology of the different printed inks before and after several oxidation/regeneration cycles: a) 5064H, b) HPS-021LV, c) PE825, d) Sicrys I50TM-119, e) U5603, f) JS-B40G.

2.3.6 Electrochemical characterization of the PE825-based microfluidic platform

The microfluidic platform built up with PE825 Ag electrodes was tested in a setup consisting of a potentiostat and a syringe pump.

The PDMS chamber of the microfluidic platform was filled with a 0.1 M NaCl solution. Afterwards, the microfluidic platform was fluidically connected to the pump by using 0.8 mm inner diameter Teflon tubes and electrically to the potentiostat in order to carry out the electrolysis of a 0.6 M NaCl sample in the shallow channel. A three channel pump setup was used: a 10 ml syringe filled with 0.6 M NaCl solution, a 10 ml syringe filled with air, and a 10 ml syringe filled with a 1 mM NaCl solution for regeneration.

The experimental protocol consists of 6 steps: (i) the shallow channel is filled with the 0.6 M NaCl solution with a flow rate of 10 µl/s, (ii) a constant positive potential is applied between WE and CE/RE for a given period of time in order to achieve electrolysis and oxidation of Ag to AgCl while

sodium ions are transferred to the 0.1 M NaCl solution, (iii) air is pumped with a flow rate of 20 μl/s in order to empty the channel, (iv) the shallow channel is filled with the 1 mM NaCl solution with a flow rate of 10 μl/s, (v) a constant negative potential is applied between WE and CE/RE for a given period of time in order to achieve the regeneration of the Ag electrode, (vi) air is pumped with a flow rate of 20 μl/s in order to free the channel by driving the 1 mM NaCl solution to the waste. Several chronoamperometric tests were carried out at different potentials and for different periods of time with the aim to find the optimal conditions for salt removal: for each test the current passing through the electrodes was recorded and integrated in order to determine the total amount of charge involved in the reaction.

The Ag WE underwent consecutive oxidation/regeneration reactions by applying increasing potentials from 0.3 V/-0.4 V to 1.1 V/-1.2 V for a time period of 60 s. Figure 2.12 shows the measured chronoamperograms for oxidation (a) and regeneration (b) which revealed that the current-time response increased with the applied potential up to +0.9 V where it leveled off. The registered charge increased as well with the applied potential, logarithmically in the case of oxidation and linearly in the case of regeneration as shown in the insets of Figure 2.12. Only a small enhancement of the charge was observed by increasing the potential from +0.9 V to +1.1 V (1.56 C vs. 1.64 C).
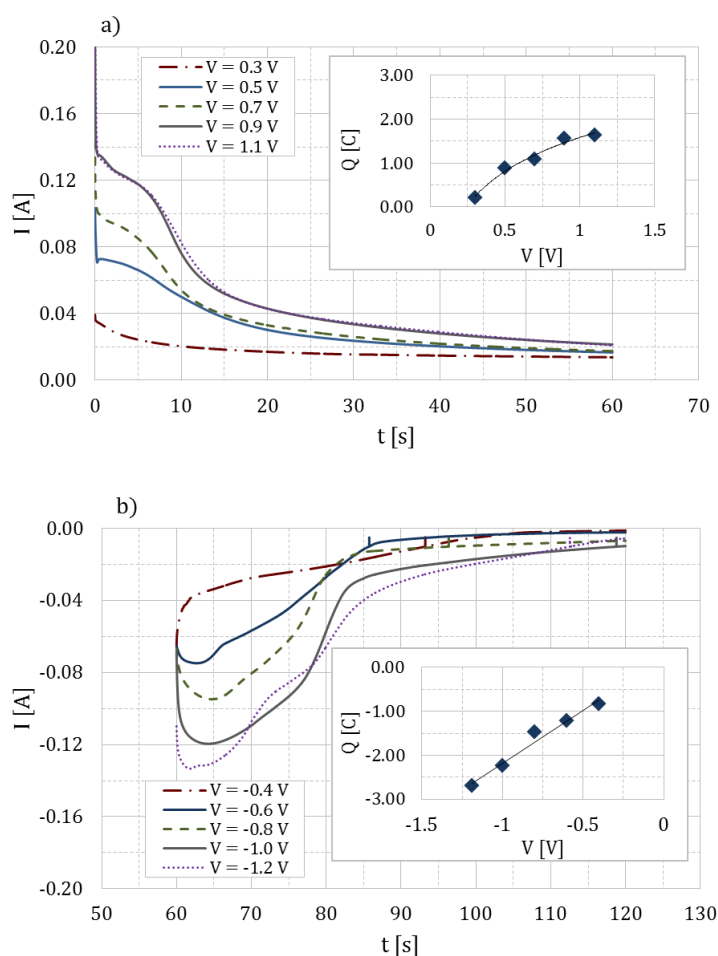
Figure 2.12. Comparison of the chronoamperograms registered for different oxidation (a) and regeneration (b) potentials during 60 s and 120 s, respectively, with the relative registered charge (insets).

The charge registered during the regeneration was higher than the respective oxidation charges showing a complete regeneration of the electrode but also that other phenomena were probably occurring at the electrode/solution interface (possibly due to the presence of copper in the ink formulation).

A second set of experiments was carried out, in which the microfluidic platform underwent consecutive oxidation/regeneration cycles by applying the same potentials (+0.9 V/-1.0 V) for an increasing period of time (from 60 s to 300 s). The results are reported in Figure 2.13 which shows the chronoamperometric measurements and registered charge for oxidation (a) and regeneration (b).

The oxidation charge is linearly increasing with time up to 240 s, while it decreases for an oxidation time of 300 s. The explanation is found in the regeneration chronoamperograms: for a time period of 240 s the electrode was not completely regenerated (Qreg=-2.5 C vs. Qox=5.12 C).

The thickness of the Ag layer oxidized to AgCl in 240 s was calculated from Equation 2.1 as being 7.9 µm. Since the measured average thickness of the electrode was 8.7 µm but the thickness was not homogeneous, a likely explanation for the low regeneration charge at 240 s is that some parts of the Ag serpentine had been completely oxidized to AgCl down to the interface with glass during the 240 s of the oxidation step.
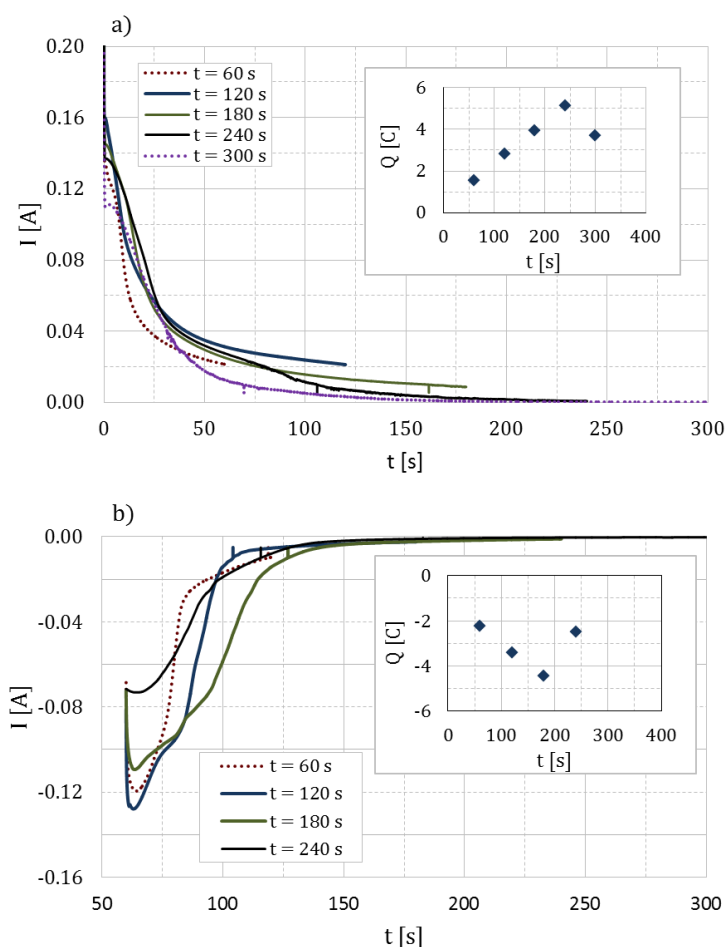
Figure 2.13. Comparison of the chronoamperograms registered during different periods of time for an oxidation potential of +0.9 V (a) and a regeneration potential of -1.0 V (b) with the relative registered charge (insets).

2.3.7   PE825 ink related issues

The different microfluidic platforms built up with PE825 ink based electrodes were found to release reaction products into the solution, whose color was turning green, not only upon electrolysis, but also when in long-term contact with NaCl solutions. This contamination of the sample is possibly due to the copper present in the ink formulation which is also playing a role in the reaction thus causing a high background current after electrolysis. Figure 2.14 shows a picture of the device with green residues (a) and the first cyclic voltammetry scan of the PE825 ink (b) which revealed two extra peaks near +0.1 V and +0.2 V that disappeared after some cycles. These two peaks could be attributed to copper oxidation.
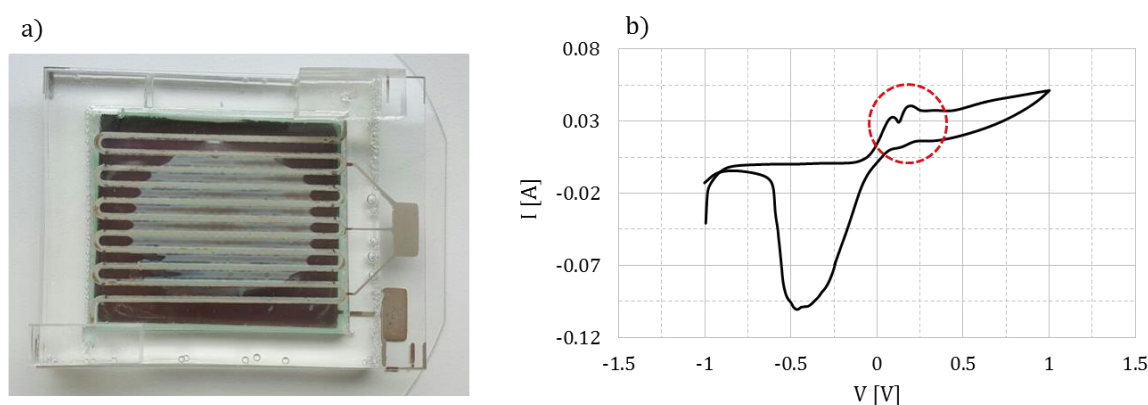
Figure 2.14. Picture of the device with green residues (a) and first cyclic voltammetry scan of the PE825 ink in 0.6 M NaCl (b).

This contamination of the sample is unacceptable since it should be then transported to the nutrients detection unit, therefore the 5064H ink was finally chosen for building the microfluidic platform.

2.3.8   Electrochemical characterization of the 5064H-based microfluidic platform

The microfluidic platform built up with 5064H Ag electrodes was electrochemically tested by CV and chronoamperometry to determine the optimal oxidation potential for desalination. The chamber and the channel were filled with 0.1 M NaCl and 0.6 M NaCl solutions, respectively.

The device was firstly characterized by cyclic voltammetry at different scan rates ranging from 100 to 25 mV/s. Figure 2.15 shows the different voltammograms and the plot of the current peaks versus the scan rate for oxidation and reduction (inset).

The linearity between the current peak and the scan rate reveals the expected thin layer behavior for both processes of oxidation and reduction. Indeed, for redox processes in thin layer systems closed to the electrode, the peak current expression is linear with respect to the scan rate according to the following relationship:

$$i_p = -\frac{n^2 F^2}{4RT} vVC$$

Equation 2.12

where R: universal gas constant, T: temperature, v: scan rate, and C: bulk concentration.
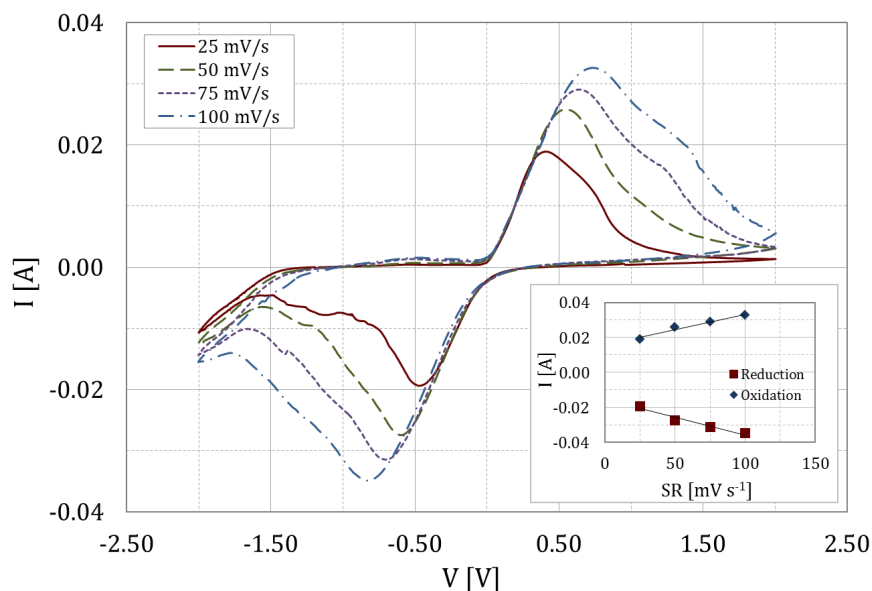
Figure 2.15. Cyclic voltammograms of the microfluidic device at different scan rates and plot of the current peaks versus scan rate for oxidation and reduction (inset).

Together with the increase of the current peak with the scan rate, also a shift of the current peak in potential was observed at higher scan rates. This may be indicative of the introduction of kinetic control (rather than diffusion) on the shorter time scale being applied or may arise due to a small amount of uncompensated resistance [102]. Since the linearity of the current peak with the scan rate reveals that we are not dealing with a diffusion-controlled process (thin-layer behavior), we can assume that the shift is caused by the kinetic control and not by an uncompensated resistance.

Furthermore, for each scan rate the reduction current peak is close to the oxidation one, revealing an excellent reversibility of the electrochemical process. The overall results obtained by cyclic voltammetry suggest the range 700-900 mV as optimal range for achieving desalination.

Chronoamperometric measurements were therefore carried out at different oxidation and reduction potentials covering the range suggested by the CV tests. The Ag WE underwent consecutive oxidation/regeneration reactions by applying increasing potentials from +0.3 V/-0.4 V to +1.1 V/-1.2 V for a time period of 60 s/120 s.

Figure 2.16 shows the measured chronoamperograms at different oxidation (a) and reduction (b) potentials together with the registered charges (insets). The oxidation chronoamperograms reveal that only at +0.9 V the exponential current-time response expected for a thin layer solution adjacent to the electrode surface is observed, as described by Equation 2.8.

The oxidation charge increases with the applied potential, made exception for the potential +0.9 V for which a lower value is found (Qox=0.969 C), which was actually the closest to the charge value expected for complete chloride removal (Qox=0.926 C).

The regeneration curves showed to have a similar behavior. The charge registered during the regeneration was higher than the respective oxidation charge for each potential, showing a complete regeneration of the electrode but also that other phenomena are probably occurring during regeneration at the electrode/solution interface. Again the best performance was found for the potential pair +0.9 V/-1.0 V for which the smallest difference between the oxidation and reduction charge (ΔQox-red=0.3 C) was found against the 0.7 C, 0.8 C, 0.9 C and 1.0 C differences registered for the other potential pairs.

Based upon all these considerations, the potential +0.9 V was found to be the optimal oxidation potential, having as well the lowest residual current (5.4 mA) and confirming the cyclic voltammetry results. The potential -1.0 V was consequently chosen as optimal regeneration potential. Neither contamination of the solution nor liquid leakage was observed, as well as an excellent adhesion to the glass substrate.
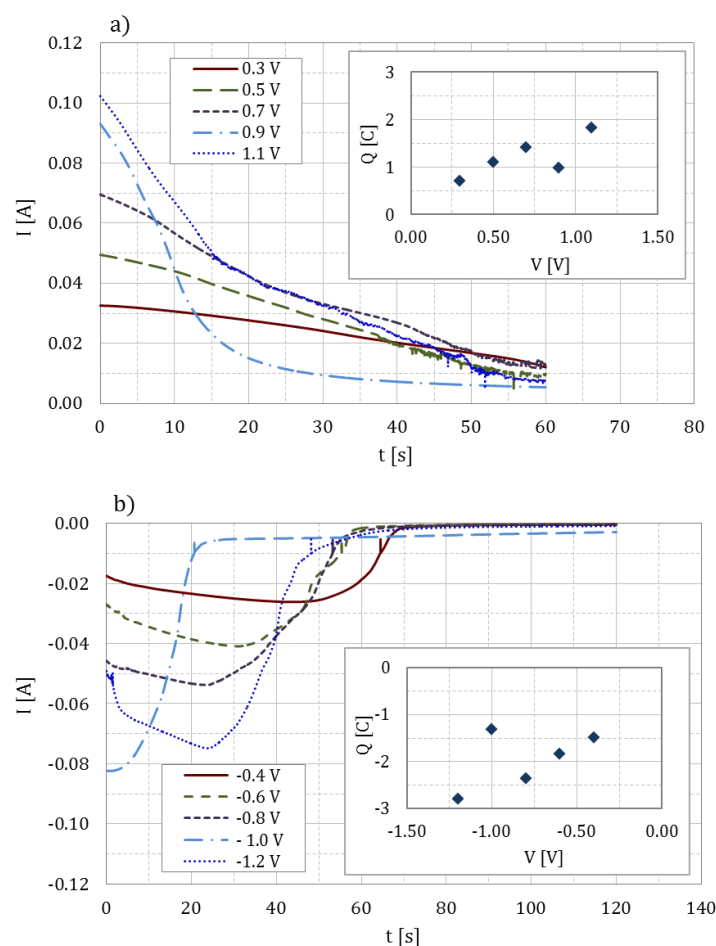
Figure 2.16. Chronoamperograms of the microfluidic device at different oxidation (a) and reduction (b) potentials with their respective measured charges (insets).

2.4   Second generation of the desalination platform

The second generation platform was a larger device and developed in order to overcome the limitations of the first one. The first generation had a sample volume of 17 µl which was not sufficient to allow downstream nutrient detection as well as the characterization of the device in terms of salt content. A new design for achieving a volume of several tens of microliters was therefore needed. Another issue encountered while carrying out the characterization of the first generation device was the precise confinement of the 0.6 M NaCl solution in the channel. The displacement of the volumes by an air flow was not easy to achieve revealing possible air leaks in some points of the hydraulic circuit. Therefore new fluidic connectors (liquid- and air-tight) were sought for driving the fluids towards the channel and the downstream sensor for characterizing the desalination efficiency. The sensor chosen for this purpose is a flow-through conductivity sensor which will be described in the following sections.

2.4.1   Requirements and proposed solutions

The main requirement for the new design is the achievement of a sample volume around six times bigger than the previous one without exceeding the maximum dimensions allowed by the submersible probe (maximum dimensions for the device: 120x63x25 mm) and by the thin-layer conditions (maximum thickness of 100 µm). Three different designs with serpentines of different lengths and widths for a total volume around 80 µl (40 µm thickness) were tested: design A (1 mm width), design B (2 mm width), design C (5 mm width). They are shown in Figure 2.17.
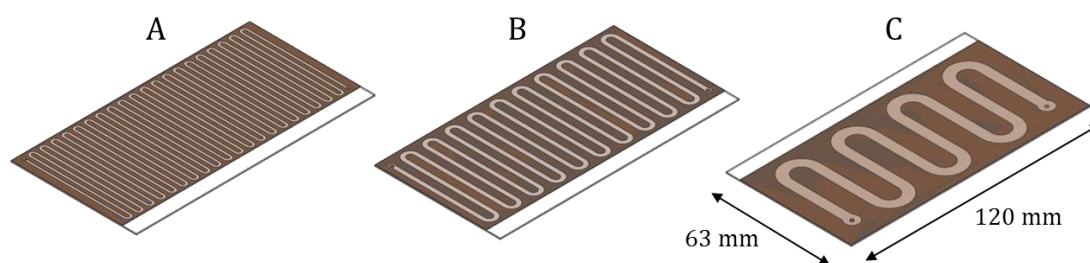
Figure 2.17. Three possible different designs (A, B and C) for the second generation device.

The design A showed fabrication issues due to the small size of the serpentine fingers: while detaching the first liner from the adhesive the fingers touched each other and the adhesive layer was destroyed. Design B was still presenting this issue but it was easier to handle. An adhesive sheet was therefore laser cut with the design B and design C serpentine. Then it was attached in between two PMMA plates for testing the fluidics. Design B was presenting liquid leaks while loading and unloading the sample, while design C was presenting leaks in some points and accumulations in some curves of the serpentine only while unloading the sample.

A more robust adhesive was therefore sought. Two different adhesives, ARcare® 90445 and ARcare® 92712 were chosen as possible candidates. They both consist of a clear, thin flexible

polyester film coated on both sides with a medical grade acrylic pressure-sensitive adhesive. These products are suggested for bonding, laminating and assembly of in-vitro diagnostic and related membrane-based immunoassay products, and passed cytotoxicity tests. They have a thickness of around 80 and 50 μm, respectively.

The adhesive 90445 was chosen in order to increase the sample volume thanks to the higher thickness still inside the thin-layer range, thus limiting the extension in the planar dimensions. The tests with the PMMA blocks showed a perfect loading and unloading of the sample without any accumulation or leak with a serpentine width of 2 mm. The final design for the channel was therefore a serpentine with a total length of 637 mm, a width of 2 mm, and a total volume of 121.64 μl.

This adhesive had the advantage to easily allow the removal of the two liners without any cooling treatment, as was required for the AR clear 8932EE handling to avoid filaments formation.

The second issue related to the confinement of the sample volume in the channel was solved by replacing the PDMS pieces providing the single inlet and single outlet fluidic connections by two PMMA blocks with multiple inlet/outlet threaded holes. Figure 2.18 shows the fabricated connectors for inlet (a) and outlet (b). Flanged fittings can be easily screwed in the PMMA connectors avoiding leakage in correspondence to the glass and allowing multiple inlets and outlets.
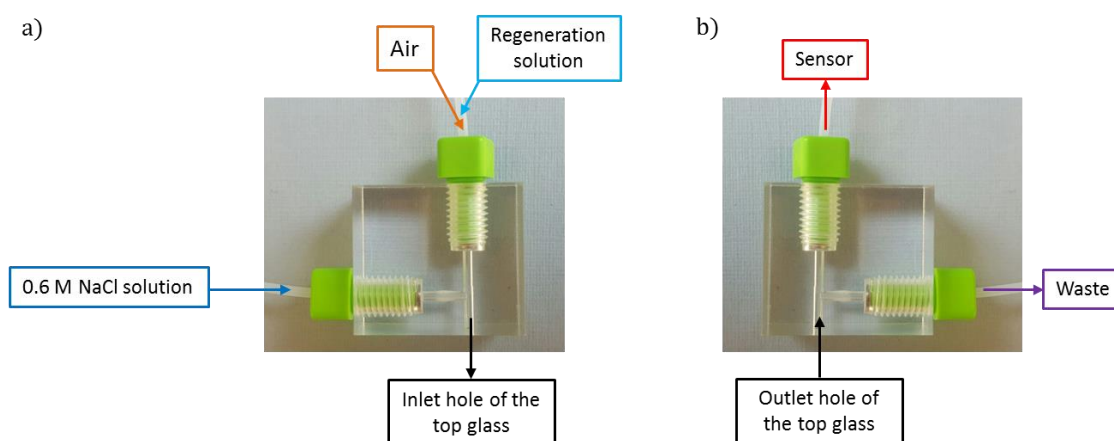
Figure 2.18. PMMA connectors for inlet (a) and outlet (b).

The 0.6 M NaCl solution can be pumped through the side hole of the inlet connector (a) towards the channel and then air coming from the top hole of the inlet connector (a) can be used to displace the precise quantity present in the channel towards the sensor through the top hole of the outlet connector (b). The solution for regeneration can be pumped through the top hole of the inlet connector (a) and driven towards the waste through the side hole of the outlet connector (b). These blocks can be sealed to the top glass of the device in correspondence of the holes by using pressure-sensitive adhesives.

2.4.2 Design and fabrication

The second generation microfluidic platform has dimensions of 120 x 63 x 23 mm as shown in Figure 2.19a. The WE is a serpentine with a total length of 637 mm and a width of 1.6 mm, while the CE/RE is a square of 95 x 40 mm. The fluidic compartments for the seawater and the 0.1 M NaCl solution have a total volume of 121.64 µl and 21.3 ml, respectively. The top and the bottom glass substrates for patterning top and bottom electrode, respectively, have dimensions of 12 x 63 x 0.55 mm; two holes are mechanically drilled in the former by the manufacturer in order to provide fluidic connections to the shallow channel. Figure 2.19b shows a picture of the fabricated device.
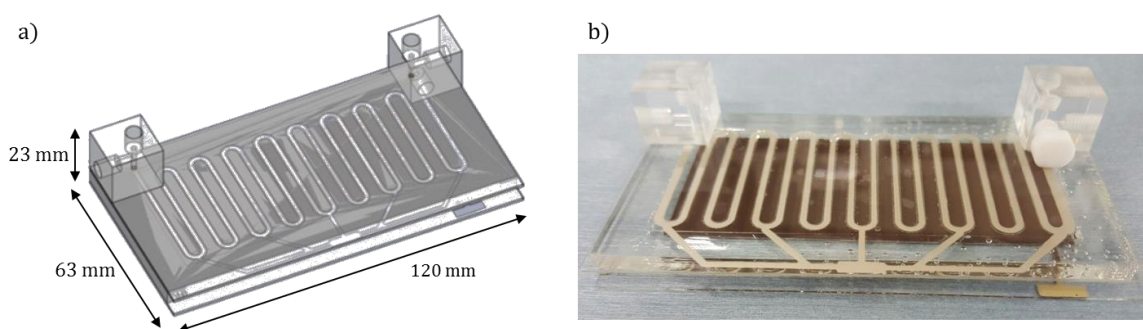
Figure 2.19. 3D drawing (a) and picture (b) of the second generation microfluidic platform.

The fabrication process flow consists of thirteen steps. They are the same as described in section 2.3.1 with three differences. The first one is that the step of holes mechanical drilling in the top glass was not necessary since it was performed by the glass plate manufacturer. The second difference is that the bonding between the PDMS frame and the PSA frame was achieved by oxygen plasma treatment (50 W, 65 s) which was required to ensure an irreversible bonding between the PDMS and the acrylic adhesive. Finally the third difference concerns the bonding of the PMMA blocks to the top glass which was achieved through a PSA layer.

2.4.3 Materials and instrumentation

Glass plates, silver ink and PDMS were the same as used for the first generation platform, while AR care 90445 Pressure Sensitive Adhesive (Adhesive Research, Ireland) was used to pattern the microfluidic shallow channel for seawater. The experimental setup consisted of the same Autolab potentiostat and four-channel NEMESYS syringe pump with the addition of a conductivity sensor. A flow-through conductivity cell ET916 (17 µl cell volume, k=1 cm^{-1} cell constant) coupled to an EP357 conductivity isoPod and an e-DAQ e-corder potentiostat was used for monitoring conductance of the sample during the experiments.

2.4.4 Experimental setup and methodology

Figure 2.20 shows the experimental setup. The PDMS chamber of the microfluidic platform was filled with a 0.1 M NaCl solution before starting the experiments.
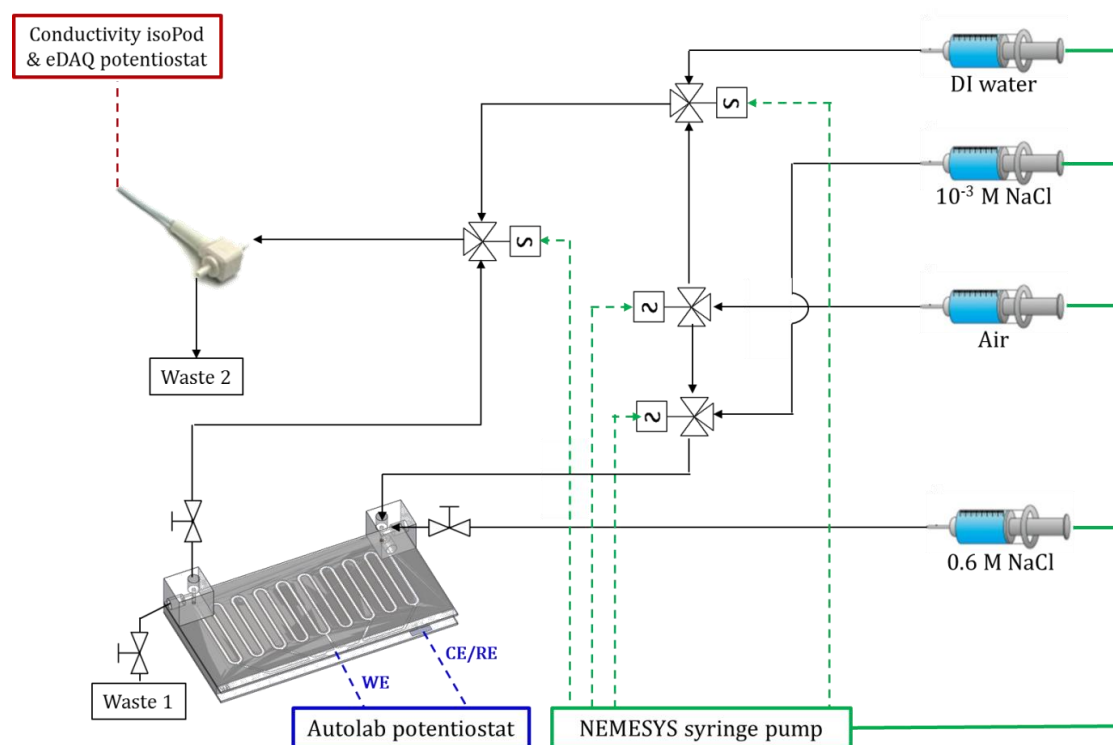
Figure 2.20. Experimental setup: the Ag WE and Ag/AgCl CE/RE are electrically connected to the potentiostat; the conductivity sensor and the shallow microfluidic channel are fluidically connected to the NEMESYS pump (four electro-valves and three on/off valves are used to switch the solutions).

The device was fluidically connected to the NEMESYS pump and electrically to the Autolab potentiostat in order to carry out the electrolysis of a 0.6 M NaCl sample in the shallow channel. A four channel configuration of the pump was used: a syringe filled with 10 ml 0.6 M NaCl solution, a 25 ml syringe filled with air, a syringe filled with 10 ml 10^{-3} M NaCl solution, and a 25 ml syringe filled with DI water. Four electro-valves and three manual on/off switch valves were used to drive the solutions to the shallow channel and/or to the conductivity sensor; the latter was connected to the outlet of the device for allowing conductance measurements and to the DI water and air syringe for washing and drying between each measurement. Figure 2.21 shows a picture of the microfluidic platform connected to the pump, the potentiostat and the sensor.

The experimental protocol consists of 7 steps and Figure 2.22 illustrates their timing with respect to the conductance measurement: (i) the shallow channel is filled with the 0.6 M NaCl solution with a flow rate of 10 µl/s, and the three manual valves are set in the off position to confine the solution and allow conditioning of the membrane for 2 hours, (ii) the conductivity sensor is washed by a constant flow of DI water (10 µl/s flow rate) and then dried by a constant air flow of 20 µl/s, (iii) a constant positive potential is applied between WE and CE/RE for a given period of time (t_{ox}) in order to achieve electrolysis and the conductance measurement is started at the same time of

electrolysis (no change of the conductance value is measured since the line is filled with air), (iv) when electrolysis is stopped, the manual valves are opened and air is pumped with a flow rate of 20 µl/s in order to drive the sample towards the conductivity sensor and then to Waste 2: a peak is registered when the sample flows through the sensor, (v) the shallow channel is filled with the 1 mM NaCl solution with a flow rate of 10 µl/s, (vi) a constant negative potential is applied between WE and CE/RE for a given period of time in order to achieve the regeneration of the Ag electrode, (vii) air is pumped with a flow rate of 20 µl/s in order to free the shallow channel by driving the 1 mM NaCl solution to the Waste 1 and allow a new cycle. The protocol is then repeated starting from step (i) without the membrane conditioning phase.
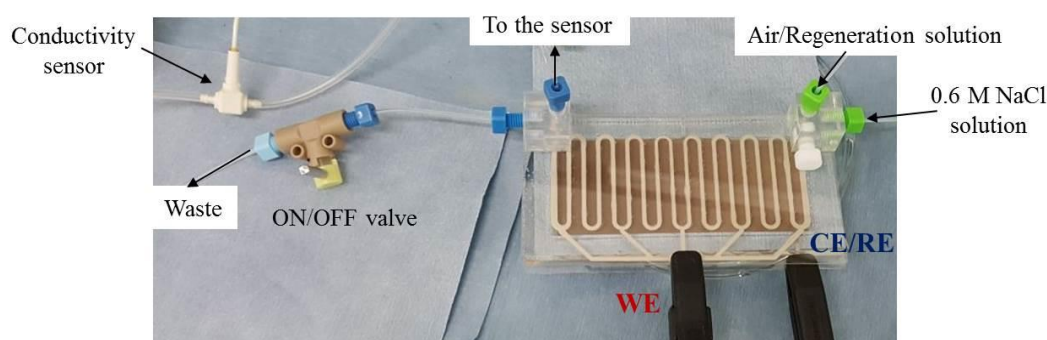
Figure 2.21. Picture of the microfluidic platform in the experimental setup: the WE and CE/RE are electrically connected to the potentiostat, the inlet/outlet ports are fluidically connected to the pump and the conductivity sensor.

The device was tested at different potentials for different periods of time: the final concentration of the sample was estimated through the charge registered during oxidation and measured through the conductance after treatment. For each experiment the total amount of charge involved in the reaction was measured, and the residual current, which could be due to oxygen interference or other competitive processes occurring at the electrode/solution interface, multiplied by the electrolysis time was subtracted. The amount of chloride removed from the solution was calculated (assuming 100% current efficiency) by applying Faraday electrolysis law (Equation 2.1).
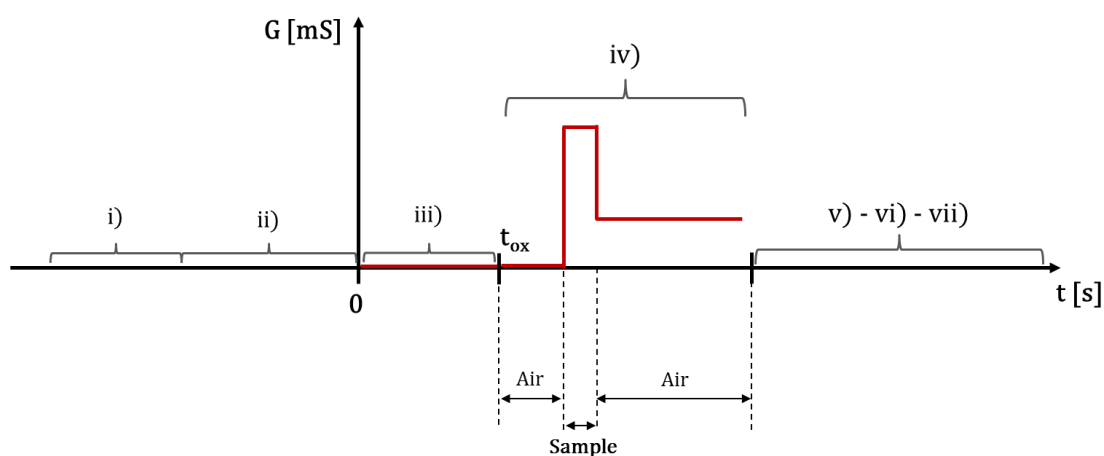
Figure 2.22. Experimental protocol timing: the conductance measurement is started at the same time as electrolysis and a peak is registered when the sample flows through the conductivity sensor.

The final concentration of the treated sample measured through the conductance should match the value obtained by applying the Faraday law in case of 100% current efficiency. The comparison of the two values allows gathering information whether or not interfering reactions are occurring at the electrode/solution interface. The target of these tests was to achieve a final concentration of millimolar levels (i.e. around 5 mM) in a time frame of few hundreds of seconds (i.e. in the range from 200 to 400 s). There was no specific requirement of accuracy and repeatability for the tests since the devices are in a prototype stage.

2.4.5   Conductivity sensor calibration

The range of measurement of the conductivity sensor suggested by the manufacturer is approximately from 2 µS to 20mS, with a cell constant k of 1 cm^{-1}. The conductivity sensor was calibrated by flow injection analysis (FIA) to confirm the value of the cell constant. A sample with different NaCl concentrations (0.6 M, 0.5 M, 0.4 M, 0.3 M, 0.2 M, 0.1 M, 10^{-2} M, 10^{-3} M, 10^{-4} M) was injected into a flowing carrier stream of DI water (10 µl/s flow rate) and a conductance peak was registered (for each point ten measurements were taken and the means of their values were used for calibration). The cell constant was found to be 1.036 cm^{-1}, close to the value declared by the manufacturer, in the range 10^{-4} to 0.1 M. The conductivity sensor could also be used in the upper range by adapting the cell constant. Two different calibration curves were indeed found, they are shown in Figure 2.23: one for the range 0.1-0.6 M (a) and one for the lower range 10^{-4}-0.1 M (b) shown in double logarithmic scale.
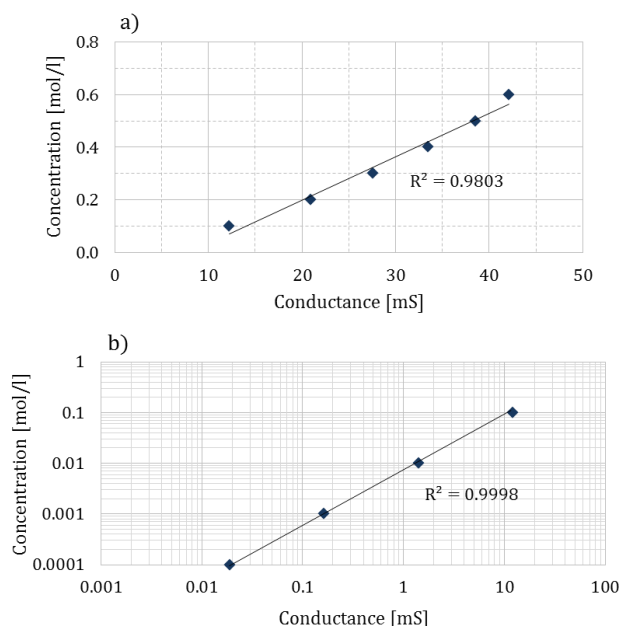
Figure 2.23. Calibration curves of the conductivity sensor for the concentration range from 0.1 M to 0.6 M, correlation: 0.0165 mol/l·mS (a) and for the range from 10^{-4} M to 0.1 M, double logarithmic scale, correlation: 0.0082 mol/l·mS (b).

The reason of using two different curve is that over the whole range of concentrations a deviation from linearity was found ($R^2 = 0.9741$), while a better linear fit was found for concentrations in the range 0.1-0.6 M ($R^2 = 0.9803$) and an excellent linearity ($R^2 = 0.9998$) was found for the lower

concentration range (10^{-4}-0.1 M). When a conductance value higher than 12 mS was measured, the first calibration curve was used to determine the sample final concentration by using the correlation y = 0.0165x-0.1298 (where x is expressed in mS and y in mol/l), while when conductance values lower than 12 mS where found, the second curve was used in order to better evaluate the concentration in the lower range, using the correlation y=0.0082x – 0.0007.

2.5   Results and discussions

2.5.1   Desalination at different potentials and time periods

Evaluation of the desalination performance of the microfluidic platform was performed using the setup described in section 2.4.4 with a potentiostat for voltage supply and current monitoring, a syringe pump for solutions displacement and a conductivity cell for on-line measurements of conductance. The device was tested at different potentials in order to choose the optimal oxidation potential, and afterwards for different periods of time at the optimal potential by evaluating the charge registered during oxidation and the conductance measured after treatment.

Desalination at different potentials
The platform was tested at the following potentials: +0.7 V, +0.9 V and +1.1 V. The lowest conductance was measured when the electrolysis was carried out at +0.9 V for 120 s, i.e. 20.36 mS, while conductances of 26.61 mS and 25.79 mS were registered when electrolysis was carried out at +0.7 V for 240 s and +1.1 V for 120 s, respectively. This confirmed the results obtained from the chronoamperometry tests of the microfluidic platform, therefore the potential +0.9 V was chosen as an optimal value and used in the further experiments.

Desalination at +0.9 V for 120 s
The result of the electrolysis carried out at +0.9 V for 120 s is presented in Figure 2.24, where the current profile registered during oxidation (a) and the conductance measured during the treatment (b) are reported (red dashed line). The NaCl concentration of the sample was lowered from the initial value of 0.6 M (41.8 mS) to a final value of 0.206 M (20.36 mS). The registered oxidation charge was 2.87 C corresponding to a final concentration of 0.356 M which is of the same order of magnitude as the value calculated by conductance measurement, revealing that the oxidation of Ag to AgCl is the only reaction occurring at the electrode/solution interface.

Desalination at +0.9 V for 240 s
The electrolysis experiment was carried out by applying a potential of +0.9 V for 240 s. The result is shown in Figure 2.24, where the current profile registered during oxidation (a) and the conductance measured during the treatment (b) are reported (green dashed line). The NaCl concentration of the sample was lowered form the initial value of 0.6 M (41.8 mS) to a final value of 0.157 M (17.37 mS). The registered oxidation charge was 9.35 C. If Equation 2.1 is applied to estimate the final concentration, a value of removed chloride mass higher than the chloride mass present in the sample would be obtained. This means that competing reactions are occurring at the electrode/solution interface contributing to the total charge which is not only due to Ag oxidation to AgCl.

Desalination at +0.9 V for 360 s

Ag oxidation was carried out by applying a potential of +0.9 V for 360 s. The result is shown in Figure 2.24, where the current profile registered during oxidation (a) and the conductance measured during the treatment (b) are reported (blue solid line). The concentration of the sample was lowered from the initial value of 0.6 M (41.8 mS) to a final value of 51.6 mM (6.38 mS). The registered oxidation charge was 18.47 C revealing, similarly to the case of the oxidation for 240 s, that competing reactions are occurring at the electrode/solution interface.
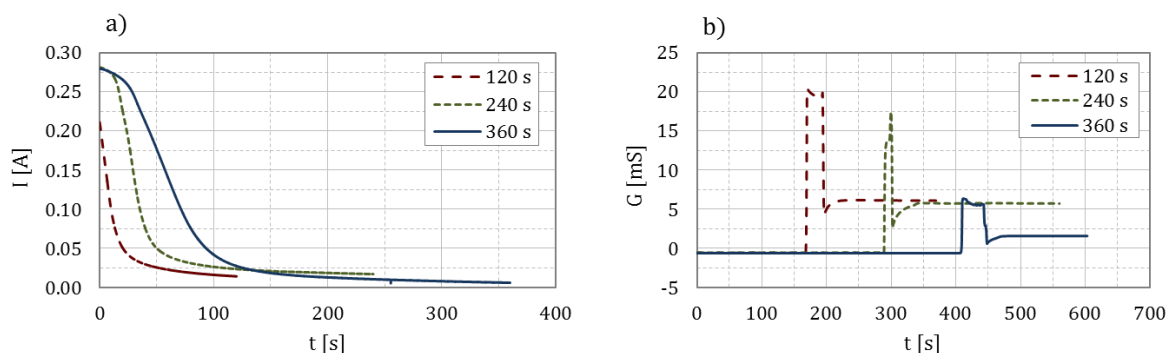
Figure 2.24. Current profile (a) and conductance measurement (b) obtained for electrolysis carried out at +0.9 V for 120 s (red dashed line), 240 s (green dashed line) and 360 s (blue solid line).

2.5.2 Desalination performance evaluation

The microfluidic platform was capable of desalinating the 0.6 M NaCl sample, thus achieving a proof-of-concept of the design and the fabrication process flow.

Table 2.5 reports the comparison of the main geometrical parameters and the performance of the devices reported in [82,84] and the present work. The herein described platform was expected to improve the performance of the device reported in [84] in terms of sealing capabilities and in terms of time needed for complete desalination, since the thickness of the shallow channel was reduced from 230 μm to 80 μm and the A/V ratio was consequently increased from 4.35/mm to 9.98/mm.

Table 2.5. Comparison of the geometrical parameters and performance of the different devices.

Configuration-reference	Channel thickness (μm)	Working electrode/ solution interface area (mm²)	Sample volume (μl)	Final concentration (mM)	Electrolysis time (s)
Tubular- [82]	30	259.18	17	3	240
Planar- [84]	230	347.83	80	5.5	600
Planar-this work	80	1207.26	121.64	51.6	360

On one hand, the improved sealing capabilities allowed to pump the solutions faster, thus lowering the time frame for channel filling: a flow rate of 600 μl/min much higher than 40 μl/min [82] and 25 μl/min [84] was used.

On the other hand, the desalination performance were not improved as much as expected, possibly due to the limited adsorption capacity of the electrodes which had a thickness of only 5 μm, five

times lower with respect to the silver foils used in [84]. A proof-of-concept of the desalination capabilities of our device was achieved, and a final concentration (51.6 mM) ten times higher with respect to the target value for allowing nutrients measurements of 5.5 mM reported in [84] was reached in a shorter time (360 vs 600 s) and for a larger sample volume (120 vs 80 μl).

Aging effect evaluation and electrodes lifetime

The mismatch of the final concentration values observed for 240 s and 360 s, as well as the large difference in the charge registered during the three experiments could also be explained by an aging effect of the electrode since the three measurements were carried out consecutively with the same device. Indeed, when electrolysis was carried out by applying a potential of +0.9 V for 120 s, the final concentration estimated through the oxidation charge and the value calculated through the conductance measurement agreed, revealing that charge was only due to the oxidation of Ag to AgCl. Instead, when electrolysis at +0.9 V was carried out for longer periods of time, a mismatch between the two values was found showing that other reactions were eventually occurring at the electrode/solution interface, as for example water hydrolysis (gas formation was observed).

Another important observation is that the initial current increased after a few cycles (from 210 mA to 275 mA). This can be explained by the fact that during oxidation and regeneration the electrode undergoes a change in morphology possibly resulting in an increase of the surface area available for the reaction (aging effect). This change in morphology was observed during the characterization of the electrodes printed with the different inks as discussed in section 2.3.5. Figure 2.25 shows two SEM pictures taken before (a) and after (b) carrying out the oxidation/regeneration experiment with the 400 mm^2 squared electrode printed with the 5064H ink.

a)   b)
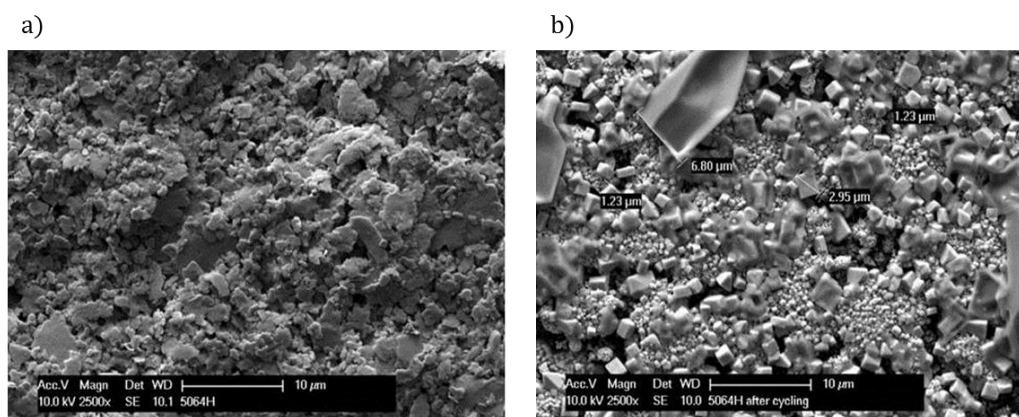
Figure 2.25. SEM pictures of the 5064H ink printed electrode before (a) and after (b) carrying out oxidation/reduction experiments (around 25 cycles). The big crystals are NaCl residues.

This can play a role in the lifetime of the electrode and was investigated by carrying out several experiments with the same device at the same conditions, i.e. desalination at +0.9 V for 360 s, and regeneration at -1.0 V for 540 s. Figure 2.26 shows the consecutive desalination (a) and regeneration (b) curves. This test allowed monitoring the change in the current profile shape, the

value of the initial current, and whether or not a change in the final concentration measured through the conductance was observed.

The first desalination showed the expected decaying profile for the current starting at the beginning of the electrolysis. The second desalination showed an increase of the initial current of around 50 mA with respect to the first one, which kept constant during the following desalinations, and a profile which was exponentially decaying after some seconds at the high values ("half-bell" shape). The following desalinations also showed the half-bell shaped profile which was always more pronounced up to the sixth one, when the *i-t* curve was reaching zero values for the current before 200 s. This behavior was observed also in the regeneration curves and it means that after five cycles the electrode is already damaged and cannot be used for more than 100 s. This is a big limitation for the device since it has a lifetime of only five cycles. The conductivity measurements were not affected by the number of desalinations, since they did not show an increasing trend or a decreasing trend. The desalination performance was therefore not affected by the aging of the electrodes, however their limited lifetime has been improved by fabricating more robust electrodes in order to deploy the device for several continuous measurements, as reported in the following paragraphs.
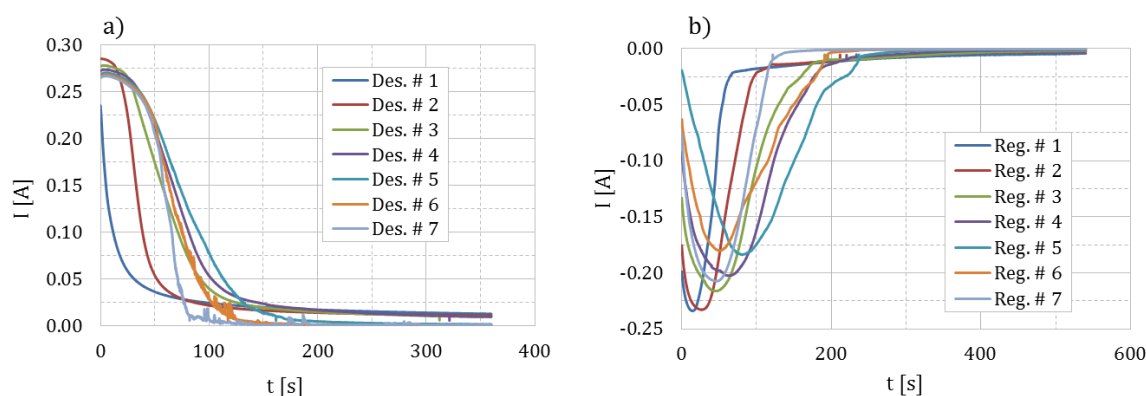
Figure 2.26. Current profiles for consecutive desalinations (a) and regenerations (b) carried out at the same conditions.

Working electrode geometry influence

During the oxidation phases, the CE/RE was observed to quickly turn grey, revealing that the counter reaction on the CE/RE (AgCl reduction to Ag) was fast and homogeneous (the squared shape geometry has lower resistance and allows a more uniform distribution of the potential) while the oxidation reaction at the serpentine WE was slower and inhomogeneous. This could be also an indication that the oxidation is being limited by the reduction of the Ag/AgCl CE/RE to Ag. Moreover, the width of the serpentine WE was 20% smaller than the channel width leading to an under-exploitation of the device capabilities. The area of the electrode/solution interface could therefore be increased by changing the geometry of the WE, passing from the serpentine to a squared shape geometry, which could improve the device performance. The first parameter which was investigated for this purpose was therefore the shape of the WE.

We expected that by changing the geometry of the WE, an improvement of the device performance could be attained: electrolysis for longer time periods can be tested and similar performance as reported in [84] can be achieved. Therefore a microfluidic platform with two squared electrodes (WE and CE/RE) was built. Figure 2.27a shows the fabricated platform.
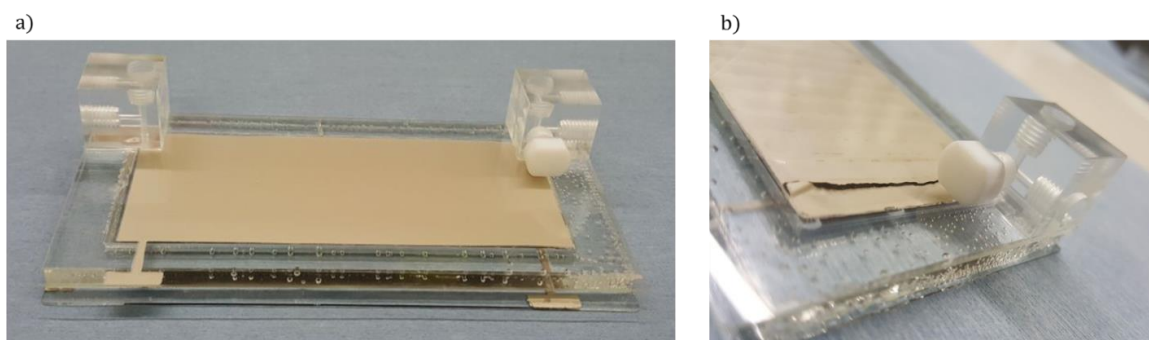
Figure 2.27. Picture of the microfluidic platform built up with squared WE and CE/RE (a) and damage to the squared WE after four redox cycles (b).

However, after carrying out four desalination/regeneration cycles, at the conditions +0.9 V, 300 s/ -1.0 V, 600 s, the WE was damaged. It broke along a crack in proximity to the inlet of the device as shown in Figure 2.27b. Figure 2.28 shows the four desalination (a) and regeneration (b) curves.
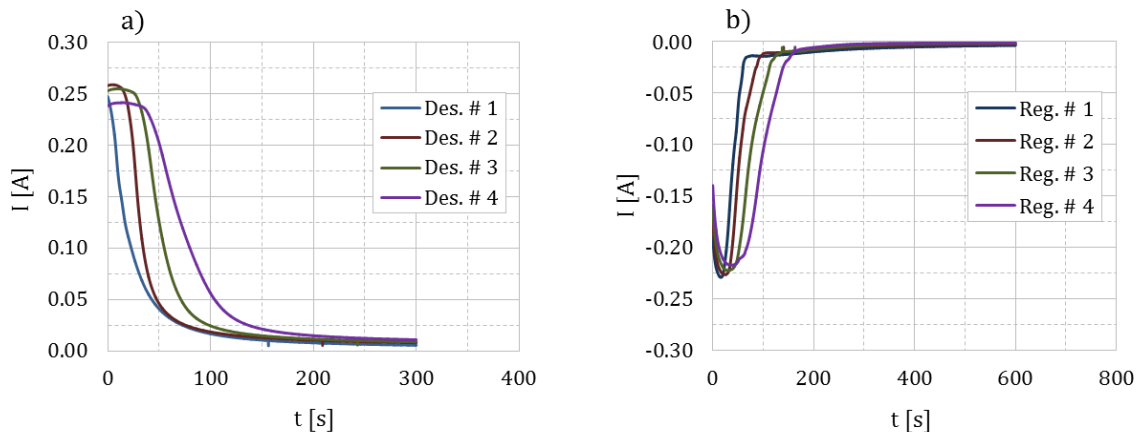
Figure 2.28. Current profiles for consecutive desalinations (a) and regenerations (b) carried out at the same conditions (+0.9 V, 300 s/ -1.0 V, 600 s) with the square shaped WE.

The tendency of the curves to assume a half-bell shape always more pronounced with respect to the exponential curve of the first desalination is similar to the serpentine shaped electrode, but the initial current did not increase from the value of the first desalination (250 mA). The rupture of the electrode can be explained by the fact that the electrode undergoes oxidation to AgCl (adsorption of chloride and expansion) and reduction to Ag (desorption of chloride and compression) only in correspondence to the serpentine. Therefore stress arises at the edges of the serpentine due to the different conditions experienced by the parts of the electrode inside and outside the serpentine

41

channel. This also occurs in the device reported in [84], however the electrodes there deployed have a thickness of 25 μm and withstand better the differential stress at the edges of the serpentine. Therefore the key to improve the device performance could rely on the thickness of the electrodes.

Another key parameter which can influence the performance of the device concerns the curing conditions of the ink. The curing temperature suggested by the manufacturer for the 5064H ink was 130 °C, which was applied for 30 minutes. These conditions may not be enough for complete removal of the solvents present in the ink formulation, mainly C11-ketones and dimethyl succinate. C-11 ketone is a low-cost, slow-evaporating, low-density mixture of ketone solvents. Ketones can react with halogens: the reaction may be carried out in an aqueous medium with the corresponding elemental halogen. In this way, chloride, bromide, and iodide can be installed selectively in the alpha position of a ketone [103], the first carbon atom that attaches to a functional group. Therefore, in case of uncomplete evaporation of ketones, this halogenation phenomenon could be one of the side reactions occurring at the electrode/solution interface during the regeneration step. The dry boiling point for C-11 ketones is 240 °C, therefore a temperature of 250 °C was used to cure the printed electrodes. Results are presented in the following paragraph.

Working electrode thickness influence

Electroless deposition [104] was investigated in order to increase the thickness of the electrode: Ag was deposited on the entire printed serpentine, but the result was a dirty glass plate hampering the following bonding steps to the other components of the device.

An alternative method to increase the thickness of the electrode is to replace the mesh used for screen printing by a laser cut PET/PDMS stencil mask with a thickness of 125/20 μm. The PDMS layer helps to avoid sliding of the mask on the glass substrate while printing.

The microfluidic platform built with the new electrodes (squared shape, thickness of around 50 μm, curing at 250 °C) was tested with the same setup as the previous ones: an oxidation step of 600 s and a regeneration step of 750 s were applied. On one hand, a significant improvement in the electrode robustness and lifetime was obtained, since the electrode was able to withstand at least 30 cycles without any damage and showing a symmetric current profile between oxidation and reduction. The charge registered during the oxidation step was close to the charge registered during the reduction step, slowing down the aging of the electrode. On the other hand, the change of the geometry and thickness of the electrode and the increase of the curing temperature did not allow an improvement of the desalination performance of the device.

Figure 2.29 shows the comparison and evolution of the current profile registered for the desalination number 1, 2, 11, 21 and 31. As in the previous case, the curves have a tendency to assume a half-bell shape already starting from the second cycle, while only the first one shows an exponential decay. This means that during the regeneration something occurs at the surface thus not allowing prompt chloride adsorption when the positive potential is applied. A possible explanation is that during the regeneration step an enrichment of the Ag electrode with sodium cations occurs while they are transferred to the regeneration solution, because of the porous structure of the electrode (the porosity increases with the number of cycles). This would require more time for the

sodium ions to diffuse out from the electrode when the positive potential is applied and enable the adsorption of chloride.
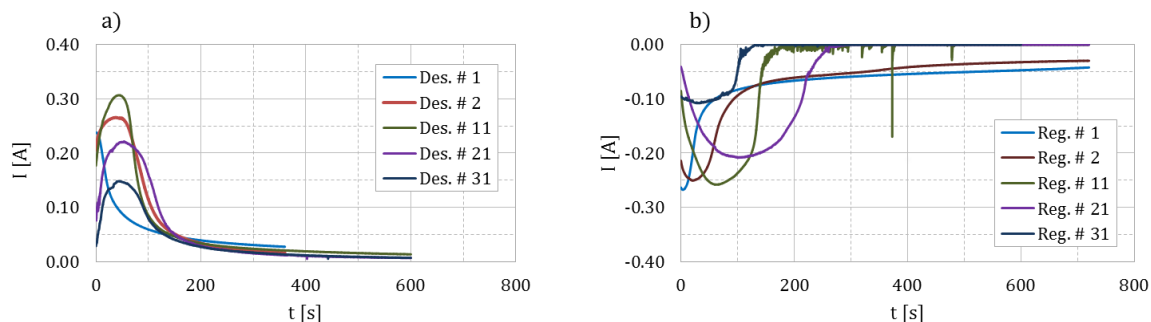
Figure 2.29. Current profiles for consecutive desalinations (a) and regenerations (b) carried out at +0.9 V, 600 s and -1.0 V, 750 s with the 50 µm thick square shaped WE cured at 250 °C.

The current amplitude was increasing during the first 15 cycles (not shown in the figure), while started to decrease during the second half of experiments showing that the electrode was losing its adsorption capacity. However an interesting observation was that by applying a higher potential the current profile with higher current intensity could be recovered, thus suggesting an increase in the impedance of the electrochemical cell. In this device, the elements which contribute to build up the resistance of the electrochemical cell are the WE, the CE/RE and the membrane. The membrane resistance can increase due to deposition of silver halide complexes ($[AgCl_n]^{n-1}$) which may diffuse from the electrode to the membrane. In order to investigate if the membrane type/thickness used in the device could have an influence on its performance, microfluidic platforms with another membrane similar to Nafion were built and the results are reported in the section below.

Membrane influence

In all the previous experiments a Nafion membrane (thickness of 25 µm) was used. However, a membrane similar to Nafion as reported in [84], the FKL cation-exchange membrane (thickness of 120-130 µm) based on perfluorinated sulfonic acid/PTFE copolymers, can be used. Membranes were purchased from Fumatech (FuMA-Tech GmbH, Germany), pre-treated in deionized water for 6 hours at room temperature and in 1 M nitric acid (HNO_3) for 1 h, and finally they were placed in 1 M NaCl for 24 h to ensure complete exchange of H^+ by Na^+. The membranes were subsequently stored in 1 M NaCl solution.

Before assembling the device, the membrane was dried in order to allow bonding to the adhesive channel. Figure 2.30 shows the FKL membrane after bonding to the top glass (a) and the microfluidic platform after assembling (b). Unfortunately, such devices presented severe leakage issues and this hampered the testing of the performance of the device for desalination due to the impossibility to drive the sample towards the conductivity sensor. The leaks were observed at the

interface between the adhesive channel and the FKL membrane, revealing a poor adhesion of the ARcare 90445 to the FKL membrane.

Consequently, only cyclic voltammetry tests of the device could be carried out. Figure 2.31 shows the results of the CV tests at different scan rates (25-50-75-100-125 mV/s) and the plot of the current peaks versus the scan rate for the oxidation and reduction reactions (inset).
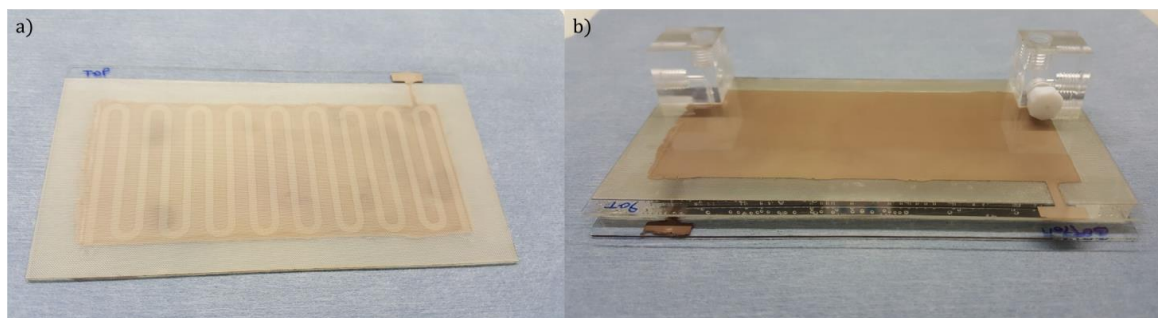
Figure 2.30. Picture of the FKL membrane bonded to the top glass (a) and of the assembled microfluidic platform (b).

Linearity between the current peak and the scan rate was observed similarly to the Nafion-based platform (voltammograms shown in Figure 2.15) confirming the thin-layer behavior for both processes of oxidation and reduction. However, the different shape and asymmetry of the voltammograms on the cathodic and anodic scan, as well as the lower reduction current peaks with respect to the oxidation ones, suggest that the electrochemical process is not completely reversible.
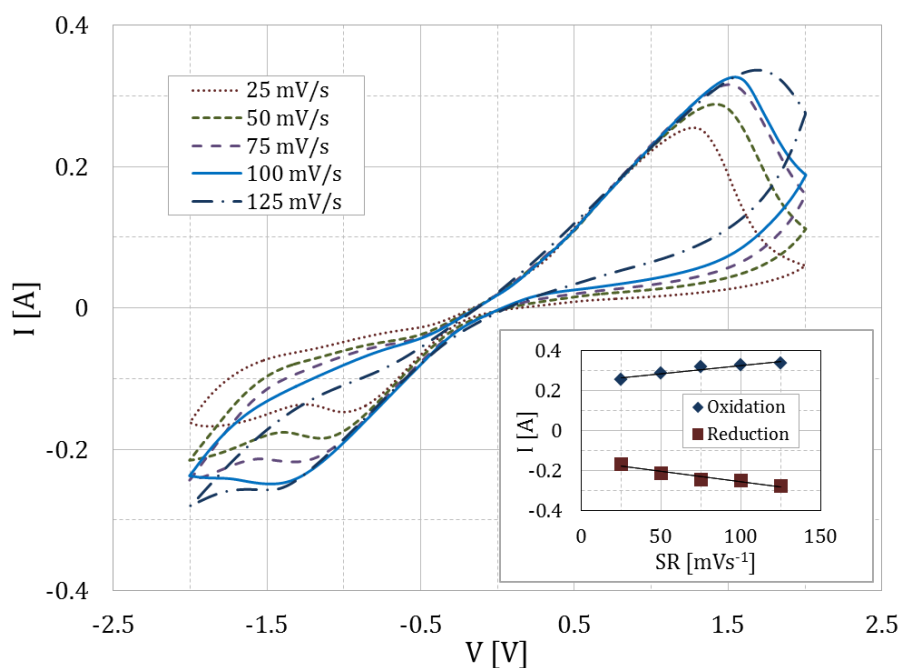
Figure 2.31. Cyclic voltammograms of the microfluidic device at different scan rates. Inset: current peaks versus scan rate for oxidation and reduction.

2.5.3 Optimization guidelines

The desalination performance of the microfluidic platform can be further improved by changing geometrical parameters, such as the thickness of the shallow channel or the depth of the second fluidic compartment.

With respect to the shallow channel, the AR care 92712 adhesive could be used to replace the AR care 90445, lowering its thickness from 80 to 50 µm. This would allow a further increase of the A/V ratio, thus reducing the time needed for exhaustive electrolysis, according to Equation 2.8. Moreover by combining this geometrical modification with a squared shaped and thicker WE, a significant enhancement of the performance of the device would be expected. Desalination with a final concentration in the order of mM in a time frame smaller with respect to the tubular configuration could be achieved thanks to a favourable A/V ratio (i.e. the WE surface area would be enhanced to 1520.5 mm^2 and the volume reduced to around 76 µl, thus having an A/V ratio of 20/mm versus the 15.25/mm ratio of the tubular device).

With respect to the second fluidic compartment, its depth could have an influence on the mass transport of the involved ions, especially on that of sodium cations. In an electrolyte, the current density can be described by using the sum of ion fluxes:

$$i_l = F \sum_i z_i N_i$$

Equation 2.13

where i_l denotes the current density (A/m^2) in the electrolyte, and N_i the flux of the species i (mol/m^2·s) with charge number z_i. The flux of an ion in an ideal solution is described by the Nernst-Planck equation which takes into account the contribution of the three mass transport phenomena involved, i.e. diffusion, migration and convection [105]:

$$N_i = -D_i \nabla c_i - z_i \mu_i F c_i \nabla \varphi_l + c_i u$$

Equation 2.14

where c_i represents the concentration of the ion i (mol/m^3), D_i its diffusion coefficient (m^2/s), μ_i its mobility (s·mol/kg), φ_l the electrolyte potential, and u the velocity (m/s).

In the case of the herein presented platform, it is possible to neglect some contributions to the ion fluxes. Firstly, it is possible to neglect the convective term for both sodium and chloride ions since the electrochemical process is carried out in a batch-wise mode and no pressure/stirring is applied during the treatment.

Concerning the chloride anions, diffusion can be neglected since this species is confined in the thin-layer adjacent to the WE thanks to the cation-exchange membrane. Current response depends in fact upon the ratio between the diffusion layer δ (layer adjacent to the electrode surface where the concentration differs from those in the bulk) and the channel thickness h. Diffusion is not important for systems exhibiting thin-layer behavior ($h \ll \delta$) since the electroactive species is electrolyzed rapidly when the potential is changed, but it is the limiting factor in the opposite case when $h \gg \delta$ (semi-infinite diffusion). The diffusion layer thickness depends on the diffusion coefficient of the species D_i and on the time scale of the experiment t_e. A dimensionless parameter can be introduced, Dt_e/h^2 [106], which defines the behavior of the system as thin-layer (if $\gg 1$) or semi-infinite diffusion (if $\ll 1$). For chloride ions ($D = 2.03 \cdot 10^{-3} cm^2/s$) and a time scale of 600 s, the

dimensionless parameter is $\gg 1$, therefore diffusion can be neglected and only migration has to be considered together with the adsorption on the Ag electrode.

Sodium ions ($D = 1.33 \cdot 10^{-3} cm^2/s$) are instead free to pass through the Nafion membrane, therefore the thickness to be considered is the complete stack (channel/membrane/chamber) for a total thickness h of 5.1 mm, leading to a value for the dimensionless parameter $\ll 1$. Both migration (due to the potential gradient) and diffusion influence therefore the mass transport of Na ions. The electric field driving these ions towards the second compartment would be higher in case of parallel WE and CE/RE closer to each other, therefore it is expected that by decreasing the thickness of the second fluidic compartment a faster migration of Na ions could be achieved, thus decreasing the timeframe of the experiment and enhancing the desalination performances. Different thicknesses could be tested to evaluate the role of the electric field in the electrochemical removal of NaCl and therefore the contribution of migration to the desalination performance.

Furthermore, the loss of adhesion of the FKL membrane from the ARcare 90445 adhesive did not allow the evaluation of the desalination performance of the device built with this kind of membrane. An irreversible bonding procedure between these two materials or between the adhesive and other cation exchange membranes could be sought with the aim to explore the performance of the microfabricated platform built with these membranes with respect to the Nafion-based device. Impedance measurements could also be performed in order to compare the membranes electrochemical properties.

Further investigations towards the improvement of the performance of the microfluidic device could also be focused on further increasing the thickness of the working electrode, on the use of emerging and more powerful (higher resolution) printing techniques such as pneumatic or aerosol jet printing, and therefore on the deployment of different types of inks.

Conclusions

In this chapter a microfluidic platform for coulometric seawater desalination produced by using microfabrication techniques was presented. In order to choose the proper ink for the electrode fabrication, a comparison of the electrochemical behavior of six printable Ag-based inks was carried out in a 0.6 M NaCl solution. The screen printed Dupont 5064H ink showed the best properties in terms of oxidation ability to AgCl (15.5 mC/mm2), good regeneration ability and absence of sample contamination during and after the redox cycles, and was therefore chosen for the fabrication of the electrodes of the desalination platform. The optimal oxidation potential of the device was found to be at +0.9 V by cyclic voltammetry and chronoamperometry. The microfluidic platform was tested in a batch-wise mode by using synthetic NaCl solution. The NaCl concentration could be lowered from the initial value of 0.6 M to a final value of 0.206 M, 0.157 M and 51.6 mM for oxidation times of 120 s, 240 s and 360 s, respectively. The final concentration value estimated from the measured charge was in agreement with the value measured through the conductance for a time period of 120 s, while in the other cases it was lower, revealing the occurrence of competing reactions at the electrode/solution interface contributing to the current. Passing from a serpentine geometry to a squared and thicker geometry allowed to significantly increase the lifetime of the device from less than 10 cycles to more than 30 cycles, thanks to the higher robustness of the thicker Ag layer and also to the increased curing temperature.

Future work could be focused on further investigating and improving the desalination performance of the device. Some guidelines were given for this purpose, which mainly foresee the optimization of the geometrical parameters of the platform (thickness of the shallow channel and second fluidic compartment) as well as the deployment of alternative membranes and improvement of their adhesion to the PSA shallow channel.

Chapter 3   Thin-film microelectrode arrays for trace metal sensing

Aquatic ecosystems are contaminated by metals from natural and anthropogenic sources which can change the ecosystems' equilibrium due to their role in biogeochemical processes [107]. As the metal speciation may vary continuously in space and time, reflecting changes in the physicochemical conditions of the aquatic ecosystem, it is obvious that punctual analyses in laboratory of total dissolved metal concentrations are inadequate. *In situ*, real-time monitoring tools are therefore required to gather information on trace metal levels at an appropriate temporal and spatial scale in order to address the ecosystem dynamics [30,107], and minimizing artifacts such as contamination or speciation changes which often occur during sampling, sample handling, and storage [108]. The mobile fraction of metals, i.e. free ions and small complexes, is the most closely related to metal bioavailability and transport processes through biological membranes [108], therefore it is the most important to be measured. Voltammetric microsensors are well suited to design submersible probes and offer the advantage to be selective to the mobile fraction of metals which diffuses quickly enough to be measured in the time scale of voltammetric techniques.

In this chapter two-electrode (WE-CE) and three-electrode (WE-CE-RE) on-chip sensors for voltammetric trace metals detection are presented. The sensors were fabricated by three photolithographic steps and electrochemically characterized. Their performance for detection and quantification of trace metals by Square Wave Anodic Stripping Voltammetry (SWASV) was investigated in synthetic sodium nitrate solutions spiked with trace metals in nanomolar levels. The three-electrode on-chip sensor was demonstrated to allow trace metal detection, while further improvements are required in order to achieve the same sensitivity of the two-electrode on-chip sensor for quantification. Parts of this chapter have been published in [109].

3.1 Introduction and state-of-the-art

3.1.1 Trace metals analysis

In situ, real-time monitoring tools are strongly required in order to perform measurements and speciation of trace metals in natural waters for quality monitoring purposes. Voltammetric techniques are well suited to develop trace metal microsensors: a large number of trace compounds of environmental interest can be measured; several analytes can be detected in the same potential scan; sub-nM detection limits can be achieved; the speciation based on the redox state and mobility, and/or lability of metals can be measured; and low cost, automated, compact equipment with low energy requirements has been designed [108,110].

Among the several voltammetric methods (i.e. Cyclic Voltammetry (CV), Linear Sweep Voltammetry (LSV), Square Wave Voltammetry (SWV) and Differential Pulse Voltammetry (DPV)), one of the most sensitive techniques for measuring low concentration levels of various trace metal species in natural waters is the square wave anodic stripping voltammetry (SWASV) [111].

In this technique, metal ions are firstly reduced and pre-concentrated by applying a negative potential for a certain period of time on the working electrode (WE). The pre-concentrated ions are then re-oxidized by scanning the potential towards positive values. Concentrations of trace metals are determined from the peaks detected by registering the current that flows through the WE as a function of the potential applied between the WE and the reference electrode (RE) [112].

As introduced in section 1.1, the most powerful electrode for voltammetric analysis of trace metals is mercury. Several metal species (Cd(II), Pb(II), Cu(II), Zn(II), Mn(II), Fe(II)) can be simultaneously quantified at concentration down to picomolar levels in natural aquatic ecosystems by using mercury electrodes [113]. Thin-film mercury electrodes (MFE) are preferred to the hanging drop mercury electrode (HMDE) since they are easier and safer to use in the field with respect to the large quantity of bulk mercury involved in HDME, moreover the instrumentation needed to operate the MFEs is simpler and can be integrated in small portable systems [114]. In 1986 Kounaves et al. [115] reported for the first time the use of iridium as suitable substrate material for the deposition of renewable mercury film due to its low solubility in mercury and good wettability.

In 1995 Tercier et al. [116] developed rugged Hg-plated Ir-based microelectrodes by electrodepositing mercury on a single Ir disc substrate showing reproducibility and reliability close to 100%. Continuous lead and cadmium measurements by SWASV in synthetic solutions over long periods of time indicated that the Hg-plated Ir-based microelectrodes could be used for several days without renewal of the mercury layer. These microelectrodes were also applied to lead and cadmium speciation directly in river waters. In 1996 Belmont et al. [117] developed mercury-plated iridium-based microelectrode arrays for SWASV analysis of trace metals: these sensors were applied to lead and cadmium speciation in river water reaching a detection limit of 50 pM for a pre-concentration time of 15 min.

The first prototypes of voltammetric submersible probes for *in situ* measurements of trace metals have been reported during the 90s [47,118–120]. These systems were limited to short-term *in situ* measurements in surface waters mainly due to the fouling of the sensor surface, the lack of reliability and sensitivity of the sensors used, the use of conventional sized electrodes (≥100 μm) and the interference from dissolved oxygen. Further investigations have led to the development of novel rugged and reliable voltammetric probes, such as voltammetric *in situ* profiling (VIP) systems allowing long-term *in situ* measurements down to 500 m depth [113,121,122]. The cores of such systems are gel integrated microsensors (GIME) developed using as substrate an array of 5 x 20 interconnected iridium (Ir) microdiscs plated with Hg, having a diameter of 5 μm and a center to center distance of 150 μm, produced by thin-film on-chip technology and photolithographic techniques [30,108,121,123].

Microelectrodes (r ≤ 10 μm) offer indeed several advantages in the field of voltammetric environmental monitoring [107,110]. Their low ohmic drop enables direct measurements without any addition of electrolyte, this avoids sample perturbations required for speciation analysis. A steady-state mass transport, resulting from hemi-spherical diffusion, is quickly established at constant potential even in quiescent solution (stirring is thus unnecessary during the pre-concentration step). Finally, thanks to their increased mass-transport and lower capacitance, a significantly larger signal-to-noise (S/N) ratio is obtained with respect to macroelectrode configurations, resulting in better sensitivity and therefore better detection limit.

Mercury is not a suitable electrode for all the trace metal species. For instance, the anodic stripping detection of arsenic by using mercury electrodes is not analytically useful due to the interference from the oxidation of mercury [124]. Arsenic is a toxic metal species widely distributed in nature and is known to be one of the world's greatest environmental hazards [125]. In water environments it is mostly present as arsenite (As (III)) and arsenate (As (V)) and, according to the World Health Organization, its maximum acceptable concentration in drinking water is 10 µg/l (133 nM), hence the challenge in the trace determination of As in the environment [126]. Forsberg et al. [127] investigated the determination of arsenic by ASV at various electrode materials (HMDE, Pt and Au). It was found that the arsenic oxidation peak appeared as a shoulder on the mercury oxidation on a HMDE, confirming the results reported by Myers et al. [124]. Platinum was a suitable electrode material but gold was found to be superior to platinum as a working electrode material due to a higher hydrogen overvoltage. This in fact solved the problem of simultaneous evolution of hydrogen while depositing arsenic [128].

Gold electrodes for As determination allow measurements with higher and better defined stripping peaks. However the high cost and the memory effect of this kind of electrodes have pushed the researchers to find alternatives like the use of noble metals nanoparticles (NPs) electro-deposited on another metallic substrate. AuNPs-modified electrodes can be indeed considered as random arrays of microelectrodes which can provide advantages such as large surface area and enhanced mass transfer [125] and allow achieving lower limit of detection (LOD) with respect to the LOD obtained by using Au macroelectrodes, i.e. around 180 nM [129]. Due to its chemical inertness, Ir has been demonstrated to be a suitable substrate also for the development of renewable AuNPs plated microelectrodes [130]. Several works have been reported in literature for determination of arsenic by using AuNPs and voltammetric techniques. Hossain et al. [131] achieved a LOD of 24 nM by combining the use of AuNPs on a glassy carbon electrode (GCE) and the LSV technique. Similarly,

Khairy et al. [132] achieved a LOD of 5.3 nM by depositing AuNPs on a screen printed electrode and by using LSV technique. Lower limits of detection were achieved by Huang et al. [133] and by Lan et al. [134] who achieved, respectively, 0.63 and 0.33 nM LOD by using GCEs modified with AuNPs.

The LOD and the sensitivity of the SWASV technique can be improved by deploying an array of microelectrodes, as it will be explained more in detail in the section 3.2. Feeney at al. [135] have developed and *in situ* tested a sensor consisting of Au microdiscs array showing a LOD for arsenic of 0.6 nM, this value could be further improved by replacing Au microdiscs by AuNPs.

All the methods described allow the detection of As(III) but not the detection of As(V) for which stronger acidic conditions are required. An alternative way with respect to the acidification of the sample is to electrochemically induce the reduction of As(V) to As(III). Recently conducting polymers have attracted interest in the development of sensors, since they have unique properties in terms of conductivity and electrochemical activity [136]. In 2006 Mu investigated the synthesis by cyclic voltammetry of poly(aniline-co-*o*-aminophenol) (PANOA) for which a good electrochemical activity was find at pH<9 [137] and in 2009 demonstrated its high catalytical activity towards As(V) reduction, proving that the PANOA electrode can be used to directly determine As(V) concentration [138]. Also Zhang et al. [136] investigated and proved the electrocatalytic reduction of As(V) to As(III) in NaCl solution at a glassy carbon electrode functionalized with PANOA copolymer, opening a way also for direct arsenate removal from seawater and therefore the arsenic pollution treatment.

AuNPs are also suitable electrodes for detection of other metal species, such as mercury(II) (Hg(II)). Mercury compounds are very toxic to humans, they accumulate in vital organ and tissues causing kidney injuries, intellectual deterioration and even death [139]. Abollino et al. [140] demonstrated the applicability of AuNPs-modified GCEs for the determination of aqueous Hg(II) by SWASV in drinking waters and sediments.

3.1.2 Solid State Reference Electrode

The second key component of the voltammetric systems, after the WE, is the reference electrode, whose on-chip integration is one of the challenging objectives of this thesis.

The reference electrode is a crucial component of electrochemical sensors because its potential must be stable even in case of changes in the electrolyte concentration in order to ensure proper device operation, reliable results and accuracy of measurements. The RE usually consists of a metal/metal salt, an inner electrolyte (highly concentrated or saturated filling solution), and a diffusion barrier. The inner electrolyte is chosen from the anion/cation pair with equal mobility and has to constantly diffuse out towards the sample solution to ensure a constant potential; the diffusion barrier ensures slow leakage. Commercially available liquid junction reference electrodes are pressure dependent and therefore not suitable for *in situ* measurements, however solutions with pressure compensation are available. The current trend towards miniaturization of electrochemical sensors has involved as well the miniaturization of the RE in all its components. The miniaturized REs have to be functional and robust and their potential must be reproducible, moreover the potential drift of the electrodes due to filling solution effusion or electrode coating degradation must be minimized [141].

The silver/silver chloride (Ag/AgCl) pseudo-reference electrode is the simplest and practical RE used in research. Ag/AgCl pseudo-REs are a very simple solution for integration into voltammetric sensors, however they can only be deployed in samples with constant chloride concentration like seawater. The Ag/AgCl electrode is in fact chloride sensitive and in solutions with low chloride levels, such as freshwater, does not ensure a stable potential. Thin electrode layers undergo fast depletion so generally the microfabrication of such electrodes is made up of two steps: a thin film deposition of a metallic seed layer and electroplating to have a thicker layer. Both Ag and AgCl need to be present: Ag can oxidize (to AgCl or Ag_2O) and AgCl can dissolve. The inner electrolyte /diffusion barrier is often replaced by an immobilized electrolyte layer e.g. using a gellified electrolyte. The problem is that the gellified electrolyte has a limited lifetime: there is no bulk reservoir assuring a constant outflow, but the potential will remain constant until the diffusion barrier reaches the Ag/AgCl electrode because of the limited thickness. Despite the higher thickness obtained by electrodeposition, the major problem related to the miniaturization of the Ag/AgCl electrode is the rapid dissolution of the small electrode volume and its consequent short lifetime (few days). Therefore, in order to develop three-electrode on-chip devices, it is necessary to microfabricate a solid-state RE (SSRE), in which the filling solution is replaced with a solid-state exchange membrane doped with the ions required for the electrode equilibrium.

For this reason many efforts have been made in order to form diffusion barriers to limit the dissolution of the electrode volume (synthetic gels, nanoporous polymer membranes, agarose gel) and different types of internal gel or solution-free references electrodes have been proposed for miniaturization [142,143]. Agarose gel membrane doped with potassium chloride (KCl) powder has been used recently to realize a solid state exchange membrane [144] . A drift of 0.0035 mV/h drift over 42h and chloride insensitivity up to 0.6 M were observed. UV curable hydrophobic dielectric polymers doped with KCl powder have also been developed showing a potential stability time of 10 days and chloride insensitivity up to 0.1 M [145].

Ionic liquids (ILs) have been recently suggested as promising materials for the development of simple "liquid-junction"-free REs [146], more particularly the ions 1-ethyl-3-methylimidazolium ([C2mim]+) and bis(trifluoromethane sulfonyl)amide ([NTf2]-) are excellent candidates to form an IL whose ions are partially soluble in water, and therefore to produce stable membrane boundary potential [147,148], thus allowing measurements in fresh water. ILs exhibit properties, such as high ionic conductivity, low vapor pressure and volatility, hence they do not have drying problems associated with KCl saturated gel electrodes when stored for long duration after manufacture. Maminska et al. [149] developed a PVC membrane containing IL (1-dodecyl-3-methylimidazolium chloride) which provided an internal solid electrolyte, maintaining constant chloride concentration in the layer and thus constant potential of the Ag/AgCl electrode in solution of different concentration of chloride and other interfering anions. The long-term stability of these electrodes was 2 months. Kakiuchi et al. [146] developed an Ag/AgCl electrode coated with AgCl saturated gelled IL (1-methyl-3-octylimidazolium bis(trifluoromethylsulfonyl)imide) which showed a long-term stability time of 3 months. ILs could be therefore used in solid-state exchange membranes for developing on-chip RE for *in situ* deployable trace metal sensors, for which a continuous monitoring over a period of around 3 weeks is required.

In this chapter newly designed two-electrode (WE-CE) and three-electrode (WE-CE-RE) on-chip devices and their comparison for *in situ* voltammetric detection and quantification of trace metals in

marine environment are presented. The key novelty of these devices is the on-chip integration of a solid-state RE towards the miniaturization of the voltammetric *in situ* profiling systems [121]. Two kinds of on-chip solid state RE were investigated: an Ag/AgCl electrode serving as pseudo reference electrode, and an Ag/AgCl electrode coated with a poly(vinyl chloride) (PVC) membrane plasticized with ionic liquids (ILs) [150] reference electrode.

3.2 Miniaturized working electrode: theoretical background

As mentioned in the previous section, microelectrodes offer several advantages with respect to macroelectrodes, such as enhanced mass transport, steady-state response, low ohmic drop and improved signal to noise (S/N) ratio.

The enhanced mass transport is due to the diffusion profile established at the electrode/solution interface. Figure 3.1 helps describing this behavior. When molecules diffuse towards a macroelectrode, their average diffusion length is shorter compared to the dimensions of the electrode and the diffusion regime is planar, i.e. diffusion path perpendicular to the electrode surface, as shown in Figure 3.1a. When the dimensions of the electrodes are reduced, more electroactive species per unit time and area can reach the electrode surface thanks to the contribution of the molecules coming from the edges, which now is not negligible. Therefore a convergent flux is established giving rise to a non-planar diffusion regime (Figure 3.1b). In case of microelectrode arrays, an additional transition to planar diffusion can occur if the simultaneously operated microelectrodes are densely packed and their diffusion layers overlap and merge together (Figure 3.1c), effect known as *shielding effect* [151]. This overlap results in the creation of an apparent planar diffusion layer and, in case of a diffusion-limited reaction, the array behaves as a large electrode whose surface corresponds to the total surface area (sum of the active and inactive parts). Shielding can be avoided if the inter-electrode spacing is sufficiently large to prevent the coalescence of the individual diffusion layers, in this case the amperometric response is given by the sum of the individual responses and the array works as a current amplifier (Figure 3.1d). In case of microdisc arrays, the minimal inter-electrode spacing necessary to avoid shielding corresponds to a distance 23 times the microdisc radius [152].
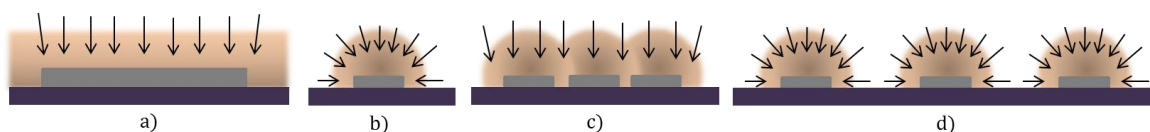
Figure 3.1. Schematic drawing of the diffusion layers and regimes at a macroelectrode (a), microelectrode (b), closely-packed (c) and loosely-packed (d) microelectrode array operated at the same potential.

The Faraday current density due to a diffusion-controlled reaction is proportional to the mass transport rate, i.e. the concentration gradient of the electroactive species at the electrode surface. For a plane geometry such as a macroelectrode, this current density shows a square root dependency on time, while for a point geometry such as a microdisc a time-independent expression is found ($I \propto 1/r$). In absence of convection, planar diffusion does not yield a steady-state response since the

diffusion layer infinitely grows due to always new material approaching the electrode surface from further portions of the bulk solution. Contrarily, for a microdisc, the main concentration drop arises at the close vicinity of the electrode surface (distance close to the electrode radius). The resulting steep concentration gradient leads to high current density which remains constant: the Faraday current tends asymptotically to a limiting value, independent on the diffusion layer.

The ohmic drop (product of the current and the resistance in solution) represents a fraction of the applied potential that has no influence on the charge transfer process. In the case of a microelectrode, the resistance in solution is several orders of magnitude higher than that at a macroelectrode, however the small current intensity generated at the tiny surface area balances such large resistance, leading to good immunity to ohmic distortions [114].

Under planar diffusion, both the Faraday and the charging current are proportional to the electrode area and the S/N ratio is similar to that obtained at a macroelectrode. Under a steady-state diffusion regime, the Faraday current shows a linear relationship with the smallest geometric dimension of the microelectrode (radius), while the charging current remains proportional to the electrode area, therefore a much more favorable S/N ratio is achieved which could be further improved by reducing the microelectrode dimension [114].

The main drawback of using microelectrodes is the small current intensity generated, whose measurement requires the use of a Faraday cage or high gain current-to-voltage converters. A way to increase the current is to use an array of widely separated and simultaneously operated microelectrode, which gives rise to a current response scaled up by the number of elements forming the array.

Regular arrays with well-defined dimensions and inter-electrode spacing have been generally fabricated by means of thin-film technology. Microdiscs fabricated by thin-film technology usually present a recessed geometry. This is due to the fabrication steps that require the deposition of a passivation layer over the electrode surface to define the microdisc geometry, as it will be shown in the following section. The slight recess, corresponding to the thickness of the passivation layer, possibly hinders the diffusion of the electroactive species to the electrode surface. Bond et al. [153] compared the amperometric response of inlaid and recessed microdisc geometry; in absence of convection and at long experimental times, the diffusion-limited current response for a recessed microdisc is given by the following equation:

$$I = 4mnFDC^*r \frac{1}{\frac{4h}{\pi r} + 1}$$

<div align="right">Equation 3.1</div>

where *m*: microelectrodes number, *n*: stoichiometric number of electrons involved in the reaction, *F*: Faraday constant (96485.33 A·s/mol), *D*: diffusion coefficient of the electrolyte species expressed in cm^2/s, c: species concentration expressed in mol/l, *r*: microelectrode radius, *h*: passivation layer thickness.

The performance of the two-electrode and three-electrode on-chip sensor will be investigated and compared by measuring trace metal amounts by SWASV. This technique was developed by Ramaley and Krause [154] and has been extensively studied by the Osteryoungs and coworkers [155–158]. As stated in the previous section, this technique consists of two steps: a pre-

concentration step where the metal species are reduced at the working electrode surface by applying a negative potential for a certain period of time, and a stripping step when the ions are re-oxidized by scanning the potential towards positive values. The potential is swept to positive values by superimposing a regular square wave onto and staircase as shown in the waveform and measurement scheme in Figure 3.2. The current is sampled at two times, i.e. at the end of the forward potential pulse and at the end of the reverse potential pulse (immediately before the potential direction is reversed).
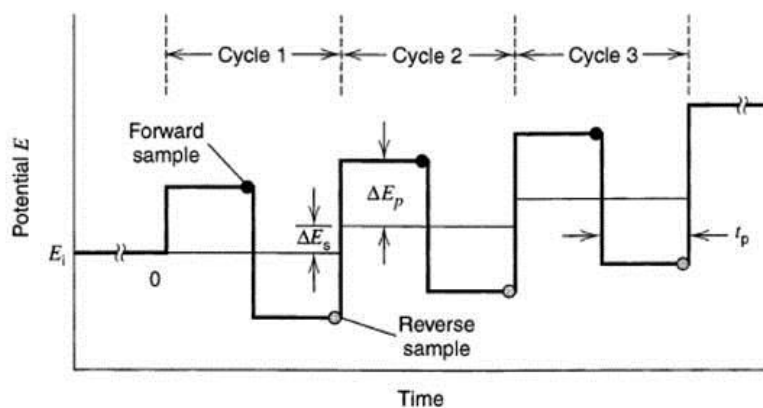
Figure 3.2. Potential waveform applied during the stripping step of the SWASV technique, ΔE_p: potential pulse amplitude, ΔE_s:staircase height, t_P: pulse width [159].

This sampling technique has shown to minimize the contribution of non-faradaic current (capacitive or charging current), becoming for this reason one of the most commonly used techniques for trace metal detection. The current waveform derived by subtracting the reverse current waveform i_R from the forward current waveform i_F is plotted versus the applied potential and the peak amplitudes are proportional to the species concentration, each peak potential being related to a certain metal species. Important parameters of the stripping step are the initial and final potential (with respect to the used RE), the potential pulse amplitude ΔE_p, the staircase height ΔE_s, and the frequency $f=1/t_p$. The performance in trace metal detection can be improved by adjusting these parameters. In general, t_p defines the experimental time scale, ΔE_s fixes the spacing of data points along the potential axis; these first two parameters define together the time required for a full scan; finally ΔE_p defines the potential window in each cycle and determines the resolution of voltammetric features along the potential axis [159].

3.3   First generation: two-electrode on-chip sensor

This section will describe the design, fabrication process flow and the electrochemical characterization of the two-electrode on-chip sensors. These devices have a microdisc array WE which can be deployed for detection of trace metals such as cadmium, lead, and copper by plating

the discs with Hg hemispheres or for the detection of arsenic by plating the discs with AuNPs. Their application to the detection of trace metals by SWASV will be shown in section 3.7.

3.3.1   Microelectrode arrays design and fabrication

Compared to previously reported microdisc arrays [108,160], the herein presented sensors differ in number of Ir microdiscs, center to center distance of the microdiscs, as well as deposition/patterning techniques used during the fabrication. We investigated a new protocol for opening the microdiscs through the silicon nitride (Si_3N_4) passivation layer which consisted in single step dry etching. This step was much faster and more reproducible with respect to the previously reported etching step which was a combination of dry and wet etching not always resulting in a complete opening of the Si_3N_4 layer [161].

Thin-film microelectrodes were fabricated on silicon wafer passivated with 200 nm of Si_3N_4 by Low Pressure Chemical Vapor Deposition (LPCVD). Figure 3.3 shows a schematic view of the microfabricated devices.
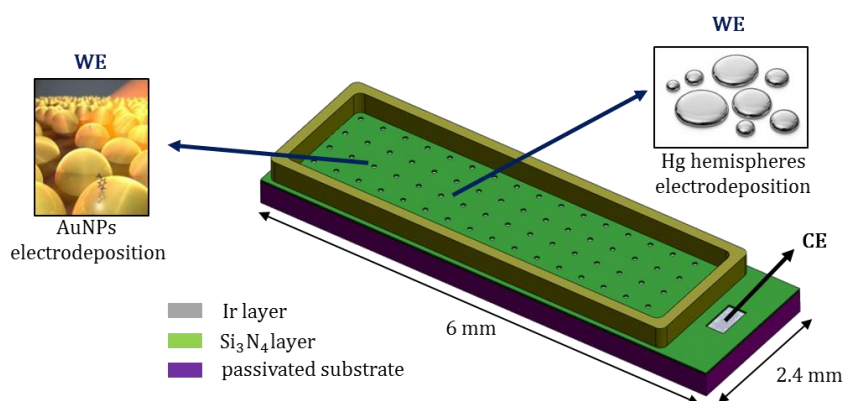
Figure 3.3. Schematic view (not to scale) of the two-electrode on-chip sensor (WE: Ir microdisc array working electrode, CE: Ir counter electrode). The WE can be plated either with AuNPs or with Hg hemispheres.

The fabrication process flow consists of three photolithography steps. Firstly, a 20 nm tantalum (Ta) adhesion layer and a 100 nm Ir layer were deposited by sputtering (the thin film resistivity ρ was 19.7 $\mu\Omega \cdot$cm) and patterned by Ion Beam Etching (IBE). The etching time needed to pattern the metallic layer was determined using a Secondary Ions Mass Spectroscopy (SIMS) system placed in the etcher chamber by observing the counts of secondary ions ejected from the sample bombarded by accelerated Argon ions (Figure 3.4). The total etching time was estimated to be 3 minutes (60 s for Ta, 100 s for Ir and a 20 s period of over-etching). Afterwards, a 200 nm Si_3N_4 layer was deposited by Plasma-Enhanced Chemical Vapor Deposition (PECVD) and patterned by Deep Reactive-Ion Etching (DRIE) to define the electrodes geometry and the bonding pads. A 150 μm thick SU-8 layer was finally patterned by photolithography to serve as containment ring for an

agarose gel membrane [123] needed to avoid fouling of the sensor. The fabrication process flow steps are summarized in Table 3.1 together with the device cross section.

Ir electrodes are used as either counter electrode (CE) without further modification or as a seed layer for the fabrication of the working electrode (WE). The CE has dimensions of 0.85 mm x 0.55 mm, and the WE is a microdisc array consisting of discs with diameter of 5 µm and serving as seed layer for Hg hemisphere or AuNPs plating.
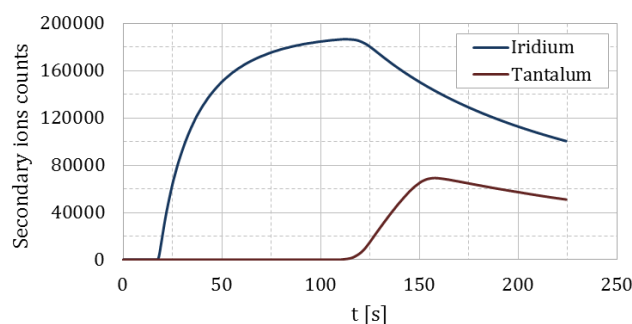
Figure 3.4. Secondary Ions Mass Spectroscopy counting of secondary ions vs. time.

Table 3.1. Fabrication process flow of the two-electrode on-chip sensors for trace metals.

Process Flow steps	Device cross section
0. 200 nm Si_3N_4 Low Pressure Chemical Vapor Deposition on Si	
1. Ta/Ir Sputtering (20 nm/100 nm)	
2. Ir/Ta Ion Beam Etching (dry etching)	
3. Si_3N_4 Plasma-Enhanced Chemical Vapor Deposition (200 nm)	
4. Si_3N_4 Deep Reactive Ion Etching (dry etching)	
5. SU-8 Photolithography (150 µm)	

The adhesion of the SU-8 ring corners was not perfect and was improved by replacing the last photolithographic step with a two-step lithography by using two different types of SU-8, one for thin structures (GM1060) and one for higher aspect ratio (GM1075). After a pre-heating step of 10 minutes at 130 °C for dehydration, the wafer was coated with a first layer of around 10 µm GM1060 and a soft bake was carried out at 130 °C for 1 h. Afterwards, a second coating with around 140 µm GM1075 was performed followed by a soft bake of 2 h at the same temperature. After that, the SU-8 was exposed to UV light, and underwent a post exposure bake (PEB) of 3 hours and a half, and after overnight relaxation, was developed in propylene glycol monomethyl ether acetate (PGMEA) for 8 minutes and then rinsed with isopropanol (IPA). Finally a hard bake was performed for 4 h at 135 °C.

The devices were also predisposed for future investigation of As(V) reduction by PANOA polymer. For this reason an interdigitated configuration of two WEs was designed, the first one being an array of microdiscs and the second one an array of microlines (5 μm width and 1.55 mm length) as schematically shown in Figure 3.5. The interdigitated configuration has been proposed in order to be able to detect sequentially As(III) on the AuNPs electrochemically deposited on the Ir-based microdisc array before and after the electrochemical As(V) reduction to As(III) induced by the PANOA polymer deposited on the microline array, thus allowing As(V) indirect measurement though subtraction of the two measurements.
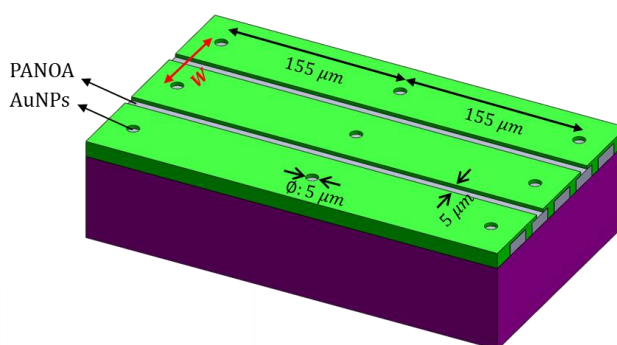
Figure 3.5. Interdigitated configuration of microdisc and microline arrays for combined As(III) and As(V) measurement; W is the inter-electrode spacing for rows.

As discussed in the previous section, in order to exploit all the advantages of the microelectrode geometry, it is necessary to avoid the occurrence of the shielding effect which leads to planar diffusion, therefore a crucial parameter for the design of the interdigitated arrays is the center-to-center spacing between the electrodes. The values of radius and center-to-center spacing for columns were fixed respectively to 2.5 and 155 μm as reported in literature [108,121,122,162], i.e. aspect ratio of 62, instead to fix the inter-electrode spacing for rows the presence of the polymer on the microlines between the microdiscs arrays was taken into account. On one hand, the spacing in the microline array should be big enough in order to avoid the shielding effect and short circuits between the microdiscs and microlines in case of lateral growth of the polymer with respect to the chip surface. On the other hand, the microline spacing should be small enough to take advantage of the interdigitated configuration which allows the As(III) generated on the microlines to be captured by the AuNPs on the microdiscs. Therefore three configurations (A, B, C) were designed with different number of electrodes and center-to-center spacing W values for the rows. Table 3.2 sums up the geometrical configurations for the three designs.

Table 3.2. Geometrical parameters of the three different designs of interconnected and interdigitated microdisc arrays.

Design	A	B	C
# microdisc rows	50	19	12
# microdiscs per row	10	10	10
microdisc radius	2.5 μm	2.5 μm	2.5 μm
microdisc center-to-center spacing (columns)	155 μm	155 μm	155 μm
microdisc center-to-center spacing W (rows)	70 μm	190 μm	310 μm

Figure 3.6 shows optical microscope pictures of the three devices: design A(a), B (b) and C (c) after SU-8 photolithography showing the height of the SU-8 ring.
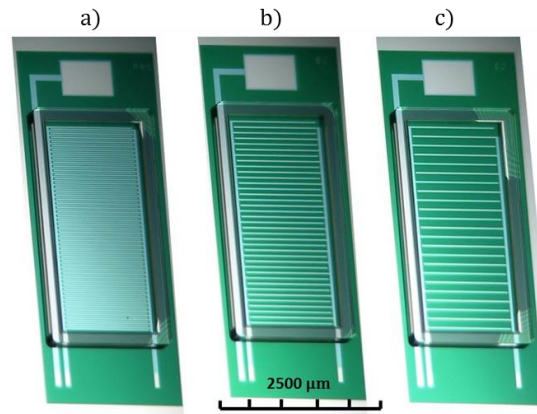
Figure 3.6. Microscope pictures of the interconnected microdisc arrays after SU-8 photolithography: design A (a), design B (b) and design C (c).

The quality of the fabrication was firstly checked by microscopy. After the dry etching of the silicon nitride layer, the electrode surface topography and cleanness were analyzed by Scanning Electron Microscopy (SEM) and Atomic Force Microscopy (AFM). Figure 3.7 and Figure 3.8 show respectively the analyses carried out with SEM and AFM which showed an excellent quality of the Si_3N_4 layer patterning in terms of geometry definition and absence of fabrication residues.
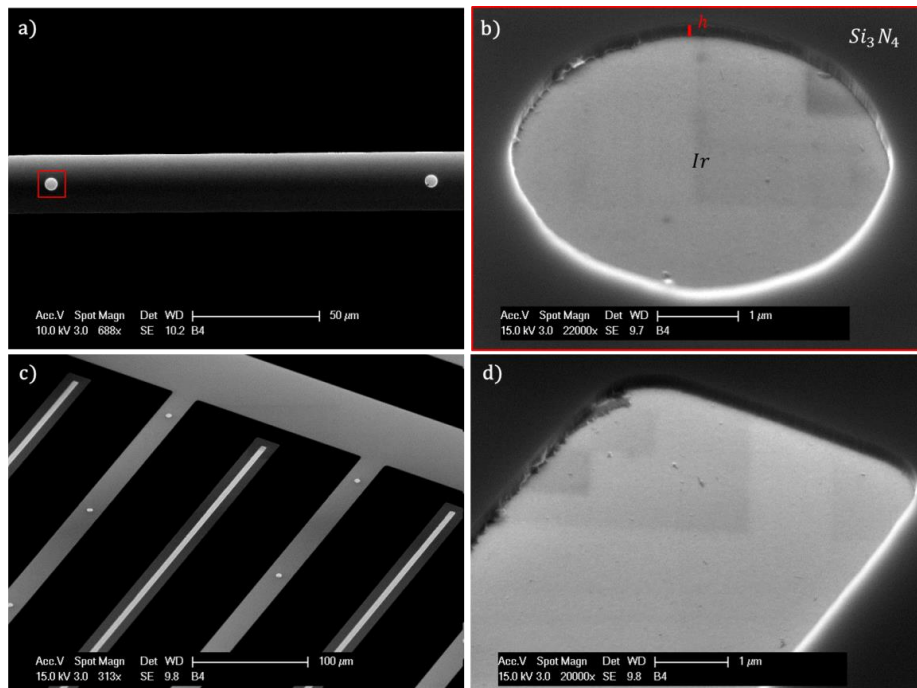
Figure 3.7. SEM pictures of two Ir microdiscs with center to center distance of 155 μm (a), of a single microdisc showing the height of the Si3N4 layer, h=200 nm (b), of the interdigitated configuration (c) and of a single microline (d).
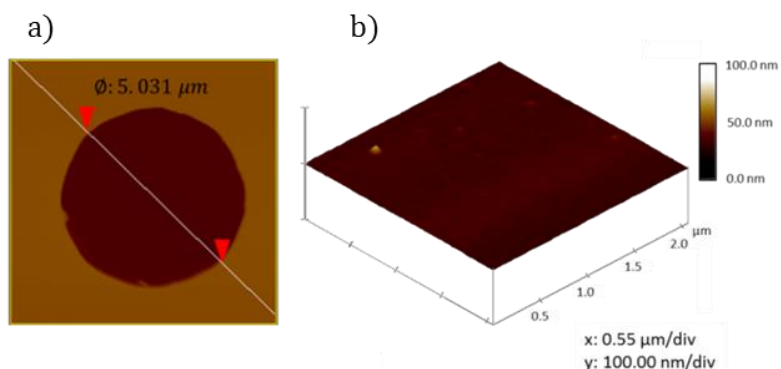
Figure 3.8. AFM picture and profile of a single microdisc electrode (2 µm x 2 µm area) confirming absence of fabrication residues and cleanness of the surface; estimated mean surface roughness: ≈0.6 nm.

The absence of pinholes in the silicon nitride layer was investigated by electrodepositing platinum black (constant potential of -0.15 V for 120 s) on the iridium electrodes. Pt-black was chosen because of its large surface area and lateral outgrowth [163] during deposition which leads to a dendritic structure growing from deposition on a single spot. Therefore, in case of pinholes, a "messy" deposition would be noticed on the device extending outside the geometry of the metallic layer. Figure 3.9 shows a picture of the device after Pt-black deposition revealing an excellent quality of the Si_3N_4 layer (only one pinhole was found throughout all the device area as pointed out by the red arrow).
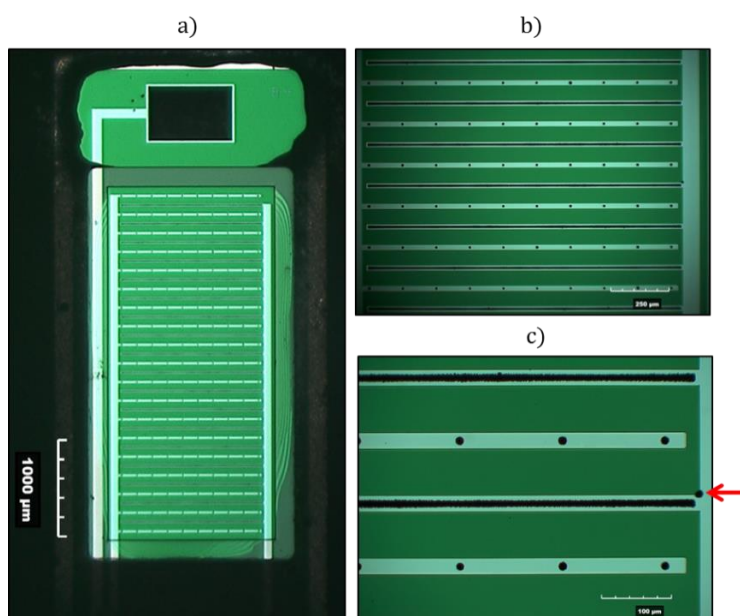
Figure 3.9. Picture of the device after Pt-black deposition (a) and zoomed pictures (b, c) showing the good quality of the silicon nitride layer.

3.3.2   Microelectrode arrays electrochemical characterization

The electrochemical response of the electrode material allows evaluating the quality of the fabrication process. As the voltammograms of bulk electrode materials are well-known, the quality of thin-films can be characterized by cyclic voltammetry (CV). The integrity and the diffusion properties of the Ir-based microdisc arrays were electrochemically characterized by CV as well.

Iridium integrity

Ir electrodes show characteristic fingerprints in their voltammograms in sulfuric acid (H_2SO_4), therefore the microdisc arrays were evaluated by CV in deaerated 1 M H_2SO_4. The cyclic voltammogram recorded for design A with a scan rate of 99 mV/s is shown in Figure 3.10. The current peak at 0.15 V on the anodic scan can be attributed to desorption of hydrogen (H_d), while at potentials above 0.4 V oxygen is absorbed and iridium oxidation occurs (O_a). On the cathodic scan the reduction of IrO_2 (O_r) and the hydrogen absorption current peak (H_a) can be observed. This result is in good agreement with literature [164]. This electrochemical test confirmed the integrity of the Ir layer and revealed an excellent quality of the fabricated electrodes which were not affected by the fabrication process steps: neither deterioration nor contamination was noticed before SU-8 processing.
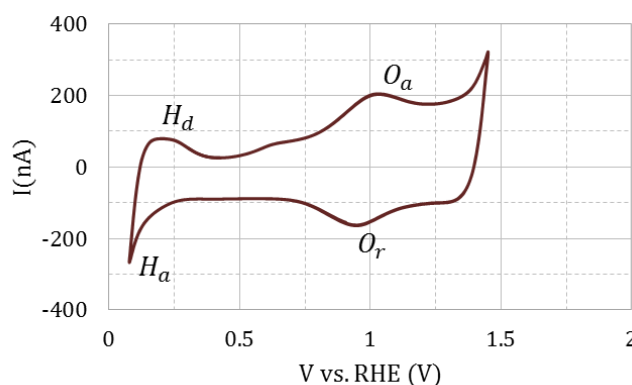
Figure 3.10. Cyclic voltammogram of Ir electrodes (design A) in 1 M H_2SO_4, 99 mV/s scan rate, potentials vs. Reversible Hydrogen Electrode; Ha, Hd: adsorption and desorption of hydrogen, Oa, Or: iridium oxidation and IrO_2 reduction.

Diffusion properties

Under optimal geometry and fabrication conditions, the current monitored during SWASV measurements should be directly proportional to the number of interconnected microelectrodes, thus achieving higher sensitivities with respect to a device with lower number of discs. This is true when the microelectrodes are characterized by a non-planar diffusion regime, therefore in absence of diffusion layer overlapping. The absence of diffusion layer overlapping was assessed in 1 mM potassium ferricyanide ($K_3Fe(CN)_6$) by CV at four different scan rates from 1 mV/s to 50 mV/s (max reduction time typically of 7 min) and by chronoamperometry (reduction time > 15 min) for

the three designs. An S-shaped CV response characteristic to hemispherical diffusion was observed for the three designs (A-B-C) as shown in Figure 3.11 (a-b-c).
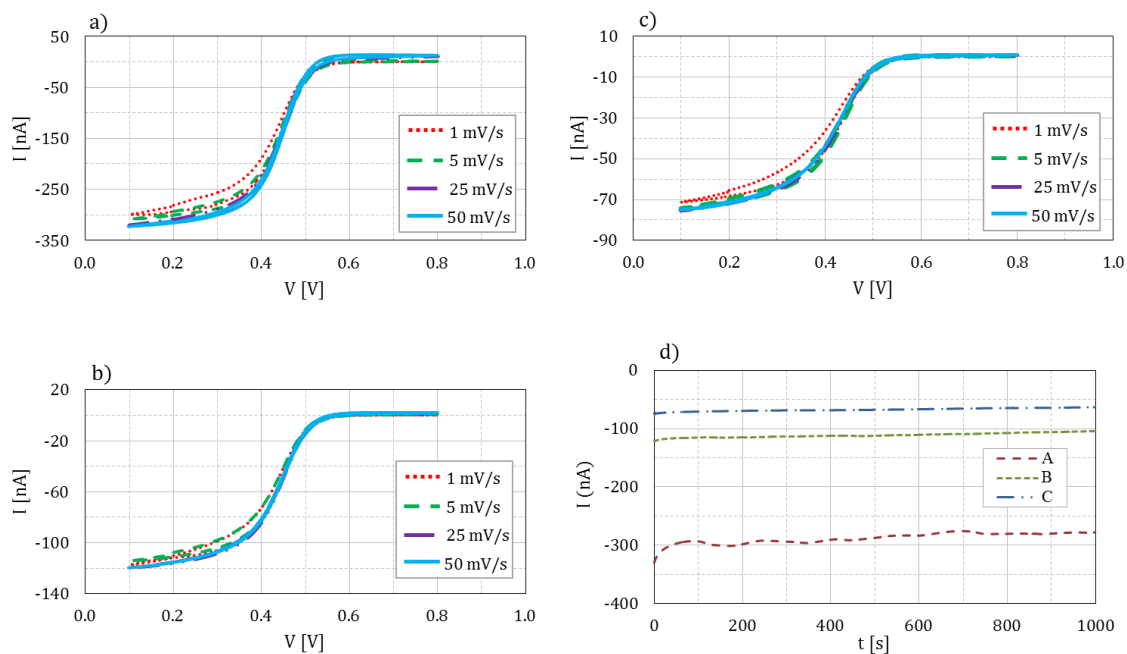
Figure 3.11. Cyclic voltammograms in 1 mM ferri-CN for design A (a), B (b) and C (c) and related chronoamperometric measurements (d).

The limiting diffusion currents, determined from the voltammograms monitored at 50 mV/s, reported in Table 3.3, were found to be in good agreement with the theoretical value [153] calculated for a recessed geometry by replacing in Equation 3.1 the diffusion coefficient of ferricyanide (7.1×10^{-6} cm^2/s), its concentration (1 mM), the value of the microelectrode radius (2.5 µm) and the passivation layer thickness (200 nm).

Table 3.3. Theoretical and experimental values of the current registered during CV in 1 mM ferri-CN.

Design	Microdisc number	Theoretical current	Measured current
A	500	313.6 nA	327.8±2.7 nA
B	190	119.46 nA	121.3±2.2 nA
C	120	74.66 nA	74.1±2.2 nA

The chronoamperometric measurements showed a significant decrease of the current for the design A while constant currents were observed for the designs B and C (Figure 3.11d). These results revealed that diffusion overlapping occurs for design A for long measurement time. A new configuration was therefore designed with 500 microdiscs whose rows had a center-to-center distance of 190 µm (the same distance used for design B) which led to a bigger size for the sensor (11 x 2.4 mm instead of 6 x 2.4 mm).

SU-8 influence on diffusion properties

After the SU-8 photolithography step, the three designs were tested again by cyclic voltammetry in a $K_3Fe(CN)_6$ solution and the S-shaped current response was not observed. Figure 3.12 shows the voltammogram registered for the first design A device (70 µm center-to-center spacing) before (red line) and after (blue line) SU-8 photolithography, showing how the current after lithography is almost zero compared with the current before lithography. This result strongly suggests that SU-8 processing significantly affects the quality of the sensor possibly due to resin residues obstructing the surface of the discs.
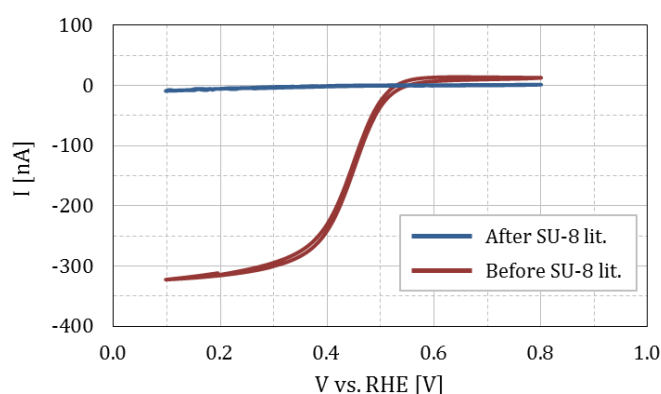
Figure 3.12. Cyclic voltammogram recorded for an Ir microdisc array (design A) before (red line) and after (blue line) SU-8 photolithography in a solution of 1 M KCl containing 1 mM ferri-CN, potentials vs. Reversible Hydrogen Electrode, sweep rate 50 mV/s.

In order to remove possible residues of SU-8 from the surface, different cleaning procedures were investigated: acetone rinsing, sodium hydroxide rinsing and Ultraviolet (UV) Ozone cleaning. The UV ozone treatment showed to work properly allowing stripping photoresist residues. The three designs underwent 15 minutes of UV Ozone cleaning, afterwards the CV test for the same four different scan rates from 1 mV/s to 50 mV/s and chronoamperometry measurements were repeated. Figure 3.13 shows the results which suggest that with respect to the voltammograms registered before SU-8 photolithography: (i) there is a higher variability among the curves at different scan rates, especially for design C, and (ii) the measured current is slightly smaller for all the designs.

However it is evident from the voltammograms that the UV Ozone cleaning has a positive effect on the shape of the signal and that thanks to this treatment it is possible to recover the S-shaped curve observed before SU-8 photolithography typical of hemispherical diffusion. An UV Ozone cleaning step of 30 minutes was therefore foreseen for each sensor before plating the Ir microdiscs with Hg hemispheres or AuNPs.

Cyclic voltammograms were also registered for the CE in order to check its behavior as macroelectrode after having carried out the SU-8 photolithography step: for this electrode a voltammogram with two well-defined peaks for oxidation and reduction should be found in the forward and reverse scan, respectively.
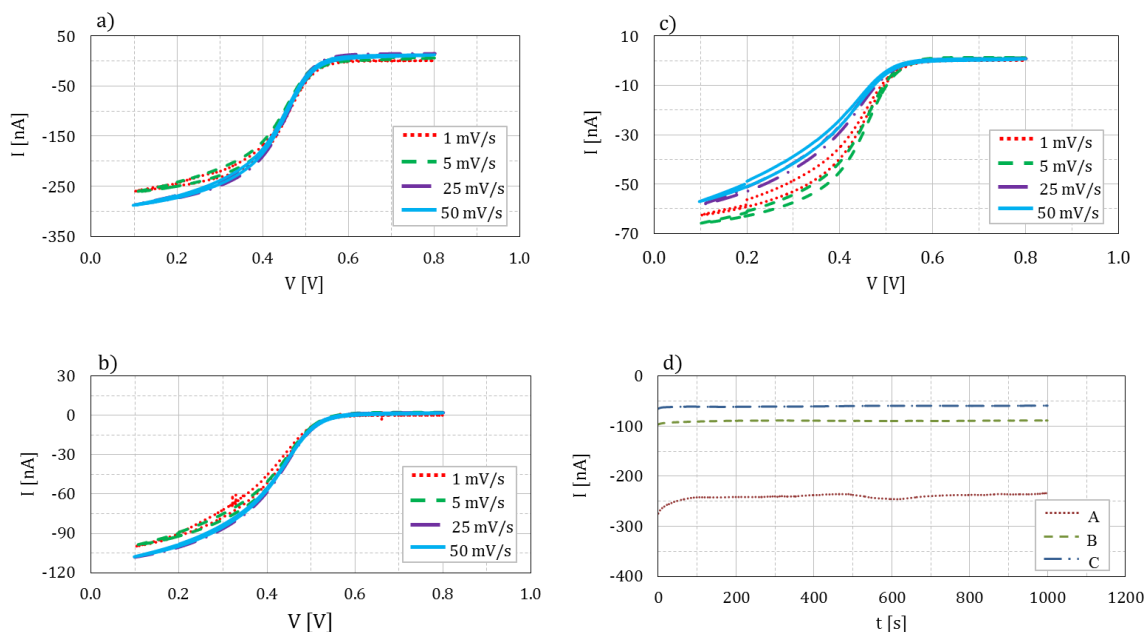
Figure 3.13. Cyclic voltammograms recorded for design A (a), B (b) and C (c) in a solution of 1 M KCl containing 1 mM ferri-CN and related chronoamperometric measurements vs. RHE (d) after SU8 photolithography and UV Ozone cleaning (15 minutes).

Without any treatment of the surface, the expected behavior is not observed, being the current almost constant around 100 nA. The UV O_3 treatment allowed recovering the expected shape with the oxidation and reduction peaks. The CV experiment was repeated one, two and six days after the UV O_3 treatment and the registered curves perfectly overlapped the curve obtained immediately after the UV O_3 treatment as shown in Figure 3.14. The voltammograms registered for the microlines (data not shown) were a combination of the shapes observed for the microdiscs and the counter electrode, as was expected having one micro- and one macro- dimension.
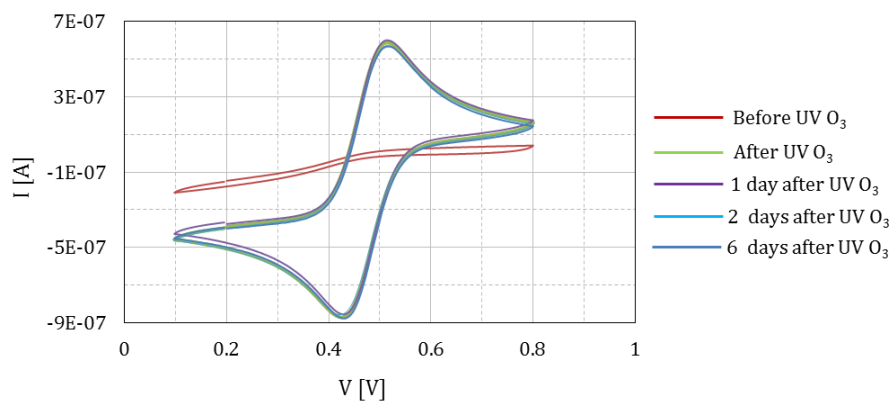
Figure 3.14. Cyclic voltammograms of the Ir CE in a solution of 1 M KCl containing 1 mM ferri-CN before (red), immediately after (green) and one (violet), two (light-blue), six (blue) days after UV ozone cleaning.

3.4 Second generation: three-electrode on-chip sensor

The second generation devices differ from the first one only for the on-chip addition of the RE. Two different electrodes were investigated as RE and will be described in the following sections. Their application to the detection of trace metals by SWASV will be shown in sections 3.7.2 and 3.7.3.

3.4.1 Device design and fabrication

The second generation sensors were fabricated on silicon wafers passivated with silicon nitride following the same process flow described in section 3.3.1. The Ir electrodes defined through the DRIE step were used as a seed layer for the fabrication of the working and reference electrode (WE, RE) or as the counter electrode (CE) without further modification. Design B and design C were used for the WE. The CE and the RE consist of two rectangles of 0.85 mm x 0.55 mm and 5 mm x 1.64 mm, respectively. The fabrication of the Ag/AgCl pseudo-RE was completed by two additional steps. A 5 μm thick layer of Ag was galvanostatically deposited by applying a constant current density of 100 $\mu A/mm^2$ in a three-electrode setup in a silver cyanide bath for 5 minutes (deposition rate of 1 $\mu m/min$). The partial chloridation (25%) of Ag to AgCl was electrochemically achieved in a 50 mM KCl solution by using a lower current density of 5 $\mu A/mm^2$ for 25 minutes, as described in [165] . Figure 3.15 shows a schematic view (a) and a picture (b) of the microfabricated device.
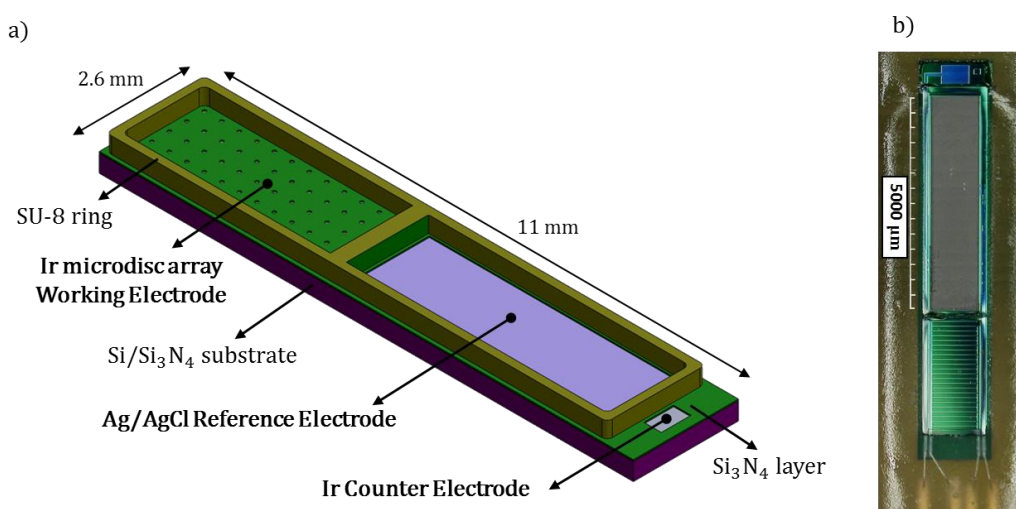
Figure 3.15. Schematic view (not to scale) of the three-electrode on-chip sensor (a) and picture of the fabricated device (b).

The PVC-IL membranes for the REs were prepared by dissolving ionic liquids (ILs) and PVC in tetrahydrofuran (THF). The Ag/AgCl/PVC-IL REs were prepared by drop-casting this cocktail onto the Ag/AgCl layer and leaving overnight for solvent evaporation. Figure 3.16 shows a picture of the Ir electrode (a) after Ag deposition (b), Ag chloridation (c) and PVC-IL membrane casting (d). The presence of the SU-8 confinement ring helped to avoid spreading of the membrane over the WE surface area, but not on the epoxy used to encapsulate the device on the printed circuit board (PCB).
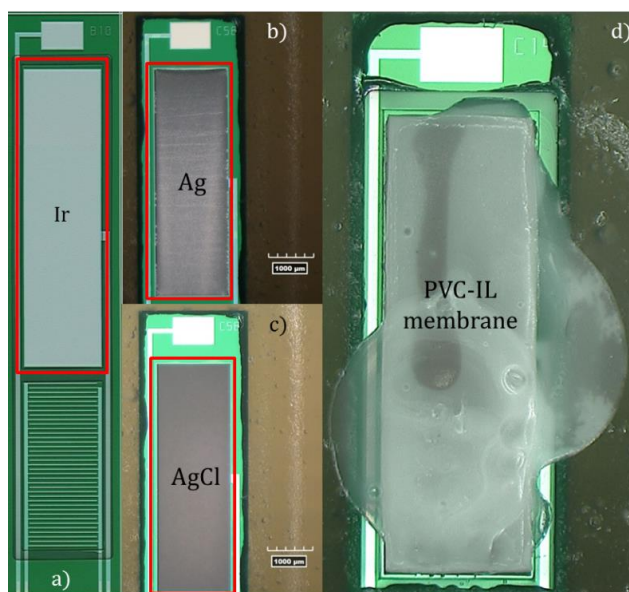
Figure 3.16. Picture of the on-chip RE fabrication: Ir seed layer (a), Ag deposition (b), Ag chloridation to AgCl (c), PVC-IL membrane casting (d).

3.4.2 On-chip RE testing: stability in time and influence of chloride concentration

The important parameters to monitor for good functioning of the RE are stability in time and influence of the chloride concentration.

Ag/AgCl pseudo-reference electrode

The Ag/AgCl electrode potential stability in time was tested in a seawater sample from Arcachon Bay against a standard Ag/AgCl/3 M KCl RE. The potential monitored was stable around 37.1±1.4 mV during more than two months as shown in Figure 3.17.
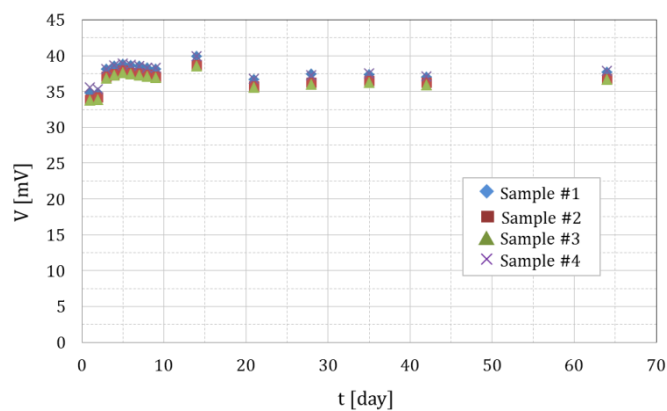
Figure 3.17. On-chip Ag/AgCl pseudo-RE of four different devices vs. standard Ag/AgCl/3 M KCl RE monitored as a function of time in seawater.

The electrode sensitivity to changes in the electrolyte concentration was checked by measuring the potential in 10^{-4} M NaCl, 10^{-3} M NaCl, 10^{-2} M NaCl and 10^{-1} M NaCl solutions against an Ag/AgCl/3 M KCl as shown in Figure 3.18a. A behavior close to the ideal Nerstian slope was found as shown in Figure 3.18b. The correlation between the potential and the logarithm of chloride concentration was linear: $E = -21.57 \ln(a_{Cl^-}) + 23.016 = -50.09 \log(a_{Cl^-}) + 23.016$.
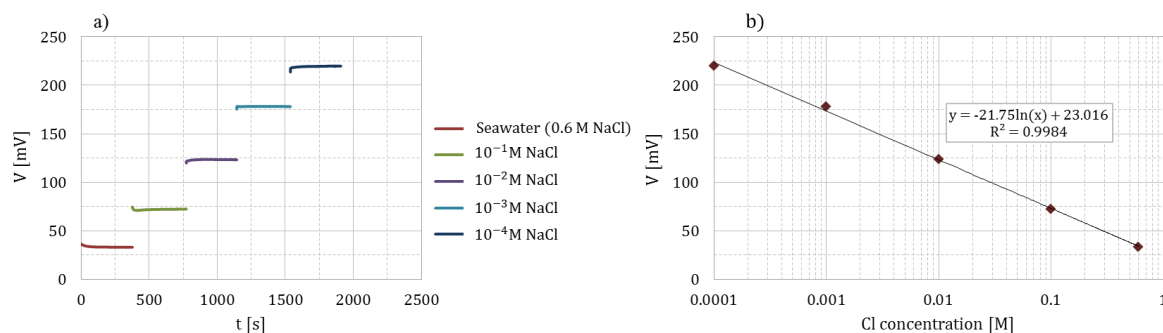
Figure 3.18. On-chip Ag/AgCl pseudo-RE potential vs. standard Ag/AgCl/3 M KCl RE monitored in solutions with different chloride concentrations (a) and correlation between the potential and chloride concentration (b).

Ag/AgCl/PVC-IL reference electrode

The Ag/AgCl/PVC-IL RE potential was measured in seawater and its value was very close to the value measured for the Ag/AgCl pseudo-RE (37.34 mV). The sensitivity towards chloride concentration was again tested by using solutions with different NaCl concentrations as shown in Figure 3.19a. The slope with respect to chloride concentration was found to be 21.32 mV/decade (Figure 3.19b), a value smaller than the slope found for the Ag/AgCl pseudo-RE. The PVC-IL membrane based RE is therefore expected to give better performance in detection and quantification of trace metals since, besides having a smaller slope, it is expected to serve as a diffusion barrier helping slowing down AgCl dissolution in solutions with low chloride levels.
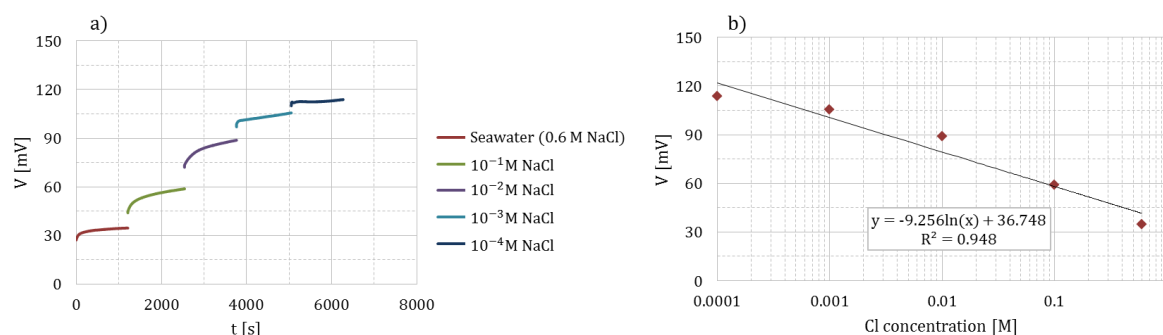
Figure 3.19. On-chip Ag/AgCl/PVC-IL RE potential vs. standard Ag/AgCl/3 M KCl RE monitored in solutions with different chloride concentrations (a) and correlation between the potential and chloride concentration (b).

The fact that the potential of the Ag/AgCl/PVC-IL RE is very close to the potential of the Ag/AgCl pseudo-RE suggests a possible loss of adhesion of the membrane and consequent solution infiltration. Some conductive polymers were tested as intermediate layers between the PVC

membrane and the AgCl layer: poly(3-octylthiophene-2,5-diyl) (POT) [150], polyaniline (PANI) and poly(3,4-ethylenedioxythiophene)-poly(styrenesulfonate) (PEDOT-PSS). They were deposited by drop-casting before the PVC-IL membrane deposition. Figure 3.20 shows the potential of the REs measured in seawater (a) and the potential measured for different chloride concentrations (b: PANI, c: POT, d: PEDOT-PSS). The potential value registered at the beginning of the test in seawater reveals that no chloride is present close to the Ag/AgCl, however this value immediately drops suggesting that the chloride concentration rises in proximity of the AgCl layer, indicating also bad adhesion of the conductive polymers. All conducting polymer interlayers still revealed chloride sensitivity, therefore they were not used for the development of on-chip RE.
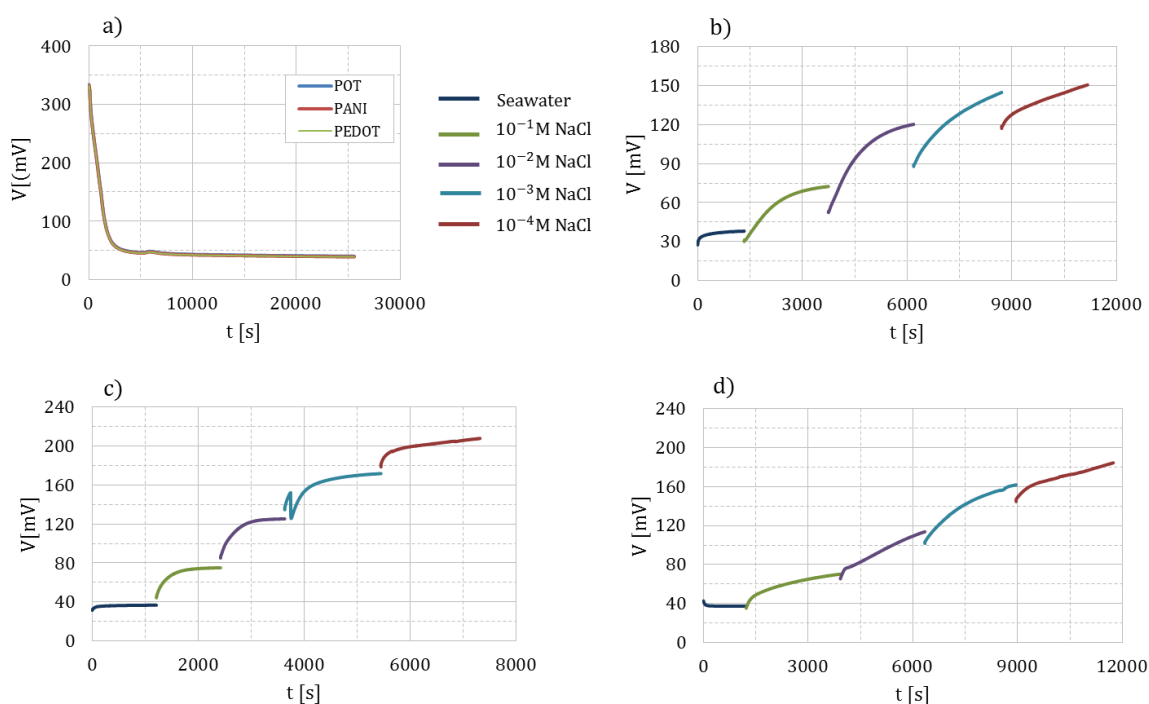
Figure 3.20. On-chip Ag/AgCl/conductive polymer/PVC-IL RE potential vs. standard Ag/AgCl/3 M KCl RE in seawater (a) and in solutions with different chloride concentrations when the conductive polymers PANI (b), POT (b) and PEDOT-PSS (c) were used.

Iridium pseudo-reference electrode

The feasibility to directly deploy Ir as pseudo-RE was also investigated. Four samples were used: an Ir square without SU-8 ring (area: 0.4675 mm^2), an Ir square with SU-8 ring (area: 0.4675 mm^2), an Ir square with SU-8 ring after UV ozone treatment (area: 8.2 mm^2), an Ir square with SU-8 ring with larger area (area: 8.2 mm^2). Their potential was tested in 0.6 M NaCl against an Ag/AgCl/3 M KCl RE for two weeks.

Figure 3.21 shows the comparison of their potential in time. The small electrode surrounded by the SU-8 ring showed the best performance, which however was not sufficient to serve as stable RE, since the voltage drop after two weeks was of around 30 mV, and the voltage drop during the last measurement was of around 25 mV. Ir was therefore discarded as possible material for on-chip RE and the Ag/AgCl based electrodes were further investigated.
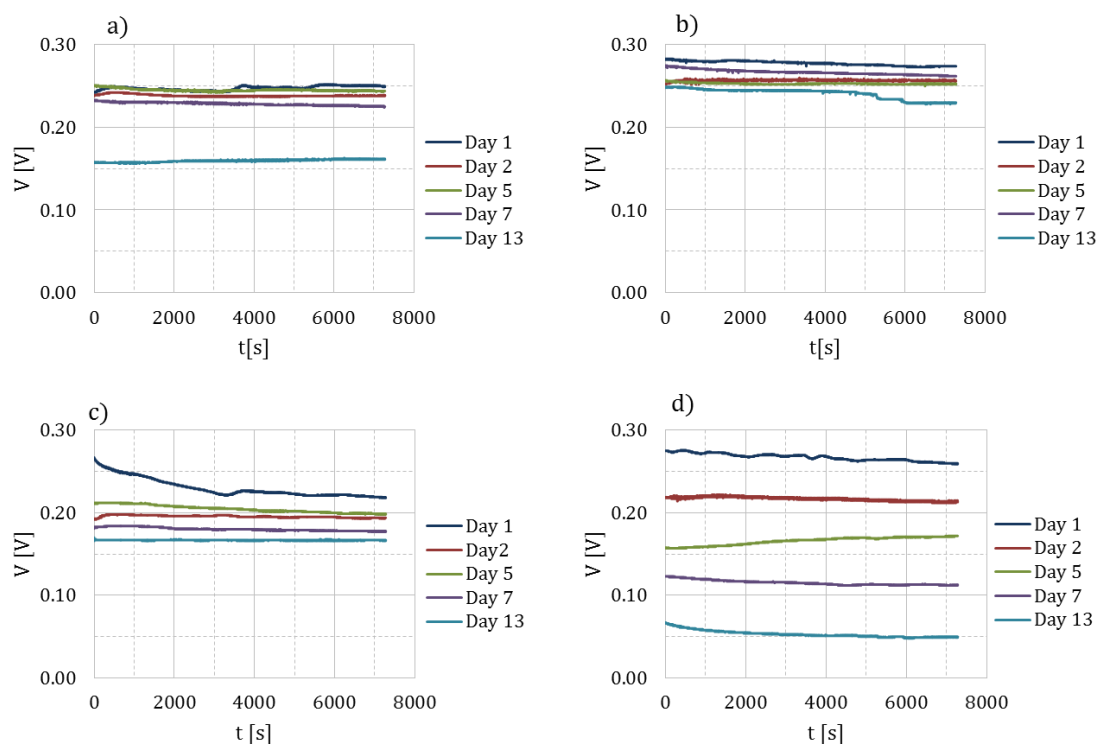
Figure 3.21. Potential vs. Ag/AgCl/3 M KCl RE of on-chip Ir electrodes in 0.6 M NaCl solution: small Ir square (a), small Ir square with SU-8 ring (b), big Ir square with SU-8 ring after UV ozone treatment (c) and big Ir square with SU-8 ring (d).

3.5   Materials and instrumentation

Standard silicon wafers with a thickness of 525 μm were used as substrates for the fabrication of the sensors. An EG&G galvanostat was used for the electrodeposition of silver (Ag) in a Silver glo 3K KAg(CN)$_2$ bath (LeaRonal AG, Littau Switzerland). Potassium chloride (KCl) used for Ag chloridation and sodium chloride (NaCl) used for potential measurements were at least p.a. quality. Reference electrode membranes were prepared by dissolving 400 mg of bis(trifluoromethanesulfonyl) amide 1-ethyl-3-ethylimidazolium ionic liquid (IL) 99.5% (IOLITEC ionic Liquid Technologies GmbH, Heilbronn, Germany) and 200 mg of poly(vinyl chloride) (PVC) in 3ml of tetrahydrofuran (THF). Selectophore grade high molecular weight PVC and anhydrous THF with 0.025% BHT (butylated hydroxytoluene) as stabilizer were purchased from Sigma-Aldrich. High purity LGL Agarose powder (molecular biology grade, Biofinex, Switzerland) was dissolved in deionized water (1.5 %) at around 80°C for forming the gel membrane.

A Metrohm Ag/AgCl/ 3 M KCl RE protected with an additional 0.1 M NaNO$_3$ salt bridge was used for SWASV measurements. An IBM analog potentiostat and a Metrohm Autolab PGSTAT12 were used for cyclic voltammetry measurements of the iridium (Ir) electrodes respectively in H$_2$SO$_4$ and K$_3$[Fe(CN)$_6$]. An eDAQ e-corder was used for on-chip RE potential measurements in seawater (Arcachon bay, April 2015) while VIP system hardware and software developed by Idronaut were used for running the SWASV measurements in plexiglas beakers. Merck Suprapur NaNO$_3$ was used

as electrolyte for spiking trace metals during the SWASV measurements. Stock solutions of Cd(II), Pb(II) and Cu(II) were prepared from 1 g/l metal standard solutions (Merck) and acidified to pH 2 using suprapur grade concentrate HNO_3 (Merck).

3.6 Experimental methodology

3.6.1 Deposition of Hg hemispheres

The microdisc arrays were plated with mercury by the reduction of Hg(II) from a solution of 0.1 M perchloric acid ($HClO_4$) containing 5mM mercury acetate ($Hg(CH_3COO)_2$). A potential of -0.4 V was applied for 8 minutes as reported in [107] vs an Ag/AgCl/3 M KCl RE protected with an additional 0.1 M $NaNO_3$ salt bridge: this step resulted in homogeneous hemispheres of 6 μm radius nicely covering each microdisc. Figure 3.22 shows an example of the deposition current of Hg hemispheres.
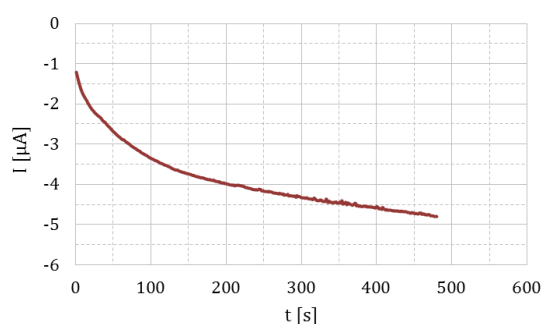
Figure 3.22. Current profile registered during the deposition of Hg hemispheres on the Ir microdiscs.

After deposition, the mercury layer was stabilized in a 0.1 M $NaNO_3$ solution by sweeping the potential from -900 mV to -100 mV (120 s at -900 mV, ramp step: 25 mV, ramp increment: 8 mV, frequency=200 Hz) and a blank measurement was obtained with the same SWASV conditions for a deposition time of 300 s in order to check the absence of any metal contamination. After carrying out the measurements, the mercury layer was removed in a 1 M potassium thiocyanate (KSCN) solution by linearly sweeping the potential from -0.3 V to +0.3 V (step: 0.04 V, SR: 0.05 V/s). An external platinum wire was used as counter electrode for mercury deposition and re-oxidation as well as during some SWASV measurements for comparison with the on-chip CE.

3.6.2 SWASV measurements

SWASV measurements were carried out in a 0.1 M $NaNO_3$ solution or seawater containing Pb(II), Cd(II) and Cu(II) in the nanomolar range in order to (i) compare the on-chip CE and RE to commercial ones, (ii) identify the SWASV peak potential of the target analytes vs. on-chip RE, (iii) evaluate the performance of the three-electrode on-chip sensors (WE, CE, RE) for detection and quantification of trace metals with respect to the two-electrode on-chip sensors (WE, CE). Before

each set of measurements, the sensors were coated with an agarose gel membrane and left conditioning one hour in milli-Q water and overnight in 0.1 M $NaNO_3$ solution. Figure 3.24 shows the experimental setup for SWASV measurement: a VIP potentiostat as used for *in situ* measurement and a laptop running VIP software allowed to gather the data.
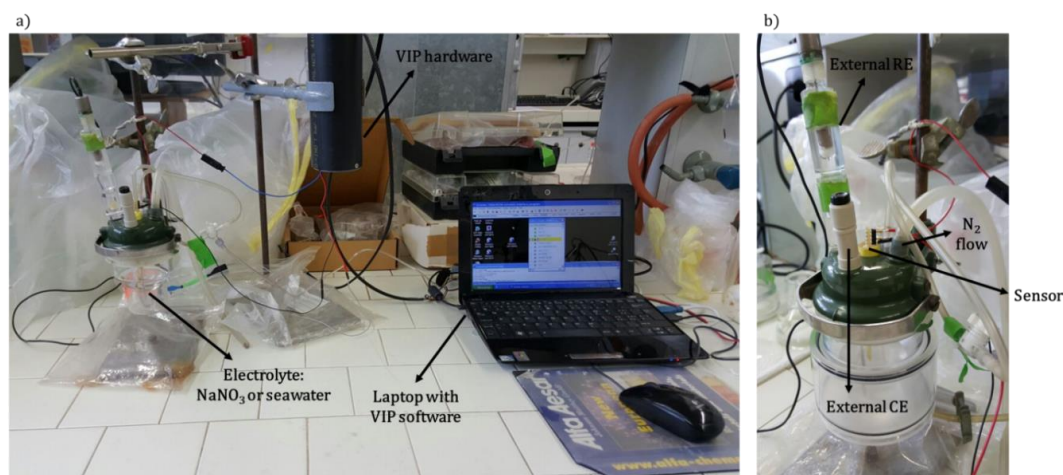
Figure 3.23. Experimental setup for SWASV measurements (a) and enlarged picture of the electrochemical cell with the sensor, the external RE and the external CE (b).

The SWASV protocol against an external RE consisted of the following steps performed in an uninterrupted sequence: (i) pre-cleaning step at $E_{pre-clean}$ (+150 mV), $t_{preclean} = 60$ s ; (ii) pre-concentration step at $E_{preconc}$ (-1100 mV), $t_{preconc} = 5$ min; (iii) equilibration step, as step (ii) but for a period of 10 s; (iv) stripping step: initial potential $Ei = E_{preconc}$, final potential $E_f = E_{pre-clean}$, frequency (f) = 200 Hz, potential pulse amplitude E_p (25 mV), potential step height E_s (8 mV). The same protocol was applied against the on-chip RE but setting different values for $E_{pre-clean}$ and $E_{preconc}$ which were -100 mV and -1250 mV, respectively. Subsequently a background scan was recorded with the same parameters but without pre-concentration and equilibration steps. The SWASV voltammograms in this chapter are presented after the subtraction of the background scan [47]. All the measurements were carried out in absence of oxygen by bubbling nitrogen in the solutions.

The final target of these tests was to achieve higher sensitivity values with respect to previously reported sensors for the two-electrode configuration due to the higher number of microdiscs, and to achieve a proof-of-concept of the detection and quantification capabilities of the three-electrode configuration.

3.7 Results and discussions

3.7.1 SWASV trace metal calibration with the first generation device

Sensors with 190 microdisc arrays were used for comparison between devices with and without on-chip RE. The voltammograms obtained after successive standard additions of the three metal

species (lead, copper and cadmium) using a device with WE and CE against an external RE are shown in Figure 3.24. The current peaks increased linearly with the concentration and sensitivity values of 2.73 nAnM^{-1} min^{-1}, 1.23 nAnM^{-1} min^{-1}, and 1.29 nAnM^{-1}min^{-1} were registered for Pb(II), Cu(II), and Cd(II), respectively. These values were around 2 times higher than those obtained using a 100 microdisc arrays developed previously [121] (1.28, 0.57 and 0.59 nAnM^{-1}min^{-1} for respectively Pb(II), Cu(II), and Cd(II)), as expected due to the ratio 190:100 discs.
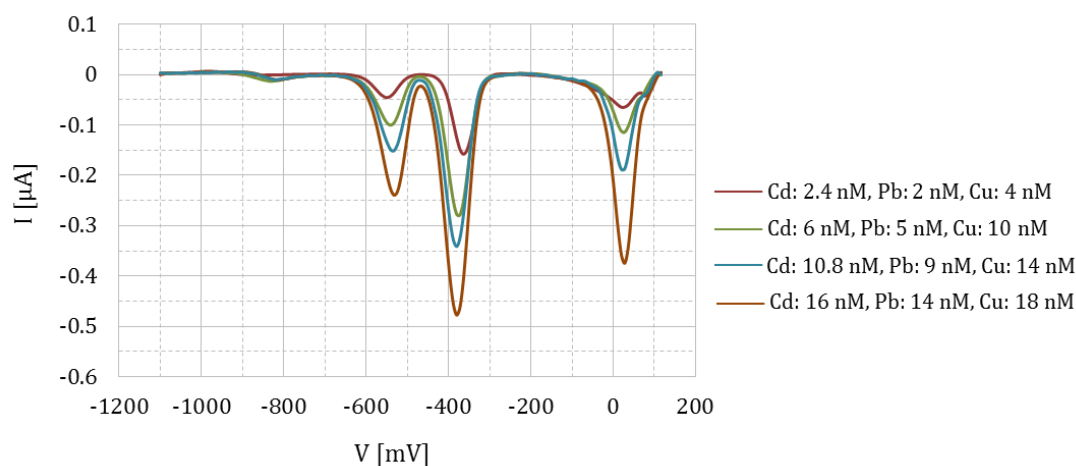
Figure 3.24. SWASV measurements of different concentrations of Pb(II), Cd(II) and Cu(II) against an external RE in 0.1 M NaNO$_3$ background electrolyte for 600 s deposition time. A device with 190 disc array and CE was used.

Table 3.4 shows the limit of detection achieved with the two-electrode (WE-CE) on-chip sensors with 190 microdiscs for a pre-concentration time of 10 and 30 minutes. The values found for a pre-concentration time of 30 minutes were smaller than the average concentration of the metal species in open sea and coastal waters, thus allowing detection and quantification in real environment.

Table 3.4. Comparison of the limit of detection (LOD) expressed in nM of the different metal species achieved with the two-electrode on-chip devices with their average concentrations in open sea and coastal waters (expressed in nM).

Species	LOD after 10' pre-concentration time	LOD after 30' pre-concentration time	Open sea concentration	Coastal waters concentration
Cu(II)	0.25	0.1	0.5-5	1-235
Pb(II)	0.02	0.005	0.005-0.09	0.03-200
Cd(II)	0.02	0.005	0.001-1.2	0.005-25

3.7.2   Voltammograms comparison between on-chip and external CE and RE

Design C devices with a 120 disc array and an Ag/AgCl pseudo RE were used for comparing the SWASV voltammograms of the target trace metals obtained using external RE and CE, external RE/on-chip CE, and on-chip RE/CE in 0.1M NaNO$_3$ synthetic solution and seawater.

Measurements in synthetic solutions

Figure 3.25a shows the SWASV measurements of 5.55 nM Pb(II), 4.96 nM Cd(II) and 15.76 nM Cu(II) in 0.1 M NaNO$_3$ vs external RE and CE (black dashed line), external RE and on-chip CE (light blue dashed line) and on-chip RE and CE (red solid line) for a pre-concentration time of 5 minutes.

The measurement vs. on-chip CE and external RE perfectly overlapped the one vs. external CE and RE, therefore all the subsequent measurements were carried out with on-chip CE.

The measurement vs on-chip CE and RE showed peaks potentials of Cd(II), Pb(II) and Cu(II) at -775 mV, -625 mV, -200 mV respectively, corresponding to a shift of around -275 mV for all peaks with respect to an external RE (Figure 3.25a).

The presence of the agarose gel did not affect the peak potentials as shown in Figure 3.25b, however a decrease in current intensity was observed for Cu(II) when the gel was used.
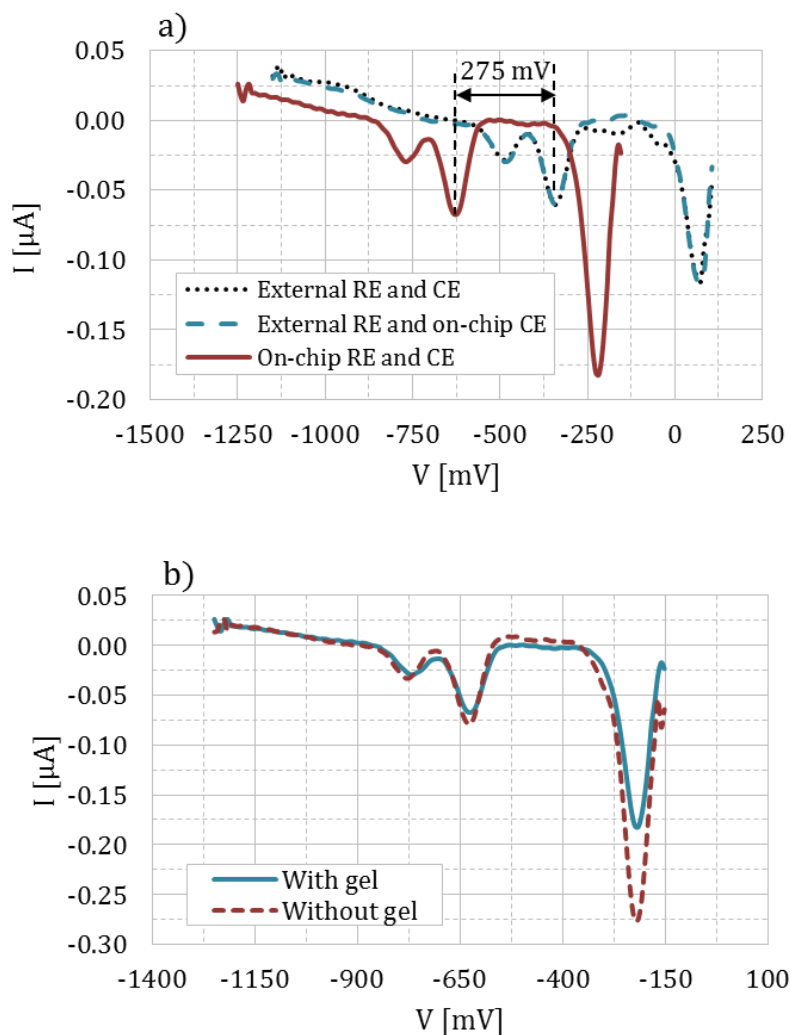
Figure 3.25. SWASV measurements (deposition time of 300 s) of 5.55 nM Pb(II), 4.96 nM Cd(II), and 15.76 nM Cu(II) in 0.1 M NaNO$_3$ (a) vs. external RE and CE (black dashed line), external RE and on-chip CE (light blue dashed line) and on-chip RE and CE (red solid line), and SWASV measurements comparison between two 120 disc devices with (light blue solid line) and without (red dashed line) agarose gel (b).

Measurements in seawater

Similar measurements were carried out in seawater. Figure 3.26 shows the SWASV measurement versus external Ag/AgCl/3 M KCl RE and on-chip Ag/AgCl pseudo-RE.

The measurements performed in seawater samples revealed a shift of typically -50 mV for all ions, much lower with respect to the shift observed in $NaNO_3$ because of the high content of chloride. This value is close to the potential registered between the on-chip pseudo-RE and a standard Ag/AgCl/3 M KCl RE in seawater as reported in section 3.4.2 (around 37 mV).

Figure 3.27 shows the SWASV measurements carried out in seawater against the on-chip RE for different pre-concentration times, from 300 to 900 s (a) and the correspondent calibration curves for lead and cadmium (b). The peak potentials were stable at -620 mV and -470 mV for Cd(II) and Pb(II) respectively.
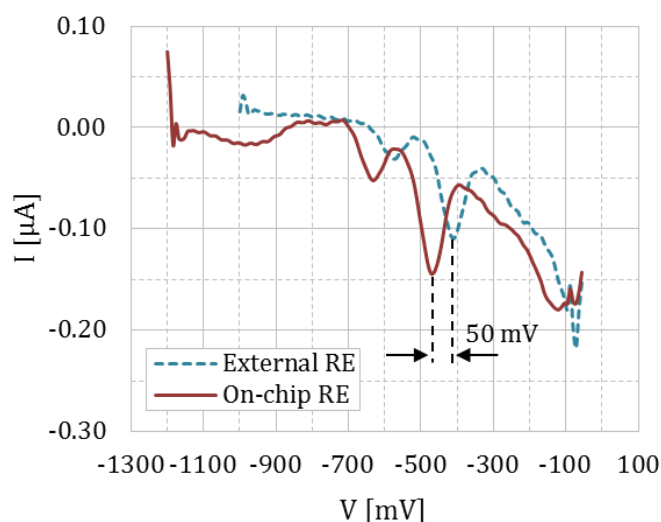
Figure 3.26. SWASV measurements (deposition time of 300 s) of 5.55 nM Pb(II), 4.96 nM Cd(II) and 15.76 nM Cu(II) in seawater vs. external RE (light blue dashed line) and on-chip RE (red solid line).

The primary goal of these tests was to find out the position of the current peak potential of each metal species and check their stability over a number of experiments, while for carrying out the calibration of the sensor SWASV voltammograms in 0.1 M $NaNO_3$ for different metal concentrations were measured, as it is reported in the section 3.7.3.The peaks amplitude increased with the pre-concentration time as expected but a perfectly linear relationship between the current peak and the pre-concentration time was not found as shown by the calibration curve of Pb(II) (R^2=0.9539) and Cd(II) (R^2=0.9465) in Figure 3.27b.
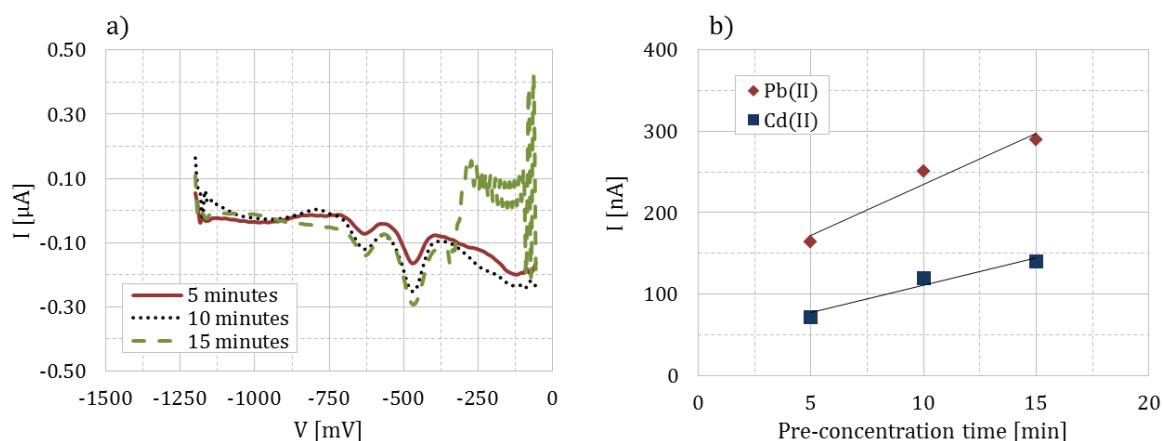
Figure 3.27. SWASV measurements of 5.55 nM Pb(II), 4.96 nM Cd(II) and 15.76 nM Cu(II) in seawater against on-chip Ag/AgCl RE for different pre-concentration times (a) and calibration curves obtained for cadmium and lead (b).

In order to confirm the stability of the current peak potentials, SWASV measurements were carried out overnight in seawater against on-chip Ag/AgCl pseudo-RE. Figure 3.28 shows the measurements over 14 hours without baseline correction (a) and the comparison between the first hour and the last hour measurement after baseline correction (b).
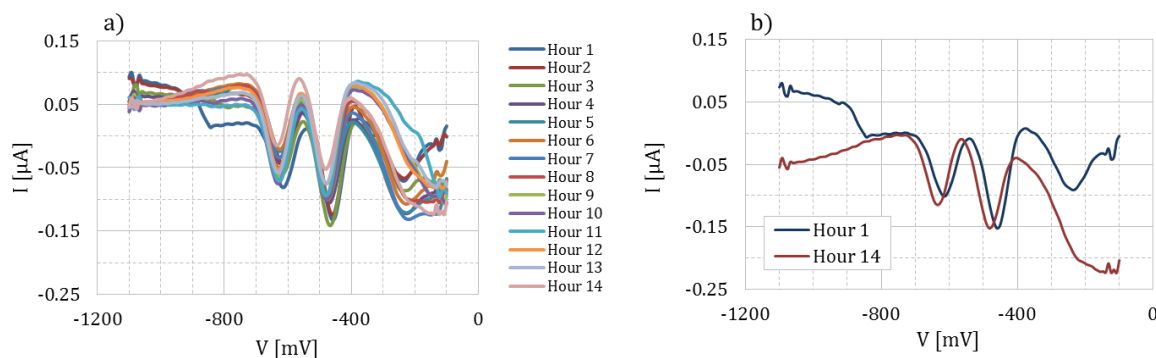
Figure 3.28. SWASV measurements vs. on-chip RE in seawater for 14 consecutive hours (a) and comparison between the first and the last measurement (b).

After 14 hours of consecutive measurements the peak potentials were stable around -620 mV and -470 mV for cadmium and lead, respectively, with a small shift of around 10 mV which is negligible for SWASV application. Figure 3.29 shows the current peaks for cadmium and lead registered during the fourteen hours revealing a spread in the current peak values even if the concentration was kept constant, hence limited repeatability for concentration quantification in seawater.
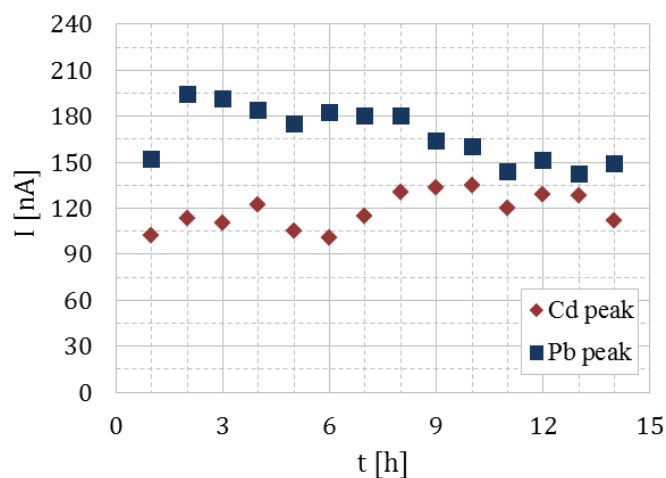
Figure 3.29. Current peaks for cadmium and lead registered during 14 hours.

The fact that the sensors showed current peaks at the same potential proved that the three-electrode on-chip sensors are capable to detect trace metals since to each potential it is possible to associate a specific ion. The investigation on the feasibility to deploy these sensors also for quantification is reported in the following section.

3.7.3 SWASV trace metal calibration with the second generation device

Sensors with 190 microdisc arrays were used for comparison of the three-electrode on-chip sensors with the two-electrode on-chip first generation devices. Measurements of additive quantities of trace metals were carried out against the external RE and the two types of on-chip RE: the Ag/AgCl pseudo-RE and the Ag/AgCl/PVC-IL RE.

Measurements against on-chip Ag/AgCl pseudo-RE

We carried out the SWASV measurements both against the on-chip RE and the external RE by using a design B device with on-chip Ag/AgCl pseudo-RE. After measurements in trace metal free NaNO$_3$, the solution was spiked with increasing concentrations of the three target analytes in a range of 4.96 to 16.96 nM, 4.44 to 16.44 nM and 15.76 to 27.76 nM for Cd(II), Pb(II) and Cu(II), respectively.

Figure 3.30 shows the SWASV voltammograms registered against the on-chip Ag/AgCl RE (a) and the external RE (b). The peak potentials were -275 mV shifted as found before. The increase of the current peaks is more pronounced for the external RE with respect to the on-chip RE.
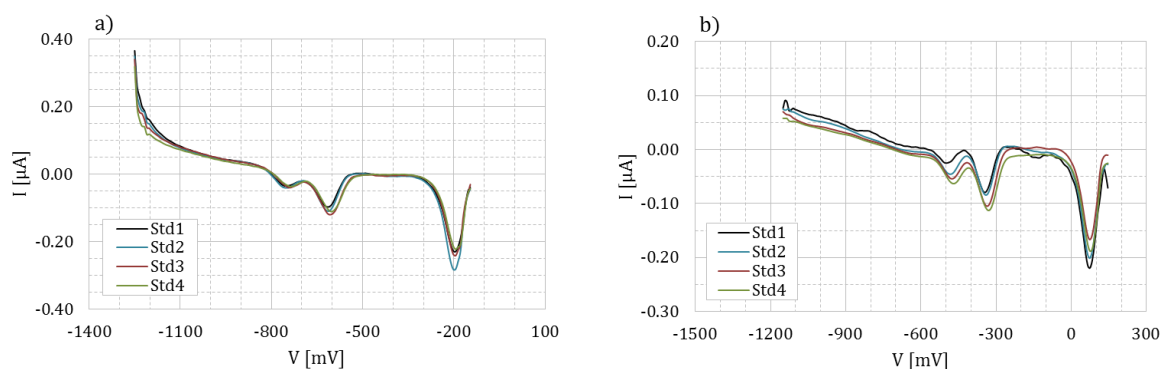
Figure 3.30. SWASV measurements of 4 different standards (Std) registered by using a 190 microdisc array vs. on-chip Ag/AgCl RE (a) and vs. external RE (b).

Figure 3.31 shows the comparison between the calibration curves of Cd(II) (a), Pb(II) (b) and Cu(II) (c) obtained against the on-chip Ag/AgCl RE and the external RE.

The measurements showed that a linear calibration curve could not be obtained either against the on-chip RE nor against the external RE, suggesting that the presence of the Ag/AgCl electrode in the solution was adversely affecting the measurements since a linear calibration curve was obtained for the two-electrode (WE-CE) on-chip sensor vs external RE.

A possible explanation is the presence of Ag/AgCl close to the mercury microdisc array leading to the re-deposition of Ag due to the dissolution of AgCl, or the damage of the Hg layer causing a decrease of the active area of the working electrode. This was confirmed by the fact that after 3-4 reoxidations of the Hg layer, residues could still be observed on the Ir microdiscs using an optical microscope.

A SEM/Energy-dispersive X-ray spectroscopy (EDX) analysis was carried out for investigating this issue in more detail. Unfortunately the removal of the agarose gel also removed the residue visible on the microdiscs, subsequently an EDX analysis of the surface of the Ag/AgCl RE was performed. Figure 3.32 shows a picture of the surface and the related EDX analysis.

The EDX quantification at 10.0 kV provided the following composition: 95.4 wt% Ag, 3.55 wt% Hg, 1.05 wt% Mg, showing the presence of mercury on the RE and of magnesium whose source is unknown. No chloride could be observed. The damage to the RE was confirmed by the measurement of the potential in seawater which dropped to 19.8 mV (vs. 37.1 mV previously measured).

These observations suggest dissolution of the AgCl. The presence of Hg on the RE may be caused by the fact that the sensor was immersed in a mercury acetate solution for Hg deposition prior to use and that mercury chloride solubility product constant (1.45×10^{-18}) is lower than those of silver chloride (1.77×10^{-10}), or could be due to the migration of mercury from the microdiscs during measurements. The presence of the PVC/IL diffusion barrier was expected to help solving this issue or at least slowing down the AgCl dissolution.
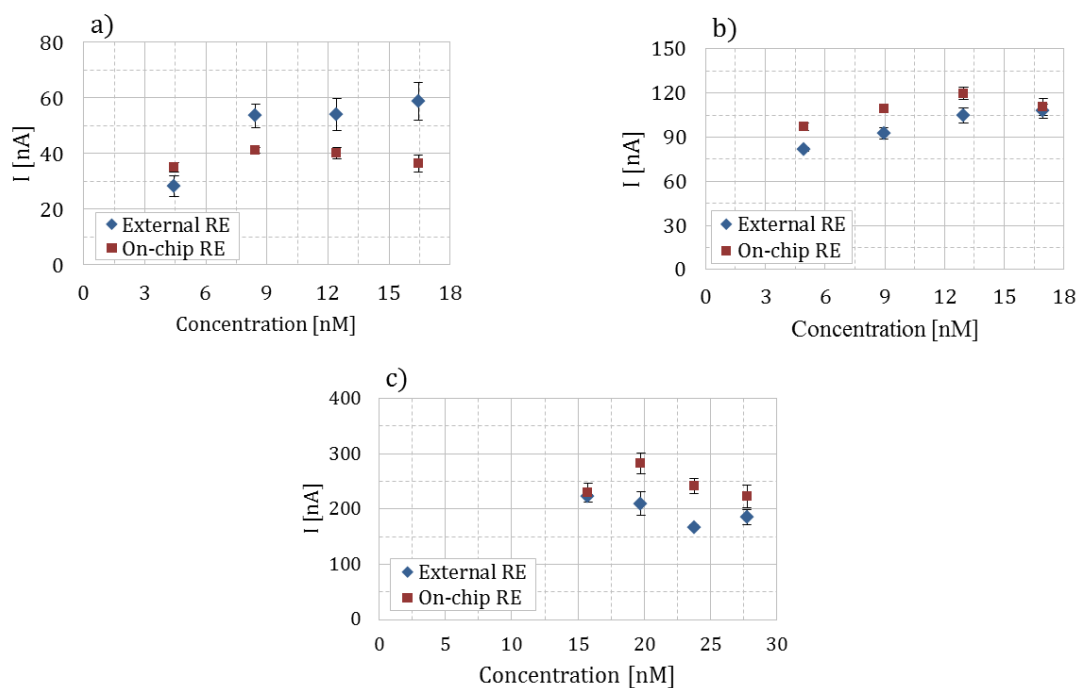
Figure 3.31. SWASV calibration curves obtained for cadmium (a), lead (b) and copper (c) with external RE and on-chip Ag/AgCl RE.
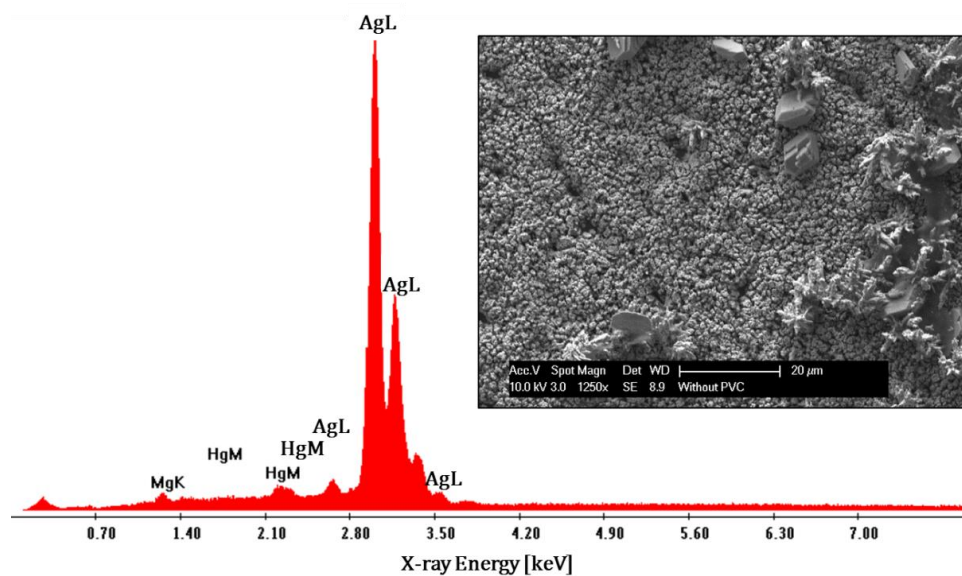
Figure 3.32. SEM/EDX analysis of the on-chip Ag/AgCl RE after SWASV measurements and Hg re-oxidation.

Measurements against on-chip Ag/AgCl/PVC-IL RE

SWASV trace metal calibrations were repeated using the on-chip Ag/AgCl/PVC-IL and the external RE to investigate if the presence of a diffusion barrier like the PVC-IL membrane on top of the AgCl layer could avoid or at least slow down the AgCl dissolution. Figure 3.33 shows the SWASV voltammograms registered against the on-chip Ag/AgCl/PVC-IL RE (a) and the external RE (b). The peak potentials were found around -750 mV, -600 mV and -175 mV for cadmium, lead and copper, respectively, showing that the shift between the measurements vs. the on-chip Ag/AgCl/PVC/IL RE and the external RE is -250 mV (i.e. the presence of the membrane caused a shift smaller of 25 mV with respect to the on-chip Ag/AgCl RE).
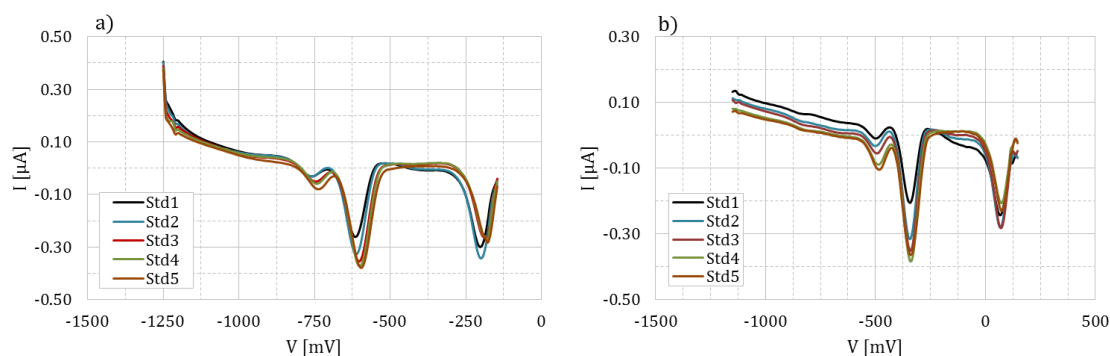
Figure 3.33. SWASV measurements of 5 different standards (Std) obtained by using a 190 microdisc array vs. on-chip Ag/AgCl/PVC-IL RE (a) and vs. external RE (b).

Figure 3.34 shows the comparison between the calibration curves of Cd(II) (a), Pb(II) (b) and Cu(II) (c) obtained against the on-chip Ag/AgCl/PVC-IL RE and the external RE.

As can be seen in Figure 3.34a, a linear calibration curve could be obtained for Cd(II) for both the external and on-chip RE. However, the sensitivity values of the measurements were significantly lower with respect to the measurements carried out with two-electrode on-chip sensors: 1.02 nAnM^{-1}min^{-1} and 0.61 nAnM^{-1}min^{-1} for the external and on-chip RE, respectively. Moreover, no linear calibration curves could be obtained for Pb(II) and Cu(II). These overall results show that PVC-IL improves the performance of the sensor but the contamination of the Hg WE with Ag is still present. Indeed, also in this case after 3-4 reoxidations of the Hg layer, residues on the Ir microdiscs could be observed using an optical microscope. A SEM/EDX of the RE could not be carried out because of the presence of the PVC membrane.

The three electrode on-chip sensors, using either an Ag/AgCl pseudo RE or an Ag/AgCl/PVC-IL RE, are capable of detecting trace metals, however, in both cases a contamination of the Hg WE seems plausible and further improvements are required in order to perform quantification. The devices with on-chip Ag/AgCl/PVC-IL RE provided a linear calibration curve for cadmium, which is a promising result for the development of such sensors for trace metals quantification.
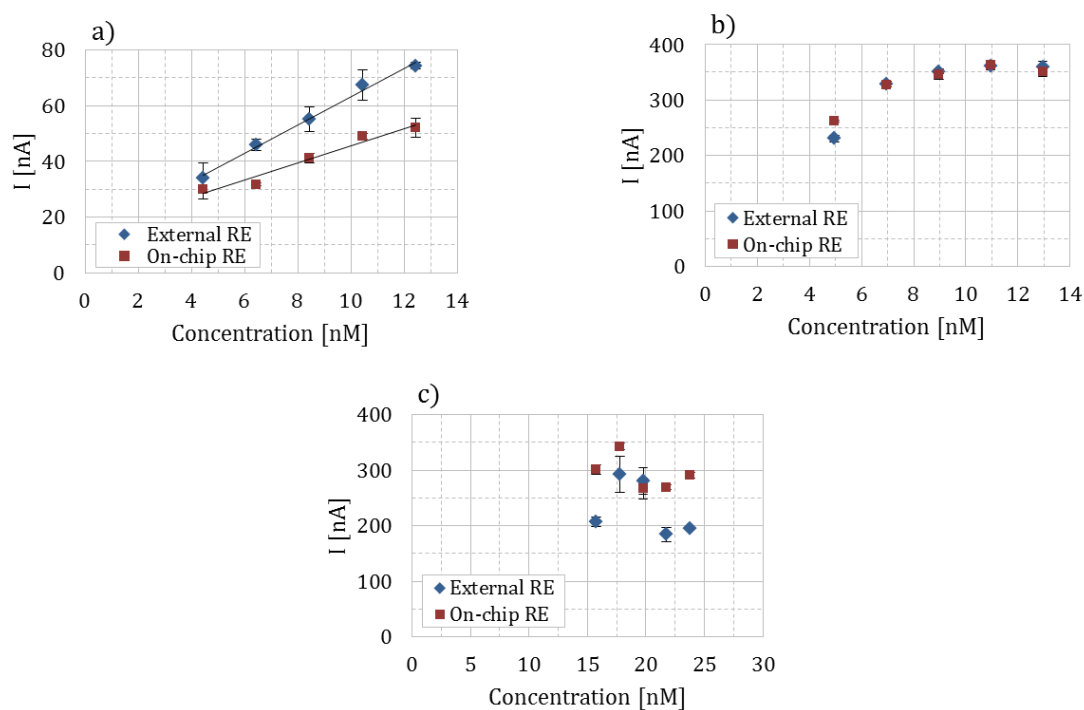
Figure 3.34. SWASV calibration curves obtained for cadmium (a), lead (b) and copper (c) with external RE and on-chip Ag/AgCl/PVC-IL RE.

The overall result of this section is summed up in Table 3.5 and Table 3.6.

Table 3.5. Potential shifts of the three-electrode on-chip sensors with respect to the external reference electrode.

On-chip RE	Electrolyte	Shift for Cd(II), Pb(II) and Cu(II)
Ag/AgCl pseudo-RE	0.1 M NaNO$_3$	-275 mV
Ag/AgCl pseudo-RE	Seawater	-50 mV
Ag/AgCl/PVC-IL RE	0.1 M NaNO$_3$	-250 mV

Table 3.6. Comparison of the sensitivity values (in nA·nM^{-1}min^{-1}) of the different sensors developed in this thesis with previously reported ones.

Species	Previously reported (119) sensors (100 discs)	Two-electrodes on-chip(190 discs)	Three-electrodes (vs. on-chip Ag/AgCl pseudo-RE)	Three-electrodes (vs. on-chip Ag/AgCl/PVC-IL RE)	Three-electrodes (vs. external RE)
Cd(II)	0.59	**1.29**	Non linear	**0.61**	**1.02**
Pb(II)	1.28	**2.73**	Non linear	Non linear	Non linear
Cu(II)	0.57	**1.23**	Non linear	Non linear	Non linear

3.7.4   SWASV measurements of As(III)

Sensors with 190 microdisc arrays were used for investigating the possibility to detect As(III) in a 0.1 M NaNO$_3$ solution after plating the Ir microdiscs with AuNPs.

Gold nanoparticles deposition

A 5 mM gold chloride (AuCl$_3$) solution in 10^{-2} M perchloric acid (HClO$_4$) and deionized water was used for gold nanoparticles (AuNPs) deposition. A potential of -0.35 V vs an Ag/AgCl/3M KCl RE was applied for 3 minutes which allowed covering most of the Ir microdiscs with AuNPs. Figure 3.35 shows an example of the deposition current of AuNPs.
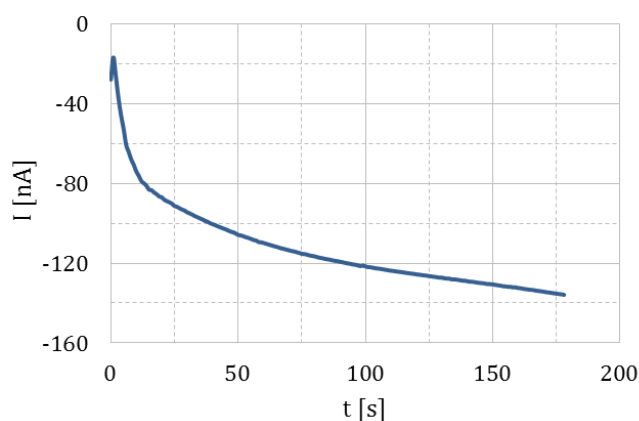
Figure 3.35. Current profile registered during the deposition of AuNPs on the Ir microdiscs.

After deposition, a stabilization step was performed for the AuNPs layer at +0.7 V for 300 s in nitric acid. After measurements, AuNPs were removed in KSCN by sweeping the potential from -0.3 V to +0.8 V (step: 0.04 V, scan rate: 0.05 V/s).

Measurements of As(III) with two-electrode on-chip sensor

A sensor with 190 discs WE and CE was deployed. Figure 3.36 shows an example of two SWASV measurements of 50 nM As(III) in 0.1 M NaNO$_3$ for different pre-concentration times: 60 s (blue line) and 180 s (red line). The peak potential of As(III) against an external RE was found to be at +50 mV. An increase of the current peak was registered accordingly to the increase of the pre-concentration time.
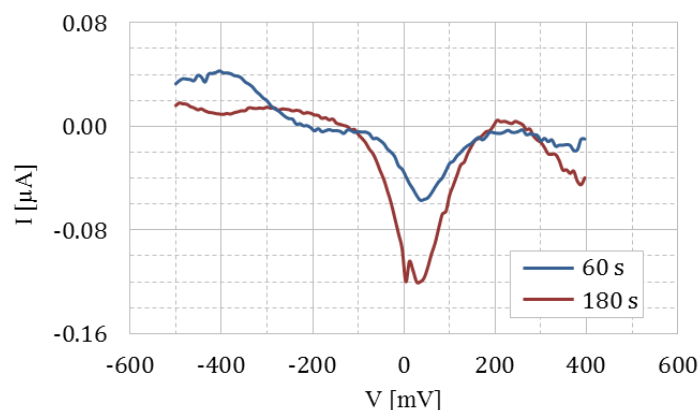
Figure 3.36. SWASV measurements of 50 nM As(III) in 0.1 M NaNO₃ for different pre-concentration times: 60 s (blue line) and 180 s (red line).

Measurements of As(III) against on-chip Ag/AgCl pseudo-RE

The shift of the SWASV peak potentials of the on-chip Ag/AgCl pseudo-REs with respect to the external RE was evaluated also by testing the device for arsenite (As(III)) detection. A single Au microelectrode was used to test and compare its performance with respect to a standard RE. Figure 3.37 shows the SWASV measurements of 30 nM As(III) carried out in 0.1 M NaNO₃ against an external RE and the on-chip Ag/AgCl RE with a pre-concentration time of 180 s. The shift of -275 mV observed in the case of lead, cadmium and copper detection, was confirmed also in this case.
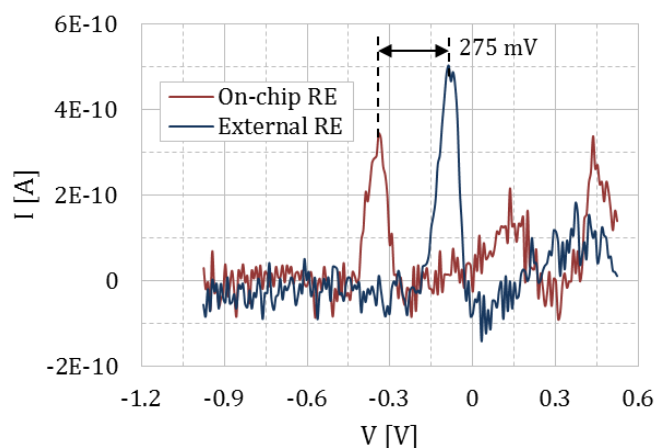
Figure 3.37. SWASV measurement of 30 nM As(III) in 0.1 M NaNO₃ obtained by using a single Au microelectrode against on-chip Ag/AgCl RE and external RE.

The same SWASV measurements were carried out by using 190 microdisc arrays against the on-chip Ag/AgCl REs and external RE but they were not reproducible. A possible explanation could be related to the gold deposition which did not give a homogeneous coverage of the Ir microdiscs. Moreover the presence of the Ag/AgCl electrode could influence the quality of the AuNPs layer

during deposition. A different recipe for gold deposition was therefore tested, more specifically gold black deposition, as explained in the section below.

Gold-black deposition

Gold black (Au-black) deposition was explored in order to develop an uniform, homogeneous and large surface area layer of AuNPs on the Ir microdiscs. Sensors with on-chip WE and CE were used. Biosensors based on metal-black such as Pt-black and Au-black have large surface area compared to that of basal electrodes, therefore the metal-black-based sensors are highly sensitive. The advantage of the Au-black is that any part of metal-black is stably and electrically connected with the basal electrode because of its fabrication process [166].

The Au-black deposition solution was prepared by adding 1.02 g of potassium tetrachloroaurate(III) (KAuCl$_4$) and 9.6 mg of lead(II) acetate (Pb(C$_2$H$_3$O$_2$)$_2$) to 33 ml of 25 mM HCl. Cyclic voltammetry was firstly carried out to find the potential regions suitable for deposition. Figure 3.38 shows the cyclic voltammogram obtained by sweeping the potential between +0.2 V and +1.0 V vs Ag/AgCl/3MKCl RE: the deposition regions were found to be at +0.2 V and at +.055 V. Therefore deposition was tested at these two potentials for 20 s.

The Ir microdiscs were nicely covered in both cases but the morphology of the gold layer was different as it was pointed out through the SEM analysis. Figure 3.39 shows the SEM pictures of the Au-black deposited on the Ir microdiscs at +0.2 V (column a) and +0.55 V (column b).
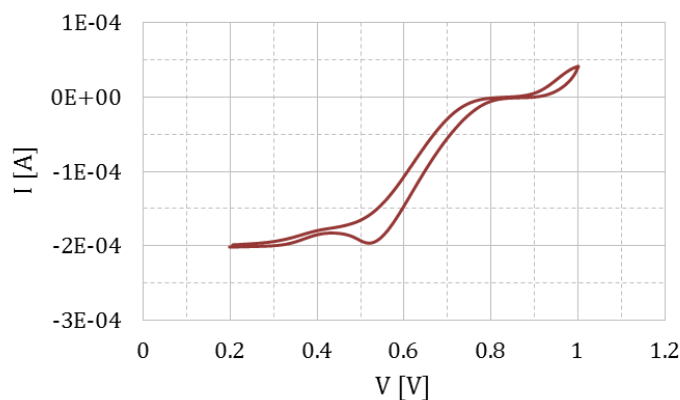
Figure 3.38. Cyclic voltammogram of the Ir microdiscs registered in the Au-black deposition solution with a scan rate of 25 mV/s vs RE.

The Au layer deposited at +0.55 V has a rounded shape similar to the shape obtained for Hg deposition, while at +0.2 V a dendritic growth was observed starting from the center of the microdiscs and extending laterally in all directions. Both deposition potentials could be used for providing an AuNPs layer on the Ir microdiscs, however the potential +0.2 V reveals to be more promising in case a larger surface area should be covered. This was observed when deposition was carried out on the Ir CE and it was found out that at +0.55 V the surface was not homogeneously covered even after UV ozone treatment and after increasing the deposition time. At +0.22 V it was not possible to cover all the area but a better coverage was achieved as shown in Figure 3.40.

a)   b)
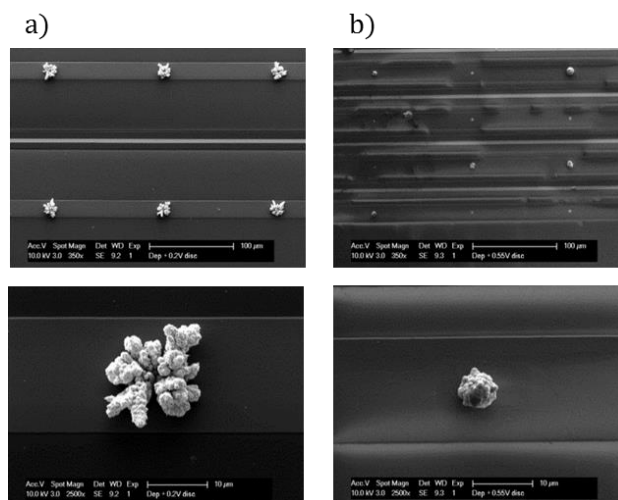
Figure 3.39. SEM pictures of the Au-black deposited on the Ir mcirodiscs at +0.2 V (column a) and +0.55 V (column b).

a)   b)

Figure 3.40. SEM pictures of the Au-black deposited on the Ir CE at +0.2 V (column a) and +0.55 V (column b).

The elemental composition of the deposited layers was also investigated in order to check if they were made of pure gold or if some contamination coming from other metals was revealed due to the presence of lead in the bath. Figure 3.41 shows the SEM/EDX analysis of the Au layer: for both cases the presence of other metals was excluded.
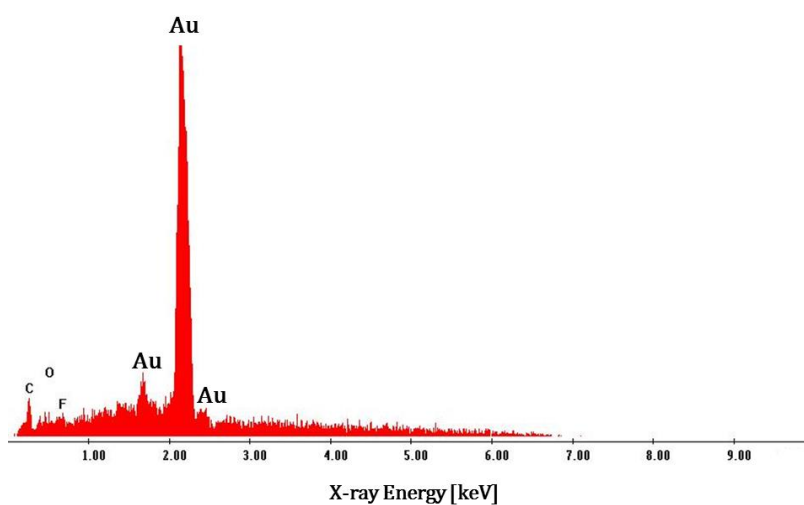
Figure 3.41. SEM/EDX analysis of the Au-black layer deposited on the Ir microdiscs.

We investigated the possibility to deposit Au-black before the deposition of Ag for the three-electrode on-chip devices. The result is the complete loss of Au-black NPs from the discs during Ag deposition, therefore Ag has to be deposited before Au-black.

The Au-black layer can be tested in further investigations for detection of arsenic replacing the AuNPs layer previously deployed.

Conclusions

In this chapter new two-electrode (WE, CE) and three-electrode (WE, CE, RE) on-chip sensors for voltammetric detection of trace metals in seawater were presented. The devices were fabricated by three photolithographic steps for definition of the electrodes geometry and a containment ring for antifouling agarose gel membrane. The fabrication of the three-electrode on-chip sensor was completed by Ag electrodeposition and chloridation, and deposition of a PVC-IL membrane for solid state RE integration.

The Ir electrodes were electrochemically tested by CV and showed excellent fabrication quality as well as similar electrochemical behavior to that reported in literature. The on-chip Ag/AgCl RE potential vs. a standard Ag/AgCl/3 M KCl RE in seawater was 37.12 ± 1.4 mV and stable over 2 months. SWASV measurements of trace metals (Cd, Pb, Cu) carried out in 0.1 M $NaNO_3$ with the two-electrode on-chip sensors showed that the current peaks increased linearly with the concentration, and sensitivity values of 2.73 $nAnM^{-1}$ min^{-1}, 1.23 $nAnM^{-1}$ min^{-1}, and 1.29 $nAnM^{-1}min^{-1}$ were registered for Pb(II), Cu(II), and Cd(II), respectively. SWASV measurements of trace metals (Cd, Pb, Cu) carried out in 0.1 M $NaNO_3$ and seawater with the three-electrode on-chip sensors showed a shift between on-chip Ag/AgCl and external RE of -275 mV and -50 mV, respectively, for each metal current peak. This shift was constant over the whole series of measurements performed and was confirmed also in the case of As(III) detection. The presence of a PVC-IL membrane on the top of the on-chip RE resulted in a potential shift of around -250 mV of the peak potentials. These sensors allow qualitative detection of trace metals but need further improvement for concentration quantification. A possible cause of this is the loss of AgCl by dissolution and its subsequent contamination of the Hg working electrodes.

The use of a PVC-IL diffusion barrier resulted in a slight improvement, providing a linear calibration curve for cadmium with a sensitivity of 0.61 $nAnM^{-1}min^{-1}$, lower with respect to the value found for the two-electrode on-chip sensor (1.29 $nAnM^{-1}min^{-1}$). This performance should be enhanced for the development of devices capable not only to detect but also to quantify the trace metal levels in natural waters, and the key for this relies on the improvement of the adhesion and performance of the PVC-IL membrane used as diffusion barrier.

Chapter 4 Technology for the development of microfluidics tools

One of the objectives of this thesis was the development of microfluidic platforms for supporting the partners of the SCHeMA project in achieving the pre-concentration of biotoxins (UNIGE-Pau) and the detection of volatile organic compounds (UULM). In this chapter the microfluidic platforms developed for these purposes are presented.

The platform for biotoxin pre-concentration was designed and predisposed for the detection of saxitoxin, one of the most harmful biotoxins, based upon an aptamer-based approach for toxin binding and pre-concentration and a temperature-based mechanism for release prior to transfer to the detection unit. The device was successfully fabricated but was not tested yet by the partners at UNIGE-Pau.

The platform for VOCs detection was designed based upon the theoretical guidelines found in literature for optimizing the performance of infrared evanescent field chemical sensors. The device was fabricated by deploying additive manufacturing techniques, such as 3D printing, and was successfully installed in the optical experimental setup developed by the partners at UULM.

4.1 Microfluidic platform for saxitoxin pre-concentration

This section presents the design, the fabrication and the preliminary characterization of an aptamer-based microfluidic platform for the pre-concentration of saxitoxin (STX). Two generations of the device are proposed: the first one consists of a channel patterned in PDMS sealed to a glass substrate, and the second one consists of the same channel sealed to a glass substrate with patterned SU-8 pillars. Different techniques to bond the two components of the system were investigated and the fabrication of both generations was successfully achieved.

Hydraulic resistance of the microfluidic channel was experimentally measured and was in good agreement with the theoretically calculated value. Functionalization of the channel surface with aptamers can be achieved by introducing amine groups and aldehyde groups on the surface of the substrate, and STX pre-concentration can be performed by binding saxitoxin to the aptamer-functionalized surface.

The integration of a transparent flexible heater was investigated in order to study the possibility to achieve the release of the STX by increasing temperature up to around 60 °C.

4.1.1 Introduction

Marine biotoxins are compounds with toxic activity that accumulate in fish or shellfish and can cause human illnesses when the fish or shellfish enter the food chain. They are usually produced by phytoplankton and reach shellfish or fish through the trophic chain.

Among the various species of biotoxins, the specific target of this work is saxitoxin (STX). STX is a low molecular weight neurotoxin mainly produced by marine dinoflagellates and is responsible for paralytic shellfish poisoning (PSP), the most worldwide spread algal-derived shellfish poisoning [167]. PSP can indeed be fatal in extreme cases, particularly in immunocompromised individuals, and has been implicated as a possible cause of sea otter and whales mortality.

In the past the main method to determine PSP toxicity was the classical mouse bioassay which is inexpensive but characterized by low sensitivity, poor precision and inability to distinguish among different toxin species. Other detection methods comprise high performance liquid chromatography with fluorescence detection (HPLC-FLD) [168] and chemosensors based on photoinduced electron transfer (PET) principle which can sense toxins by means of synthetic fluorophores. The detection limit of the mouse bioassay used for PSP toxin determination is approximately 1 μM of STX, and the detection limit of the chemosensor assay, for instance based on boron azadipyrrin crown ethers, is slightly better than this [169].

Detection of STX in marine environment is extremely difficult owing to its low concentration. Therefore emphasis has been placed on developing screening assays relying on incorporating analyte recognition elements such as bio-recognition molecules, i.e. antibodies. In 2008 Meagher R. J. et al. [170] developed a microfluidic chip in which the detection of biological toxins was performed using microfluidic electrophoretic immunoassays integrated with sample pre-concentration and mixing of analytes with fluorescently labeled antibodies. Pre-concentration was

enabled by photopolymerizing a thin nanoporous membrane in the sample loading region of the chip.

Antibodies present some limiting factors such as limited availability, high cost, and use of animals for their production. Recently the research efforts shifted towards the development of new analytical recognition elements able to bind to the target with high affinity and specificity, i.e. aptamers. Aptamers are nucleic acids or peptides which bind to a specific target molecule; they are selected through Systematic Evolution of Ligands by Exponential enrichment (SELEX) and display several advantages over antibodies: stability in time, lower cost, ease of production, independency on animal usage. Additional advantages are that binding affinities of aptamers are in the mM to nM range, and that aptamers are simple to modify thus allowing easy introduction of reactive groups. The only disadvantages are that they are susceptible to enzymatic degradation by nucleases, thus requiring highly pure environments, and that long sequences are difficult to achieve [171]. In 2012 a DNA aptamer that targets STX with high affinity and specificity has been developed by Handy et al. [172] by using a saxitoxin–protein conjugate. The aptamer sequence is the following: 5'-GGT ATT GAG GGT CGC ATC CCG TGG AAA CAT GTT CAT TGG GCG CAC TCC GCT TTC TGT AGA TGG CTC TAA CTC TCC TCT-3'.

The main goal of this work is to develop a microfluidic platform in which STX can be pre-concentrated by STX binding to an aptamer-functionalized surface (glass or glass/SU-8), and then released for allowing transfer to the optochemical detection unit developed by the partners at TUGRAZ.

Two different microfluidic devices (first generation and second generation) have been designed and fabricated. The first generation of the microfluidic platform consists of a channel patterned in PDMS sealed onto a glass substrate. In this device aptamers should be immobilized directly on the glass side of the channel. The second generation platform has the same channel patterned in PDMS, but this time the channel is sealed to a glass substrate on the top of which SU-8 pillars are patterned in the channel-path. SU-8 is an epoxy-based negative photoresist commonly used for patterning structures of high aspect ratio and for a range of applications such as microfluidics, bio-MEMS, microlenses, etc. In the microfluidic platform SU-8 pillars are introduced in order to increase the total surface area available for aptamers immobilization.

SU-8 is a material which allows immobilization of for instance enzymes such as glucose oxidase [173,174]. Immobilization can be achieved by binding amine groups of the enzyme to epoxy groups of the SU-8 that remain available after the cross-linking of the material. The possibility to immobilize DNA on SU-8 structures by a covalent bond has been reported in literature [175]. Examples of SU-8 pillars are shown in Figure 4.1.
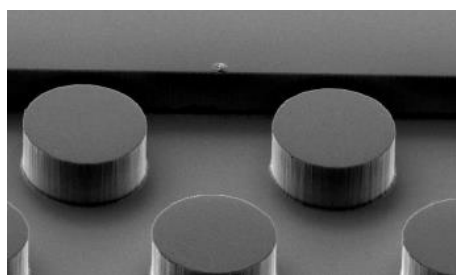
Figure 4.1. SEM picture of SU-8 pillars patterned on a glass substrate [173].

The following sections describe the design and the fabrication process flow of the microfluidic platform for STX pre-concentration, as well as the characterization of the developed devices in terms of hydraulic resistance.

4.1.2 Design of the microfluidic platform

For the design of the device two requirements have been taken into account: a minimum volume of 80 µl for the seawater sample for allowing downstream detection, and dimensions fitting the submersible probe, which has an outer diameter of 100 mm and an inner diameter of 68 mm. The device has therefore been designed with dimensions of 57 mm x 19 mm x 4 mm. In order to obtain a volume of at least 80 µl, the channel was designed with a "serpentine" shape, which is more space efficient with respect to a straight channel. The channel has the following geometrical dimensions: total length L of ~24.5 mm, width w of 1 mm and height h of 500 µm.

An important parameter for designing the microfluidic channel is the hydraulic resistance R_{hyd} due to the viscous dissipation of mechanical energy into heat by internal friction of the fluid. In a straight channel, a constant pressure drop Δp results in a constant flow rate Q in case of pressure-driven steady-state flow of an incompressible Newtonian fluid. This result can be summarized in the Hagen-Poiseuille law:

$$\Delta p = R_{hyd}Q \qquad \text{Equation 4.1}$$

The optimal geometrical configuration for a microfluidic channel in order to minimize the hydraulic resistance is a circular shape for its cross section. However fabricating such a cross section is more challenging and time consuming than fabricating a rectangular shaped channel. In this case simple fabrication processes can be used in order to fabricate the channel and it is possible to minimize the hydraulic resistance by designing the width and the height of the channel with an aspect ratio of 2:1 [176]. For a rectangular shaped straight channel, hydraulic resistance has the following expression:

$$R_{hyd} = \frac{12\eta L}{1 - 0.63(h/w)}\frac{1}{h^3 w} \qquad \text{Equation 4.2}$$

where η is the viscosity of the fluid. By inserting the geometrical parameters of the channel designed for the microfluidic platform into Equation 4.2 together with the value of η for seawater ($0.00108\ Pa \cdot s$), a value of around $3.71 \cdot 10^{10}\ \frac{Pa \cdot s}{m^3}$ is found for the hydraulic resistance. However the channel is not a straight channel, and this value has to be experimentally validated. A way to measure the hydraulic resistance is to apply a constant pressure drop between inlet and outlet of the device and measure the flow rate, as it will be explained more in detail in section 4.1.6.

The 3D drawings of the two generations of the device drawn with *SolidWorks 2014* software are shown in Figure 4.2.

For the second generation device, the diameter and number of the SU-8 pillars was fixed respectively to 240 µm and 445 (89 for each of the 5 straight parts of the channel). An increase in surface area available for aptamers binding (ΔS) can be achieved by changing the height of the pillars: for instance 6.0% for 50 µm high pillars, 19.6% for 150 µm high pillars. In order to study the possibility to immobilize aptamers onto SU-8 surface, the height of pillars was initially fixed to

50 µm for the development of the first devices. After proving the concept of immobilization of aptamers on SU-8, it could be possible to study the dependence of the amount of the immobilized aptamers upon the surface area available for binding. Figure 4.3 shows the top view scheme of the pillars patterned on the glass substrate (a) and the geometrical dimensions of the pillars and their inter-distance (b).
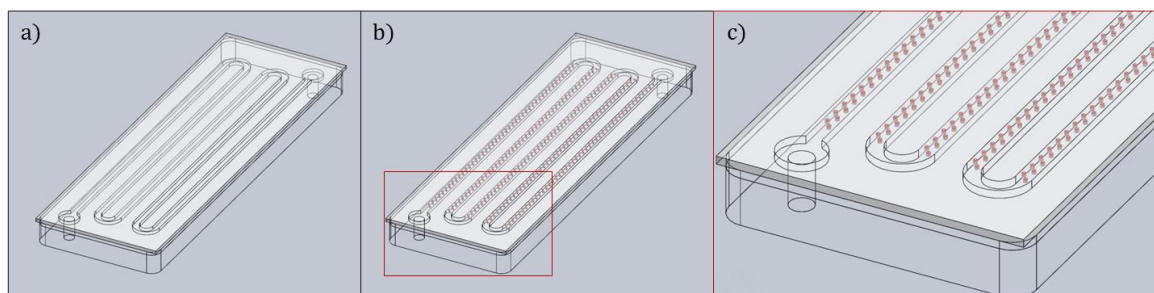
Figure 4.2. SolidWorks 3D drawings of the two generations of the microfluidic platform: device without SU-8 pillars in the channel (a), device with SU-8 pillars in the channel (b) and zoom of the channel with SU-8 pillars (c).
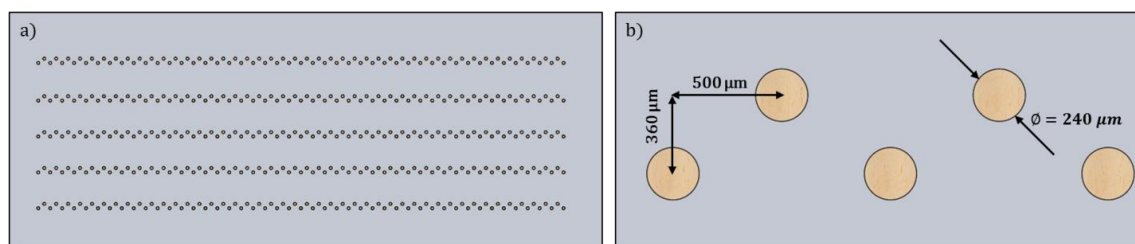
Figure 4.3. Top view scheme of the SU-8 pillars (a) and geometrical parameters of the pillars (b).

4.1.3   Fabrication of the microfluidic platform

The devices were fabricated by using soft lithography techniques in the grey and clean room of Microcity, Neuchâtel. The fabrication process flow slightly differs for the two generations of the device.

First generation platform

The steps of the fabrication process flow are shown in Figure 4.4, and are listed below:

1. Fabrication of a poly(methyl methacrylate) (PMMA) mold for PDMS microchannel patterning through CNC (Computer Numerical Control) machining (Figure 4.4a-b).
2. Mixing of PDMS base and hardener (Sylgard 184, Dow Corning, 10:1 weight ratio), degassing in vacuum chamber and casting in the mold. Curing in an oven at 65 °C for 2 hours (Figure 4.4c).
3. De-molding of the PDMS channel using a scalpel and opening of the inlet and outlet holes of the channel with a bio-puncher (Figure 4.4d).

4. Cleaning of a 500 µm thick glass substrate by rinsing with acetone, iso-propanol (IPA) and de-ionized (DI) water, and drying with nitrogen stream.

5. Oxygen plasma treatment (50 W, 45 s), or ultraviolet ozone (UV O_3) treatment for 15 minutes, of the glass substrate and PDMS and bonding of the two pieces after alignment (Figure 4.4e).
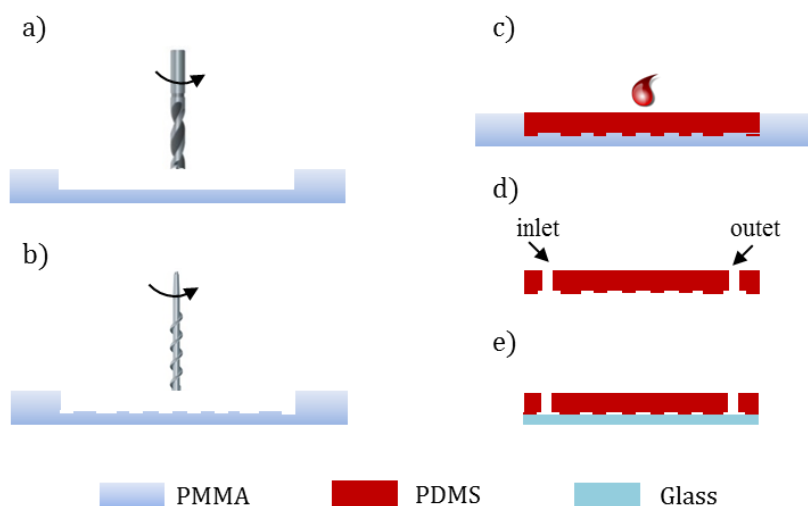
Figure 4.4. Fabrication steps of the microfluidic platform: a) drilling of the first 3 mm PMMA layer, b) drilling of the negative pattern of the microfluidic channel (0.5 mm), c) PDMS casting, d) PDMS de-molding and opening holes for inlet and outlet of the microchannel, e) bonding of the patterned PDMS to the glass substrate.

PDMS patterning of step 1-2 is standardly achieved by using an SU-8 mold patterned on a silicon wafer, but this kind of process is time consuming and requires clean room facilities. By using CNC machining it is possible to produce several PMMA molds in one machining run which requires almost 10 minutes for each mold. Different machining parameters (tool speed in X, Y and Z direction, bit diameter, bit spin speed, etc.) were modified in order to find the best conditions for obtaining a smooth PMMA surface: the smoother the surface, the easier is the bonding of the PDMS to the glass substrate. Figure 4.5 shows the pictures of the PMMA mold fabricated by CNC machining (a) and of the final device obtained after bonding of the PDMS to the glass substrate (b).
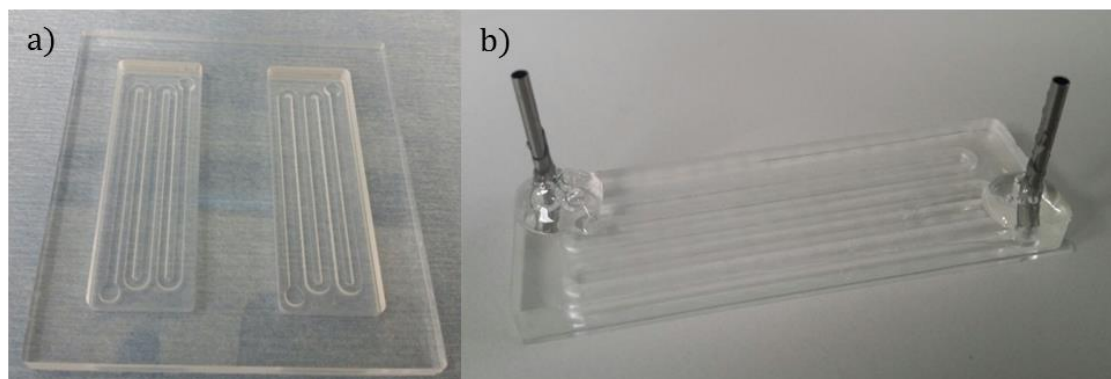
Figure 4.5. Pictures of the PMMA mold for PDMS patterning fabricated by CNC machining (a) and of the microfabricated device after PDMS-glass bonding (b).

The bonding obtained through oxygen plasma treatment was irreversible, while the bonding obtained through UV O_3 treatment was irreversible in the central part but poor at the corners of the PDMS piece.

Second generation platform

The second generation is a microfluidic platform made of a PDMS channel and a glass substrate on which SU-8 pillars are patterned in correspondence to the channel path. In this device the aptamers can be immobilized on the glass and/or the SU-8 pillars patterned on glass depending on the solvent used for the surface chemistry modification as explained in the following section.

SU-8 GM 1075 was the photoresist used in order to reach a thickness of 50 µm. The fabrication of the PMMA mold and the PDMS channel was achieved through the first three steps listed for the process flow of the first generation device. The fabrication steps concerning the glass substrate fabrication are summarized as follows:

1. Glass wafer piranha cleaning in 96% sulfuric acid (H_2SO_4) and hydrogen peroxyde (H_2O_2) bath at 100°C for 10 minutes and rinsing in DI water.
2. Oxygen plasma treatment to enhance adhesion of the resist to the glass.
3. SU-8 photolithography step.
4. Dicing of the wafer into 4 different glass slides (1.9 x 5.7 mm).

The photolithography step (3.) consisted in the following steps: SU-8 spin coating (average speed: 3500 rpm), relaxation time to obtain a homogeneous layer (~30 minutes), soft bake (105 minutes, ramp with maximum temperature of 130 °C), exposure (347 mJ/cm^2), post exposure bake (200 minutes, maximum temperature: 85 °C), relaxation overnight, development in propylene glycol monomethyl ether acetate (PGMEA) (6 minutes), rinsing with isopropanol and drying with nitrogen. Figure 4.6 shows a picture of a portion of an SU-8 pillars line (a) and of a single pillar after the photolithography step with the measurement of its diameter (b).

Figure 4.6. Picture of a portion of an SU-8 pillars line (a) and picture of a single pillar with the measurement of its diameter (b).

Surprisingly, the standard procedure used for irreversible bonding of PDMS to glass, i.e. oxygen plasma treatment (50 W, 45 s), did not work. Additional tests revealed a possible contamination of the glass substrate with photolithography step residues. For this reason different bonding procedures including steps such as UV O_3 cleaning, vapor- and liquid-phase silanization, heating and their combination were tested. They are listed in Table 4.1.

Table 4.1. Combinations of different bonding procedures and their result.

Procedure	Result
O_2 plasma (50 W, 107 s)	Bonding failed
UV O_3 treatment (15') + heating (70°C, 20 min)	Bonding failed
UV O_3 treatment (30') + heating (70°C, 20 min)	Bonding failed
O_2 plasma (50 W, 214 s) + heating (70°C, 20 min)	Bonding failed
Glass: 2 hours vapor-phase silanization (tetramethoxysilane). PDMS: O_2 plasma(50 W, 214 s)	Bonding failed
Glass: overnight vapor-phase silanization ((3-aminopropyl)triethoxysilane (APTES)). PDMS: O_2 plasma (50 W, 214 s)	Poor bonding
Glass: 40 min liquid-phase silanization (10% APTES in ethanol). PDMS: O_2 plasma (50 W, 55 s). Heating (70°C, 30 min).	Bonding failed
Glass: UV O_3 treatment (30') + overnight vapor-phase silanization (APTES). PDMS: O_2 plasma (50 W, 55 s). Heating (75°C, 25 min)	Irreversible bonding except at one corner

The majority of these procedures lead to poor bonding or to a failure. However the APTES vapor-phase silanization treatment combined with a previous cleaning step in UV ozone allowed an irreversible bonding on the overall surface except for one corner of the device. In addition to this, two other approaches were investigated: bonding using a pressure sensitive adhesive (PSA) sheet and bonding after exposing the glass substrate to hydrofluoric acid (HF).

ARclear® 8932EE (PSA sheet made of a 40 µm double side adhesive layer) was cut by CO₂ laser and a negative pattern of the microfluidic channel was obtained. Afterwards one liner was removed and the adhesive side was aligned and attached to the PDMS channel. The 3 layer stack (PDMS, adhesive, liner) was placed in the freezer for about 30 minutes with weight on top to avoid deformation of the adhesive on the PDMS. This step allowed an easier removal of the second liner before alignment and bonding to the glass slide with patterned SU-8 pillars. Irreversible bonding was achieved.

In order to test the hypothesis that the glass surface is contaminated with some substance not removed by oxygen plasma treatment, an HF etching step was investigated. Two pieces of the glass wafer on which SU-8 was coated and then developed were tested. The two pieces were immersed in HF for respectively 5 and 30 seconds and then rinsed with DI water. Afterwards the two glass pieces and two PDMS pieces underwent O_2 plasma treatment (50 W, 45 s) and irreversible bonding was achieved without any heating step between glass and PDMS thus showing that an HF dipping was sufficient to remove the contamination.

In conclusion three bonding procedures allowed an irreversible bonding between SU-8 treated glass and PDMS: UV ozone-APTES silanization-oxygen plasma treatments combination, PSA and HF etch-oxygen plasma combination. Device fabrication can be completed by applying any of them, however in this thesis only the PSA approach was used and evaluated in terms of resistance to water flow and maximum bearable pressure.

4.1.4 Aptamer-Saxitoxin binding in the microfluidic platform: proposed strategy

The immobilization of aptamers can be achieved by applying the surface chemistry modification procedure reported in literature to enable immobilization of oligonucleotide brushes [177]. It consists of the following steps:

1. APTES liquid silanization of the substrate: 1% (v/v) solution of APTES in water-free toluene for 2 h at room temperature to introduce amino groups (-NH_2) on the surface, and rinsing with toluene.

2. Immobilization of aldehyde groups (-CHO) onto the surface: 1% (v/v) aqueous solution of glutaraldehyde for 1 h, and rinsing in water.

3. Aptamer immobilization on the surface: injection of the oligonucleotides sequence [172] into the platform.

This procedure can be used to immobilize aptamers in the first generation device, i.e. on the glass side of the channel. For the second generation device in which SU-8 pillars are patterned in the channel, another solvent for the APTES liquid silanization should be used since toluene could destroy the patterned SU-8 layer. Ethanol could be a candidate for this purpose.

After the aptamers immobilization, the solution containing STX or a toxin model (e.g. protein model) can be pumped into the channel and STX model-aptamers binding properties can be studied by fluorescence microscopy.

4.1.5 Release of saxitoxin approach upon temperature change: heater integration

After pre-concentration, saxitoxin has to be released and transferred with a carrier electrolyte to the detection unit. The release of the STX could be potentially performed upon a temperature- or pH-control. The release upon change in pH would require a reservoir with a basic or acid solution and would pose issues related to the compatibility with the detection unit materials. Therefore a temperature-control approach is preferred.

Zhu J. et al. [178] have reported the possibility to release cells captured on a surface-patterned aptamers microchamber by temperature mediation: the cells release was achieved by increasing the temperature from room temperature to around 48 °C in ~10 s without detectable damage of the cells.

To test the possibility to release STX by a temperature increase, a heater needs to be integrated onto the glass substrate. The integration of a heater could be obtained by patterning it by photolithography on the back side of the glass substrate or by using an external heating element to be attached to the back side of the glass. Flexible heaters are indeed available on the market. The Thermal-Clear™ Transparent Heater H6985 shown in Figure 4.7 was purchased from Minco (Minneapolis). It is a micro-thin wire heating element laid in a pattern between optical grade polyester sheets.
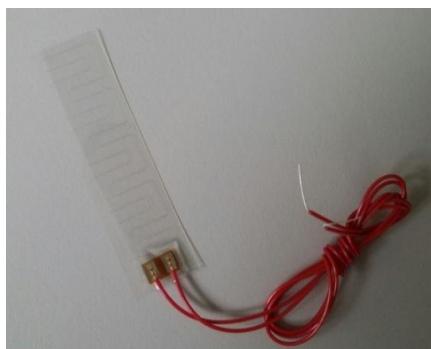
Figure 4.7. Thermal-Clear™ Transparent Heaters H6985 purchased from Minco (Minneapolis).

The total amount of the power required for an application is given by the sum of the warm-up power (watts required to bring an object to a certain temperature in a given time) and the heat loss (heat lost during the warm-up). The warm-up power is given by the formula:

$$P = \frac{m c_p (T_f - T_i)}{t} \qquad \text{Equation 4.3}$$

where m: mass of the object (expressed in g), c_p: specific heat of the material (expressed in $J/g/°C$), T_f: final temperature of the object ($°C$), T_i: initial temperature of the object ($°C$), t: warm-up time (s). The heat loss can be assumed to be 20% of the warm-up power. The heater has to withstand the power density required to reach the desired temperature.

The object to warm up is the glass substrate ($c_p = 0.75 \ J/g/°C$, mass density $\rho = 2.64 \ g/cm^3$) and has the following dimensions: 57 mm x 19 mm x 0.5 mm. Concerning T_i, this temperature should represent the average temperature in the ocean. The temperature of the ocean surface waters varies mainly with latitude and the average temperature is of about 17 °C (National Earth Science Teachers Association data). Concerning the choice of T_f, this value is given by the temperature needed to achieve the release of STX from aptamers. The parameters reported by Zhu J. et al. [178] to release aptamer-captured cells by temperature mediation are a temperature of 48 °C and a time period of around 10 s to reach it. Therefore values of 10 s and 60°C (more than 48 °C in order to ensure the possibility to go higher in temperature if needed in case of saxitoxin release) were respectively chosen for time t and temperature T_f. By inserting all these values in Equation 4.3, a warm-up power value of 4.6 W is obtained and the total power required is 5.5 W (20% heat loss added). The furnisher provides graphs showing the relationship between power density bearable and the temperature. Figure 4.8 shows the graph of the H6985 heater on which the red line represents the temperature required for this application, 60 °C, and the blue line the bearable power density.

For a temperature of 60°C, the maximum power withstood by a Thermal-Clear heater mounted with acrylic PSA is ~0.8 W/cm². Since the power required for saxitoxin release is 5.5 W and the dimensions of the H6985 heater are 55.9 mm x 14.7 mm, the power density required is 0.67 W/cm² which is lower than the limit. Therefore this kind of heater can be used for this application. The heater has a resistance of 89.4 Ω, therefore the voltage supply needed for its operation is $\sim 22.17 \ V$. The heaters can be mounted on the glass substrates by using their acrylic PSA.
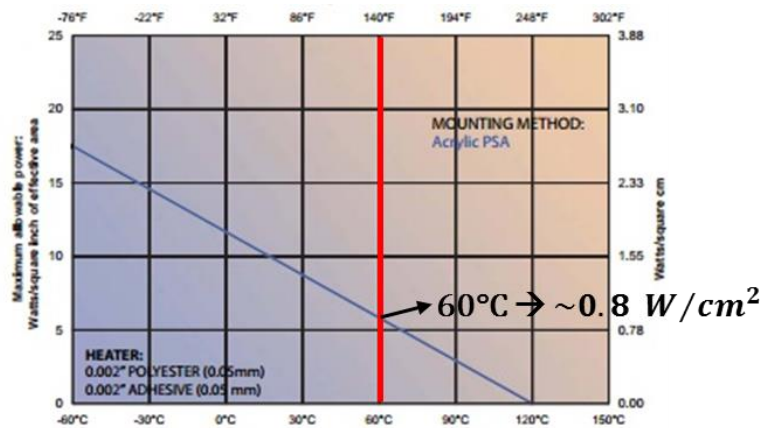
Figure 4.8. Thermal-Clear heaters maximum power density values in function of temperature.

4.1.6 Preliminary experimental tests

The aim of the first experimental test was to measure the hydraulic resistance of the channel and to confirm the value theoretically calculated. In order to perform the measurement, metallic tubes were glued at the inlet and outlet holes of the microfluidic channel with Norland Optical Adhesive glue (NOA 63) which was cured for one hour with UV light.

The setup is composed by the following components: a laptop, a high precision pneumatic pressure controller (MFCS-8C-345, Fluigent) with a pressure range from 0 to 345 mbar and a microfluidic interface between the MFCS and the microfluidic platform. Figure 4.9 shows the experimental setup for the hydraulic resistance measurement (a) and the microfluidic interface (b) made of a reservoir in which liquid, i.e. DI water, can be pushed by a gas stream and driven to the microfluidic platform.
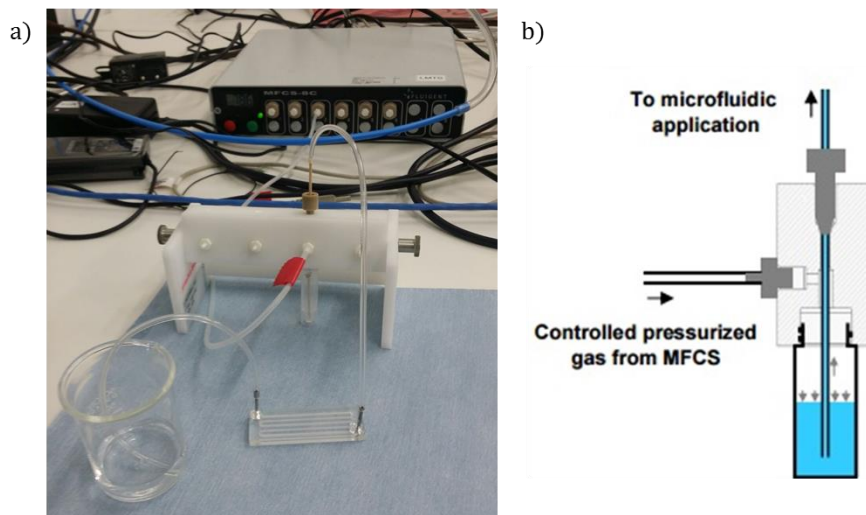
Figure 4.9. Experimental setup for the measurement of the channel hydraulic resistance (a) and microfluidic interface: a controlled pressurized gas stream pushes water into the tube connected to the microfluidic platform (b).

DI water was flushed by applying a pressure of around 30 mbar in order to completely fill the channel before performing the measurements. This was done in order to avoid that presence of air bubbles in the channel and capillarity effects could distort the measurement. For the measurement the pressure drop Δp was fixed to 10 mbar and the volume of DI water in the microfluidic interface was fixed to 1 ml.

The measurement of the hydraulic resistance was performed by measuring the time needed to empty the reservoir thus obtaining the flow rate Q and by using the equation (1): $\Delta p = R_{hyd}Q$. Thirteen measurements were carried out giving a mean value for the hydraulic resistance of $3.83 \cdot 10^{10} \frac{Pa \cdot s}{m^3}$ and a standard deviation σ of $0.52 \cdot 10^{10} \frac{Pa \cdot s}{m^3}$. The main value is very close to the value calculated by approximating the serpentine channel to a straight channel, i.e. $3.71 \cdot 10^{10} \frac{Pa \cdot s}{m^3}$.

The device tested for the hydraulic resistance measurement was the second generation device with SU-8 pillars, for which the PDMS/glass bonding was achieved by PSA method. During the measurements no liquid leakage was observed (pressure values up to 70 mbar were applied).

4.2 Microfluidic platform for VOCs detection

This section reports on the development of a microfluidic platform for integration into the optical detection system for VOCs developed by the partners of UULM of the SCHeMA project. The microfluidic platform has to fit the polymer-coated optic fiber which is the core of the optical system. In order to improve the sensitivity and the limit of detection of this system, as well as the number of target analytes, the contribution of micro-technology is required to provide a flow cell with a channel height in the order of a few tens of microns.

The design and fabrication of the microfluidic platform are presented. The design is based upon the guidelines given in literature for the modelling of infrared evanescent wave chemical sensors. The fabrication is achieved by exploiting additive manufacturing techniques, i.e. 3D printing.

Different designs were initially proposed for the device, but one of them was afterwards optimized by improving its geometry and microfluidic connections. This device was installed in the optical setup and successfully tested for detection of ten different species of VOCs by the partners at UULM.

4.2.1 Introduction and background

The ocean surface is a natural source of atmospheric VOCs [179] through a variety of biogeochemical and photo-induced processes. VOCs air–sea exchange plays indeed an important role in the earth's biogeochemical cycles and in the chemistry of the atmosphere. Marine biological, physical and photochemical processes cause an emission to (or an uptake from) the overlying atmosphere for a range of organic gases which significantly impact the atmosphere, influencing ozone photochemistry and aerosol physics even at trace concentrations [180].

For instance, oxygenated VOCs (OVOCs) are ubiquitous throughout the troposphere and have an influence on the oxidative capacity of the atmosphere [181–183], but the role of the ocean in the cycling of these compounds remains unanswered [184]. The mechanisms governing their formation and destruction in seawater is indeed largely unknown [185]. Some of the uncertainties result from the limited number of measurements of dissolved VOCs concentrations in seawater [186] hindered by the low marine VOCs concentrations and by the limited sensitivity of the most common detection techniques [187].

Moreover, organic substances such as hydrocarbons (HCs) and chlorinated HCs (CHCs) are among the priority pollutants in water defined by international environmental authorities [188] and are considered to be significant indicators of urban and industrial pollution [189].

In order to monitor the changes in VOCs concentration and their impact on the environment, a more frequent analysis and more accurate and precise measurements of a larger numbers of organic compounds in seawater, even at very low concentration levels, are required [187]. Advanced screening instrumentation based on sensitive, reliable and robust analytical method is therefore demanded for continuous *in situ* monitoring of these contaminants and their discrimination.

The detection technique investigated by the partners at UULM is based on mid-infrared (MIR) spectroscopy. The feasibility of the approach based on the deployment of fiber-optic evanescent wave sensors (MIR-FEWS) operating in the spectral range 3–20 μm has been demonstrated for the detection of chlorinated hydrocarbons in the low ppb concentration range in artificial seawater samples [190]. In comparison with UV/VIS spectroscopy and near-IR spectroscopy, the MIR spectral range provides pronounced substance-specific information and high sensitivity, thus making the concept of MIR-FEWS the most promising approach for continuous multicomponent VOCs pollution monitoring in water [190].

The sensor developed at UULM for detection of dissolved VOCs in seawater is a miniaturized optochemical mid-infrared sensor consisting of an infrared light source, a polymer-coated flattened AgX-fiber (active sensing region) and a spectrometer detector. The AgX-fiber has to be fixed in a microfluidic platform which enables the seawater sample to flow in contact with the fiber thus allowing enrichment of the polymer layer with the target analytes. The evanescent wave partially penetrates the polymer layer (around 8 μm thick) and through the interaction between the evanescent field and the enriched polymer, information about the concentration of VOCs can be gathered by analyzing their absorbance spectra.

In order to improve the detection limit and the response time of this technique, a microfluidic platform with a channel thickness in the order of a few tens of microns is required. Indeed, it is widely considered that miniaturization of the cross-sectional area of the sensor flow cell results in reduction of the response time, as well as the threshold of detection [191].

C. Phillips et al. [191] have reported a model-based methodology for optimal design of polymer-coated infrared evanescent field chemical sensors. Figure 4.10 shows the schematic of the baseline flow cell for such sensors. In this work fluid mechanics and mass transfer are combined in order to propose optimized geometries of the sensor flow cell thus improving the response time of the chemical sensor.
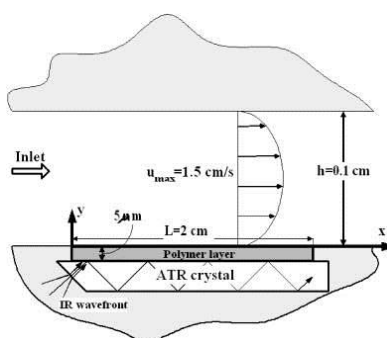
Figure 4.10. Schematic of the baseline flow cell for polymer-coated infrared evanescent field chemical sensors [191].

The authors show that for the optimal channel height the resistances to advective transport (R_{adv}, parallel to the flow) and to cross-channel diffusion (R_{diff}, perpendicular to the flow) depend on the polymer-coated length (L), the height of the flow cell (h), the average flow velocity (u_{av}) and the diffusion coefficient of the analyte in the aqueous phase (D_a). The two resistances are defined as follows:

$$R_{adv} = \frac{1}{u_{av}h}$$
Equation 4.4

$$R_{diff} = \frac{h_{opt}}{D_a L}$$
Equation 4.5

For the optimal channel height that minimizes the response time, the two resistances become equal, therefore the optimal channel height is given by:

$$h_{opt} = \sqrt{D_a L / u_{av}}$$
Equation 4.6

The diffusion resistance is dominant when the channel height is greater than optimal height, and the advection resistance is dominant at channel heights smaller than optimal height. At the optimal height, the analyte travels the shortest distance in a straight line from the top of the inlet to the bottom of the exit, providing the least possible total resistance to mass transfer in the flow cell and thus resulting in the fastest sensor response.

The authors also proposed other two configurations for reducing the overall resistance to mass transfer and speeding up the response time of the sensor. In the first proposed geometry shown in Figure 4.11a, the inlet (flow entry) is centered in the top plate of the flow cell: the smallest channel height simulated (10 µm) yielded to the fastest response time. The second one is a geometry in which the channel height is linearly tapered over the length of the channel from the baseline height (1000 µm) to the smallest simulated value (10 µm) as shown in Figure 4.11b.
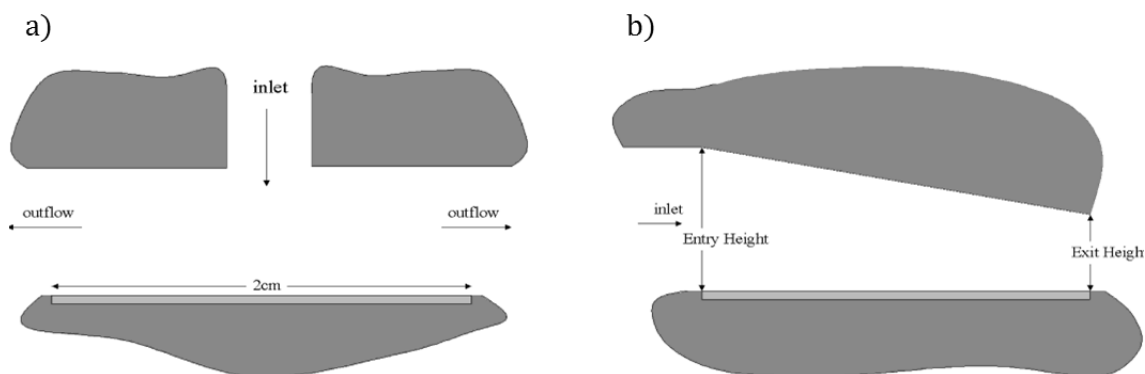
Figure 4.11. Schematic of the flow cell with top centerline flow entry (a) and of the flow cell with tapered height (b) [191].

4.2.2 Design of the microfluidic platform

Equation 4.6 was used for designing the microfluidic platform. The diffusion coefficient of the analytes of interest (VOCs) in the aqueous phase is $D_a = 10^{-5}\ cm^2/s$, while the average velocity is $u_{av} = \frac{2}{3}u_{max}$ with $u_{max} = 1.5\ cm/s$. The geometrical dimensions of the optic fibers can be schematically summarized as reported in Figure 4.12. The length of the flattened part of the fiber is of about 45 mm, however the channel length was fixed to 35 mm since the transition parts to the cylindrical endings were 10 mm long. By using the Equation 4.6, the optimal channel height for this flow cell was found to be 63.8 µm.
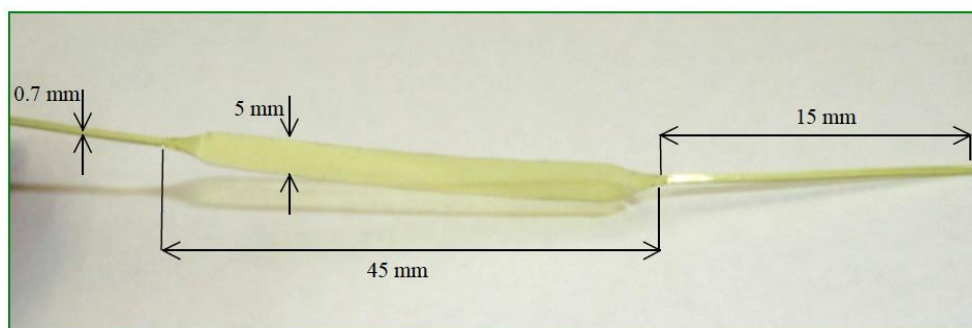
Figure 4.12. Dimensions of the silver halide fiber sensor. The flattened part of the fiber is coated with the enrichment polymer membrane.

4.2.3 Fabrication of the microfluidic platform

For building the different configurations proposed by Phillips et al., technology with a resolution of tens of microns is required. Soft lithography would allow achieving the desired channel height for the first two proposed geometries of the flow cell by using an SU-8 mold with the required thickness (60 µm or 10 µm) for patterning PDMS, but it would not be possible to obtain a smooth tapered height for the last proposed geometry. Moreover, two parts in PDMS would be produced, whose degree of swelling varies as a function of VOCs concentration due to their absorption [192], therefore a microfluidic platform made of PDMS would swell in contact with VOCs and alter the measurements, thus making this technology not appropriate for the application. Furthermore, this

103

technology would require fabrication of masks, clean room facilities and therefore be time-consuming. Other machining techniques such as CNC machining would not allow to smoothly achieve the desired thickness in the order of tens of microns, therefore attention was focused on additive manufacturing techniques.

Additive manufacturing technologies may be classified depending on the state of the prototype material before part formation: liquid (e.g. solidification of a liquid polymer), discrete-particles (e.g. fusing of particles by laser), solid sheets (e.g. bonding of sheets with adhesive). All these processes require input from a 3D solid CAD model, from which prototypes can be rapidly produced in a few hours [193], they are indeed usually referred to as rapid prototyping (RP) techniques.

The most popular process involving a liquid is stereolithography (SLA), technique which relies on a photosensitive monomer resin which forms a polymer and solidifies when exposed to UV light. The resolution of these systems depends on the laser beam spot diameter which is around 75 μm. High-resolution SLA systems have been recently developed for bioprinting living cells achieving a resolution of 50 μm [194].

Fused deposition modelling (FDM) is another commonly used additive manufacturing technique. It consists of a moving bed along z-axis and a print head with a heating element; thermoplastic is forced into the print head, melts, and is squeezed out. The bed is usually cooled so that the plastic hardens soon after being placed down. The resolution of this layer by layer process depends on the nozzle diameter which is typically around 200 μm.

3D inkjet printing is similar to FDM, with the difference that the plastic is held in a liquid state inside the machine before being dispensed. This technique belongs to the ballistic particle manufacture category in which a stream of molten material is ejected from a nozzle. The print head is a piezo print head which allows depositing either photo-curable plastic resins or wax materials drop by drop. Figure 4.13 shows the inkjet printing system.
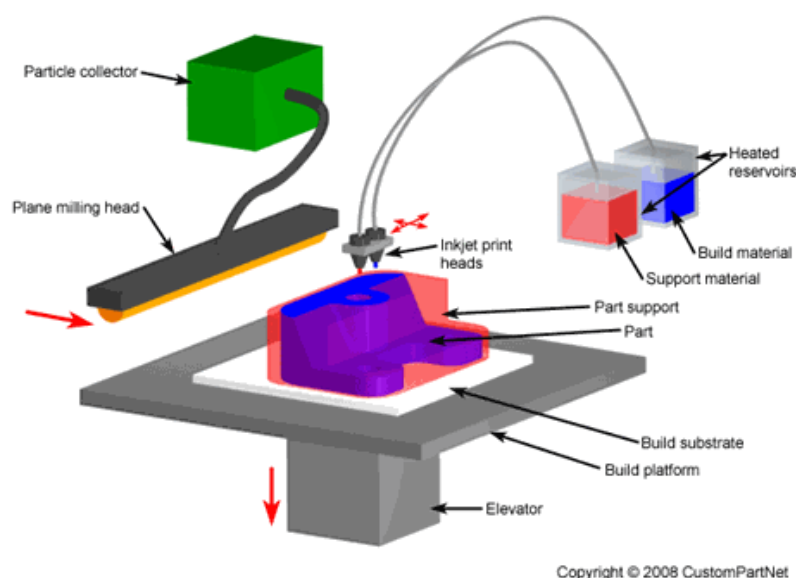
Figure 4.13. 3D inkjet printing technology system.

As soon as the print head dispenses the liquid thermoplastic, it cools and solidifies on the substrate. The wax is instead used as a support material if needed. Another feature typically included in this technology is a plane milling stage. Between each layer a plane is rolled over the model, cutting extraneous material off of the top layer. This ensures that the layer is precisely flat but slows down the printing speed. The 76 µm diameter droplets which flatten on impact giving discs with a diameter of 101 µm and a thickness of 63 µm, are milled after each layer is deposited, achieving accurate dimensions in the z direction [193]. This process allows very smooth finishing of the printed parts.

MultiJet Modelling (MJM) is another implementation of this technology, in which many printing heads simultaneously dispense plastics. It employs hundreds of nozzles and offers the highest Z-direction resolution among all these technologies with a layer thicknesses as low as 16 microns.

MJM was therefore chosen as 3D printing technique for the fabrication of the microfluidic flow cell and 3D models of the three different geometrical configurations for the channel were drawn in *SolidWorks*. The devices were fabricated at the Additive Manufacturing Workshop of EPFL by using a MJM 3D printer Connex 500.

The first geometry is the baseline channel with a thickness of around 63.8 µm. Figure 4.14 shows the optical fiber drawing (a), and the bottom piece of the microfluidic platform (b) in which six holes are present for allowing sealing to the top piece by screws. Figure 4.15 shows the top (a) and bottom (b) view of the top piece of the microfluidic platform with the inlet/outlet ports and two rubber layers with a thickness of 0.5 mm printed at the same time to improve the sealing.
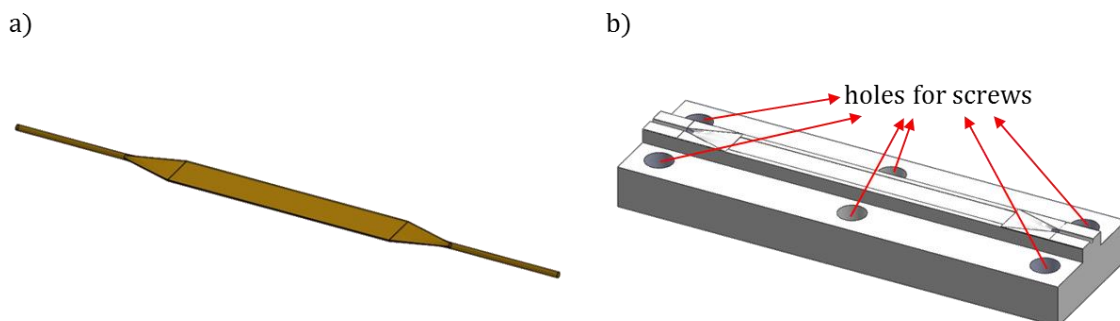
Figure 4.14. 3D drawings of the optic fiber (a) and of the bottom piece of the microfluidic platform (b).
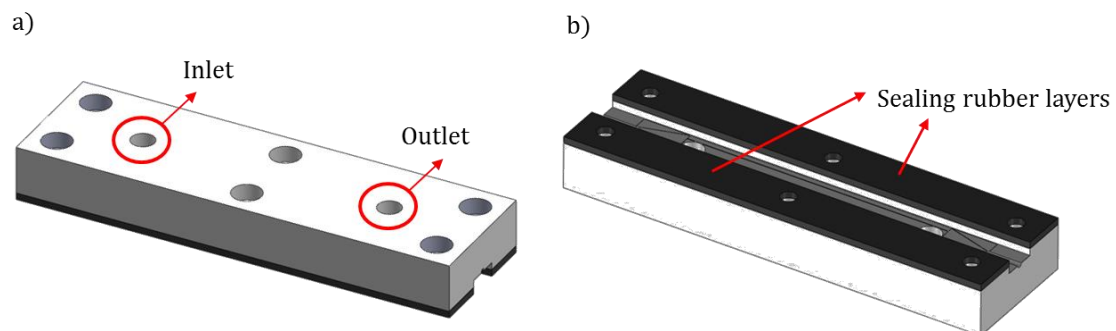
Figure 4.15. 3D drawings the top piece of the microfluidic platform with the two rubber layers: top view (a) and bottom view (b).

With the MJM Connex 500 printer it is in fact possible to print two different materials consecutively. A stiff transparent material was printed for the body of the platform (VeroClear) and a softer rubber material with hardness shore 40 was printed to serve as sealant (TangoBlack). The rubber-like material is a mixture of acrylic compounds, in its formulation several additives are mixed with the acrylic monomer and the photo-initiator.

Two additional holes are present in the top piece of the platform to provide the inlet and outlet connections for the seawater sample: polytetrafluoroethylene (PTFE) tubes are used for this purpose. Figure 4.16 shows the bottom pieces of the other two configurations: the centered inlet (a) and the tapered height (b) one.
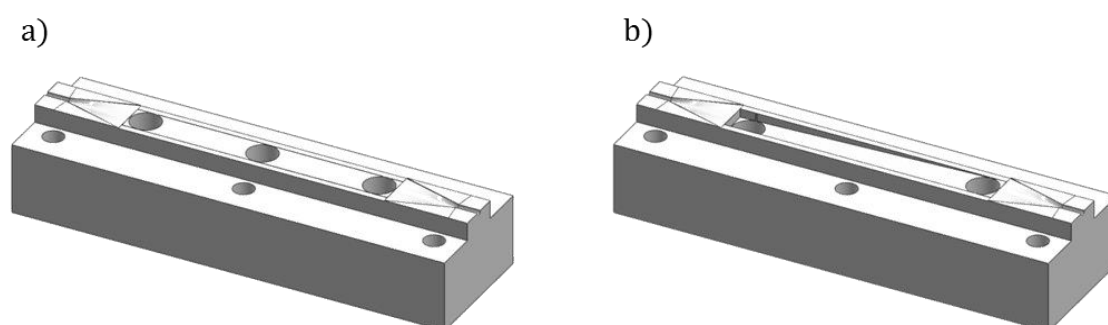
Figure 4.16. 3D drawings the bottom piece of the inlet centered (a) and tapered height (b) microfluidic platform.

The MJM Connex 500 has a resolution (minimum layer thicknesses) of 33 μm, therefore the channel height was fixed to 66 μm, very close to the desired value (63.8 μm). For the second configuration a height of 33 μm was the minimum possible thickness. Figure 4.17 shows the picture of the fabricated top and bottom pieces (a) of the first configuration platform and the assembled platform fitting the optical fiber (b).
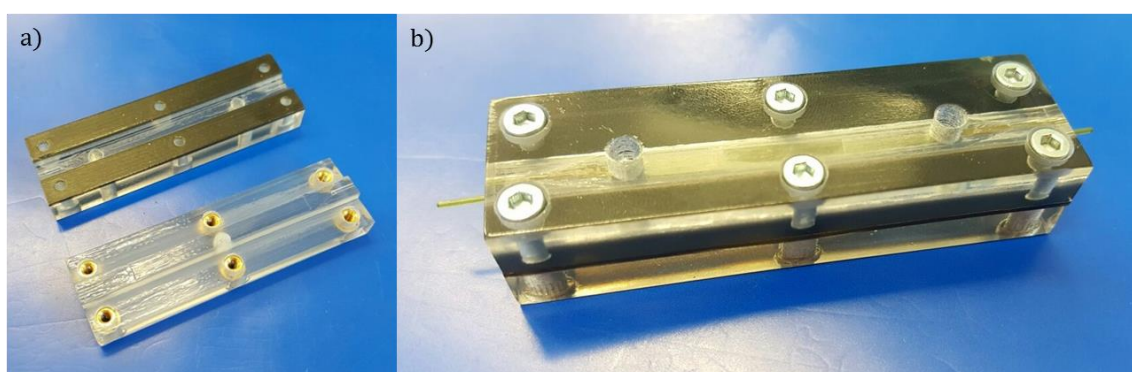
Figure 4.17. Pictures of the fabricated top and bottom pieces (a) of the first configuration platform and of the assembled platform fitting the optical fiber (b).

The three devices were tested by the partners at UULM and leakage problems were observed during the experiments. The leakage issues were most probably linked to the length of the microfluidic flow cell which did not always fit the longer fibers (the length of the produced fibers is variable)

and to the thickness of the rubber layer which could not totally ensure the sealing of the two parts. The optimization of the flow cell carried out to solve the above mentioned problems is reported in the following section.

4.2.4   Second generation microfluidic platform for VOCs detection

A second generation microfluidic platform was designed and fabricated. The main changes with respect to the first generation were: (i) the introduction of conical liquid connectors on the top piece of the device to allow a better fixing the PTFE tubes, (ii) the channel length increase up to 40 mm in order to host fibers with different lengths, and (iii) the increase of the thickness of the rubber layer up to 1 mm to improve the sealing.

Moreover, the bottom piece of the device was equipped with a hole and M32 thread in the center in order to fix the flow cell in the experimental setup developed at UULM. Figure 4.18 shows the 3-D drawings of the top (a) and bottom (b) pieces of the device and Figure 4.19 shows some pictures of the fabricated device.
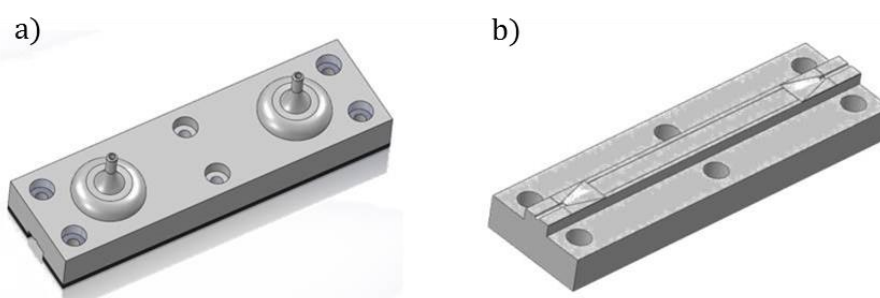
Figure 4.18. 3D drawings of the second generation microfluidic platform: top (a) and bottom (b) pieces.
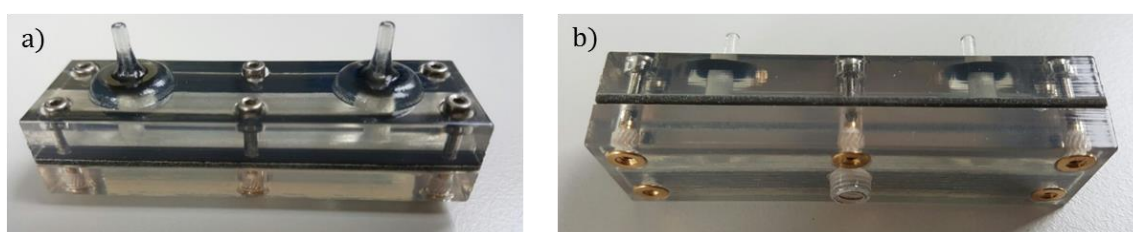
Figure 4.19. Pictures of the second generation microfluidic platform showing the inlet/outlet ports on the top piece (a) and the thread on the bottom piece (b).

These devices were tested by partners at UULM. Figure 4.20 shows an example of the absorbance spectra they measured for seven VOCs species in seawater with the second generation microfluidic platform. Figure 4.21 shows an example of the calibration curves obtained for seven VOCs measured at the same time in seawater with the second generation microfluidic platform [195].
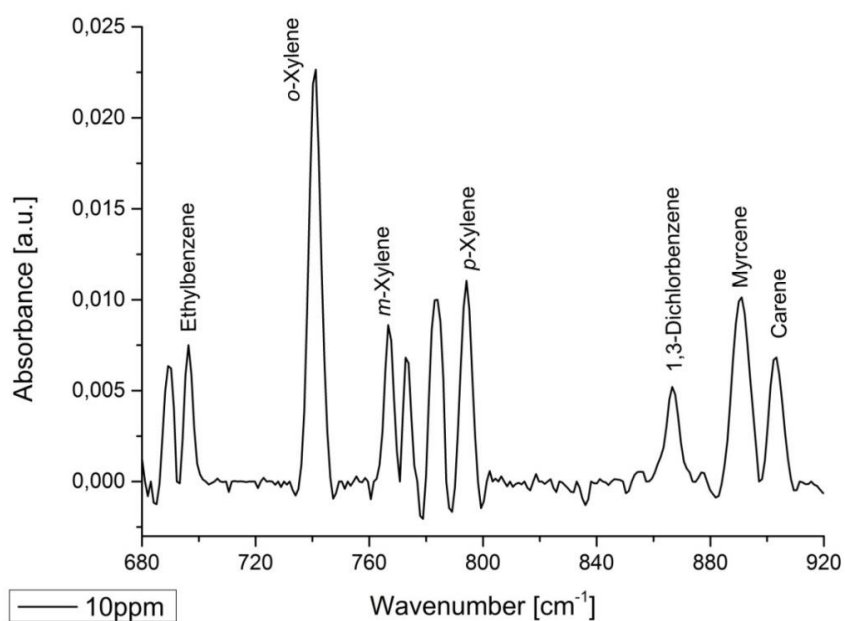
Figure 4.20. Absorbance spectrum of seven VOCs species measured in seawater with the second generation flow cell (UULM) [195].
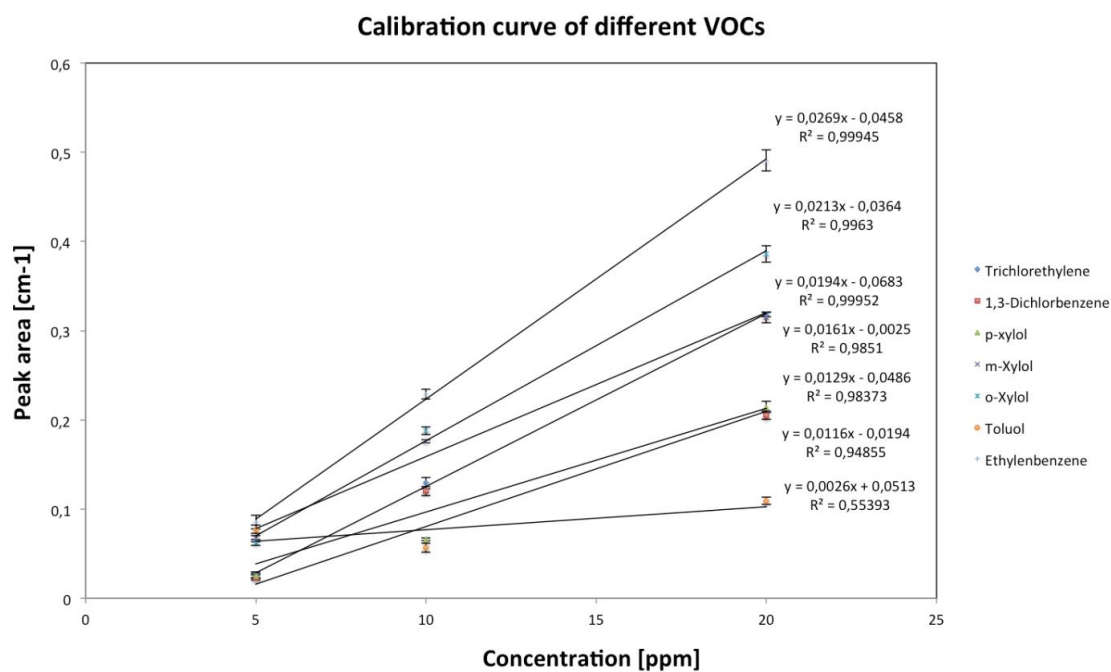
Figure 4.21. Calibration curves of seven VOCs species measured in seawater (from Portofino) with the second generation flow cell (UULM) [195].

With this microfluidic platform the leakage issue was not observed during measurements and problems related to air bubble and signal losses were reduced. Limit of detection (LOD) was improved and it was possible to detect VOCs in the ppb range. Despite these good results and the observed improvement, a practical issue surfaced: sometimes during the measurements the sealing of the tubes to the inlet/outlet conical connectors was insufficient. Therefore this configuration was further improved.

4.2.5   Third generation microfluidic platform for VOCs detection

The third generation platform differs from the previous one only for the top piece in which the inlet/outlet connectors were replaced by two threaded ports where it is possible to fasten flanged fittings. Figure 4.22 shows the 3-D drawings of the top (a) and bottom (b) pieces of the optimized platform and in Figure 4.23 a picture of the final device with a screwed flanged fitting is reported.

These devices have been tested by our partners at UULM. The optimized device allowed pumping the sample without any leakage and without any air bubble occurrence during measurements. Issues related to signal losses were not encountered. Moreover, LOD was further improved (sub-ppb) and up to ten analytes could be measured at the same time.
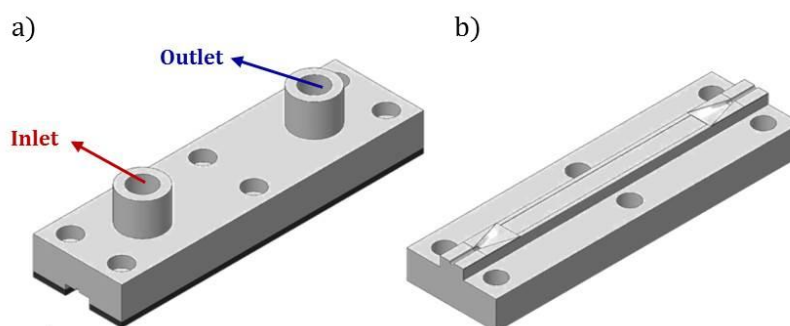
Figure 4.22. 3D drawings of the third generation platform: top (a) and bottom (b) pieces.
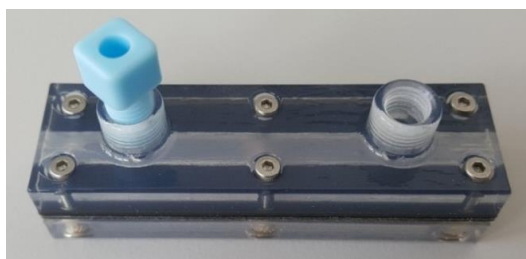
Figure 4.23. Picture of the third generation microfluidic platform showing the inlet/outlet threaded ports with a screwed flanged fitting.

Table 4.2 shows the comparison of the three different generations of the microfluidic platform.

Table 4.2. Geometrical parameters and features of the different generations of the microfluidic platform.

Microfluidic platform	Channel length	Channel height	Rubber thickness	Inlet/outlet connections	Positive/Negative results
First generation	35 mm	66 μm	0.5 mm	Holes	-/ Leakage
Second generation	40 mm	66 μm	1 mm	Conical connectors	Good sealing, ppb LOD, 7 analytes measured at the same time / Disconnection of tubes
Third generation	40 mm	66 μm	1 mm	Flanged fittings	Good sealing, sub-ppb LOD, 10 analytes measured at the same time / -

The third generation was therefore chosen as the final device for the integration in the VOC species optical detection system and in the SCHeMA probe.

Figure 4.24 shows an example of the absorbance spectrum measured by the partners at UULM for 30 mg/l concentration of ten VOCs species in seawater at 0 and 21 °C.
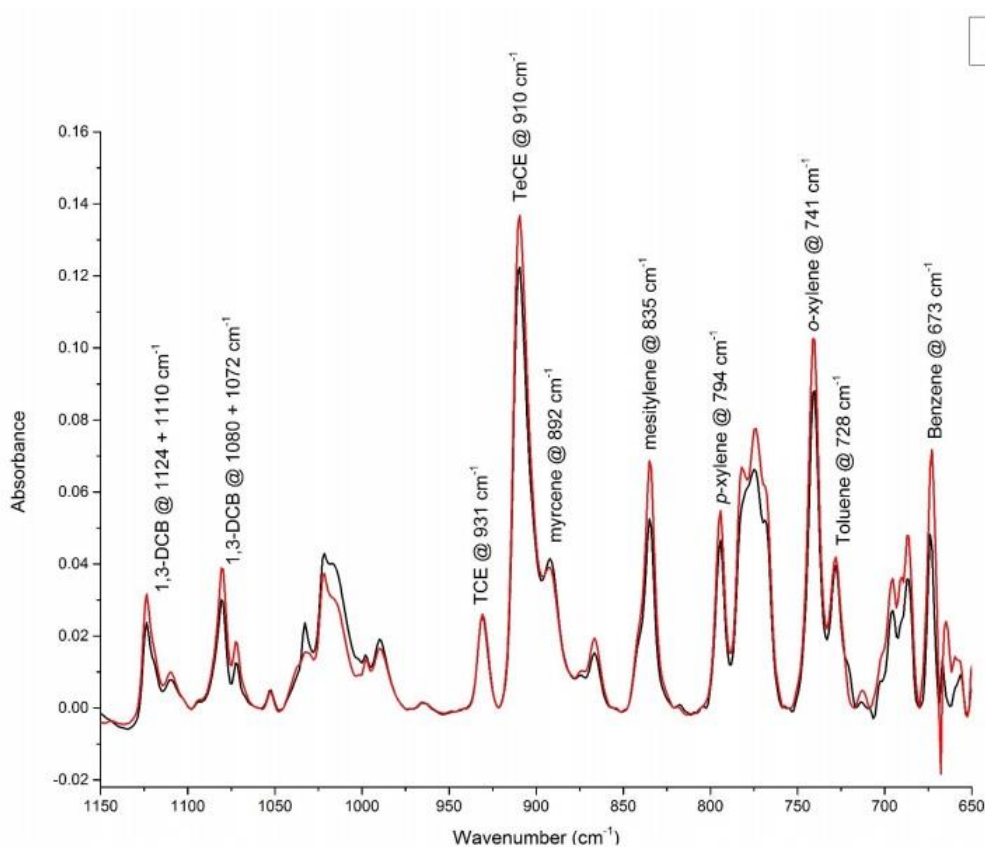
Figure 4.24. Absorbance spectrum of ten VOC species (30 mg/l concentrations) measured in seawater with the third generation microfluidic platform at 0 and 21 °C (UULM) [196].

Conclusions

In this chapter two microfluidic platforms for the pre-concentration of STX and for the detection of VOCs have been presented.

Two generations of the device for biotoxin pre-concentration were proposed in order to compare the dependence of immobilized aptamers amount on the surface area available for binding. The fabrication of the first generation device consisting of a PDMS channel and a glass substrate was achieved by bonding the two components through oxygen plasma treatment. The fabrication of the second generation made of the PDMS channel and a glass substrate with patterned SU-8pillars was achieved by three different bonding procedures: UV ozone-APTES silanization-oxygen plasma treatments combination, PSA bonding and HF etch-oxygen plasma treatments combination. The hydraulic resistance of the channel was theoretically calculated and experimentally measured by using a high precision pneumatic pressure controller. The measured value $(3.83 \cdot 10^{10} \frac{Pa \cdot s}{m^3})$ was in good agreement with the theoretical one $(3.71 \cdot 10^{10} \frac{Pa \cdot s}{m^3})$. For the PSA bonded device no liquid leakage was observed when pressure values up to 70 mbar were applied. The aptamer immobilization can be achieved by introducing amine groups and aldehyde groups on the surface of the microfluidic channel. Afterwards, the solution containing saxitoxin can be pumped though the channel for toxin capture and then its release can be achieved through a temperature increase. The integration of a transparent flexible heater was indeed investigated in order to study the possibility to achieve the release of the STX by increasing temperature up to around 60 °C.

The microfluidic platform for integration into an optical system for VOCs detection was designed based upon guidelines for the modelling of infrared evanescent wave chemical sensors and its fabrication was successfully achieved by 3D printing. The first microfabricated platform was tested and presented leakage-related issues. The addition of inlet/outlet fluidic conical connectors and the increase of the rubber layer thickness between the two parts of the device improved the performance of the flow cell: absence of leakage, improved LOD (ppb), up to 7 analytes could be measured at the same time. However the sealing of the tubes to the inlet/outlet conical connectors was insufficient to guarantee a 100% leakage-proof device. This lead to the development of a third generation device in which threaded ports for flanged fittings replaced the conical connectors. This device was chosen as final device for the integration in the optical detection system due to the absence of leakage, the improved LOD (sub-ppb) and the possibility to measure up to 10 analytes in seawater.

Chapter 5   Summary and outlook

5.1   Conclusions

The main goal of this thesis was to develop new micro-engineered tools to enhance the performance of electroanalytical methods such as voltammetry and coulometry for *in situ* detection of natural and anthropogenic compounds in seawater.

The quality status of the marine ecosystem can be assessed by detection and quantification with high spatial and temporal resolution of a number of important analytes, thus gathering information about their role in the marine biogeochemical processes as well as the potential risks for aquatic and human life. Among these compounds, nutrients, trace metals, biotoxins and volatile organic compounds were the main targets of the devices presented in this thesis, i.e. sensors for detection of trace metals, pre-treatment units for seawater desalination and saxitoxin pre-concentration, and a microfluidic platform for VOCs detection.

Nutrients such as nitrate, nitrite and phosphate, play an important role in the trophic chain of marine ecosystem, exerting a strong control on the ocean primary productivity and growth of living organisms. Trace metals from natural and anthropogenic sources can change the ecosystem equilibrium due to their role in the biogeochemical processes: their speciation changes reflect changes in physicochemical conditions of ocean environment. Metal species such as iron, cobalt and zinc, present in the plankton biomass, are essential or toxic depending on their concentrations, while metal species such as lead, arsenic, mercury, and aluminum are extremely toxic even at low concentrations. Marine biotoxins, usually produced by phytoplankton, are compounds with toxic activity that accumulate in fish or shellfish through the trophic chain and can cause human illnesses. Among the various species of biotoxins, saxitoxin is a low molecular weight neurotoxin mainly produced by marine dinoflagellates responsible for paralytic shellfish poisoning, the most worldwide spread algal-derived shellfish poisoning. Volatile organic compounds are among the priority pollutants in seawater established by international environmental authorities, and are considered to be significant indicators of urban and industrial pollution. Their presence in seawater plays an important role in the earth's biogeochemical cycles due to the uptake from and emission to the atmosphere. The mechanisms of formation and destruction, as well the biological, physical and photochemical processes that cause their exchange with the atmosphere are largely unknown.

Robust and reliable instrumentation with minimized impact on the environment, based on accurate and sensitive analytical methods, are therefore required in order to *in situ* monitor and quantify the concentration of these compounds in seawater.

Among the wide variety of sensors based on optical, electrical and thermal transduction, electrochemical sensors are amongst the simplest, low-cost, reliable and practical sensors, in which the analyte concentration can be studied by electroanalytical methods by transducing the quantity of the chemical analyte into an electrical signal.

In chapter 2, a microfluidic system for achieving sodium chloride removal from seawater, a pre-treatment required for allowing nutrients detection, was presented. Due to the high chloride concentration hampering the measurement of the nutrients, the goal was to reduce the chloride concentration of seawater to mM levels, starting from an initial value of 0.6 M. The design of the device was based on exploiting bulk electrolysis by controlled potential thin layer coulometry. The working principle is based on salt removal upon electrolysis: by applying a positive potential chloride ions are extracted by oxidation of an Ag electrode in contact with the solution to AgCl and sodium ions are transported towards a second fluidic compartment through a cation exchange membrane. The Ag electrodes are then regenerated by inversing the applied potential. A thin (80 µm) layer of solution was trapped in contact with the Ag electrode thus achieving the required conditions on the electrode area/solution volume ratio for carrying out bulk electrolysis.

Printing techniques were chosen for the fabrication of the Ag electrodes to overcome the limitations of conventional techniques for Ag deposition. Six commercial Ag inks were tested and compared in order to choose the best ink for the fabrication of Ag electrodes in terms of oxidation ability (highest oxidation charge), robustness in water environment and adhesion to glass (number of repetitive oxidation/reduction cycles before adherence loss). The ink which best matched all these criteria was the Dupont 5064H ink.

Microfluidic platforms with Ag electrodes printed with this ink were tested by cyclic voltammetry for confirming the thin-layer behavior of the system (kinetic-controlled chemical reaction rather than diffusion-controlled) and finding the optimal potential window for carrying out electrolysis. This was found to be in the range 700-900 mV. Chronoamperometric tests were carried out at potentials between +0.3 V and +1.1 V for a time period of 60 s. The best potential for carrying out electrolysis was found to be +0.9 V for which an exponential trend was found for the current profile, as predicted by the theory.

A second generation of devices was designed and fabricated for increasing the volume of the desalinated sample thus allowing quantification of the salt content after the treatment and for improving the microfluidic inlet/outlet connections for more precisely displacing the sample to be desalinated. The concentration after treatment was quantified through conductance measurements performed by a conductivity flow-through two-electrode sensor placed at the outlet of the microfluidic platform.

The device was tested at the optimal potential +0.9 V for different periods of time with a synthetic seawater sample. A proof-of-concept of the desalination capabilities of the microfluidic platform was achieved. The device was capable of reducing the initial concentration of 0.6 M (41.8 mS) to a final value of 0.206 M (20.36 mS) for a time period of 120 s, 0.157 M (17.37 mS) for a time period of 240 s and to 51.6 mM (6.38 mS) for a time period of 360 s.

The influence of some geometrical parameters, such as the Ag electrode geometry (square vs. serpentine) and the electrode thickness (50 µm vs. 5 µm), on the desalination performance of the device was investigated. The use of a square-shaped Ag electrode resulted in a less robust electrode which broke down after four redox cycles because of the stress arisen at the edges of the microfluidic channel. The use of a thicker electrode (50 µm) cured at higher temperature (250 °C) allowed improving the robustness of the electrode and significantly increasing the device lifetime up to tens of redox cycles (more than 30 cycles).

In chapter 3, a two-electrode (WE, CE) and three-electrode (WE, CE, RE) on-chip sensor configurations allowing trace metals voltammetric detection in seawater were presented. The goal was to develop a new sensor integrating on-chip the three electrodes necessary for carrying out the SWASV measurements of different metal species, towards the miniaturization of the submersible probe for *in situ* measurements. The three electrodes are an array of interconnected Ir microdiscs serving as the WE, a square-shaped CE and a square-shaped RE. Three different designs were proposed with a different number of discs and different inter-electrode spacing. The fabrication process flow consisted of three photolithographic steps: patterning of an Ir metallic layer, patterning of the silicon nitride passivation layer for defining the disc geometries and patterning of an SU-8 containment ring for antifouling agarose gel membrane. Afterwards the Ir arrays were plated with Hg hemispheres or AuNPs depending on the trace metal species of interest: lead/cadmium/copper or arsenic and mercury, respectively. Two types of solid state REs were developed: an Ag/AgCl pseudo-RE and an Ag/AgCl/PVC-IL RE.

The sensors were tested by cyclic voltammetry for confirming the quality and integrity of the Ir layer (CV in sulfuric acid) and for evaluating the diffusion properties of the Ir microdisc arrays (CV in potassium ferrocyanide). The S-shaped current profile characteristic of microelectrode behavior in potassium ferrocyanide confirmed the absence of diffusion layer overlapping between the discs and a non-planar diffusion regime for all the designs for small measurement time (pre-concentration time < 7 min). The design with the highest number of discs and the lowest inter-electrode spacing showed diffusion layer overlapping for long measurement time (pre-concentration time > 15 min). However when this test was repeated after SU-8 photolithography, a current level close to zero was found revealing the presence of epoxy resin residues on the surface of the discs. Different cleaning procedures were tested, but only the UV ozone cleaning treatment resulted in the recovery of the S-shaped profile of the current, albeit with slightly lower current values.

The stability in time of the REs potential was tested in seawater and the sensitivity to chloride changes was tested by using synthetic solutions of NaCl from 10^{-4} to 10^{-1} M against an Ag/AgCl/3 M KCl RE. The potential of the Ag/AgCl pseudo-RE was stable around 37.1 ± 1.4 mV for more than two months and the slope with respect to chloride concentration was of 50.09 mV/decade, not far from the ideal Nernstian behavior (59.16 mV/decade). The potential of the Ag/AgCl/PVC-IL RE was 37.34 mV and its slope 21.32 mV/decade, much smaller than the Ag/AgCl pseudo-RE but still far from the desired insensitivity to chloride concentration changes.

SWASV measurements in synthetic 0.1 M $NaNO_3$ solutions were performed with on-chip WE-CE /external RE sensors for quantification of lead, copper and cadmium. The current peaks increased

linearly with the concentration and sensitivity values of 2.73 nAnM^{-1} min^{-1}, 1.23 nAnM^{-1} min^{-1}, and 1.29 nAnM^{-1}min^{-1} were registered for Pb(II), Cu(II), and Cd(II), respectively.

SWASV measurements of Pb(II), Cd(II) and Cu(II) in synthetic 0.1 M NaNO$_3$ solutions and seawater samples were also carried out with the WE/CE/RE on-chip sensors and compared to the same measurements performed before. The devices proved to be able to detect trace metals. A shift of all the species peaks with respect to the external RE was observed of -275 mV and -250 mV for the Ag/AgCl pseudo-RE and the Ag/AgCl/PVC-IL RE, respectively, in NaNO$_3$. The shift of -275 mV in sodium nitrate was confirmed also by the measurement of As(III) against the on-chip Ag/AgCl pseudo-RE. In seawater, with high chloride concentration, a shift of -50 mV was observed with the Ag/AgCl pseudo-RE. The possibility to quantify trace metals with the three-electrode on-chip sensors was investigated. Unfortunately, linear calibration curves could not be obtained against the on-chip Ag/AgCl pseudo-RE possibly due to the dissolution of the AgCl layer. The addition of the PVC-IL membrane was found to give better results slowing down this dissolution process. A linear calibration curve could be obtained for cadmium against the on-chip Ag/AgCl/PVC-IL RE and a sensitivity of 0.61 nAnM^{-1}min^{-1} was registered (half the value registered for the two-electrode on-chip sensors).

The developed devices allowed detection of trace metals but further improvements, especially concerning the adhesion of the PVC-IL membrane, are required to develop robust and reliable three-electrode on-chip sensors for trace metals quantification.

In chapter 4, two microfluidic platforms for the pre-concentration of saxitoxin and for the detection of VOCs were presented. The first device was designed in order to allow immobilization of aptamers in a microfluidic channel and achieve the pre-concentration of saxitoxin by a selective binding to the aptamer that specifically targets saxitoxin. Two generations of the platform were fabricated: the first one consisted of a simple PDMS channel bonded to a glass substrate, on which the aptamers can be immobilized, the second one consists of the same glass/PDMS channel provided with SU-8 pillars patterned on the glass side of the channel for studying the possibility to bind the aptamers to SU-8 thus enhancing the surface area available for binding. The devices were equipped with a transparent adhesive heater on the back side of the glass for allowing the release of the saxitoxin after capture upon increase of the temperature.

The second device (for VOCs detection) was designed by following the guidelines reported in literature for the optimization of mid-infrared evanescent wave chemical sensors. The core of the chemical sensor is an optical fiber coated with a polymer layer partially penetrated by an evanescent wave. The fiber is kept in place by a microfluidic platform which allows the seawater sample to flow in contact with the polymer to be enriched with the analytes. The optimal channel height for optimizing the enrichment of the polymer layer of the sensor with the VOCs of interest was found to be of around 64 μm. The technique chosen for its fabrication was multijet 3D printing, thanks to which a smooth surface and robust double-material microfluidic platform was successfully fabricated. The two printed materials were a transparent hard material for the body of the platform and a softer rubber-like material serving as a sealant between the two parts of the platform to avoid liquid leakage. Unfortunately, the first generation microfabricated platform suffered from leakage

issues possibly due to a non-perfect fitting of the optical fibers whose dimensions differ among the different fabrication batches provided by the manufacturer.

The second generation was characterized by the addition of inlet/outlet fluidic conical connectors and by the increase of the channel length and of the rubber layer thickness. These changes significantly improved the performance of the platform: no leakage was observed, the LOD could be improved (ppb), and up to seven analytes could be measured at the same time. The only drawback of this device was that the sealing of the tubes to the inlet/outlet conical connectors was insufficient. Therefore a third and last configuration of the device was designed and fabricated in which threaded ports for flanged fittings replaced the conical connectors. This device was chosen as final device for the integration in the optical detection system, with improved LOD (sub-ppb) and the possibility to measure up to ten analytes in seawater.

5.2   Future development

The results achieved in this thesis are promising for the further use and development of the designed and fabricated devices towards their deployment for *in situ* continuous monitoring of different compounds in marine environment.

The Ag ink-based desalination platform allowed the reduction of chloride concentration up to ten times with respect to the initial value present in the sample. However, further improvement of its performance is expected by studying the effect of other geometrical parameters, such as the thickness of the shallow channel and/or the thickness of the second fluidic compartment.

The latter could play an important role in the sodium chloride removal mechanism, since the electric field driving the sodium ions towards this compartment (mass transport due to migration) is higher when reducing the distance between the WE and the CE/RE. Another way to improve the performance of the microfabricated platform is investigating other printing techniques which are nowadays emerging as more powerful printing tools, such as pneumatic or aerosol jet printing, opening the possibility to use additional/new types of inks. Furthermore increasing the thickness of the Ag electrode is expected to improve the desalination performance; this would provide a more robust electrode which could withstand more redox cycles. Besides increasing the lifetime, also a higher adsorption capacity would be achieved. Once all these issues related to robustness and lifetime solved, also improving the desalination performance, real seawater samples could be used to test the platform in order to investigate the selectivity of the device towards NaCl removal with respect to other ions, opening the possibility for *in situ* deployment.

The developed trace metal sensors allowed the detection of different trace metal species with both configurations: on-chip WE/CE with external RE and on-chip WE/CE/RE. However the quantification was achieved only by the former for which linear calibration curves with higher sensitivity values than those reported in literature where obtained.

This suggests that the second configuration with three electrodes on-chip should be improved for reaching the same performance of the on-chip WE/CE sensor with external RE configuration. The main issue is related to the adhesion of the PVC-IL membrane to the AgCl layer which could be

improved by using a chemical anchoring mechanism. Some authors have shown that plasticized PVC membranes could be covalently bonded to oxide surfaces using a silane coupling agent with an amine group [189]. The recipe reported by van der Wal and co-authors was deployed in a quick and dirty test for anchoring the PVC to the AgCl layer using an adhesive layer mixture composed of PVC, bis(2-ethylhexyl)sebacate (DOS) and 3-amino-propyltriethoxysilane (APS). This procedure did not allow improving the adhesion of the PVC membrane to Ag/AgCl, however, a modification of this method would possibly help to improve adhesion to AgCl or SU-8. The enhanced PVC adhesion should allow a longer lifetime for the RE and therefore the quantification of trace metals such as Pb(II), Cd(II) and Cu(II) with the three-electrode on-chip configuration. Moreover, in seawater Ag/AgCl could work with respect to RE stability, but has shown issues related to Hg migration. Possibly increasing the distance between RE and WE (by for example switching the position of the RE and CE) could help to minimize the migration of the Hg layer to the RE.

The two generation devices (two- and three-electrode on-chip) require several improvements for detection of arsenic. Firstly, reproducible As(III) measurements with the two-electrode on-chip configuration (WE-CE) should be achieved by producing a stable and homogeneous layer of Au or Au-black nanoparticles on the Ir microdiscs and optimizing the SWASV protocol. Furthermore, the electrochemical synthesis of PANOA on the Ir microlines should be investigated in order to achieve a stable PANOA electrode. This would open the possibility to study the speciation of As(III) and As(V) through the two interdigitated electrodes configuration (WE1-WE2-CE) and optimize the SWASV protocol for the indirect measurement of As(V) after its reduction to As(III) electrochemically catalyzed by the PANOA copolymer.

The microfluidic platform for saxitoxin pre-concentration has not been tested yet. The functionalization of the channel with aptamers and saxitoxin pre-concentration upon aptamer binding can be tested by fluorescence microscopy, as well as the possibility to release the toxin upon a temperature increase. Furthermore, once the protocol for binding aptamers to SU-8 is established, the influence of the SU-8 number and surface area on the quantity of bounded aptamers needs to be investigated. This system could afterwards be coupled to a detection unit for saxitoxin quantification.

The microfluidic platform for VOCs detection excellently worked in the optical setup developed at UULM and allowed detection of up to ten VOCs species. However its performance could be further improved by applying the changes related to the channel length, the rubber thickness and the fluidic connectors applied to the baseline flow cell also to the other two configurations initially proposed, i.e. the top centerline flow entry cell and the flow cell with tapered height. As described in the literature these configurations could help reducing the overall resistance to mass transfer and speeding up the response time of the sensor.

Finally, all these systems can be integrated in the SCHeMA submersible probes for continuous *in situ* measurements in marine environment. The trace metal sensors with on-chip WE and CE developed in this thesis have already been successfully deployed for several field campaigns throughout the duration of the project.

References

[1]   Sciences B. Basic Education in Analytical Chemistry 2001;17:571–3.

[2]   Cuenca a., Agrisuelas J, García-Jareño JJ, Vicente F. Alternating current electrogravimetry of copper electrodissolution in a sulfuric acid solution. Electrochim Acta 2017;235:374–83. doi:10.1016/j.electacta.2017.03.079.

[3]   Arakelyan VG, Sakodynskii KI. The contribution of gas chromatography to the identification of substances. Chromatogr Rev 1971;15:93–110. doi:10.1016/0009-5907(71)80015-7.

[4]   Coppa M, Revello-Chion A, Giaccone D, Ferlay A, Tabacco E, Borreani G. Comparison of near and medium infrared spectroscopy to predict fatty acid composition on fresh and thawed milk. Food Chem 2014;150:49–57. doi:10.1016/j.foodchem.2013.10.087.

[5]   Miller KE, Synovec RE. Review of analytical measurements facilitated by drop formation technology. Talanta 2000;51:921–33.

[6]   Laitinen H a. History of Analytical Chemistry. Talanta 1989;36:1–9. doi:10.1016/B978-0-08-010980-0.50005-5.

[7]   Koudelka-hep M, Wal PD Van Der. Microelectrode sensors for biomedical and environmental applications 2007;45:2437–41.

[8]   Hahn CEW. Tutorial ReviewElectrochemical analysis of clinicalblood-gases, gases and vapours. Analyst 1998;123:57–86. doi:10.1039/a708951a.

[9]   Machini WBS, Martin CS, Martinez MT, Teixeira SR, Gomes HM, Teixeira MFS. Development of an electrochemical sensor based on nanostructured hausmannite-type manganese oxide for detection of sodium ions. Sensors Actuators, B Chem 2013;181:674–80. doi:10.1016/j.snb.2013.01.030.

[10]   Wang J. Electrochemical Glucose Biosensors. Chem Rev 2007;108:814–25. doi:10.1021/cr068123a.

[11]   Razumas V, Kanapieniené J, Nylander T, Engström S, Larsson K. Electrochemical biosensors for glucose, lactate, urea, and creatinine based on enzymes entrapped in a cubic liquid crystalline phase. Anal Chim Acta 1994;289:155–62. doi:10.1016/0003-2670(94)80098-7.

[12]   Adams RN. Probing brain chemistry with electroanalytical techniques. Anal Chem 1976;48:1126A–1138A. doi:10.1021/ac50008a001.

[13]   Jovic M, Zhu Y, Lesch A, Bondarenko A, Cortes-Salazar F, Gumy F, et al. Inkjet-printed microtiter plates for portable electrochemical immunoassays. J Electroanal Chem 2017;786:69–76. doi:10.1016/j.jelechem.2016.12.051.

[14]   Ochiai LM, Agustini D, Figueiredo-Filho LCS, Banks CE, Marcolino-Junior LH, Bergamini MF. Electroanalytical thread-device for estriol determination using screen-printed carbon electrodes modified with carbon nanotubes. Sensors Actuators B Chem 2017;241:978–84. doi:10.1016/j.snb.2016.10.150.

[15] de Macedo IYL, Garcia LF, Oliveira Neto JR, de Siqueira Leite KC, Ferreira VS, Ghedini PC, et al. Electroanalytical tools for antioxidant evaluation of red fruits dry extracts. Food Chem 2017;217:326–31. doi:10.1016/j.foodchem.2016.08.082.

[16] Chaocharoen W, Schulte a., Suginta W. hYKL-40 cancer biomarker electroanalysis in serum samples and model cell lysates: capacitive immunosensing compared with enzyme label immunosorbent assays (ELISA). Analyst 2017;142:503–10. doi:10.1039/C6AN02239A.

[17] Teixeira MFS, Segnini A, Moraes FC, Marcolino-Júnior LH, Fatibello-Filho O, Cavalheiro ÉTG. Determination of vitamin B6 (pyridoxine) in pharmaceutical preparations by cyclic voltammetry at a copper(II) hexacyanoferrate(III) modified carbon paste electrode. J Braz Chem Soc 2003;14:316–21. doi:Doi 10.1590/S0103-50532003000200021.

[18] Fojta M, Danhel A, Havran L, Vyskocil V. Recent progress in electrochemical sensors and assays for DNA damage and repair. TrAC - Trends Anal Chem 2016;79:160–7. doi:10.1016/j.trac.2015.11.018.

[19] Rivera L, Izquierdo D, Garcés I, Salinas I, Alonso J, Puyol M. Simple dip-probe fluorescence setup sensor for in situ environmental determinations. Sensors Actuators, B Chem 2009;137:420–5. doi:10.1016/j.snb.2009.01.064.

[20] Martínez-Cisneros CS, Ibáñez-García N, Valdés F, Alonso J. LTCC microflow analyzers with monolithic integration of thermal control. Sensors Actuators, A Phys 2007;138:63–70. doi:10.1016/j.sna.2007.04.059.

[21] Gallardo J, Alegert S, Del Valle M. A flow-injection electronic tongue based on potentiometric sensors for the determination of nitrate in the presence of chloride. Sensors Actuators, B Chem 2004;101:72–80. doi:10.1016/j.snb.2004.02.027.

[22] Plata MR, Contento AM, Ríos A. State-of-the-art of (bio)chemical sensor developments in analytical Spanish groups. Sensors (Basel) 2010;10:2511–76. doi:10.3390/s100402511.

[23] Pang X, Shaw MD, Lewis AC, Carpenter LJ, Batchellier T. Electrochemical ozone sensors: A miniaturised alternative for ozone measurements in laboratory experiments and air-quality monitoring. Sensors Actuators, B Chem 2017;240:829–37. doi:10.1016/j.snb.2016.09.020.

[24] Marrazza G, Chianella I, Mascini M. Disposable DNA electrochemical biosensors for environmental monitoring. Anal Chim Acta 1999;387:297–307. doi:10.1016/S0003-2670(99)00051-3.

[25] Miura N, Lu G, Yamazoe N. Progress in mixed-potential type devices based on solid electrolyte for sensing redox gases. Solid State Ionics 2000;136–137:533–42. doi:10.1016/S0167-2738(00)00411-2.

[26] Li J, Kuang D, Feng Y, Zhang F, Xu Z, Liu M. A graphene oxide-based electrochemical sensor for sensitive determination of 4-nitrophenol. J Hazard Mater 2012;201–202:250–9. doi:10.1016/j.jhazmat.2011.11.076.

[27] Ciglenečki I, Bura-Nakić E, Inzelt G. Voltammetry as an alternative tool for trace metal detection in peloid marine sediments. Electroanalysis 2007;19:1437–45. doi:10.1002/elan.200703877.

[28] Orr JC, Fabry VJ, Aumont O, Bopp L, Doney SC, Feely R a., et al. Anthropogenic ocean acidification over the twenty-first century and its impact on calcifying organisms. Nature

2005;437:681–6. doi:10.1038/nature04095.

[29] Elser JJ, Bracken MES, Cleland EE, Gruner DS, Harpole WS, Hillebrand H, et al. Global analysis of nitrogen and phosphorus limitation of primary producers in freshwater, marine and terrestrial ecosystems. Ecol Lett 2007;10:1135–42. doi:10.1111/j.1461-0248.2007.01113.x.

[30] Tercier-Waeber M Lou, Stoll S, Slaveykova VI. Trace metal behavior in surface waters: Emphasis on dynamic spéciation, sorption processes and bioavailability. Arch Des Sci 2012;65:119–42.

[31] Wakeham SG, Canuel a, Hole W, a WHM a US, Doering PH. Geochemistry Mesocosm of volatile organic compounds in seawater : experiments with " 14C-model compounds. Geochim Cosmochim Acta 1986;50.

[32] Smith V. Eutrophication of freshwater and coastal marine ecosystems a global problem. Environ Sci Pollut Res 2003;10:126–39. doi:10.1065/espr2002.12.142.

[33] Poletti R, Milandri a., Pompei M. Algal biotoxins of marine origin: New indications from the European Union. Vet Res Commun 2003;27:173–82. doi:10.1023/B:VERC.0000014136.98850.b1.

[34] Clarke JS, Achterberg EP, Connelly DP, Schuster U, Mowlem M. Developments in marine pCO2 measurement technology; towards sustained in situ observations. TrAC - Trends Anal Chem 2017;88:53–61. doi:10.1016/j.trac.2016.12.008.

[35] Sato H. Characterization of amine-functionalized electrode for aqueous carbon dioxide (CO2) direct detection 2017;20046:20046. doi:10.1063/1.4975279.

[36] Zehr JP, Ward BB. Nitrogen Cycling in the Ocean : New Perspectives on Processes and Paradigms MINIREVIEW Nitrogen Cycling in the Ocean : New Perspectives on Processes and Paradigms. Appl Environ Microbiol 2002;68:1015–24. doi:10.1128/AEM.68.3.1015.

[37] Wang T, Schlueter KT, Riehl BL, Johnson JM, Heineman WR. Simplified nitrate-reductase-based nitrate detection by a hybrid thin-layer controlled potential coulometry/spectroscopy technique. Anal Chem 2013;85:9486–92. doi:10.1021/ac400987u.

[38] Moorcroft MJ, Davis J, Compton RG. Detection and determination of nitrate and nitrite: a review. Talanta 2001;54:785–803.

[39] Li QP, Hansell DA, Zhang J. OCEANOGRAPHY : METHODS Underway monitoring of nanomolar nitrate plus nitrite and phosphate in oligotrophic seawater 2008:319–26.

[40] Adornato LR, Kaltenbacher E a, Greenhow DR, Byrne RH. High-resolution in situ analysis of nitrate and phosphate in the oligotrophic ocean. Environ Sci Technol 2007;41:4045–52.

[41] Feng S, Zhang M, Huang Y, Yuan D, Zhu Y. Simultaneous determination of nanomolar nitrite and nitrate in seawater using reverse flow injection analysis coupled with a long path length liquid waveguide capillary cell. Talanta 2013;117:456–62. doi:10.1016/j.talanta.2013.09.042.

[42] Transactions ECS, Society TE. Microfabricated Systems to Measure Marine Variables S. Aravamudhan 2012;50:513–21.

[43] Sohail M, De Marco R, Lamb K, Bakker E. Thin layer coulometric determination of nitrate in fresh waters. Anal Chim Acta 2012;744:39–44. doi:10.1016/j.aca.2012.07.026.

[44] Morel FMM. The Biogeochemical Cycles of Trace Metals in the Oceans. Science (80-) 2003;300:944–7. doi:10.1126/science.1083545.

[45] Achterberg EP, Braungardt C. Stripping voltammetry for the determination of trace metal speciation and in-situ measurements of trace metal distributions in marine waters. Anal Chim Acta 1999;400:381–97. doi:10.1016/S0003-2670(99)00619-4.

[46] Wang J, Lu J, Hocevar S, Farias P, Ogorevc B. Bismuth-coated carbon electrodes for anodic stripping voltammetry. Anal Chem 2000;72:3218–22.

[47] Tercier ML, Buffle J, Zirino a., De Vitre RR. In situ voltammetric measurement of trace elements in lakes and oceans. Anal Chim Acta 1990;237:429–37. doi:10.1016/S0003-2670(00)83947-1.

[48] Etienne M, Bessiere J, Walcarius a. Voltammetric detection of copper (II) at a carbon paste electrode containing an organically modifed silica. Synthesis (Stuttg) 2001;76:531–8.

[49] Yantasee W, Lin Y, Zemanian TS, Fryxell GE. Voltammetric detection of lead(ii) and mercury(ii) using a carbon paste electrode modified with thiol self-assembled monolayer on mesoporous silica (SAMMS). Analyst 2003;128:467–72. doi:10.1039/b300467h.

[50] Laschi S, Palchetti I, Mascini M. Gold-based screen-printed sensor for detection of trace lead. Sensors Actuators, B Chem 2006;114:460–5. doi:10.1016/j.snb.2005.05.028.

[51] Nolan M a., Kounaves SP. Microfabricated array of iridium microdisks as a substrate for direct determination of Cu2+ or Hg2+ using square-wave anodic stripping voltammetry. Anal Chem 1999;71:3567–73. doi:10.1021/ac990126i.

[52] Kokkinos C, Economou A, Raptis I, Efstathiou CE. Lithographically fabricated disposable bismuth-film electrodes for the trace determination of Pb(II) and Cd(II) by anodic stripping voltammetry. Electrochim Acta 2008;53:5294–9. doi:10.1016/j.electacta.2008.02.079.

[53] Kefala G, Economou a, Voulgaropoulos a, Sofoniou M. A study of bismuth-film electrodes for the detection of trace metals by anodic stripping voltammetry and their application to the determination of Pb and Zn in tapwater and human hair. Talanta 2003;61:603–10. doi:10.1016/S0039-9140(03)00350-3.

[54] Zou Z, Jang a, Macknight E, Wu P, Do J, Bishop P, et al. Environmentally friendly disposable sensors with microfabricated on-chip planar bismuth electrode for in situ heavy metal ions measurement. Sensors Actuators B Chem 2008;134:18–24. doi:10.1016/j.snb.2008.04.005.

[55] Waeber MT, Bakker E, Nardin C, Mongin S, Prado E, Botia MC, et al. FP7-OCEAN-2013 - SCHeMA : integrated in Situ Chemical MApping Probes 2015.

[56] Ma J, Adornato L, Byrne RH, Yuan D. Determination of nanomolar levels of nutrients in seawater. TrAC Trends Anal Chem 2014;60:1–15. doi:10.1016/j.trac.2014.04.013.

[57] Fighera M., van der Wal P.D. SH. Comparison of six different printed Ag inks for coulometric removal of chloride ions from seawater : Towards an integrated microfluidic platform for desalination. ECS Trans 2016;75:1–12. doi:10.1149/07541.0001ecst.

[58]   Fighera M, Wal PD Van Der, Shea H. Microfluidic Platform for Seawater Desalination by Coulometric Removal of Chloride Ions through Printed Ag Electrodes. J Electrochem Soc 2017;164. doi:10.1149/2.1761712jes.

[59]   Jaber a. MY, Mehanna N a., Sultan SM. Determination of ammonium and organic bound nitrogen by inductively coupled plasma emission spectroscopy. Talanta 2009;78:1298–302. doi:10.1016/j.talanta.2009.01.060.

[60]   Chapple G, Byrne JP. Direct determination of trace metals in sea-water using electrothermal vaporization inductively coupled plasma mass spectrometry. J Anal At Spectrom 1996;11:549. doi:10.1039/ja9961100549.

[61]   Jia X, Gong D, Han Y, Wei C, Duan T, Chen H. Fast speciation of mercury in seawater by short-column high-performance liquid chromatography hyphenated to inductively coupled plasma spectrometry after on-line cation exchange column preconcentration. Talanta 2012;88:724–9. doi:10.1016/j.talanta.2011.10.026.

[62]   Grygolowicz-Pawlak E, Bakker E. Thin layer coulometry with ionophore based ion-selective membranes. Anal Chem 2010;82:4537–42. doi:10.1021/ac100524z.

[63]   Gong G, Nagasawa H, Kanezashi M, Tsuru T. Reverse osmosis performance of layered-hybrid membranes consisting of an organosilica separation layer on polymer supports. J Memb Sci 2015;494:104–12. doi:10.1016/j.memsci.2015.07.039.

[64]   Sadrzadeh M, Mohammadi T. Sea water desalination using electrodialysis. Desalination 2008;221:440–7. doi:10.1016/j.desal.2007.01.103.

[65]   Abdulrahim HK, Darwish M a. Thermal desalination and air conditioning using absorption cycle. Desalin Water Treat 2015;55:3310–29. doi:10.1080/19443994.2014.939492.

[66]   Najafi B, Shirazi A, Aminyavari M, Rinaldi F, Taylor R a. Exergetic, economic and environmental analyses and multi-objective optimization of an SOFC-gas turbine hybrid cycle coupled with an MSF desalination system. Desalination 2014;334:46–59. doi:10.1016/j.desal.2013.11.039.

[67]   Farmer JC. Capacitive Deionization of NaCl and NaNO[sub 3] Solutions with Carbon Aerogel Electrodes. J Electrochem Soc 1996;143:159. doi:10.1149/1.1836402.

[68]   Biesheuvel PM, van der Wal a. Membrane capacitive deionization. J Memb Sci 2010;346:256–62. doi:10.1016/j.memsci.2009.09.043.

[69]   Lee JH, Choi JH. The production of ultrapure water by membrane capacitive deionization (MCDI) technology. J Memb Sci 2012;409–410:251–6. doi:10.1016/j.memsci.2012.03.064.

[70]   Li H, Zou L. Ion-exchange membrane capacitive deionization: A new strategy for brackish water desalination. Desalination 2011;275:62–6. doi:10.1016/j.desal.2011.02.027.

[71]   AlMarzooqi F a., Al Ghaferi A a., Saadat I, Hilal N. Application of Capacitive Deionisation in water desalination: A review. Desalination 2014;342:3–15. doi:10.1016/j.desal.2014.02.031.

[72]   Li M, Anand RK. Recent advancements in ion concentration polarization. Analyst 2016:3496–510. doi:10.1039/C6AN00194G.

[73] Rubinstein I, Shtilman L. Voltage against current curves of cation exchange membranes. J Chem Soc Faraday Trans 2 1979;75:231. doi:10.1039/f29797500231.

[74] Holtzel A, Tallarek U. Ionic conductance of nanopores in microscale analysis systems: Where microfluidics meets nanofluidics. J Sep Sci 2007;30:1398–419. doi:10.1002/jssc.200600427.

[75] Kim SJ, Ko SH, Kang KH, Han J. Direct seawater desalination by ion concentration polarization. Nat Nanotechnol 2010;5:297–301. doi:10.1038/nnano.2010.34.

[76] Knust KN, Hlushkou D, Anand RK, Tallarek U, Crooks RM. Electrochemically mediated seawater desalination. Angew Chemie - Int Ed 2013;52:8107–10. doi:10.1002/anie.201302577.

[77] MacDonald BD, Gong MM, Zhang P, Sinton D. Out-of-plane ion concentration polarization for scalable water desalination. Lab Chip 2014;14:681–5. doi:10.1039/C3LC51255J.

[78] Smith KC, Dmello R. Na-Ion Desalination (NID) Enabled by Na-Blocking Membranes and Symmetric Na-Intercalation : Porous-Electrode Modeling 2016;163. doi:10.1149/2.0761603jes.

[79] Smith KC. Electrochimica Acta Theoretical evaluation of electrochemical cell architectures using cation intercalation electrodes for desalination. Electrochim Acta 2017;230:333–41. doi:10.1016/j.electacta.2017.02.006.

[80] Porada S, Bukowska P, Shrivastava A, Biesheuvel PM, Smith KC. Nickel Hexacyanoferrate Electrodes for Cation Intercalation Desalination n.d.

[81] Lee J, Kim S, Yoon J. Rocking Chair Desalination Battery Based on Prussian Blue Electrodes 2017. doi:10.1021/acsomega.6b00526.

[82] Grygolowicz-Pawlak E, Sohail M, Pawlak M, Neel B, Shvarev A, de Marco R, et al. Coulometric sodium chloride removal system with Nafion membrane for seawater sample treatment. Anal Chem 2012;84:6158–65. doi:10.1021/ac301096r.

[83] Bu P. Carrier-Based Ion-Selective Electrodes and Bulk Optodes . 2 . Ionophores for Potentiometric and Optical Sensors 1998;2665.

[84] Cuartero M, Crespo A, Bakker E. Tandem Electrochemical Desalination − Potentiometric Nitrate Sensing for Seawater Analysis 2015. doi:10.1021/acs.analchem.5b01973.

[85] Lingane JJ. Coulometric Analysis. J Am Chem Soc 1945;67:1916–22. doi:10.1021/ja01227a013.

[86] R. de Levie. Electrochemical response of porous and rough electrodes. Adv Electrochem Electrochem Eng 1967;6:329–97.

[87] A.J. Bard and L.R. Faulkner. Electrochemical methods Fundamentals and applications. 1980.

[88] Confalonieri F. Idronaut communication 2014.

[89] T.C. Hodge SAB-A and PAK. Stresses in Thin Film Metallization. IEEE Trans Components, Packag Manuf Technol 1997;20:241–50.

[90] De Rossi F, Brown TM, Reale A, Di Carlo A. Large-Area Electrodeposition of

Counterelectrodes Utilizing the Same Integrated Conductive Grid for Fabrication of Parallel Flexible Dye Solar Cell Modules. IEEE J Photovoltaics 2014;4:1552–9. doi:10.1109/JPHOTOV.2014.2354255.

[91]   Matlosz M, Vallotton PH, West a C, Landolt D. Nonuniform current distribution and thickness during electrodeposition onto resistive substrates. J Electrochem Soc 1992;139:752–61. doi:10.1149/1.2069297.

[92]   Zhang Z, Zhu W. Controllable synthesis and sintering of silver nanoparticles for inkjet-printed flexible electronics. J Alloys Compd 2015;649:687–93. doi:10.1016/j.jallcom.2015.07.195.

[93]   Kim J, Duraisamy N, Lee T-M, Kim I, Choi K-H. Screen printed silver top electrode for efficient inverted organic solar cells. Mater Res Bull 2015;70:412–5. doi:10.1016/j.materresbull.2015.04.052.

[94]   Jin Lee S, Kim Y-J, Young Yeo S, Lee E, Sun Lim H, Kim M, et al. Centro-Apical Self-Organization of Organic Semiconductors in a Line-Printed Organic Semiconductor: Polymer Blend for One-Step Printing Fabrication of Organic Field-Effect Transistors. Sci Rep 2015;5:14010. doi:10.1038/srep14010.

[95]   Kim J, Kim J, Ahn B, Hassinen T, Jung Y, Ko S. Optimization and improvement of TIPS–pentacene transistors (OTFT) with UV–ozone and chemical treatments using an all-step solution process. Curr Appl Phys 2015;15:1238–44. doi:10.1016/j.cap.2015.07.012.

[96]   Morrin A, Ngamna O, O'Malley E, Kent N, Moulton SE, Wallace GG, et al. The fabrication and characterization of inkjet-printed polyaniline nanoparticle films. Electrochim Acta 2008;53:5092–9. doi:10.1016/j.electacta.2008.02.010.

[97]   Gao G, Schilling AF, Hubbell K, Yonezawa T, Truong D, Hong Y, et al. Improved properties of bone and cartilage tissue from 3D inkjet-bioprinted human mesenchymal stem cells by simultaneous deposition and photocrosslinking in PEG-GelMA. Biotechnol Lett 2015;37:2349–55. doi:10.1007/s10529-015-1921-2.

[98]   Parashkov R, Becker E, Riedl T, Johannes HH, Kowalsky W. Large area electronics using printing methods. Proc IEEE 2005;93:1321–9. doi:10.1109/JPROC.2005.850304.

[99]   Hayat A, Marty J. Disposable Screen Printed Electrochemical Sensors: Tools for Environmental Monitoring. Sensors 2014;14:10432–53. doi:10.3390/s140610432.

[100] da Silva ETSG, Miserere S, Kubota LT, Merkoçi A. A simple on-plastic/paper inkjet-printed solid-state Ag/AgCl pseudo-reference electrode. Anal Chem 2014:190–6. doi:10.1021/ac503029q.

[101] Kim M, Jia M, Kim T. Ion concentration polarization in a single and open microchannel induced by a surface-patterned perm-selective film. Analyst 2013;138:1370–8. doi:10.1039/c2an36346a.

[102] F. Marken, A. Neudeck AMB. Electroanalytical methods. 2nd ed. Springer-Verlag Berlin Heidelberg; 2010.

[103] Bruice PY. Organic Chemistry. 5th ed. Pearson Prentice Hall; 2007.

[104] Chitvoranund N, Jiemsirilers S, Kashima DP. Effects of surface treatments on adhesion of

silver film on glass substrate fabricated by electroless plating. J Aust Ceram Soc 2013;49:62–9. doi:10.4028/www.scientific.net/AMR.664.566.

[105] R. Greef, R. Peat, L.M. Peter, D. Pletcher JR. Instrumental Methods in Electrochemistry. Ellis Horwood Limited; 1985.

[106] Bott AW, Ph D. Electrochemical Techniques for the Characterization of Redox Polymers 2001;3:71–5.

[107] Tercier-Waeber M-L, Taillefert M. Remote in situ voltammetric techniques to characterize the biogeochemical cycling of trace metals in aquatic systems. J Environ Monit 2008;10:30–54. doi:10.1039/b714439n.

[108] Tercier ML, Buffle J, Geneva CH. Gel-Integrated Microelectrode Arrays for Direct Voltammetric Measurements of Heavy Metals in Natural Waters and Other Complex Media. Anal Chem 1998;70:2949–56. doi:10.1021/ac971194c.

[109] Fighera M., van der Wal P.D., Tercier-Waeber M.-L. SH. Three-electrode on-chip sensors for voltammetric detection of trace metals in natural waters. ECS Trans 2016;75:303–14. doi:10.1149/07516.0303ecst.

[110] Buffle J, Tercier ML, Parthasarathy N, Wilkinson KJ. Analytical Techniques for the in situ Measurement and Speciation of Trace Compounds in Natural Waters. Chimia (Aarau) 1997;51:690–3.

[111] Wang J. Stripping Analysis: Principles, Instrumentation, and Applications. VCH, New York; 1985.

[112] Buffle J. TWM-L. In situ voltammetry: concepts and practice for trace analysis and speciation. situ Monit. Aquat. Syst. Chem. Anal. Speciat. Wiley, 2000.

[113] Tercier-Waeber M-L, Buffle J, Confalonieri F, Riccardi G, Sina a, Graziottin F, et al. Submersible voltammetric probes for in situ real-time trace element measurements in surface water, groundwater and sediment-water interface. Meas Sci Technol 1999;10:1202–13. doi:10.1088/0957-0233/10/12/312.

[114] Fiaccabrino GC. Thin-Film Microelectrode Arrays: Materials & Designs. University of Neuchâtel, 1996.

[115] Kounaves SP. Deposition and Stripping Properties of Mercury on Iridium Electrodes. J Electrochem Soc 1986;133:2495. doi:10.1149/1.2108457.

[116] Tercier M-L, Parthasarathy N, Bufle J. Reproducible, reliable and rugged Hg-plated Ir-based microelectrode for in situ measurements in natural waters. Electroanalysis 1995;7:55–63.

[117] Belmont C, Tercier ML, Buffle J, Fiaccabrino GC, Koudelka-Hep M. Mercury-plated iridium-based microelectrode arrays for trace metals detection by voltammetry: Optimum conditions and reliability. Anal Chim Acta 1996;329:203–14. doi:10.1016/0003-2670(96)00116-X.

[118] Wang J, Foster N, Armalis S, Larson D, Zirino A, Olsen K. Remote stripping electrode for in situ monitoring of labile copper in the marine environment. Anal Chim Acta 1995;310:223–31. doi:10.1016/0003-2670(95)00155-S.

[119] Herdan J, Feeney R, Kounaves SP, Flannery AF, Storment CW, Kovacs GT a, et al. Field evaluation of an electrochemical probe for in situ screening of heavy metals in groundwater. Environ Sci Technol 1998;32:131–6. doi:10.1021/es970389z.

[120] Luther GW, Reimers CE, Nuzzio DB, Lovalvo D. In situ deployment of voltammetric, potentiometric, and amperometric microelectrodes from a ROV to determine dissolved O2, Mn, Fe, S(-2), and pH in porewaters. Environ Sci Technol 1999;33:4352–6. doi:10.1021/es9904991.

[121] Tercier-Waeber ML, Confalonieri F, Riccardi G, Sina A, Nöel S, Buffle J, et al. Multi Physical - Chemical profiler for real-time in situ monitoring of trace metal speciation and master variables: Development, validation and field applications. Mar Chem 2005;97:216–35. doi:10.1016/j.marchem.2005.03.004.

[122] Tercier-Waeber M-L, Confalonieri F, Koudelka-Hep M, Dessureault-Rompré J, Graziottin F, Buffle J. Gel-Integrated Voltammetric Microsensors and Submersible Probes as Reliable Tools for Environmental Trace Metal Analysis and Speciation. Electroanalysis 2008;20:240–58. doi:10.1002/elan.200704067.

[123] G. C. Fiaccabrino, N. F. de Rooij, M. Koudelka-Hep JH and A van den, Berg. No Title. In: G.Hoarvai JB, editor. situ Monit. Aquat. Syst. Chem. Anal. Speciat., Wiley; 2000, p. 571–610.

[124] Myers DJ, Osteryoung J. Determination of arsenic(III) at the parts-per-billion level by differential pulse polarography. Anal Chem 1973;45:267–71. doi:10.1021/ac60324a033.

[125] Liu Z-G, Huang X-J. Voltammetric determination of inorganic arsenic. TrAC Trends Anal Chem 2014;60:25–35. doi:10.1016/j.trac.2014.04.014.

[126] Abdolmohammad-Zadeh H, Talleb Z. Speciation of As(III)/As(V) in water samples by a magnetic solid phase extraction based on Fe_3O_4/Mg-Al layered double hydroxide nano-hybrid followed by chemiluminescence detection. Talanta 2014;128:147–55. doi:10.1016/j.talanta.2014.04.070.

[127] Gustaf Forsberg, Jerome W. O'Laughlin and RGM. Determination of Arsenic by Anodic Stripping Voltammetry and Differential Pulse Anodic Stripping Voltammetry. Anal Chem 1975;47.

[128] Hung DQ, Nekrassova O, Compton RG. Analytical methods for inorganic arsenic in water: a review. Talanta 2004;64:269–77. doi:10.1016/j.talanta.2004.01.027.

[129] Simm A, Banks C, Compton R. Sonoelectroanalytical Detection of Ultra-Trace Arsenic. Electroanalysis 2005;17:335–42. doi:10.1002/elan.200403110.

[130] Touilloux R, Tercier-Waeber M-L, Bakker E. Direct arsenic(III) sensing by a renewable gold plated Ir-based microelectrode. Analyst 2015;140:3526–34. doi:10.1039/C5AN00151J.

[131] Hossain MM, Islam MM, Ferdousi S, Okajima T, Ohsaka T. Anodic Stripping Voltammetric Detection of Arsenic(III) at Gold Nanoparticle-Modified Glassy Carbon Electrodes Prepared by Electrodeposition in the Presence of Various Additives. Electroanalysis 2008;20:2435–41. doi:10.1002/elan.200804339.

[132] Khairy M, Kampouris DK, Kadara RO, Banks CE. Gold Nanoparticle Modified Screen Printed Electrodes for the Trace Sensing of Arsenic(III) in the Presence of Copper(II).

Electroanalysis 2010;22:2496–501. doi:10.1002/elan.201000226.

[133] Huang J-F, Chen H-H. Gold-nanoparticle-embedded nafion composite modified on glassy carbon electrode for highly selective detection of arsenic(III). Talanta 2013;116:852–9. doi:10.1016/j.talanta.2013.07.063.

[134] Lan Y, Luo H, Ren X, Wang Y, Wang L. Glassy Carbon Electrode Modified with Citrate Stabilized Gold Nanoparticles for Sensitive Arsenic (III) Detection. Anal Lett 2012;45:1184–96. doi:10.1080/00032719.2012.673108.

[135] Feeney R, Kounaves SP. On-Site Analysis of Arsenic in Groundwater Using a Microfabricated Gold Ultramicroelectrode Array 2000;72:2222–8.

[136] Zhang Y, Li Q, Sun L, Zhai J. The electrocatalytic reduction and removal of arsenate by poly(aniline-co-o-aminophenol). J Electroanal Chem 2009;636:47–52. doi:10.1016/j.jelechem.2009.09.009.

[137] Mu S. Poly(aniline-co-o-aminophenol) nanostructured network: Electrochemical controllable synthesis and electrocatalysis. Electrochim Acta 2006;51:3434–40. doi:10.1016/j.electacta.2005.09.039.

[138] Mu S. Direct determination of arsenate based on its electrocatalytic reduction at the poly(aniline-co-o-aminophenol) electrode. Electrochem Commun 2009;11:1519–22. doi:10.1016/j.elecom.2009.05.050.

[139] Bontidean I, Mortari A, Leth S, Brown NL, Karlson U, Larsen MM, et al. Biosensors for detection of mercury in contaminated soils. Environ Pollut 2004;131:255–62. doi:10.1016/j.envpol.2004.02.019.

[140] Abollino O, Giacomino A, Malandrino M, Piscionieri G, Mentasti E. Determination of mercury by anodic stripping voltammetry with a gold nanoparticle-modified glassy carbon electrode. Electroanalysis 2008;20:75–83. doi:10.1002/elan.200704044.

[141] Shinwari MW, Zhitomirsky D, Deen I a, Selvaganapathy PR, Deen MJ, Landheer D. Microfabricated reference electrodes and their biosensing applications. Sensors (Basel) 2010;10:1679–715. doi:10.3390/s100301679.

[142] J. Buffle MLT-W. No Title. In: J. Buffle GH, editor. situ Monit. Aquat. Syst. Chem. Anal. Speciat., Wiley; 2000, p. 279–405.

[143] G. W. Luther, III, A. B. Bono MT and SCC. No Title. In: M. Taillefer TFR, editor. Environ. Electrochem. Anal. Trace Elem. Biogeochem., Chemical Society, Washington, DC; 2002, p. 54–72.

[144] Huang I-Y, Huang R-S. Fabrication and characterization of a new planar solid-state reference electrode for ISFET sensors. Thin Solid Films 2002;406:255–61. doi:10.1016/S0040-6090(01)01783-7.

[145] Tymecki Ł, Zwierkowska E, Koncki R. Screen-printed reference electrodes for potentiometric measurements. Anal Chim Acta 2004;526:3–11. doi:10.1016/j.aca.2004.08.056.

[146] Kakiuchi T, Yoshimatsu T, Nishi N. New class of Ag/AgCl electrodes based on hydrophobic ionic liquid saturated with AgCl. Anal Chem 2007;79:7187–91. doi:10.1021/ac070820v.

[147] Bakker E. Hydrophobic Membranes as Liquid Junction-Free Reference Electrodes. Electroanalysis 1999;11:788–92. doi:10.1002/(SICI)1521-4109(199907)11:10/11<788::AID-ELAN788>3.0.CO;2-4.

[148] A. Vincze GH. No Title. In: A. J. Ricco, M. A. Butler, P. Vanysec, G. Horvai AFS, editor. Chem. Biol. Sensors Anal. Electrochem. Methods, Electrochem. Soc. Proc. Ser., Sensor and Physical Electrochemistry Divisions, Pennington, NJ; 1997, p. 550–555.

[149] Mamińska R, Dybko A, Wróblewski W. All-solid-state miniaturised planar reference electrodes based on ionic liquids. Sensors Actuators B Chem 2006;115:552–7. doi:10.1016/j.snb.2005.10.018.

[150] Cicmil D, Anastasova S, Kavanagh A, Diamond D, Mattinen U, Bobacka J, et al. Ionic Liquid-Based, Liquid-Junction-Free Reference Electrode. Electroanalysis 2011;23:1881–90. doi:10.1002/elan.201100137.

[151] Bard AJ, Crayston J a., Kittlesen GP, Varco Shea T, Wrighton MS. Digital simulation of the measured electrochemical response of reversible redox couples at microelectrode arrays: consequences arising from closely spaced ultramicroelectrodes. Anal Chem 1986;58:2321–31. doi:10.1021/ac00124a045.

[152] J. Guo EL. Cyclic Voltammograms at Coplanar and Shallow Recessed Microdisc Electrode Arrays: Guidelines for Design and Experiment. Anal Chem 2009;81(1):130–8. doi:10.1242/jcs.03292.Multiple.

[153] Bond A. M., Luscombe D., Oldham K. D. ZCG. Comparison of the Chronoamperometric Response at Inlaid and Recessed Disc Microelectrodes. J Electroanal Chem Interfacial Electrochem 1988;249:35–62.

[154] Ramaley L, Krause MS. Theory of Square Wave Voltammetry. Anal Chem 1969;41:1361–5. doi:10.1021/ac60280a005.

[155] R. A. Osteryoung JO. No Title. Phil Trans Roy Soc London, Ser A 1981;302:315.

[156] J. Osteryoung JJO. No Title. Electroanal Chem 1986;14:209.

[157] J. O., Accts Chem Res 1993;26:77.

[158] O 'dea JJ, Osteryoung JG. Characterization of Quasi-Reversible Surface Processes by Square-Wave Voltammetry. Anal Chem 1993;65:3090–7. doi:10.1021/ac00069a024.

[159] Bard AJ, Faulkner LR, York N, @Bullet C, Brisbane W, Toronto SE. ELECTROCHEMICAL METHODS Fundamentals and Applications. 1944. doi:10.1016/B978-0-12-381373-2.00056-9.

[160] Belmont C, Tercier ML, Buffle J, Fiaccabrino GC, Koudelka-Hep M. Mercury-plated iridium-based microelectrode arrays for trace metals detection by voltammetry: Optimum conditions and reliability. Anal Chim Acta 1996;329:203–14.

[161] Frey O. Personal communication n.d.

[162] Tercier M-L, Buffle J. Antifouling Membrane-Covered Voltammetric Microsensor for in Situ Measurements in Natural Waters. Anal Chem 1996;68:3670–8. doi:10.1021/ac960265p.

[163] Ilic B, Czaplewski D, Neuzil P, Stanczyk T, Blough J, Maclay GJ. Preparation and

characterization of platinum black electrodes. J Mater Sci 2000;35:3447–57. doi:10.1023/A:1004884723515.

[164] El Sawy EN, Birss VI. Nano-porous iridium and iridium oxide thin films formed by high efficiency electrodeposition. J Mater Chem 2009;19:8244. doi:10.1039/b914662h.

[165] Arquint P. Integrated Blood Gas Sensor for pO2, pCO2 and pH Based on Silicon Technology. 1994.

[166] Toyama S, Takei O, Tsuge M, Usami R, Horikoshi K, Kato S. Surface plasmon resonance of electrochemically deposited Au-black. Science (80-) 2002;4:540–4.

[167] Vilariño N, Fonfría ES, Louzao MC, Botana LM. Use of biosensors as alternatives to current regulatory methods for marine biotoxins. Sensors (Basel) 2009;9:9414–43. doi:10.3390/s91109414.

[168] Lawrence J.F. NB. Quantitative Determination of Paralytic Shellfish Poisoning Toxins in Shellfish by Using Prechromatographic Oxidation and Liquid Chromatography Fluorescence Detection. J AOAC 2001;84:1099–108.

[169] R.E. Gawley, H. Mao, M.M. Haque, J.B. Thorne, and J.S. Pharr, Visible Fluorescence Chemosensor for Saxitoxin. J Org Chem 2007;72:2187–91. doi:10.1038/jid.2014.371.

[170] Meagher RJ, Hatch A V., Renzi RF, Singh AK. An integrated microfluidic platform for sensitive and rapid detection of biological toxins. Lab Chip 2008;8:2046. doi:10.1039/b815152k.

[171] Campbell K, Rawn DFK, Niedzwiadek B, Elliott CT. Paralytic shellfish poisoning (PSP) toxin binders for optical biosensor technology: problems and possibilities for the future: a review. Food Addit Contam Part A Chem Anal Control Expo Risk Assess 2011;28:711–25. doi:10.1080/19440049.2010.531198.

[172] Handy SM, Yakes BJ, DeGrasse J a, Campbell K, Elliott CT, Kanyuck KM, et al. First report of the use of a saxitoxin-protein conjugate to develop a DNA aptamer to a small molecule toxin. Toxicon 2013;61:30–7. doi:10.1016/j.toxicon.2012.10.015.

[173] Talaei S., Frey O., Psoma S., van der Wal P.D. de RNF. Smart SU-8 pillars implemented in a microfluidic bioreactor for continuous measurement of glucose. Procedia Eng. 5, 2010, p. 448–51.

[174] Thomas N. et al. --. Proc. IEEE Micro Electro Mech. Syst., 2011, p. 233–6.

[175] Marie R, Schmid S, Johansson A, Ejsing L, Nordstr??m M, H??fliger D, et al. Immobilisation of DNA to polymerised SU-8 photoresist. Biosens Bioelectron 2006;21:1327–32. doi:10.1016/j.bios.2005.03.004.

[176] Bruus H. Theoretical Microfluidics. Oxford University Press; 2007.

[177] Razumovitch J, De França K, Kehl F, Wiki M, Meier W, Vebert C. Optimal hybridization efficiency upon immobilization of oligonucleotide double helices. J Phys Chem B 2009;113:8383–90. doi:10.1021/jp902383m.

[178] Zhu J., Shang J., Jia Y., Pei R., Stojanovic M. L q. Spatially selective release of aptamer-captured cells by temperature mediation. Nanobiotechnology 2014;8:2–9.

[179] Guenther A, Hewitt CN, Erickson D, Fall R, Geron C, Graedel T, et al. A global model of natural volatile organic compound emissions. J Geophys Res 1995;100:8873. doi:10.1029/94JD02950.

[180] J. Williams, Organic Trace Gases in the Atmosphere: An Overview. Environ Chem 2004;1(3):125–36.

[181] Atkinson R. Atmospheric chemistry of VOCs and NO(x). Atmos Environ 2000;34:2063–101. doi:10.1016/S1352-2310(99)00460-4.

[182] Tie X. Biogenic methanol and its impacts on tropospheric oxidants. Geophys Res Lett 2003;30:3–6. doi:10.1029/2003GL017167.

[183] Millet DB, Golstein AH, Allan JD, Bates TS, Boudries H, Bower KN, et al. Volatile organic compound measurements at Trinidad Head, California, during ITCT 2K2: Analysis of sources, atmospheric composition, and aerosol residence times. J Geophys Res D Atmos 2004;109:1–16. doi:10.1029/2003JD004026.

[184] Beale R, Liss PS, Dixon JL, Nightingale PD. Quantification of oxygenated volatile organic compounds in seawater by membrane inlet-proton transfer reaction/mass spectrometry. Anal Chim Acta 2011;706:128–34. doi:10.1016/j.aca.2011.08.023.

[185] Singh HB, Tabazadeh A, Evans MJ, Field BD, Jacob DJ, Sachse G, et al. Oxygenated volatile organic chemicals in the oceans: Inferences and implications based on atmospheric observations and air-sea exchange models. Geophys Res Lett 2003;30. doi:10.1029/2003GL017933.

[186] Kameyama S, Tanimoto H, Inomata S, Tsunogai U, Ooki A, Takeda S, et al. High-resolution measurement of multiple volatile organic compounds dissolved in seawater using equilibrator inlet-proton transfer reaction-mass spectrometry (EI-PTR-MS). Mar Chem 2010;122:59–73. doi:10.1016/j.marchem.2010.08.003.

[187] Mesarchaki E, Yassaa N, Hein D, Lutterbeck HE, Zindler C, Williams J. A novel method for the measurement of VOCs in seawater using needle trap devices and GC-MS. Mar Chem 2014;159:1–8. doi:10.1016/j.marchem.2013.12.001.

[188] EC Council Directives 76/464/EEC, 86/280/EEC, 88/347/EEC, 90/415/EEC and 91/692/EEC n.d.

[189] S. R. Chlorinated Organic Compounds in the Environment (Boca Raton, FL: Chemical Rubber Company) 1997.

[190] Mizaikoff B. Mid-infrared evanescent wave sensors - a novel approach for subsea monitoring. Meas Sci Technol 1999;10:1185–94. doi:10.1088/0957-0233/10/12/310.

[191] Phillips C, Jakusch M, Steiner H, Mizaikoff B, Fedorov AG. Model-based optimal design of polymer-coated chemical sensors. Anal Chem 2003;75:1106–15. doi:10.1021/ac020471z.

[192] Ning X., Yang J., Zhao C.L. CCC. PDMS-coated fiber volatile organic compounds sensors. Appl Opt 2016;55:3543–8.

[193] Pham D., Gault R. A comparison of rapid prototyping technologies. Int J Mach Tools Manuf 1998;38:1257–87. doi:10.1016/S0890-6955(97)00137-5.

[194] Wang Z, Abdulla R, Parker B, Samanipour R, Ghosh S, Kim K. A simple and high-resolution stereolithography-based 3D bioprinting system using visible light crosslinkable bioinks. Biofabrication 2015;7:45009. doi:10.1088/1758-5090/7/4/045009.

[195] M. Fighera P van der W. Delivravble D5.3 – Optimized microfluidic platform for VOCs and biotoxin preconcentration 2016.

[196] Dettenrieder C. SCHeMA 42M project meeting - Arcachon, France 2017.

Glossary

AFA	Atelier de Fabrication Additive
AFM	Atomic Force Microscopy
Ag/AgCl	Silver/Silver Chloride
AgCN	Silver Cyanide
AgX	Silver halide
APS	Aminopropyltriethoxy silane
APTES	(3-Aminopropyl)triethoxysilane
As(III)	arsenite
As(V)	arsenate
AuNPs	Gold Nanoparticles
BPE	Bipolar electrode
Ca^{2+}	Calcium
Cd(II)	Cadmium(II)
CDI	Capacitive De-Ionization
CE	Counter Electrode
CMi	Center of Micronanotechnology
CNC	Computer Numerical Control
CNTs	Carbon Nanotubes
CO	Carbon monoxide
CO_2	Carbon dioxide
$CO_3{}^{2-}$	Carbonate
Cu(II)	copper(II)
CV	Cyclic Voltammetry

DI Water	De-Ionized Water
DRIE	Deep Reactive Ion Etching
ED	Electro Dialysis
EDX	Energy-Dispersive X-ray
ELISA	Enzyme-Linked Immunosorbent Assay
FDM	Fused Deposition Modelling
Fe(II)	Iron(II)
FEWS	Fiber-optic Evanescent Wave Sensors
FIA	Flow Injection Analysis
FME	Film Mercury electrode
GCE	Glassy Carbon Electrode
GIME	Gel-integrated microelectrode
GO	Graphite oxide
H_2	Hydrogen
HCl	Hydrogen Chloride
HDME	Hanging Drop Mercury Electrode
HF	Hydrogen fluoride
Hg	Mercury
H_2SO_4	Sulfuric acid
ICP	Ion Concentration Polarization
ILs	Ionic Liquids
IPA	Isopropanol
Ir	Iridium
IR	Infra-Red
IrO_2	Iridium Oxide

KCl	Potassium chloride
$K_3Fe(CN)_6$	Potassium ferricyanide
OGC-SWE	Open Geospatial Consortium-Sensor Web Enablement
LMTS	Microsystems for Space Technology Laboratory
LOD	Limit of detection
LPCVD	Low Pressure Chemical Vapor Deposition
LSV	Linear Sweep Voltammetry
MCDI	Membrane Capacitive De-Ionization
MED	Multi-Effect Distillation
Mg	Magnesium
MIR	Mid-Infrared
MJM	Multijet Modelling
Mn(II)	Manganese(II)
MSF	Multi-Stage Flash distillation
NaCl	Sodium chloride
$NaNO_3{}^-$	Sodium nitrate
$NO_3{}^-$	Nitrite
$NO_2{}^-$	Nitrate
NO_x	Nitrogen oxides
NP	nitrophenol
O_3	Ozone
PANI	Polyaniline
PANOA	poly(aniline-co-*o*-aminophenol)
Pb(II)	Lead(II)
PDMS	Polydimethylsiloxane

PECVD	Plasma-Enhanced Chemical Vapor Deposition
PEDOT-PSS	Poly(3,4-ethylenedioxythiophene) polystyrene sulfonate
PGMEA	Propylene glycol monomethyl ether acetate
pH	Potential of hydrogen
PMMA	Poly(methyl methacrylate)
POT	Poly(3-octylthiophene-2,5-diyl)
PPy	Polypyrrole
PSA	Pressure Sensitive Adhesive
Pt	Platinum
PTFE	Polytetrafluoroethylene
PVC	Poly(vinyl chloride)
RE	Reference Electrode
RO	Reverse Osmosis
SCHeMA	in Situ Chemical Mapping probe
SEM	Scanning Electron Microscopy
Si_3N_4	Silicon nitride
SLA	Stereolithography
SNaR	Nitrate reductase
SPE	Screen Printed Electrode
STX	Saxitoxin
SWASV	Square Wave Anodic Stripping Voltammetry
THF	Tetrahydrofuran
Ti	Titanium
TMs	Trace Metals
UNIGE	University of Geneva

UULM	University of Ulm
VIP	Voltammetric In situ Profiling
VOCs	Volatile Organic Compounds
WE	Working electrode
Zn(II)	Zinc(II)

Photographic credits

Curriculum vitae

CONTACT INFORMATION   MARIANNA FIGHERA

PERSONAL INFORMATION   EPFL-STI-IMT-LMTS
RUE DE LA MALADIÈRE 71B
2002, NEUCHÂTEL 2
SWITZERLAND
marianna.fighera@epfl.ch

EDUCATION

2013-2017   **École Polytechnique Fédéral de Lausanne (EPFL) –Switzerland**
Institute of Microengineering (Microcity)
PhD student in Mycrosystems for Space Technology Laboratory (LMTS)

2010-2013   **La Sapienza University of Rome – Italy**
MSc degree in Biomedical Engineering (110/110 cum laude)
Thesis title: Development of closed electrowetting systems with on-chip luminescence detection

2007-2010   **La Sapienza University of Rome – Italy**
BSc degree in Clinical Engineering (110/110)
Thesis title: Numerical characterization of TRIMprob device in presence of materials with different conductivity

2002-2007   **Liceo Scientifico De Ruggieri – Italy**
Scientific high school Diploma (100/100)

LANGUAGES

ITALIAN   FLUENT (MOTHER TONGUE)

SPANISH   FLUENT (AUTO EVALUATION C2)

ENGLISH   FLUENT (AUTO EVALUATION C1)
CERTIFIED B2 LEVEL: CAMBRIDGE ENGLISH FIRST CERTIFICATE - FCE

FRENCH   COMPETENT (AUTO EVALUATION B1-B2)

GERMAN   BASIC ELEMENTS (AUTO EVALUATION A1)
CERTIFIED A2 LEVEL: GOETHE INSTITUT FIT IN DEUTSCH 2

PUBLICATIONS

1. Fighera M., P.D. van der Wal, and H. Shea, *Microfluidic Platform for Seawater Desalination by means of Coulometric Removal of Chloride Ions through Printed Ag Inks Electrodes*, Journal of the Electrochemical Society, 164 (12): H836-H845, 2017. doi: 10.1149/2.1761712jes.

2. M. Fighera, P.D. van der Wal, M.-L. Tercier-Waeber, J.L. Kowal, and H. Shea, *New designed interconnected microelectrode arrays and their evaluation for trace metal detection*, (in preparation).

3. M.-L. Tercier-Waeber, S. Mongin, J.L. Kowal Justyna, M. Fighera, P.D. van der Wal, E. Bakker, *Hg(II) detection in natural waters: characterization of the species selectively quantified by voltammetry on antifouling gel integrated microelectrodes*, (in preparation).

4. M.-L. Tercier-Waeber, F. Confalonieri, M. Fighera, P.D. van der Wal, E. Bakker, *Lab-on-Cable for in situ real-time monitoring of the bioavailable fraction of a range of trace metals*, (in preparation).

CONFERENCES

1. Fighera M., P.D. van der Wal, and H. Shea, *Comparison of Six Printed Ag Inks for Coulometric Removal of Chloride Ions from Seawater: Towards an Integrated Microfluidic Platform for Desalination*, ECS Transaction, 75 (41) 1-12 (2017) - oral presentation at PRiME 2016, 2-7 October 2016, Honolulu, Hawaii.

2. Fighera M., P.D. van der Wal, M.-L. Tercier-Waeber, and H. Shea, *Three-Electrode on-Chip Sensors for Voltammetric Detection of Trace Metals in Natural Waters*, ECS Transactions, 75 (16) 303-314 (2016) - oral presentation at PRiME 2016, 2-7 October 2016, Honolulu, Hawaii.

3. Fighera M., van der Wal P.D., Shea H., *Feasibility study of coulometric chloride removal from seawater using inkjet and screen printed Ag electrodes* - Abstract accepted and poster presented at the 3rd Swiss e-Print Conference, 1-2 October 2015, Neuchâtel, Switzerland.

4. Fighera M., van der Wal P.D., Tercier- Waeber M.-L, Shea H., *Interconnected microelectrode arrays for trace metal detection in natural waters: fabrication and electrochemical characterization* – Abstract accepted and poster presented at the 13th International Estuarine Biogeochemistry Symposium, 7-10 June 2015, Bordeaux, France.

5. *FP7-OCEAN-2013 – SCHeMA: Integrated in situ mapping probes*, MTS/IEEE OCEANS 2015 - Genova: Discovering Sustainable Ocean Energy for a New Word, (2015), Genova, Italy.

PROJECT DELIVERABLES

1. Fighera M., P.D. van der Wal*,* Nardin C., Luxenburger F., D5.4- *Optimized microfluidic platform for VOCs and biotoxin preconcentration*, November 2016.

2. Fighera M., P.D. van der Wal*,* Nardin C., *D5.3- Development of a microfluidic platform for VOCs optical detection systems*, January 2016.

3. Fighera M., P.D. van der Wal*, D5.2- Microfluidic platform for biotoxin preconcentration*, September 2015.

4. Fighera M., P.D. van der Wal*, D5.1- New generation of interconnected and interdigitated microsensors and on-chip integrated three electrode system*, July 2015.

SUMMER SCHOOLS

1. SCHeMA summer school, 14-16 June 2016, Marine Station in Plentzia, Bilbao, Spain – oral presentation "From nano to macro...micro-technology solutions for sensors and microfluidic systems development".

2. 9th Nano and Micro Systems International School (NAMIS) – 29 June–3 July 2015, Polytechnique de Montreal, Montréal, Canada.